UNIVERSITY OF GLASGOW

Facial Shape Analysis

by

Liberty Vittert

A thesis submitted in fulfillment for the
degree of Doctor of Philosophy

in the
School of Mathematics and Statistics

September 2015

Declaration of Authorship

I, Liberty Vittert, declare that this thesis titled, 'Facial Shape Analysis' and the work presented in it are my own. I confirm that:

- This work was done wholly while in candidature for a research degree at this University.
- Where any part of this thesis has previously been submitted for a degree or any other qualification at this University or any other institution, this has been clearly stated.
- Where I have consulted the published work of others, this is always clearly attributed.
- Where I have quoted from the work of others, the source is always given. With the exception of such quotations, this thesis is entirely my own work.
- I have acknowledged all main sources of help.
- Where the thesis is based on work done by myself jointly with others, I have made clear exactly what was done by others and what I have contributed myself.

Signed: _____

Date: _____

"I was gratified to be able to answer promptly, and I did. I said I didn't know."

Mark Twain

UNIVERSITY OF GLASGOW

Abstract

School of Mathematics and Statistics

Doctor of Philosophy

by Liberty Vittert

Stereophotogrammetric imaging systems produce representations of surfaces (two-dimensional manifolds in three-dimensional space) through triangulations of a large number of estimated surface points. Traditional forms of analysis of these surfaces are based on point locations (manually marked anatomical landmarks) as described in Chapter 1. An advanced application of these types of landmarks will be thoroughly examined in Chapter 2 through the concept of Ghost Imaging. The results of this chapter necessitated a reliability study of stereophotogrammetric imaging systems which is discussed in Chapter 3. Given the results of the reliability study, an investigation into new definitions of landmarks and facial shape description is undertaken in Chapter 4. A much richer representation is expressed by the curves which track the ridges and valleys of the dense surface and by the relatively smooth surface patches which lie between these curves. New automatic methods for identifying anatomical curves and the resulting full surface representation, based on shape index, curvature, smoothing techniques, warping, and bending energy, are described. Chapter 5 discusses new and extended tools of analysis that are necessary for this richer representation of facial shape. These methods will be applied in Chapter 6 to different shape objects, including the human face, mussel shells, and computation imaging comparisons. Issues of sexual dimorphism (differences in shape between males and females), change in shape with age, as well as pre and post facial surgical intervention will be explored. These comparisons will be made using new methodological tools developed specifically for the new curve and surface identification method. In particular, the assessment of facial asymmetry and the questions involved in comparing facial shape in general, at both the individual and the group level, will also be considered. In Chapter 7, Bayesian methods are explored to determine further ways in which to understand and compare human facial features. In summary, this thesis shows a novel method of curve and full facial mesh identification that is used, successfully, in pilot case studies of multiple types of surfaces. It then shows a novel proof of principle for using Bayesian methods to create a fully automatic process in facial shape characterisation. In order to view this thesis in full, please view in Adobe Reader.

Acknowledgements

I offer my profoundest gratitude and admiration to my supervisor, Professor Adrian Bowman. Without his integrity, graciousness, patience, and unreserved kindness, this thesis would never have been completed. From observing and being the honoured recipient of an extensive amount of his valuable time, I have seen time and time again the manner in which he chooses to conduct himself with others, a manner that can only be described as profound altruism. I have been privileged to be his student.

To my Mother, Father and Lucky thank you for your unwavering support and love.

To Craig and Henry, for always having confidence in me and making every day brighter.

Contents

List of Figures

List of Tables

For my father.

Chapter 1

Introduction

1.1 Motivation for Studying Three-dimensional Facial Shape

While there are certain undeniable commonalities between human faces and features, there is an immense complexity of shape that identifies and defines each of us as a unique individual - as normal, abnormal, attractive, or even unattractive - all within a glance. One can tell gender, age, ethnic background, and potentially a host of other interesting factors about an individual simply from a first glance. In order to describe a face sufficiently, it must be compared to other faces, potentially within the same gender, age group, ethnic group, etc. Faces are highly complex 2-dimensional manifolds, meaning the ability to accurately map these three-dimensional objects requires quite specific statistical and computational methods.

The applications of facial shape analysis are varied, but have an especially necessary function in the medical field, including characterising individuals with specific diseases or illnesses or defining the success of surgical intervention. In this thesis there will be an example of statistical tool development for an investigation into the quantitative assessment of orthognathic surgery (*surgery of the jaw*). A comparison is conducted not only between pre- and post-intervention facial shape, but also between the post-intervention facial shape and a control group facial shape. Both analyses are necessary to fully determine the success of the surgery. This creates a need not only to quantify the facial shape of surgical intervention patients, but also to construct a database that characterises and quantifies control facial shape.

A potential aim of analysis is to produce better surgical outcomes by identifying the facial shape differences that still exist between post-surgical intervention and a control group. The nature of the problem may be clear but the quantification of it is not.

Surprisingly, it can be quite unclear what exactly is 'different' or precisely 'amiss' with a pre-surgical face. A tool that determines the quantitative differences between a pre-surgical intervention facial shape and the control facial shape could lead to a more precise understanding of the surgical aims. This could lead to producing better surgical outcomes and a need for fewer procedures.

Hammond et al. [2004] describe facial 3D morphology by using dense surface models in order to provide visualisations of facial shape variation (especially for particular syndromes) for training physicians. Using a database of controls, as well as patients with Noonan syndrome (an autosomal congenital disorder) and patients with velo-cardio-facial syndrome, the study aims to help inexperienced clinicians make more immediate diagnoses in young children or help identify facial features should the clinician have had limited experience with a particular syndrome. Allanson et al. [1993] document characteristic features and the change in these features over time for individuals with Down's syndrome; Allanson and Hennekam [1997], for those with Rubinstein-Taybi syndrome; and Loos et al. [2003], for those with Cornelia de Lange syndrome. This thesis will describe the many applications of facial shape analysis given a richer description of facial shape as detailed in Chapter 4.

1.2 How is Facial Shape Captured and Classically Defined

Three-dimensional surface imaging techniques have a rapidly expanding range of applications in diverse medical and scientific fields. Their use in craniofacial imaging has improved surgical planning, assessment of outcomes, and the study of pathologic and normal morphology, as well as growth and development. This technology is already being used to delineate facial dimensions in pathologic states and there are several systems commercially available. The ©Di3d 3D facial image capture system is a passive stereo photogrammetry solution for the creation of accurate, high-resolution, full colour 3D facial surface images. The data that is retrieved from the image capture is a collection of multiple polygonal meshes and accompanying colour maps (Figure 1.1).

Shape is defined as the geometrical information that remains when the effects of location, scale, and rotation are removed from an object [Dryden and Mardia, 1998]. In order to compare different shapes Procrustes Analysis is used, which filters out translation (location), scale, and rotational effects. There are two types of Procrustes Analysis: Ordinary Procrustes Analysis which compares one shape to one other shape, or compares each of a set of shapes to one arbitrary reference shape; and General Procrustes Analysis which simultaneously compares a set of objects, producing a reference shape that is optimally determined, a so-called 'mean shape'.

There are different ways in which these objects or sets of objects can be represented for comparison. An object can be represented by surface methods that are computer generated or as a set of discrete points capturing the geometrical information of the given form using vertices, control points, etc. In the following section the traditional method of representing facial shape as well as key characteristics of surface shape are discussed.

1.2.1 Landmarks

Facial objects are traditionally represented by landmarks, which are points of correspondence on all the observed objects that match between and within all interested populations. Let $X = x_{ij}$, where $i = 1, \ldots, k$ and $j = 1, \ldots, m$ such that the object χ with k landmarks in m dimensions is represented by matrix X.

A widely recognised set of anatomical landmarks for the human face is detailed in Farkas and Schendel [1995]. These anatomical landmarks each determine an anatomically significant location on the surface of the face, (e.g. the tip of the nose). The 25 landmarks that are manually marked on all faces in the control data set used in this thesis are listed

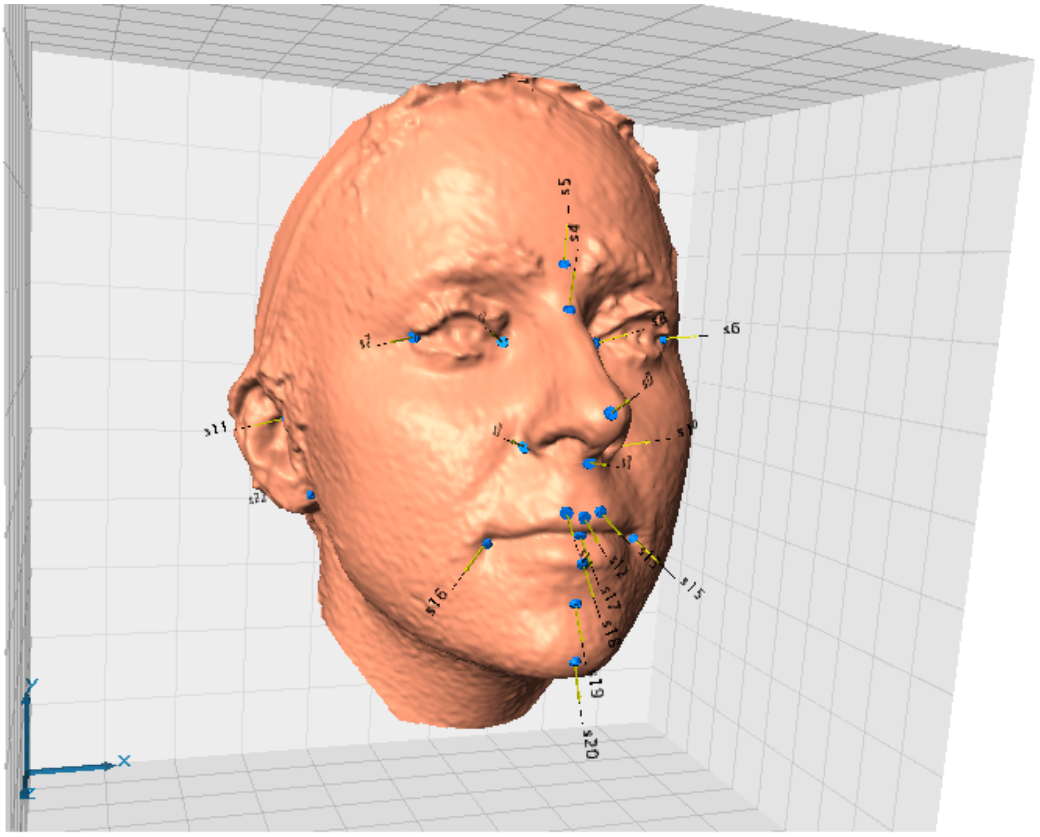

FIGURE 1.1: Visualisation tool for landmarking [McNeil, 2012]

in Table 1.1. Each facial image captured from the camera system was loaded into a software package called ©Landmark, developed by the IDAV (*Institute for Data Analysis and Visualisation*), which allows the facial image to be visualised in three-dimensions and manually landmarked. This virtual three-dimensional image can be rotated in any direction. Specific areas of interest can also be magnified in order to view the facial surface from every angle. When identifying anatomical landmarks, the ability to view the facial shape in this way is highly advantageous, especially when identifying points of maximum curvature, such as the *pronasale* landmark on the nose.

TABLE 1.1: Anatomical Landmarks for Control Participants

Code	Region	Side	Abr.	Name
SO	nose	middle	pn	*pronasale*
S1-S2	nose	left/right	a	*alare*
S3-S4	nose	left/right	ac	*alare crest*
S5	nose	middle	sn	*subnasle*
S6	nose	middle	se	*sellion*
S7	nose	middle	n	*soft tissue nasion*
S8-S9	eye	left/right	ex	*exocanthion*
S10-S11	eye	left/right	en	*endocanthion*
S12-S13	ear	left/right	t	*tragion*
S14	middle	middle	ls	*labiale superius*
S15-S16	lips	left/right	cph	*crista philtri*
S17-S18	lips	left/right	ch	*cheilion*
S19	lips	middle	sto	*stomion*
S20	lips	middle	li	*labiale inferius*
S21	chin	middle	sl	*sublabiale*
S22	chin	middle	pg	*soft tissue gnathion*
S23-S24	ear	left/right	a	*otobasion inferrius*

Once all landmarks are manually identified on the object these landmarks are represented as matrices $X_{3\times k}$. For analysis translation effects are removed by locating the mean (centroid) of all the object's landmarks at the origin, and scale effects removed by scaling the objects such that the root mean square distance (RMSD) from all points to the translated origin (centroid size) is 1 (or the average centroid size). Lastly, rotation effects are removed by using one object as the reference shape and rotating the other object(s) about the translated origin until an optimal angle of rotation is achieved such that the sum of squares distance between the corresponding points is minimized. The error that exists as a result of manual landmarking will be discussed in Chapter 3.

1.3 Surface of a Shape

Landmarks are the traditional method used in analysing shape, but there is a significant amount of information about a shape that is lost when only landmarks are used. Figure 1.2 is the shape that is represented solely by landmark information. This is barely, if at all, recognizable as a human face.

There are other characteristics of shape that are not used in traditional landmarking methods. For example, both the type and strength of curvature of a surface has a significant amount of detail. These concepts have already been deeply explored by Koenderink and Doorn [1992]. Local shape [Koenderink and Doorn, 1992] can be described at any point on a surface as

$$z = \frac{1}{2}(\kappa_1 x^2 + \kappa_2 y^2), \tag{1.1}$$

where the orthogonal axes x, y lie on the tangent plane and z lies in the normal or perpendicular plane. These axes are defined relative to the point of interest on the surface and will change as this surface point is changed. The tangent axes correspond to

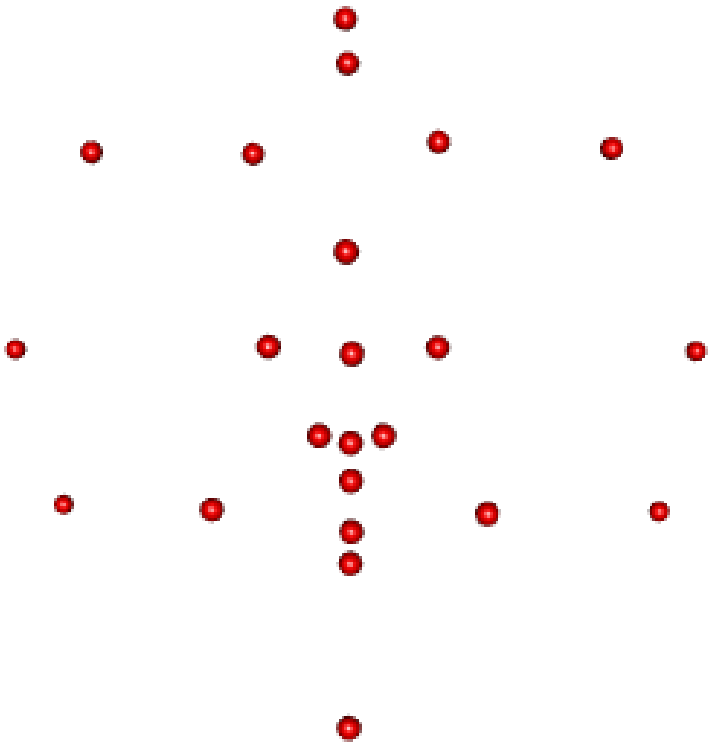

FIGURE 1.2: 3-dimensional anatomical landmarks from a face

the directions of the principal curvatures (κ_1 and κ_2, where $\kappa_1 \geq \kappa_2$), which document the largest and smallest rates of bending of that particular surface.

There exists a significant amount of study in categorizing 2D manifolds (especially in the context of $3D$ face recognition [Huang et al., 2006]). The differential structure of the manifold is defined by the local Hessian matrix. The principal curvatures of the surface are the eigenvalues of the Hessian matrix. Shape index (S) is a quantifiable measure which describes the type of curvature at any point, while the strength of curvature, the principal curvatures, independent of the location and orientation of the surface, give a complete description of shape. This index which characterises local surface shape in a systematic and interpretable manner is defined as

$$S = \frac{1}{2} - \frac{1}{\pi} arctan \left(\frac{\kappa_1(p) + \kappa_2(p)}{\kappa_1(p) - \kappa_2(p)} \right). \tag{1.2}$$

Notice that the shape index (S) is a function of the ratio of κ_1 and κ_2, such that S describes the type, but not the size of the curvature. The curvedness at point p is defined as

$$K(p) = \sqrt{\frac{\kappa_1^2(p) + \kappa_2^2(p)}{2}}$$

where κ_1 and κ_2 are the principal curvatures at fixed point p. Gaussian curvature is used to describe the strength of curvature at any point on the surface such that

$$G = \kappa_1 \kappa_2.$$

The surface normals are approximated [Koenderink and Doorn, 1992] by averaging the crossproducts of neighbouring points (with the averaging helping to reduce the noise found in the 'orange peel effect') with an arbitrary choice of tangent plane directions. Using a least squares approach based on a cubic model and no linear terms, the eigenvectors and values are found giving directions to the gradients around the point of interest, thereby defining the shape index at every point on the surface. Values of S close to -1 indicate a 'spherical cup' with the principal curvatures being positive. As S increases to 0 the surface bends smoothly through 'trough', 'rut', and 'saddle' shapes until S becomes positive toward the value of 1. The process is reversed as the surface moves toward a 'spherical cap'. As illustrated in Figure 1.3, Koenderink and van Doorn (1992) [Koenderink and Doorn, 1992] give the ranges of S with a description of the associated type of shape and the matching verbal descriptors and colour coding.

When viewing a 3-dimensional facial image coloured by its shape index (constructed by simply fitting a quadratic surface to each surface point within a 1cm radius of each of the surface point locations), the shape index colour descriptors clearly indicate the

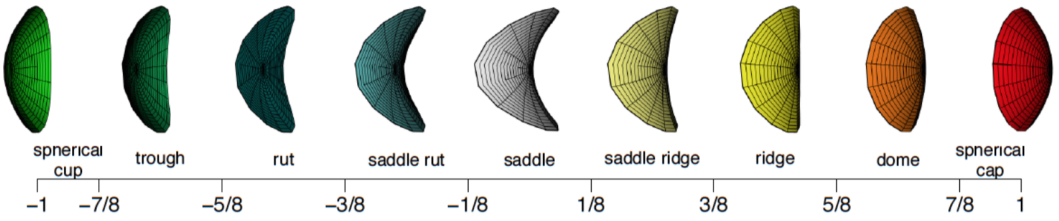

FIGURE 1.3: The local surfaces associated with the shape index on the scale from -1 to 1, with colour coding to identify each shape category [Katina, 2015b].

different major facial features. This creates the prospect of identifying landmarks based upon these major facial features. This means that in order to identify these landmarks, there are two points to consider. First, facial curves that track the valleys and ridges of the surface must be found since the landmarks lie at the crossings of these curves. Second, each landmark will be defined as the surface point where these two curves have the strongest curvature or bend. Informally, a *ridge* is defined as a continuous set of points, each of which has a shape index appropriate to a ridge point and which locally has a stronger ridge shape index than neighboring values that are at right angles to the direction of the ridge at that location [Katina, 2015b]. A *rut* can be described in the same manner, but using the opposite values on the shape index scale. Moreover, it is necessary to further examine the definition of the curvature of a curve and what the bending of a curve means. A precise definition given by Koenderink et al. [Koenderink and Doorn, 1992] shows that the curvature K at any point on the arc length (s) of the curve defined by $x(s), y(s), z(s)$, is

$$K(s) = \frac{\sqrt{(z''y' - y''z')^2 + (x''z' - z''x')^2 + (y''x' - x''y')^2}}{(x'^2 + y'^2 + z'^2)^{\frac{3}{2}}}. \tag{1.3}$$

Given this method of describing shape as opposed to landmarks, Figure 1.4, a much richer and more descriptive way of viewing the face is available. New methods analysing the type of curvature of a surface are not prevalent. However, Bonde et al. [2013] developed Multi Scale Shape Index (MSSI) which again associates different types of shape to a real valued index. The difference being that MSSI uses closed form scale space equations that then compute a characteristic scale at every 3D point of a point cloud (not a specific 3D mesh surface), and this scale is then used to estimate the shape index. However, for the purposes of analysis, these 3D mesh surfaces are sufficiently defined.

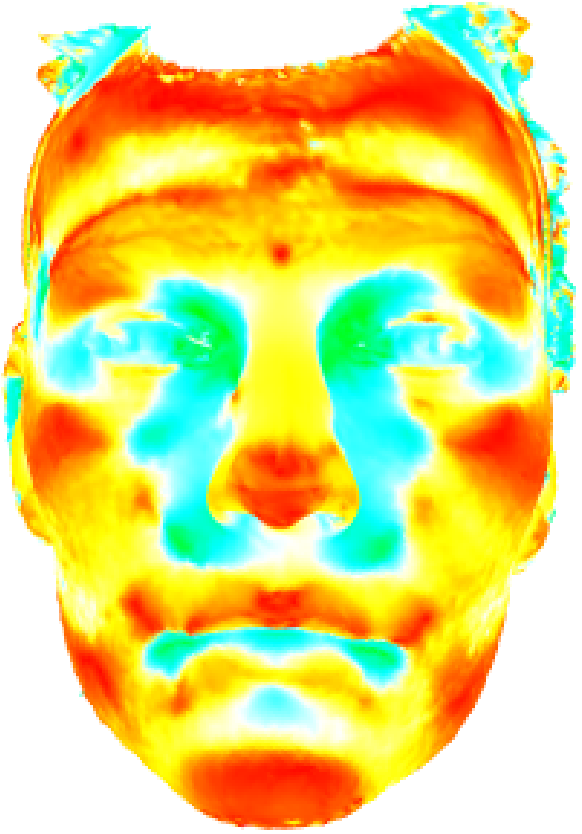

FIGURE 1.4: Facial image coloured by shape index

1.4 New concepts in Analysing Shape

There have been recent attempts to determine new techniques to utilise the information gained from 3D facial image surfaces beyond simple manual landmark configurations. As will be discussed in Chapter 3, there is error associated with manual landmarking. Naftel and Trenouth [2004] use an automated approach which combines a stereo-assisted active shape model for 3D landmark extraction. It incorporates an active shape detection phase for the automatic localisation of 2D facial features in greyscale stereo images. Use of those detected features create new 3D soft tissue landmarks through stereo correlation matching and disparity map interpolation. An error of $0.5 - 1.0$mm is achievable using this method.

Samir et al. [2006], given a 3D facial surface, are able to represent these surfaces by unions of level curves and then compare these shapes implicity through a differential geometry approach. This approach defines facial curves to be closed, arc-length parameter, planar curves rescaled to length 2π and then computes the geodesic lengths between these closed curves on the manifold.

Hennessy et al. [2002] use 3D laser surface scanning with geometric morphometric analysis to examine sexual dimorphism. The aim of this is to determine potential craniofacial dymorphogensis and when disturbances in schizophrenia are exhibited. After manually landmarking with the standard anatomical landmarks, but with aid in locating some landmarks (surface curvatures), the local surface properties near that location were determined by a surface fitting method using Gaussian curvature and shape index as a descriptor. While only two landmarks are determined through this process, soft tissue *nasion* and *sublabiale*, it begins to extend the concept of anatomical facial curves as a configuration to describe 3D facial shape.

In addition to the concept of automatic landmarking, there is a distinct interest in identifying anatomical curves of the face from either manually or automatically identified landmarks. A significant amount of information is lost on the surface of the facial image when just using landmarks as seen in Figure 1.4 versus Figure 1.2. Anatomical curves provide a much richer expression of facial shape. Bowman et al. [2014] use principal curves to navigate across the anatomical surface in 3D, use an assessment of curvature in order to recognise the relevant boundary of the surface patch of interest and use change-point detection to assess the evidence for the presence of the surface feature of interest.

This thesis will attempt not only to identify a novel method of using the facial surface information to obtain automatic landmarks, but also define new methods to identify anatomical curves from a dense facial surface (Chapter 4). This enables the construction of a full facial mesh that completely defines the surface of the face: a novel method. From that new tools of analysis are developed and old tools are extended in order to encompass the additional information found by the novel method in Chapter 4. Finally, this facial shape description and tools are used in multiple case studies in order to prove the efficacy of the methods.

In Chapter 2 an advanced application of landmarks will be demonstrated that resulted in a paper being being published in *Science* [Sun et al., 2013].

Chapter 2

Computational 3D Ghost Imaging - Advanced Landmarks

2.1 3-Dimensional Computational Ghost Imaging

There are many applications resulting from the invention of 3-dimensional camera imaging systems and the analysis that arises from comparing landmark configurations of different facial shapes. One such application undertaken is the comparison of a new concept of ghost imaging (imaging without a camera) to a 3-dimensional ©Di3D imaging system.

The Optics group in the School of Physics at the University of Glasgow developed a system of ghost imaging, where a 3-dimensional image can be taken without the use of a camera, but rather with a single-pixel detector using a measurement of light reflection. Using several single-pixel detectors in different locations, the information in the total light collected allows the 3-dimensional object to be reconstructed. Sun et al. [2013] compare an object produced by the ghost imaging system (Figure 2.1) and one produced by the ©Di3D stereo-photogrammetric camera system.

Computational imaging (GI or ghost imaging) enables the retrieval of the spatial information of a free form object with the use of single-pixel detectors. GI removes the need for a spatially resolving detector and uses an algorithm which correlates the spatial information of a changing light field with the reflected light intensity. With the projection of known, random light patterns and then the measured backscattered intensity, multiple 2-dimensional images are reconstructed. These multiple 2-dimensional images are taken from each single-pixel detector (all appearing to be illuminated differently)

and the shadow information in the images creates a surface gradient from which a 3-dimensional image can be reconstructed. This 3-dimensional image is then compared to the ©Di3D stereophotogrammetric system.

In order for the reciprocity to be maintained between this computational imaging system and photometric stereo (uses multiple images but each with a different illumination taken from the same viewpoint) the brightness of an image must depend on the angle between the surface of the object and the non-imaging element rather than the angle between the surface and the imaging piece. This is inherent to the use of single pixel detectors. The general rule is that the brightness of an object is independent of the viewing angle, in which case, all the detectors should obtain the same image. Using the single pixel detectors, the luminance of the image depends on the different angle, resulting in different images to each detector.

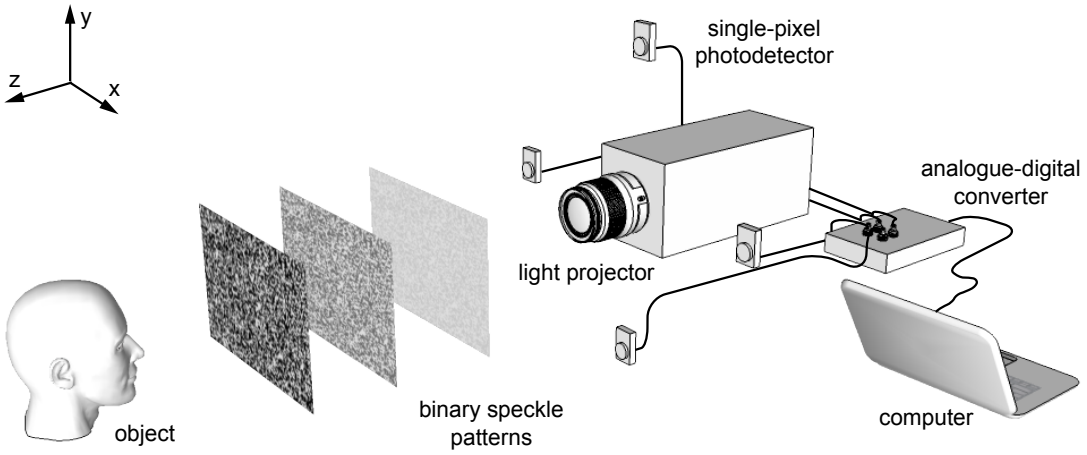

FIGURE 2.1: 3D computational ghost imaging system - the light projector projects the randomly generated binary speckle pattern onto the object (foam mannequin), whereby the light is then collected by the four single-pixel photodetectors. These signals are then measured and reconstructed into a 3D object description [Sun et al., 2013]

Many previous experiments in single-pixel computational imaging [Bromberg et al., 2009] use only small (< 10 cm) 2D images, but this experiment aims to capture a 3D object by having several single-pixel detectors placed in different areas relative to the 3D object.

This particular setup involves a digital light projector which then illuminates the object (under binary speckled patterns of a white black 1-1 ratio), the four, single-pixel detectors which measure the light intensity, an analogue-to-digital converter to digitize the photodetector signals, and then a computer which does the actual construction of the multiple images into a 3D surface and generates the random speckle pattern Figure 2.1.

The 2-dimensional object is rendered through an algorithm which averages, over many iterations, the product of the measured photodetector signal and the incident pattern. The 2D rendering (an estimate of the object) is

$$I(x,y) = \frac{1}{M}\sum_{i}^{M}(S_i - \hat{S}_i)(P_i(x,y) - P_i(\hat{x},y)) \tag{2.1}$$

where M is the length of the sequence of binary patterns $P_i(x,y)$ reflected from the object giving S_i, the sequence of measured signals. From the four single pixed photodetectors, 4 2-dimensional reconstructions are found using Equation 2.1. Since all four images are derived from the same set of projected patterns, the (x,y) locations are precisely the same for every image. An extension of the 'shape from shading' technique [Horn and Brooks, 1989] uses the four 2-dimensional images to create a surface gradient based upon shadows of the geometric features in order to construct a depth for each image. The intensity of a single pixel $I(x,y)$, obtained for the i^{th} detector is

$$I_i(x,y) = I_s\alpha(\hat{d}_i \cdot \hat{n}) \tag{2.2}$$

where α is the surface reflectance, $\hat{d}_i$ is the unit illumination vector pointing from the detector to the object, I_s is the source intensity, and $\hat{n}$ is the surface normal unit vector of the object. From this, the gradient between adjacent pixels is obtained, hence rendering the surface geometry by integrations [Sun et al., 2013]. Once this is done, an optimisation step further clarifies the object by setting each individual pixel height such that it matches the mean estimate from each of its nearest neighbours for each iteration.

2.2 Analysis

The question arose about which object to use to compare the ghost imaging system and the Di3D camera system. The ghost imaging system is most effective with a white object, whereas the Di3D system needs surface texture (a surface which is continuous with no holes) from which to reconstruct a useable surface estimate. A speckled light pattern was focused on the object during imaging to try to create surface texture, but the flashes of the camera system obscured this. After experimenting with fake skulls, styrofoam balls, a bust, and a styrofoam mannequin's head (dimensions 190mm $\times$ 160mm $\times$ 250mm), the mannequin produced the best reconstruction. The ghost image 3D reconstruction of the white mannequin was taken first, then painted red with watercolour paint (texture creation) for use in the stereophotogrammetric camera system. The camera system produces a high quality reconstruction with accuracy errors discussed in Chapter 3.

2.2.1 Ordinary Procrustes Analysis

Configurations of the landmark coordinates listed in Section 1.2.1 are unique to each facial image. There is no common origin or size across these configurations. They are therefore independent and not comparable to each other. Procrustes analysis methods (Ordinary and General Procrustes Analysis) can be used to standardise these configurations to the same origin and size in order to compare these configurations.

Ordinary Procrustes Analysis (OPA) is the optimal superimposition of two objects, or two landmark configurations. Considering that shape is described as '*all the geometrical information about X that is invariant under location, rotation and isotropic scaling (Euclidean distance transformations)*' by Dryden and Mardia [1998], in order to compare these objects the effects of translation, scale and rotation must be removed.

Consider two configuration matrices X_1 and X_2, both $k \times m$ matrices where k is the number of landmarks and m the number of dimensions for each configuration. Assume that both X_1 and X_2 have been centred in order to give a proper pre-shape. Using least squares matching of the two configurations (by the similarity transformations), the optimal similarity parameters can be identified by minimizing the squared Euclidean distance

$$D^2_{OPA}(X_1, X_2) = \left\| X_2 - \beta X_1 \Gamma - \mathbf{1}_k \gamma^T \right\|^2 \tag{2.3}$$

where $\|X\| = \sqrt{trace\,(X^T X)}$ is the Euclidean norm. β is a scale parameter, $(\beta > 0)$, Γ is a $(m \times m)$ rotation matrix $(\Gamma \in SO(m))$ and γ is an $(m \times 1)$ location matrix.

The minimum of Equation 2.3 is the Ordinary Procrustes Sum of Squares, $OSS(X_1, X_2)$, given by $(\hat{\gamma}, \hat{\beta}, \hat{\Gamma})$ where

$$X_2^T X_1 = \|X_1\| \|X_2\| V \lambda U^T$$

with $U, V \in SO(m)$ and λ a diagonal $m \times m$ matrix of positive elements except for potentially the last element and

$$\beta = \frac{trace(X_2^T X_1 \hat{\Gamma})}{trace(X_1^T X_1)}.$$

Therefore, given $\rho(X_1, X_2)$ as the Procrustes distance (the closest great circle distance between the two pre-shape space configurations on the pre-shape sphere)

$$OSS(X_1, X_2) = \|X_2\|^2 sin^2 \rho(X_1, X_2).$$

Therefore, the Procrustes coordinates of X_1 can then be written as

$$X_1^P = \hat{\beta} X_1 \hat{\Gamma} + \mathbf{1}_k \hat{\gamma}^T, \tag{2.4}$$

where the superscript P denotes the Procrustes superimposition of X_1 onto X_2. The residual matrix after Procrustes matching is defined as

$$R = X_2 - X_1^P, \tag{2.5}$$

which is simply the Procrustes registered configuration subtracted from the reference figure. We define the Ordinary Procrustes Sum of Squares (OSS) as

$$OSS = \|\hat{A} - \hat{B}\|^2$$

where $\hat{A}$ is the centred configuration of the reference figure and $\hat{B}$ is the Procrustes registered configuration B which was transformed.

The residual matrices give an interpretation of the difference in the shape of the two objects. If there are large residuals limited to one region of the shape, then it could explain a large difference between the two facial shapes in that particular area as opposed to the rest of the facial shape.

Ghost imaging produces a height map in z coordinates (relative height, not absolute) with a set x-scale of 20cm and a y-scale of 27cm. After creating vertices and triangulating these distances a file is created which reads the ghost image as a mesh in the same way the camera system does for the camera image. In order to perform Ordinary Procrustes Analysis (translating and rotating the ghost image to match the camera image as closely as possible) a scaling is applied to the z-axis of the ghost image and optimized over this scaling in order to be able to perform the best matching possible between the ghost image and camera image. The Root Mean Square Distance (RMSD) is defined as

$$RMSD = \sqrt{\frac{OSS}{k}}$$

where k is the number of landmarks in the configuration.

The head mould is scaled differently for both 3D imaging systems. Scaling in the x and y directions are clear, but the depth scale (z) needs to be examined more closely. Ghost imaging produces a height map in the z-direction, but lack of knowledge of the reflectivity sufficient means that the height measurements are relative rather than absolute. Therefore, while the distance in the x-direction and the y-direction are specified, scaling in the z-direction needs to be considered. The aim for analysis is to minimise

the Ordinary Procrustes Sum of Squares (OSS). In order to do this, the ghost landmark configuration is multiplied by a diagonal rotation matrix where the z-coordinate is a parameter β over which the OSS can be minimised. Figure 2.2 illustrates both images, the one produced by the ghost image, scaled, and that produced by the camera.

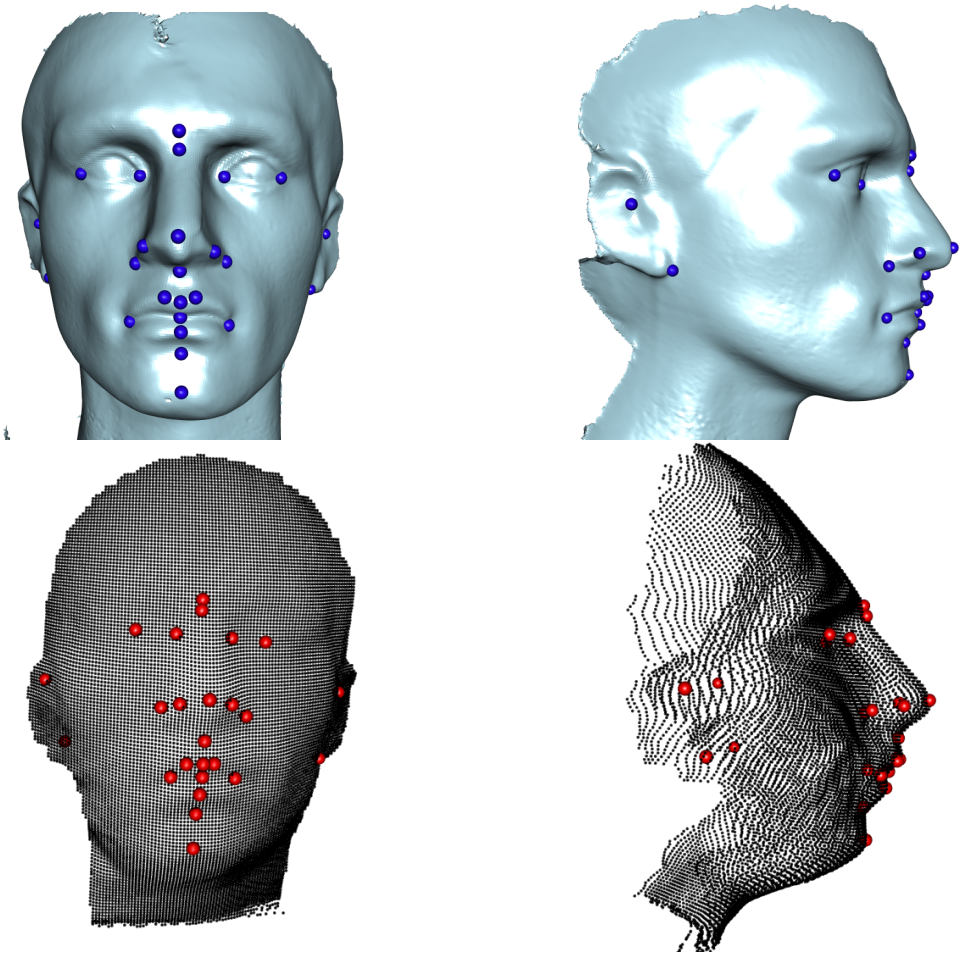

FIGURE 2.2: Midsagittal view (top left) and Coronal view (top right) of the original camera image - Midsagittal view (bottom left) and Lateral view (bottom right) original ghost image with the 25 anatomical landmarks

2.2.2 Comparisons

Multiple comparisons are performed between the stereocamera image and the ghost images. Figure 2.3 shows the Procrustes matched figures, with the light green face and green landmarks representing the stereocamera reconstruction and the pink with red landmarks representing the ghost image configuration. Notice that the ghost image is 'pulled back' in almost a cone-like manner, potentially due to the algorithm of the ghost imaging system which assumes a beginning cone-like shape.

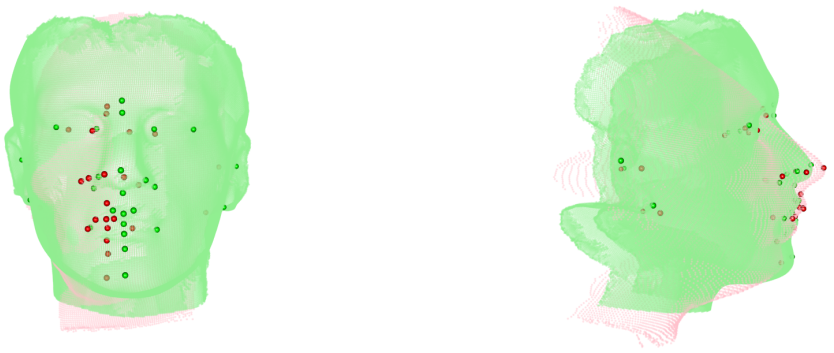

FIGURE 2.3: Comparison 1 Midsagittal view (left) and Coronal view (right) comparison

After this initial comparison, the stereocamera image is compared with four new ghost images which all have different background subtractions to try to adjust for the cone distortion. Table 2.1 shows the RMSD values of the original stereocamera image compared with the ghost image.

TABLE 2.1: Root Mean Square Distance of Ghost Landmark configurations matched to original 3D stereocamera image(mm)

Image	With Ear Landmarks	Without Ear Landmarks
original	9.77	7.91
depth 1	10.58	6.34
depth 2	10.46	5.82
depth 3	10.37	6.47
depth 4	10.36	7.16

The findings of the reliability study, discussed in Section 3.2, shows a distinct lack of definition around the ear region. In the ghost image, the ears are particularly problematic, most likely as a result of the projected pattern expanding at a greater depth [Sun et al., 2013]. Therefore, the ear landmarks are removed (Figure 2.4). While this significantly decreases the RMSD (by almost half in some cases), it means that comparison is limited to the front of the face. This does, however, support quantitatively the hypothesis that the ghost imaging system stretches the object back significantly, shown clearly in a larger z scale (*pronasale* to *otobasion* or *tragion*).

For the final comparison, the initial 'cone-shape' algorithm distortion is changed, the scaling issues in the x-direction and y-direction are decided upon, and the pixel dimension is set. The inaccuracy around the ears due to the expansion of the projected pattern is minimised by using a lens with a suitable focal length for projection. The

FIGURE 2.4: Comparison 2 of Midsagittal view (left) and Coronal view (right) without ear landmarks

pixel dimension relates the the scaling issues in the x-direction and y-direction. The ghost image system does not just receive height values of the head mould, but of a set rectangle (in this case 300 cm by 300cm). Choosing the exact dimensions of the ghost image takes experimentation, but is decided upon by the minimum RMSD. All of this results in a significantly better match between the two images. The final ghost image rendering is shown in Figure 2.5. The final matching (excluding the ear landmarks), produces a RMSD of 3.92mm.

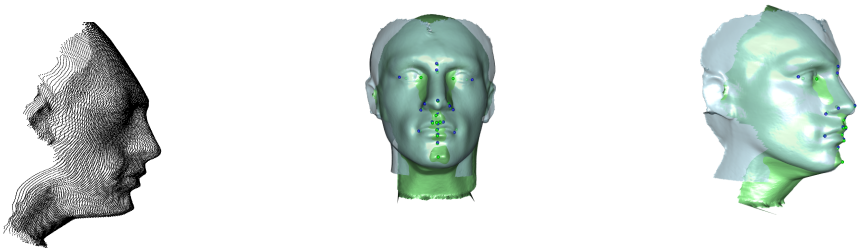

FIGURE 2.5: Ghost Image (green) and stereo-photogrammetric (blue) reconstructions with 21 anatomical landmarks(colour-coded blue and green respectively) and final ghost image rendering (far left)

2.2.3 Revision to Lambertian Surfaces, etc.

Lambertian reflectance is the property that defines an ideal diffusely reflecting surface reflection of light such that an incident ray is reflected at many angles rather than just one angle. The observed brightness of a Lambertian surface to the observer is the same regardless of the angle from which the observer is viewing the object, i.e. constant across the surface of the object. As stated by Tagare et al. [1991], the surface's luminance is isotropic, and the intensity of the luminance must obey Lambert's cosine law.

It is important to note that this surface reflectance is of a Lambertian nature. The reflected intensity as a function of the angle (single-pixel detector position) for a flat surface made of the same material as the head mould is measured. There is close agreement between this reflectivity curve and the theoretical curve representing Lambert's cosine law for luminous intensity. All of the data are recorded through cross polarizers in the illumination and detection apparatus, removing all specular reflections. It then follows that the head mould is also of a Lambertian nature.

Showing that the head mould is Lambertian, the concern arises of whether the images are reciprocal (perspective and shading match) with a conventional camera. The light travels in opposite directions for the two imaging systems, but for computational imaging systems, the imaging component is the projector and the detector is the non-imaging element. This allows for the rule that the luminance of the image depends on the angle between the surface and non-imaging element as discussed previously.

Following these changes, images are obtained which are the the result of two more iterations. This action produces a less accurate image in terms of RMSD than that previously taken without ear landmarks RMSD of 5.03mm and with ear landmarks of 8.28mm shown in Figure 2.6.

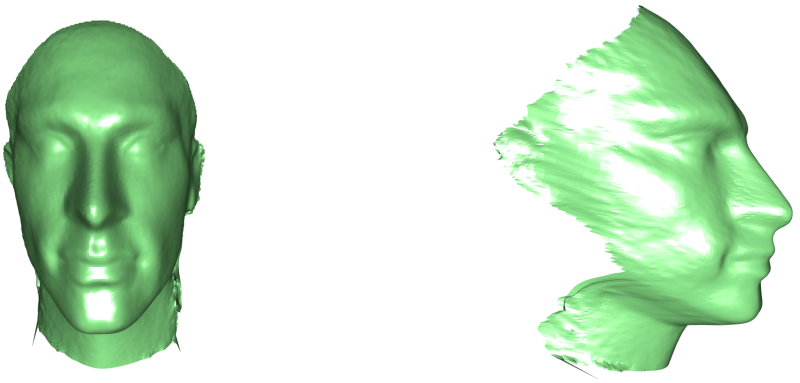

FIGURE 2.6: Midsagittal view (left) and Lateral view (right) Data 2 Ghost Image

Recall the integration method of the reconstruction algorithm which created the ghost image. After integration is performed, providing an initial estimate of the shape of the object, there is an optimization step which refines the shape, where the cost function is the sum of the squared differences between the gradients of the reconstructed surface and the gradients recovered from the photometric stereo system, working one pixel at

a time. Every iteration sets the pixel's height such that it matches the mean estimate from each of its nearest neighbors.

This means that the optimisation stage, applied to the recovered 3D surface post-integration, sets the Laplacian of the reconstructed height field equal to the Laplacian calculated from the measured gradient data. For the pixels at the edge of the object (where some information can be lost), this is equivalent to assuming the gradient measured perpendicular to the edge of the object is accurate [Sun et al., 2013]. Finding the less accurate results puzzling, the image is retaken four times. Each time, the head mould, which is lying on its side, is rotated in an upward angle i.e. the direction of the face pointing towards the sky. The results are significantly better with an ear landmark RMSD of 7.42mm and without ear landmarks RMSD of 3.93mm, illustrated in Figure 2.7.

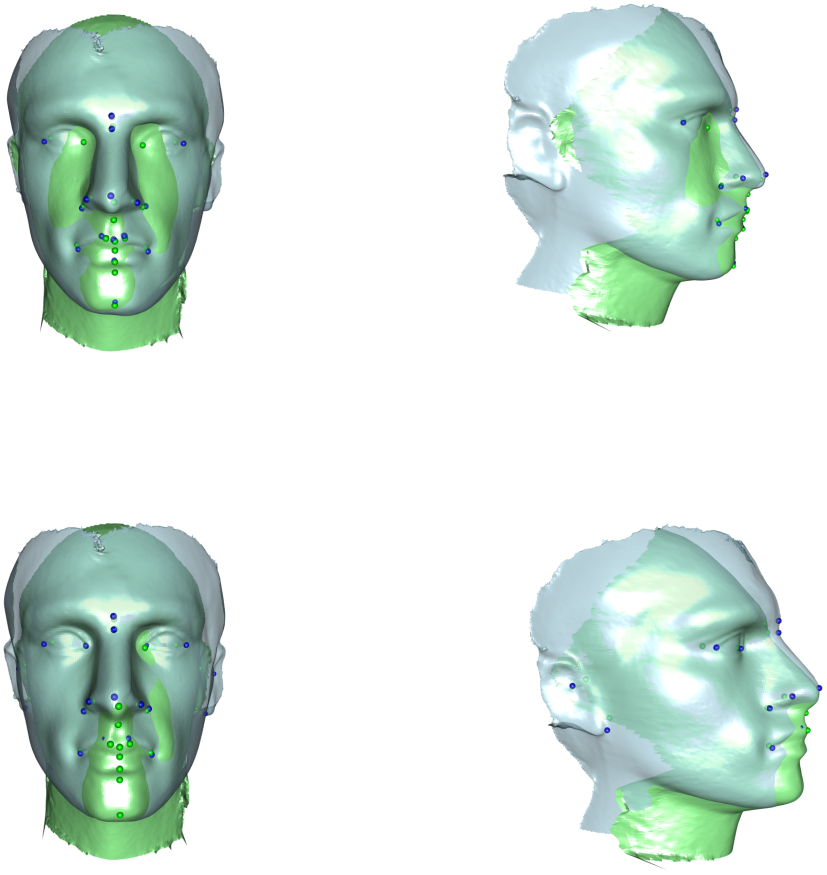

FIGURE 2.7: Data 2 without ears (top) and Data 2 with ears (bottom)

Interestingly, comparison 3 has a with-ear landmark RMSD of 7.34mm (Figure 2.8) and without ear landmark RMSD of 4.01mm. Recall that this is a more accurate with ear landmark RMSD, but a less accurate without ear landmark RMSD.

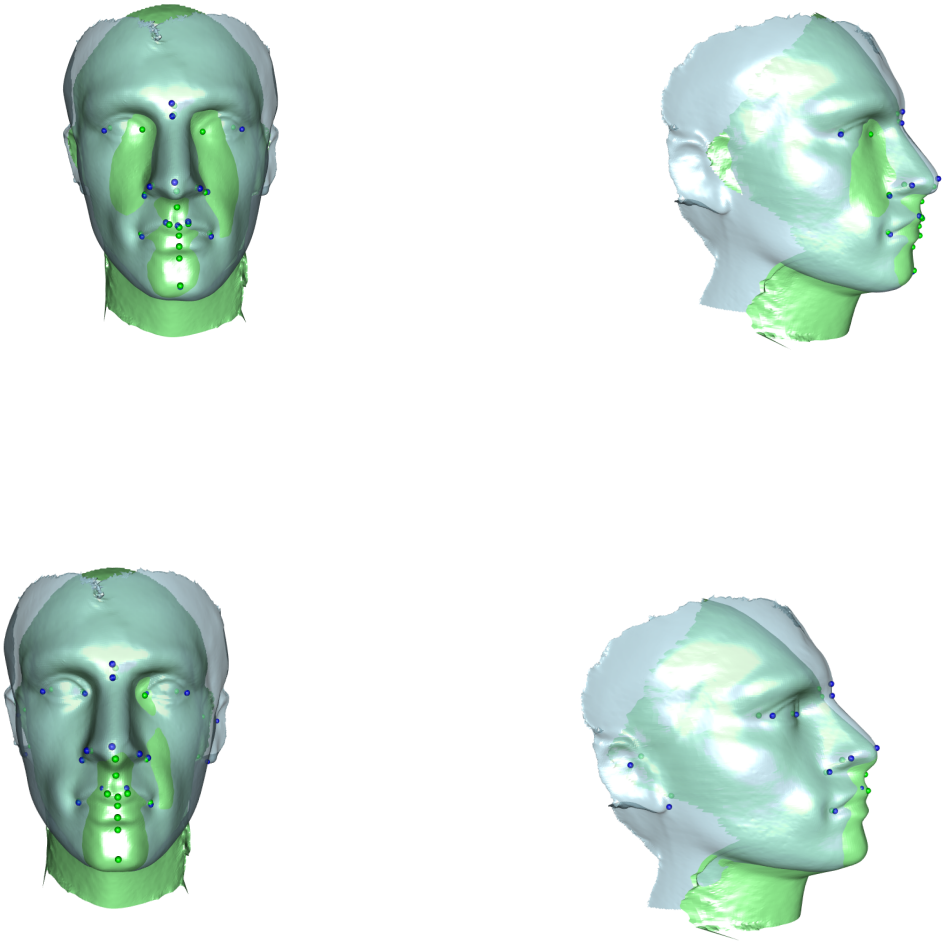

FIGURE 2.8: Data 3 without ears (top) and Data 2 with ears (bottom)

This chapter has clearly illustrated the importance and advance applications of facial landmarking. Considering the level of accuracy of landmarks is a very important goal in future work, and clearly, given the many interesting applications, the validity of these landmarks is of upmost importance. It provides the basis for all further analysis. The level of accuracy of the camera system must be determined in order to give any conclusive evidence to the work above and future work. Chapter 3 will introduce a camera reliability study that is designed and implemented by the author (with much input and aid from others).

Chapter 3

3D Imaging Variability - Advanced Landmarks

3.1 Motivation for Reliability Study

Landmark analysis is widely used as the main characterisation of soft-tissue facial shape. This reliability study investigates the accuracy and reliability of the ©Di3D camera system, both in the commonly studied central region of the face and in the potentially more problematic areas near the ears. Inter- and intra-observer error is also discussed. By anthropologically measuring a set of physically determined distances, computing the relevant landmarks on a subject's face, and comparing those measurements with measurements derived from a 3D image, the reliability of the system can be investigated thoroughly.

There are studies that accurately determine the validity of these types of 3D stereo camera systems. Since these systems are not only used to capture the face, multiple studies determine a camera's accuracy for different types of free forms objects such as the breast [Henseler et al., 2011]. Muquit and Shibahara [2006] created their own three-dimensional measurement system using multi-camera passive stereo vision with the aim to reconstruct the 3D surfaces of free form objects such as the face. The basic concept of this system is an efficient stereo correspondence technique that consists of (i) coarse-to-fine correspondence searching and (ii) an earlier detection and correction system which both employ phase-based image matching. From experimental conditions, this system allows about 0.5mm accuracy in a 3D measurement with narrow baseline (50mm) stereo camera heads.

Due to the growing number of 3D stereo cameras, it is necessary to investigate the differences amongst those systems that could give rise to varying degrees of error. Rueß et al. [2012] give a detailed accuracy analysis for stereo processing based upon different processing techniques such as the influence of radial distance to the projection centre, i.e. radial distortion and baseline camera parameters. There is a varying degree of accuracy dependent upon the type of lighting, heterogeneous or homogeneous camera features, and upon the radius of the projection centre.

In order to fully understand the capabilities of the commercial camera system in this thesis' analysis, it is necessary to do an independent validation study. Considering that there are only 25 landmarks that comprise the facial configuration description, very small dimensions (.5mm) can greatly affect the analysis. Also considering this thesis' investigation into anatomical curves of the face, all the semi-landmarks that comprise the curves between two landmarks are then affected. This study determines differences between physically measured anatomical landmarks and those which are measured in the camera and reconstructs landmarks by physically measured distances.

3.2 Design of the Reliability Study

Four adult (one male and one female aged $20-30$, and one male and one female aged $50-60$) faces were physically landmarked with 6 different anatomical points (Figure 3.1). Physical distance measurements were then taken (15 linear distances), repeated two times by three different evaluators.

This same study is repeated at Masaryk University, Department of Anthropology in Brno. Using a different 3-dimensional camera system, as well as observers trained in the same method, yet by different trainers, allows for a more comprehensive study of reliability. The Brno study involves six subjects (one male and one female aged $9-11$, one male and one female aged $20-30$, and one male and one female aged $50-60$). The analysis of two of the Brno subjects (male and female aged $9-11$) are removed. All other aspects of the study are identical except for the 3D camera systems used. In Glasgow, the Di3D Dimensional Imaging System (texture resolution 14 megapixels; geometry resolution: 0.1mm/pixel triangle edge length; capture time: 1ms) is used for the study, while in Brno, the Vectra M1 3D Facial Imaging Solution Camera (texture resolution 14 megapixels; geometry resolution: 0.1mm/pixel triangle edge length; capture time: 1ms) is utilised.

The six landmarks are defined in Table 3.1:

TABLE 3.1: Anatomical Landmarks Allocated for Reliability Study

ID	Code	Region	Position	Abr.	Name
6	S5	nose	middle	n	*soft tissue nasion*
5	S4	nose	middle	sn	*subnasale*
2,4	S1,S3	ear	right/left	t	*tragion*
1,3	S0,S2	ear	right/left	oi	*otobasion inferius*

1) *subnasale* − the point at which the nasal septum merges with the upper cutaneous lip in the midsagittal plane

2) *soft tissue nasion* − the midpoint on the soft tissue contour of the base of the nasal root at the level of the frontal al suture

3) *L/R tragion* − the point located at the upper margin of each tragion

4) *L/R otobasion inferius* − the point of attachment of the ear lobe to the cheek, which determines the lower border of the ear insertion

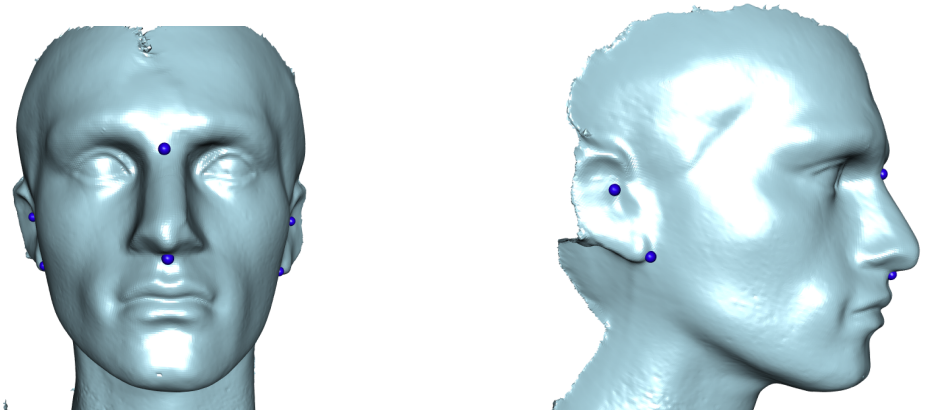

FIGURE 3.1: Coronal Plane Landmarks (left) and Midsagittal Plane Landmarks (right)

The fifteen selected Euclidean distances are as follows:

TABLE 3.2: Selected Euclidean Distances for Measurement - x denotes use of the spreading caliper and o denotes used of the sliding caliper

	L *oi*	R *oi*	L *t*	R *t*	*sn*	*n*
L *oi*		$1-x$	$5-o$	$2-x$	$8-o$	$7-o$
R *oi*				$6-o$	$12-o$	$11-o$
L *t*		$4-x$		$3-x$	$10-o$	$9-o$
R *t*					$14-o$	$13-o$
sn						
n					$15-o$	

Each subject had a 3D photograph taken twice. The image capture protocol follows that of the standard image capture protocol used for the collection of control data (detailed in Chapter 6). The system is calibrated before every subject image capture. Also, between every image capture, participants are invited to move, stand-up, and relax their facial features, so that it was assured no two images were of the exact same pose.

For every Subject X:

Calibration of System

Session A

i.A Image Capture,

ii.A Observer 1: Measurement of 15 Euclidean distances,

iii.A Observer 2: Measurement of 15 Euclidean distances,

iv.A Observer 3: Measurement of 15 Euclidean distances.

Session B

i.B Image Capture,

ii.B Observer 1: Measurement of 15 Euclidean distances,

iii.B Observer 2: Measurement of 15 Euclidean distances,

iv.B Observer 3: Measurement of 15 Euclidean distances.

This process was repeated for each subject individually.

The subject code for all analysis will be as follows in Table 3.3.

In Glasgow, the two 3D camera images are taken for each subject and then landmarked in the @IDAV system Landmark, with the six chosen landmarks. Two trained landmark observers agree upon each landmark placed for the subjects. In Brno, the same procedure for the 3D camera images is followed as with the physical distance measurements, and each observer landmarks the image twice.

TABLE 3.3: Subject Description

Location	Person Code	Sex	Age
Glasgow	*1*	Female	Mature
	2	Male	Mature
	3	Female	Young
	4	Male	Young
Brno	*1*	Female	Mature
	2	Male	Mature
	3	Male	Young
	4	Female	Young
	5	Male	Child
	6	Female	Child
*See Appendix for Person Code 5 and 6 analysis			

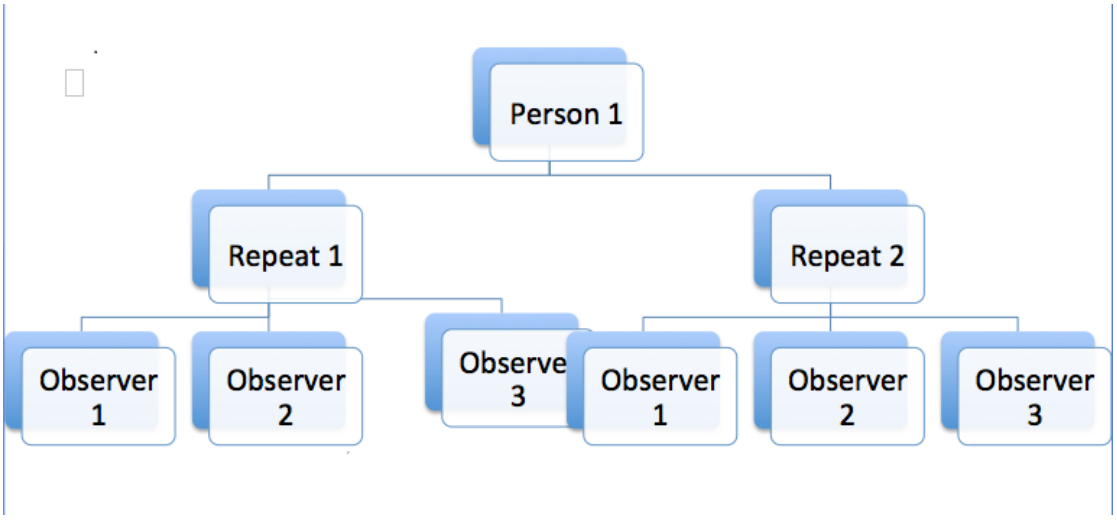

FIGURE 3.2: Hierarchical Model of Reliability Study Design

3.3 Analysis

After the data collection, the 3D images are landmarked with the same six chosen landmarks and the fifteen physical distances were generated. These distances and landmarks are then compared to those derived from the anthropologically measured distances in order to assess the accuracy of the camera system. Between-observer error is also thoroughly discussed.

3.3.1 Measured Distance Reliability-Observer error

It is necessary to identify the human error associated with the measurement of anatomical distances. The simplest approach to investigating error is to compare the repeat images, by each observer, of each of the four subjects, independently. More generally, the structure of the variation in any single distance can be expressed by a mixed effects model

$$y_{ijk} = \mu + \alpha_i + \beta_{ij} + \gamma_k + \epsilon_{ijk},$$

where

μ is the fixed mean over the entire population,

α_i the random effect (adjustment in position) for Person (P) i,

β_{ij} the random effect in Repeat (R) j of person i,

γ_k the random effect associated with a particular Observed (O),

ϵ_{ijk} the error for each measurement.

All of these terms, apart from the fixed μ are treated as random variables with their own associated standard deviations. Specifically,

$$\alpha_i \sim N(0, \sigma_P^2),$$

$$\beta_{ij} \sim N(0, \sigma_R^2),$$

$$\gamma_k \sim N(0, \sigma_O^2),$$

$$\epsilon_{ijk} \sim N(0, \sigma^2).$$

Note, that the when looking at the hierarchal structure in Figure 3.2 that while the repeat images of the individual person are nested within that particular person, the

observers are treated as a crossed effect (i.e. the same person is observer 1 for all four subjects). Table 3.4 (Glasgow) and Table 3.5 (Brno) display the estimated standard deviations of the errors at each level of the hierarchy and crossed effects as well, for each individual distance.

TABLE 3.4: Glasgow Physically Measured Distances – Standard Deviation (cm)

Dist	Person (σ_P)	Repeat(σ_R)	Obs (σ_O)	$\sigma_{residual}$
	Glasgow	Glasgow	Glasgow	Glasgow
1	0.821	0.000	0.000	0.122
2	0.873	0.061	0.000	0.106
3	0.711	0.000	0.001	0.094
4	0.922	0.001	0.000	0.124
5	0.523	0.001	0.002	0.103
6	0.530	0.006	0.003	0.062
7	0.720	0.000	0.000	0.091
8	0.821	0.001	0.030	0.103
9	0.630	0.041	0.000	0.122
10	0.942	0.001	0.039	0.082
11	0.802	0.003	0.026	0.101
12	0.856	0.025	0.003	0.091
13	0.590	0.002	0.041	0.081
14	0.880	0.024	0.011	0.072
15	0.092	0.002	0.040	0.080
Mean	0.712	0.010	0.011	0.091

TABLE 3.5: Brno Physically Measured Distances – Standard Deviation (cm)

Dist	Person (σ_P)	Repeat(σ_R)	Obs (σ_O)	σ
	Brno	Brno	Brno	Brno
1	1.464	0.000	0.250	0.203
2	1.119	0.000	0.083	0.161
3	0.683	0.000	0.126	0.094
4	1.100	0.000	0.057	0.168
5	0.183	0.085	0.011	0.151
6	0.273	0.126	0.000	0.075
7	0.583	0.019	0.033	0.080
8	0.698	0.016	0.000	0.087
9	0.487	0.000	0.039	0.062
10	0.618	0.000	0.019	0.077
11	0.809	0.072	0.058	0.106
12	0.854	0.034	0.065	0.115
13	0.542	0.000	0.000	0.062
14	0.628	0.038	0.000	0.111
15	0.347	0.019	0.042	0.047
Mean	0.693	0.027	0.052	0.115

The standard deviation for the person effect (σ_P) will be ignored since this simply measures the variability across individuals. It would clearly be expected to be somewhat

high between our four subjects (male/female, young/adult). The repeat error has a very small standard deviation, and at times is an almost negligible effect. For example, in Table 3.4, the mean repeat error in Glasgow is 0.01cm across all distances; for Brno, (Table 3.5) 0.027cm. This is to be expected since it is the standard deviation within each of the three observers, simply repeating the same measurements. As for observer error, there is a surprisingly small amount of error. Note that the larger distances (*otobasion inferius* to *otobasion inferius* or *tragion*), have a very small error compared to measurements between the mid-sagittal landmarks and the coronal landmarks (*otobasion inferius* or *tragion* to *nasale* or *subnasale*). This could simply be due to the awkwardness of the caliper.

As for the error at the lowest level of the hierarchal model ($\sigma_{residual}$), the error for each individual measurement, it is clear that all the distances have approximately the same level of error. Theoretically, the same value is expected for all of the 15 Euclidean distances, but an uniform residual error is not expected since some distances are nearly three times smaller than others. The results of the comparison between the study in Brno (Table 3.5) and the study in Glasgow (Table 3.4) are very similar and show a high level of reproducibility in physical measurements taken.

3.3.2 Variation between Physically Measured Distances and Calculated 3-dimensional Camera Distances

The variation in physical distances measured anatomically on each subject's face and the distance calculated from the landmarks made on the 3D camera system images are compared. The same 15 distances are calculated from the 6 landmarks simply using Euclidean distances,

$$Distance = \sqrt{(x_1 - x_2)^2 + (y_1 - y_2)^2 + (z_1 - z_2)^2}.$$

The tables below reflect the camera repetitions (the distances calculated from the 3D picture coordinates) subtracted from the mean of the 6 measured configurations (each subject was measured a total of 6 times). If the physical measurements are viewed as 'truth', a positive value reflects the camera image making a face 'smaller' and a negative value as the camera image making the face 'bigger'.

When examining Table 3.6 it is clear that distances 7 (*L otobasion−nasion*), 8 (*L otobasion−subnasale*), 11 (*R otobasion−nasion*), and 12 (*R otobasion −subnasale*) have double and even four times the amount of variation as the rest of the distances. Recall the difficulties that arise when physically measuring the subjects. Due to the nature of the sliding caliper, it is quite difficult to measure the longer distances. With the *Right/Left*

TABLE 3.6: Glasgow: Variation between Physical Distances and 3−dimensional Camera Distances (cm)

Distance	Person 1		Person 2	
	Rep 1	Rep 2	Rep 1	Rep 2
1	-0.007	-0.091	-0.335	-0.448
2	0.214	-0.172	-0.189	-0.146
3	-0.409	-0.265	-0.310	-0.256
4	-0.309	–0.266	-0.343	-0.457
5	-0.200	-0.161	-0.103 -	0.163
6	-0.223	-0.130	-0.177	-0.142
7	1.628	1.712	1.491	1.691
8	-1.790	-1.764	-1.540	-1.296
9	-0.066	-0.08	-0.447	-0.439
10	0.060	-0.065	0.348	0.457
11	1.388	1.543	1.065	1.064
12	-1.967	-1.922	-1.339	-1.304
13	-0.103	0.150	-0.714	-0.805
14	-0.109	-0.032	0.772	0.704
15	-0.237	-0.087	-0.200	-0.189

TABLE 3.7: Glasgow: Variation between Physical Distances and 3−dimensional Camera Distances (cont.) (cm)

Distance	Person 3		Person 4		Mean
	Rep 1	Rep 2	Rep 1	Rep 2	
1	0.869	1.017	-1.696	-1.845	-0.317
2	0.446	0.554	-1.248	-1.325	-0.287
3	0.155	0.389	-0.755	-0.757	-0.276
4	0.576	0.795	-1.405	-1.475	-0.360
5	-0.289	-0.445	-0.162	-0.155	-0.210
6	0.093	0.057	-0.138	-0.121	-0.098
7	1.728	2.139	-0.408	-0.483	1.187
8	-0.007	0.249	-2.054	-2.101	-1.288
9	0.799	0.999	-2.066	-2.123	-0.428
10	2.047	2.225	-0.922	-0.952	0.400
11	1.395	1.757	-0.385	-0.477	0.919
12	0.191	0.571	-1.773	-1.859	-1.175
13	0.699	0.491	-2.105	-2.089	-0.560
14	2.218	2.077	-0.547	-0.519	0.570
15	-0.061	-0.092	-0.109	-0.126	-0.138

otobasion, there is more difficulty in locating the exact point since the earlobe must be physically moved at times.

Note that distances $8, 12$ (the *subnasale* $-$ *R/L otobasion* measurements) are both negative, indicating that the camera image is making the face 'bigger' or more stretched back at the ears, but that distances $7, 11$ (the *nasale* $-$*R/L otobasion* measurements)

are positive indicating that the camera is making the face 'smaller' or less stretched back. This indicates that as the 'z' distance (front of face towards the back of the head) increases, there is a significant stretching back. There is no more than about a 2 centimeter variation (positive/negative) for any distance. Figure 3.3 shows the full variation between physical distances and 3D camera distances.

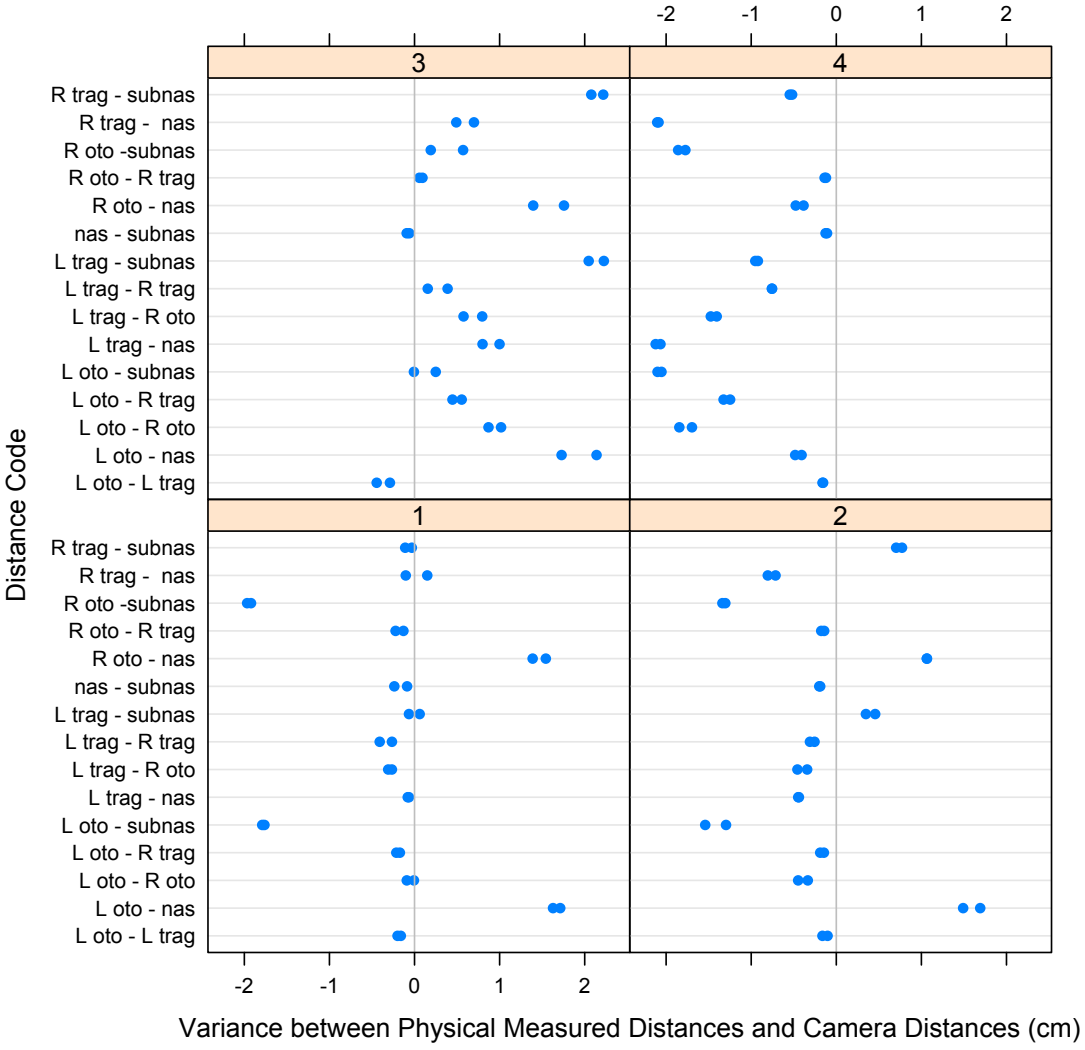

FIGURE 3.3: Glasgow Variation Physical Distances and 3-dimensional Camera Distances (cm)- Subjects 1, 2, 3, 4, respectively labelled in Panels

Table 3.7 demonstrates a very interesting phenomenon where Person 3 (young male) is always positive (camera is making the face 'smaller') and Person 4 (young female) is always negative (camera making the face 'bigger'). It is possible that the angles of the four cameras, should potentially be changed based upon the curvature (width and depth) of the particular subject's face.

When comparing the Brno data (Tables 3.8 - 3.9) to the Glasgow data, there is a

Table 3.8: Brno: Variation between Physical Distances and 3−D Camera Distances (cm)

Distance	Person 1		Person 2	
	Rep 1	Rep 2	Rep 1	Rep 2
- 1	-2.661	-2.810	-2.663	-2.611
2	-2.020	-2.110	-2.023	-1.926
3	-1.151	-1.298	-1.257	-1.038
4	-1.698	-1.863	-1.759	-1.648
5	-0.211	-0.178	-0.139	-0.203
6	0.127	0.226	0.208	0.059
7	-1.097	-1.111	-1.137	-1.206
8	-1.846	-1.817	-1.762	-1.787
9	-0.307	-0.310	-0.358	-0.452
10	-1.080	-1.022	-0.965	-1.035
11	-1.366	-1.319	-1.338	-1.323
12	-2.059	-2.004	-1.965	-1.969
13	-0.968	-0.901	-0.893	-0.954
14	-1.474	-1.364	-1.296	-1.436
15	-0.262	-0.237	-0.203	-0.204

Table 3.9: Brno: Variation between Physical Distances and 3D Camera Distances (cm) (CONT.)

Distance	Person 3		Person 4		Mean
	Rep 1	Rep 2	Rep 1	Rep 2	
1	-1.980	-1.336	-0.651	-0.612	-1.916
2	-1.516	-1.006	-0.557	-0.480	-1.455
3	-0.887	-0.588	-0.443	-0.396	-0.882
4	-1.336	-0.976	-0.608	-0.544	-1.304
5	-0.188	-0.200	-0.055	0.047	-0.141
6	-0.009	-0.052	-0.053	0.093	0.075
7	-0.916	-0.631	-0.332	-0.332	-0.845
8	-1.236	-0.763 -	0.265	-0.344	-1.228
9	-0.458	-0.376	-0.346	-0.339	-0.368
10	-0.807	-0.564	-0.289	-0.298	-0.758
11	-0.972	-0.624	-0.266	-0.284	-0.936
12	-1.417	-0.904	-0.341	-0.367	-1.378
13	-0.736	-0.547	-0.245	-0.215	-0.682
14	-1.162	-0.930	-0.521	-0.423	-1.076
15	-0.308	-0.343	-0.363	-0.287	-0.276

significantly more accurate comparison between the physically measured distances and the calculated distances from the 3D camera system for Brno. Recall in the discussion of the standard deviation of the physical measurements in Brno that there is a greater observer error than in Glasgow. This would then suggest that the camera system in Brno is much more accurate than the camera system in Glasgow. This is likely due to the three different image captures in Brno (frontal and both lateral sides) giving a fuller

view of the ear region. Figure 3.4 shows the full variation between physical distances and 3D camera distances.

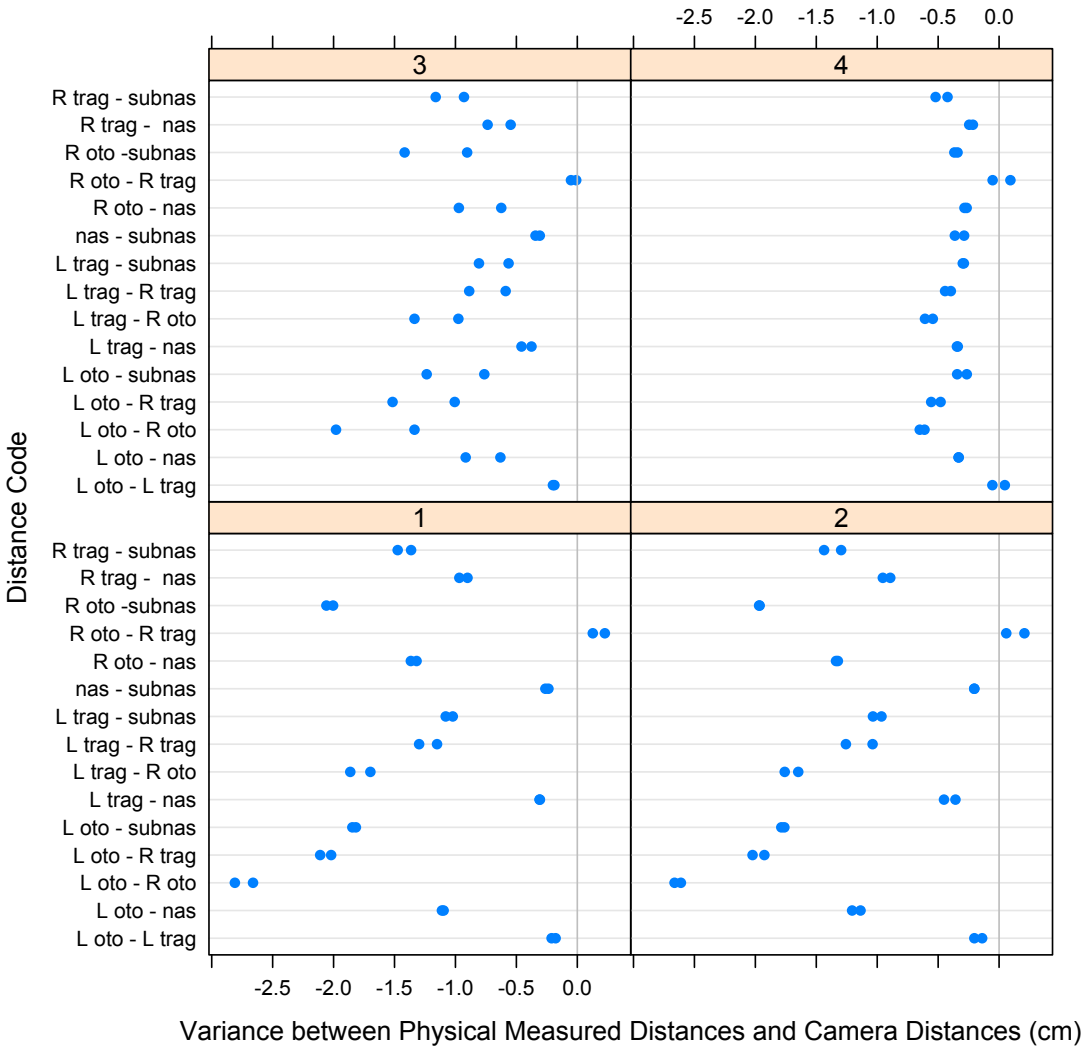

FIGURE 3.4: Brno Variation between Physically Measured Distances and 3-dimensional Camera Distances (cm)- Subjects 1, 2, 3, 4, respectively labelled in Panels

When examining Figure 3.9, again the phenomenon that occurs in Glasgow occurs where the variation in certain subjects' faces are either all negative values (indicating that the camera is making the face 'bigger') or all positive values (indicating that the camera is making the face 'smaller'). However, what is most interesting is that in Brno, the faces are almost completely negative, indicating that the camera system is consistently making the face look 'bigger'. To fully understand this occurrence, a further study would be necessary.

3.3.3 Comparison of Reconstructed Landmarks from Physical Measurements and 3D picture Landmarks

The organisation of the landmark configurations comes in two parts. First, the 6 specified landmarks from the 15 physically measured distances (6 total configurations per subject) need to be reconstructed. This is accomplished using metric multidimensional scaling (MDS).

MDS aims to transform a distance matrix into coordinates from which the calculated Euclidean distances best approximate the original values of the distance matrix. First, the distance matrix is transformed into a cross-product matrix (scalar product between two vectors corresponds to the cross-product matrix and can be easily transformed into a distance). A principal component analysis is done through the eigen-decomposition of the cross-product matrix. Note that the eigen-decomposition of a distance matrix cannot be directly computed because it is not a positive semi-definite matrix.

Using the notation of Cox and Cox [2000], let the Euclidean distance between two points (landmarks) a and b with I elements be

$$d^2(a,b) = (a-b)^T(a-b)$$

and to find the scalar product, simply expand the above such that

$$d^2(a,b) = (a-b)^T(a-b) = a^Ta + b^Tb - 2a^Tb.$$

Create a matrix X, $I \times J$ data matrix where I is the number of observations described by J variables. The crossproduct matrix is then

$$S = XX^T,$$

where S is $I \times I$. It is easily seen that a distance matrix can be directly computed where

$$D = s1^T + 1s^T - 2S,$$

where D is also $I \times I$. Revert the distance matrix D to the crossproduct matrix X in order to do the eigen decomposition. The only concern is that different cross product matrices can produce the same distance matrix (because distances don't depend on the origin). Therefore, the origin of the distance is chosen as the center of gravity of the dimensions. The cross-product matrix is then recalculated given the origin constraint.

Given a mass vector m $(I \times 1)$ where I_i is the mass of row I_i of distance matrix D then

$$m^T 1 = 1.$$

Notice that if each row has equal importance then each element $I_i = \frac{1}{I}$. Let X the $I \times I$ centering matrix be

$$X = I - 1m^T.$$

Then the cross-product matrix is

$$S = \frac{-1}{2} X D X^T$$

with eigen decomposition

$$S = U \Lambda U^T,$$

where Λ is a diagonal matrix of eigenvalues and $U^T U = I$.

This means that the matrix of scores is

$$F = M^{\frac{-1}{2}} U \Lambda^{\frac{1}{2}}$$

where $M = \text{diag}\ (m)$. The variance matrix of the scores is then equal to the eigenvalues

$$F^T M F = \Lambda.$$

After MDS is performed to calculate the 6 reconstructed landmarks of all the images, both these and the 3D camera landmarks must be rotated into the same shape space. General Procrustes Analysis (GPA), without scaling, is applied with respect to each individual. In order to create the same shape plane (i.e.. '+z'-axis is up, '+x'-axis is to the right, and the '+y'-axis is out of the page), the Procrustes mean shape of all six reconstructions is found for the physically reconstructed cases and for the 3D camera landmarks.

The Procrustes mean is then rotated about the x, y, and z-axis such that the angles between the configuration and the axes are all equal to 0. This means that the mean shape configuration (chosen landmarks) is exactly in the proper frontal rotation. The landmark configurations are Procrustes registered and then rotated using the angles calculated from the mean shape, placing all the configurations in the same, properly rotated, shape space. A comparison is performed between the landmarks of the calculated physically reconstructed configurations and also a comparison of the 3D camera landmarks to these physically reconstructed landmarks (Figure 3.5).

FIGURE 3.5: Glasgow Frontally (left) and Profile(right) Rotated Landmarks (both Physically Reconstructed (black) and Camera (red) for all Four Subjects)

TABLE 3.10: Glasgow Reconstructed Landmarks−Standard Deviation (mm)

Lmk	(σ_P)			(σ_R)		
	x	y	z	x	y	z
R otobasionbasion	4.433	5.600	4.446	0.000	0.000	0.000
R Tragion	4.746	2.132	5.242	0.000	0.000	0.000
L otobasionbasion	4.831	1.729	5.150	0.000	0.000	0.000
L Tragion	4.746	7.251	5.184	0.000	0.000	0.000
Subnasale	4.526	3.402	4.423	0.295	0.000	0.000
Nasion	4.220	6.888	4.309	0.000	0.000	0.000
Mean	4.582	4.475	4.805	0.049	0.000	0.000

Tables 3.10-3.11 examine the standard deviation between the Glasgow reconstructed landmarks. The model is exactly the same as the model for the distances (fitted in *lme4* using the *lmer* *R* package) except that there is now a x, y, and z component to each landmark (which is each distance in the previous model). Recall,

$$y_{ijk} = \mu + \alpha_i + \beta_{ij} + \gamma_k + \epsilon_{ijk}$$

where, μ is the fixed mean over the entire population, α_i the random effect for person i, β_{ij} the random effect in repeat j of person i, γ_k the random effect of the observed measurement, ϵ_{ijk} the error for each measurement.

TABLE 3.11: Glasgow Reconstructed Landmarks-Standard Deviation (mm) (Continued)

Lmk	(σ_O)			$\sigma_{residual}$		
	x	y	z	x	y	z
R otobasionbasion	0.536	0.000	1.575	1.877	0.996	10.431
R Tragion	0.719	0.000	1.146	1.784	1.029	11.692
L otobasionbasion	0.000	0.308	1.569	1.838	0.861	10.313
L Tragion	0.719	0.000	1.309	1.783	1.046	11.025
Subnasale	0.000	0.325	2.808	0.781	1.802	16.533
Nasion	0.118	0.245	2.264	0.725	1.457	18.361
Mean	0.348	0.163	1.778	0.731	1.198	13.059

Again, the person (σ_P) component is ignored since the difference across the subjects is irrelevant. The deviation over repeats (for which there were 2 per subject), is essentially 0mm for all the landmarks. The observer error is also very small at no more than 3mm and also close to 0mm for many of the landmarks. Lastly, the residual error per measurement is significant at about 1cm (and approximately 1.5cm in some cases), especially evident in the z-scale, which is consistent with the difficultly in using the caliper.

Considering the landmarks individually, there are no particularly large differences, except the z-scale for the *subnasale* and *nasion*. These are the two significantly difficult landmarks to measure due to the placement on the face.

From Tables 3.10-3.11 it is difficult to pinpoint any particular correlation between the standard deviations of the physically measured distances and the landmarks which are reconstructed from them.

TABLE 3.12: Brno Reconstructed Landmarks−Standard Deviation (mm)

Lmk	(σ_P)			(σ_R)		
	x	y	z	x	y	z
R otobasionbasion	5.884	2.460	5.851	0.000	0.203	3.530
R Tragion	8.758	2.103	5.654	0.000	0.000	3.502
L otobasionbasion	6.534	1.537	6.433	0.000	0.000	3.985
L Tragion	8.729	3.202	6.099	0.000	0.000	3.987
Nasion	0.644	3.553	9.643	0.273	0.000	0.000
Subnasale	0.879	3.976	9.156	0.000	0.000	0.001
Mean	5.238	2.805	7.139	0.046	0.033	2.471

When examining the Brno data in Tables 3.12-3.13, it is clear that Brno has very similar standard deviations among the physically reconstructed landmarks. However, there is more error in both the repeat measurement and the observer error. There is a consistently larger residual error of all landmarks at between $1.5 - 2$cm, but more so a

TABLE 3.13: Brno Reconstructed Landmarks−Standard Deviation (cont.) (mm)

Lmk	(σ_O)			$\sigma_{residual}$		
	x	y	z	x	y	z
R otobasionbasion	0.318	0.212	4.057	1.150	0.776	14.908
R Tragion	0.426	0.261	4.019	1.564	0.960	14.766
L otobasionbasion	0.251	0.214	4.085	0.947	0.787	15.008
L Tragion	0.335	0.326	3.972	1.231	1.199	14.595
Nasion	0.173	0.212	5.511	0.634	0.777	20.247
Subnasale	0.223	0.184	5.355	0.820	0.676	19.675
Mean	0.288	0.235	4.483	1.058	0.863	16.517

discrepancy in most of the 'z', or front of face to back of face plane. Just as with the Glasgow data, there is also a slightly larger error for the *nasion* and *subnasale*. The awkwardness of the calipers means that the 'z' direction is the most difficult to measure. Considering the differences in the distance variation, a 1cm error is expected. Glasgow camera landmarks do not have a repeat error (σ_R) or observer (σ_O) error since all of the camera landmarks are placed through agreement by two of the observers.

TABLE 3.14: Glasgow 3D Camera Landmarks − Standard Deviation (mm)

Lmk	(σ_P)			$\sigma_{residual}$			Squared Error of Resid
	x	y	z	x	y	z	
R otobasionbasion	4.445	2.579	3.661	0.558	0.099	1.294	1.413
R Tragion	3.542	3.732	4.930	0.419	0.373	1.190	1.316
L otobasionbasion	3.615	1.818	2.471	0.474	0.305	0.991	1.140
L Tragion	3.385	2.862	4.989	0.646	0.503	0.489	0.954
Subnasale	1.814	1.601	3.903	0.294	0.412	0.396	0.643
Nasion	1.516	6.883	2.212	0.472	0.534	0.658	0.970
Mean	2.886	3.246	3.690	0.477	0.371	0.836	1.032

TABLE 3.15: Brno 3D Camera Landmarks-Standard Deviation (mm)

Lmk	(σ_P)			(σ_R)		
	x	y	z	x	y	z
R otobasion	9.573	2.350	2.316	0.000	0.000	0.000
R Tragion	6.363	2.003	2.710	0.000	0.187	0.000
L otobasion	9.102	2.565	1.610	0.318	0.000	0.351
L Tragion	6.292	1.794	3.134	0.000	0.000	0.000
Nasion	0.975	3.164	3.362	0.224	0.273	0.266
Subnasale	0.523	2.348	4.009	0.348	0.000	0.000
Mean	5.517	2.624	2.857	0.148	0.077	0.103

Examining the Tables 3.14-3.16, the standard deviations for Glasgow and Brno of the 3D camera landmarks are examined. Glasgow has a small residual error of about .5mm. This is consistent with how the landmark system works. Two observers agreed upon the

TABLE 3.16: Brno 3D Camera Landmarks − Standard Deviation (mm) cont.

Lmk	(σ_O)			$\sigma_{residual}$			Squared Error of Resid
	x	y	z	x	y	z	
R otobasionbasion	0.000	0.000	0.000	1.055	0.765	0.908	0.951
R Tragion	0.000	0.235	0.173	0.853	0.785	1.135	1.018
L otobasionbasion	0.000	0.100	0.000	0.934	0.518	0.672	1.262
L Tragion	0.000	0.000	0.000	0.900	0.628	0.704	1.304
Nasion	0.000	0.255	0.000	0.554	0.406	0.751	1.588
Subnasale	0.000	0.133	0.000	0.380	0.543	0.682	1.622
Mean	0.000	0.121	0.029	0.779	0.608	0.809	1.277

placed landmarks. Brno, has a larger variability, but the difference is very small; Figure 3.6 showcases these results.

What is of the greatest interest is the final comparison between the 3D camera landmark configurations and the calculated landmark configuration from the physical distance measured face. This is done using Ordinary Procrustes Analysis (OPA), without scaling, between the two mean shapes of the configurations for each subject respectively. Ordinary Procrustes Analysis (OPA) produces the optimal superimposition of two objects or a set of shapes compared to an arbitrary reference shape. In order to do this, the effects of translation, scale and rotation must be removed as discussed in Chapter 2.

After performing this calculation, the skewing of the camera image, bigger or smaller, seems to mainly come from the 4 coronal landmarks (*R/L otobasion inferius* and *R/L tragion*). This unfoundedly creates a skewing in the *subnasale* and *nasale*. Based upon the variation between the physical and camera distances, it is clear that the distance between the *subnasale* and *nasale* is highly accurate. This is justified since the average Glasgow variation between those two landmarks is a bit over 1mm and the average Brno variation is similar.

Now that there is a fixed distance between the two mid−sagittal landmarks, the mean point is calculated between the two and fixed in space. This is done as an average of the 6 configurations per person for the physically reconstructed distances. But, for the 3D camera landmarks, the two configurations are kept separate. The mean point of the 3D camera configurations is translated to the mean shape of the physical reconstructions. Lastly, the configuration is rotated about the y−axis (x−z plane) and minimised over the rotation angle which gives the minimum OSS in order to find the best match between all the landmarks (i.e. the lowest root mean square distance).

Note that while there are 6 landmarks, two of them are fixed (the subnasale and the nasion). Therefore when the RMSD is calculated, there is an assumption of using only 4

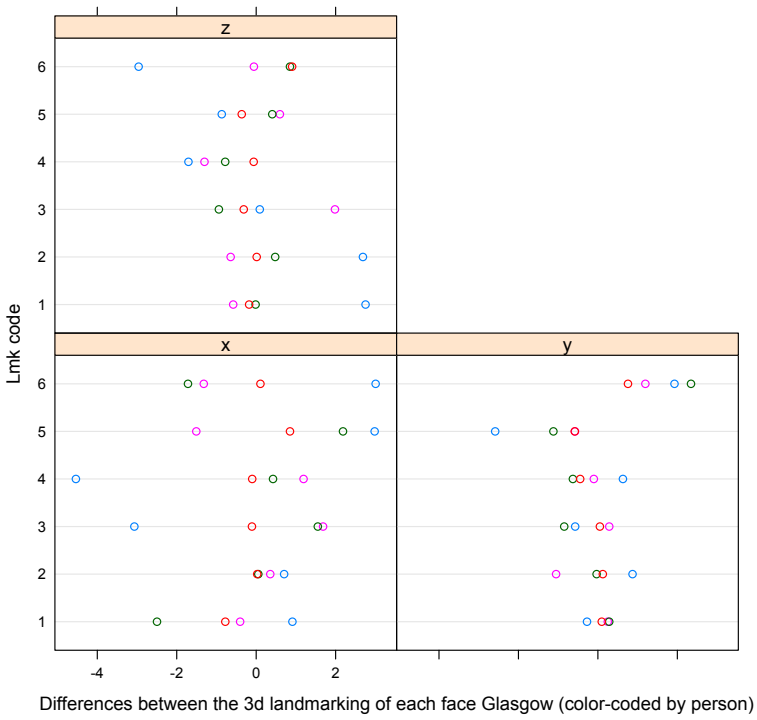

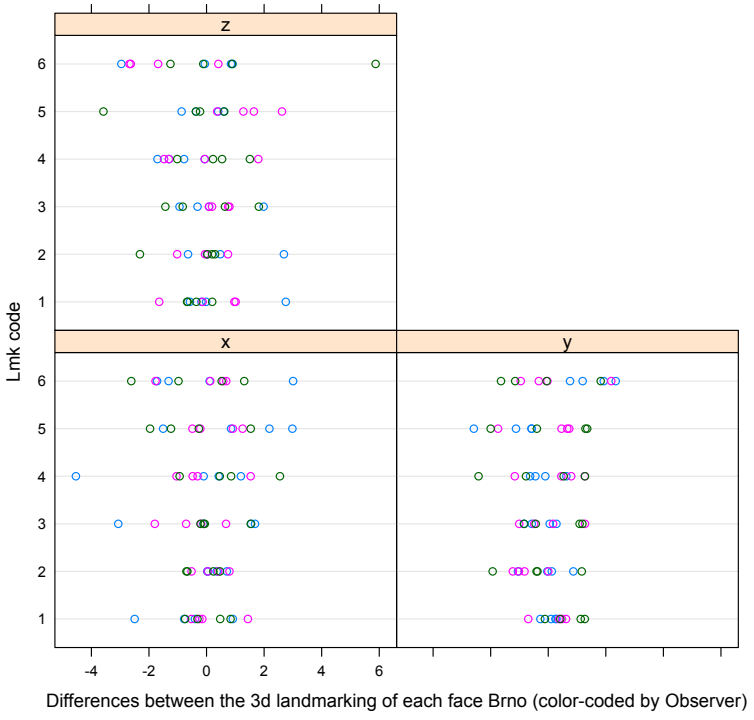

FIGURE 3.6: Differences between 3D landmarking Glasgow and Brno - each colour coded by the Subject of interest

landmarks about which the configurations are matched since the mid−sagittal landmarks are assumed exact. This is called special (adjusted) Procrustes superimposition.

Table 3.17: Brno: Root Mean Square Error of 3D Camera Landmarks and Reconstructed Landmarks (mm)

Person	RMSD (mm)		
	Repeat 1	Repeat 2	Mean
1	2.876	2.176	2.526
2	1.987	1.002	1.495
3	3.109	3.001	3.055
4	1.007	1.063	1.035

Table 3.18: Glasgow: Root Mean Square Error of 3D Camera Landmarks and Reconstructed Landmarks (mm)

Person	RMSD (mm)		
	Repeat 1	Repeat 2	Mean
1	4.572	4.018	4.359
2	4.437	4.749	4.533
3	9.199	10.634	10.156
4	10.134	10.823	10.423

In the final comparison between the 3-dimensional camera landmarks and the physically reconstructed landmarks, there is a similar correlation in the root mean square distance in relation to the error of the variation between the distances of the camera picture and the physically measured distances. Given that many of the distances have a variance of up to 2 centimeters, it is expected that the landmarks themselves have about a half a centimeter or more of error. Observing the mean, it seems that Person 1 and Person 2 have about a half a centimeter error on average, whereas Person 3 and Person 4 are at approximately a centimeter of error between the configurations. Considering the standard deviations of about 2 this is then, on average, appropriate.

When comparing the distances between the physical measurements and those calculated from the camera landmarks, recall that Person 1 and 2 have some negative (camera made the face 'smaller') and some positive values (camera made the face 'bigger') values, whereas Person 3 and 4 consistently have either all positive or all negative values of variation. It then makes sense that Person 3 and 4 will have significantly larger RMSD values. However, the fact that there exists such a large error of 1cm for the average landmark, the ramifications must be considered. Given how low the average error of observer measurement is in the physically reconstructed distances, most of the RMSD does come from the camera system.

3.3.4 Scaling with Addition of *Gnathion*

In order to understand if a scaling of the distances will show any systematic effect in the facial shape, an additional landmark is added to the 3D camera images (Figure 3.7). There will be an investigation of different relative scaling distances for each of the subjects. The additional landmark is the *soft tissue gnathion* (abbreviation *gn*), which is defined as the most anterior−inferior midpoint of the chin.

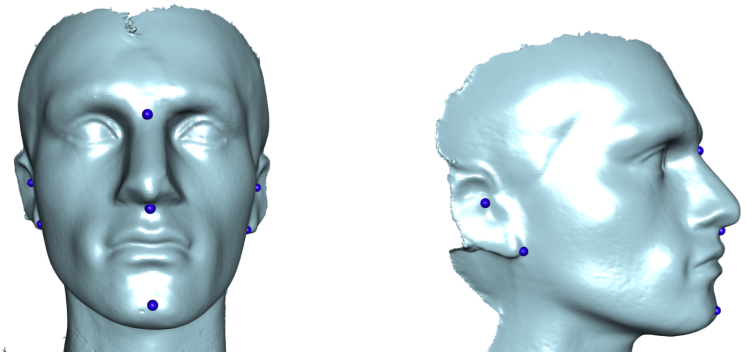

FIGURE 3.7: Midsagittal Plane Landmarks (left) and Coronal Plane Landmarks (right)

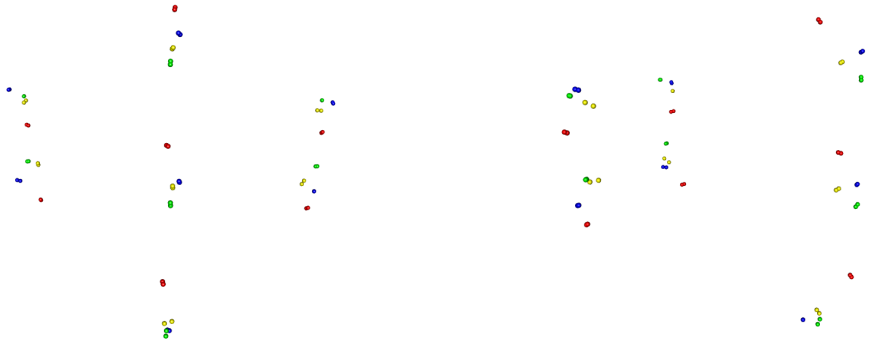

FIGURE 3.8: 3D Camera Landmarks Glasgow Frontal (left) and Lateral (right) View with Addition of *gnathion* colour-coded by Subject

The addition of the *gnathion* landmark allows a clearer view of the length of the face for scaling purposes (Figure 3.8). A facial width is also included (the most distant points on the face in the $x-$direction. This is calculated by finding the maxillary arc through a geodesic cut from the *left tragion* to the *subnasale* to the *right tragion*. First, the cross product between the two vectors formed between the *tragions* and the *subnasale* is taken.

$$\hat{P} = (tR - sn) \otimes (tL - sn).$$

Then the set of points (which have been projected onto the vector $\hat{P}$), which are no more than 1mm from the projection are calculated. This is simply the set of points for which

$$\|i \cdot \hat{P} - sn \cdot \hat{P}\| < 1\text{mm}.$$

This gives all the points on the image within a 2mm distance of the plane cut. This allows the ability to calculate cheek protrusion and give a clearer view of other relative distances instead of simply using the *tragions* to calculate the facial width. This now gives the ability to look at many different scaling effects. However, these results were inconclusive and can be seen in Appendix A.

3.3.5 Further Discussion

This study has two main findings, one is that the camera system systematically shows an image as either larger or smaller than it actually is, and that there is significant error in the ear region created by Glasgow's camera system. In order to more fully understand how the camera system smears specific individuals ear regions, it could be useful to use a styrofoam head mould to understand where the landmark 'smearing' error comes from and why some subjects' faces are made 'smaller' by the camera whereas other subjects' faces are made 'bigger' by the camera. There are camera systems that take full, around the head, images versus these camera systems that only take images of a certain distance around the head. In the Appendix A, there are plane cuts (*otobasion inferius R/L* through the *subnasale*) of all four subjects from each location which could help determine this inaccuracy. For the purposes of this thesis analysis, the ear region will be removed in order to not skew results.

The data from the two Brno children (male and female) was removed from the study due to the fact that there was no comparable study done in Glasgow.

3.4 New approach to Landmarks

It is very clear that a significant amount of information is lost from simply relying on the 25 or so manually identified anatomical landmarks. As discussed previously, the concept of facial surface curvature could lead to a much richer value of information than that of simply anatomical points. However, in order for curves to be used to describe

the face, there must be a re-defining of anatomical landmarks. Katina et al. [Katina, 2015b] contest that the current definitions of anatomical landmarks previously discussed are entrenched in two-dimensional origins. New definitions take an interdisciplinary approach, addressing issues associated with imaging, including biological and clinical motivations, and a route to definitions based on mathematical definitions of surface shape using differential geometry. Katina [2015b], beyond providing a more global view of landmarks that is fundamentally three-dimensional and independent of orientation, carry out a validation study. The study provides evidence that variation is reduced at the observer level of a hierarchical model with the new definitions of curve-based landmarks as compared to the old set of anatomical landmarks provided by Farkas et al. [Farkas and Schendel, 1995]. This new approach to landmarks allows for a new approach to characterising a 3D facial image as a whole and is further discussed in Chapter 4

3.4.1 Concerns with Standard Landmarks

Farkas and Schendel [1995] define the standard set of anatomical landmarks in a two-dimensional view. This requires a very specific orientation of the head that gives a well-defined and reproducible identification of the landmarks in question. The most common method uses both a horizontal, *Frankfurt horizontal*, and vertical, *mid-sagittal*, plane to define the orientation of the head for landmarking. The *mid-sagittal plane* is found using the mid-line face landmarks, causing the need for a compromise across multiple landmarks as well as the error associated with placing these landmarks before the plane is in place [Katina, 2015b].

Many of the same concerns arise using the *Frankfurt horizontal* which is defined by three landmarks: left *orbitale* and the left and right *portion*. The left *orbitale*, the inferior margin of the left orbit, which is defined by bone, allows for significant potential error once soft tissue is introduced on top. The *portion* landmarks, defined as the upper margin of each ear canal, are all quite difficult to define and take careful training in order to identify.

In the next chapter, new definitions for landmarks are proposed based upon a differential geometry approach to local surface shape. This is a novel method from which a paper is in the Journal of Anatomy that the author of this thesis is part of [Katina, 2015b]. This determines a quantifiable measure of surface shape that are both independent of orientation and genuinely three-dimensional. From these definitions and a new approach to characterizing facial shape, facial curves are identified and discussed as a richer way of describing three-dimensional facial shape. The method described in Chapter 4 is a novel method.

Chapter 4

The Identification of Anatomical Curves

4.1 Introduction

In recent years, there has been significant study into the analysis of 3-dimensional facial objects. Many advances in the field of 3-dimensional scanning devices and other tools have greatly accelerated access to very high quality three-dimensional data. Therefore, there is a growing need for automatic methods to analyse this 3D data. In this chapter a novel method will be described with the aim to develop a statistical framework for categorizing and describing 3-dimensional facial shape by curvature. This novel method aims to create a richer description of facial shape by exploiting the intrinsic characteristics shape, which has not been carried out in previous work.

The key features of the face can be viewed as a set of ridges and valleys where for example the nose profile is a ridge and the mid-line of the lip is a valley. This leads to a natural way of characterising the face as a set of ridges and valleys with varying degrees of steepness and depth. Given a set of manually marked facial landmarks, the aim is to then automatically produce the curve information of the face just given those basic elements. This is equivalent to identifying the points which have the maximal curvature on a 3-dimensional manifold with two fixed points (landmarks). Much work has been done into this field of study in relation to facial recognition. There are a few significant methods of extracting curve information from a 3D object, for example an analysis of the curvature tensor on the surface in order to obtain parabolic and ridge curves [Hallinan et al., 1999] or the use of surface gradients in order to extract crest lines [Yoshizawa et al., 2008].

Note that these methods are subject to observation noise since the computation of gradients and curvatures involve higher order derivatives. In order to combat this Bronstein et al. [2005] use a geodesic distance function that crops the boundary, showing that geodesic length is invariant to rigid motions. Samir et al. [2005] use a different approach entirely by choosing a height function and studying the level set of the function as it leads to planar curves, using the range maps instead of the mesh data usually used for curve extraction of facial images.

However, the definition of level curves changes based on the global orientation of a face or object. As a result, the shape is not invariant to rotation. Samir et al. [2009] define facial curves as level curves of a surface distance function and find the length of the shortest path between that point and a fixed reference point along the facial surface (meaning that the function is invariant to rotation and translation of the object). The geodesic distance is then approximated by an algorithm [Dijkstra, 1959] based on edge lengths. The level curve is then extracted by selecting the appropriate vertices (based upon the distance calculation) which are then ordered using a Euclidean Minimum Spanning Tree algorithm.

Curves, themselves, can provide a strong basis for landmark definitions. This encourages the belief that curves are the key features from which the face can be characterised, giving a rich and informative description of the facial surface.

4.2 New Definitions of Landmarks

Given the critical importance of landmarks in defining highly necessary information regarding 3-dimensional facial shape, a great emphasis is put on redefining these anatomical landmarks due to the issues that are associated with the standard definitions of landmarks as discussed in Section 3.4.

Figure 4.1 shows a 3D facial image landmarked with the new definitions of landmarks and anatomical curves as well as the same face coloured by shape index. Tables 4.1, 4.2 and 4.3 are proposed by Katina et al. [Katina, 2015b] as the new set of anatomical curves and the associated landmarks respectively. The validation study showed an excellent reproducibility for this new definition of landmarks referenced in Table 4.4. For further documentation see Katina et al. [Katina, 2015b]. Given this new set of landmarks defined by local surface shape rather than specific points on the surface, anatomical curves are now investigated as a means of describing three-dimensional facial shape.

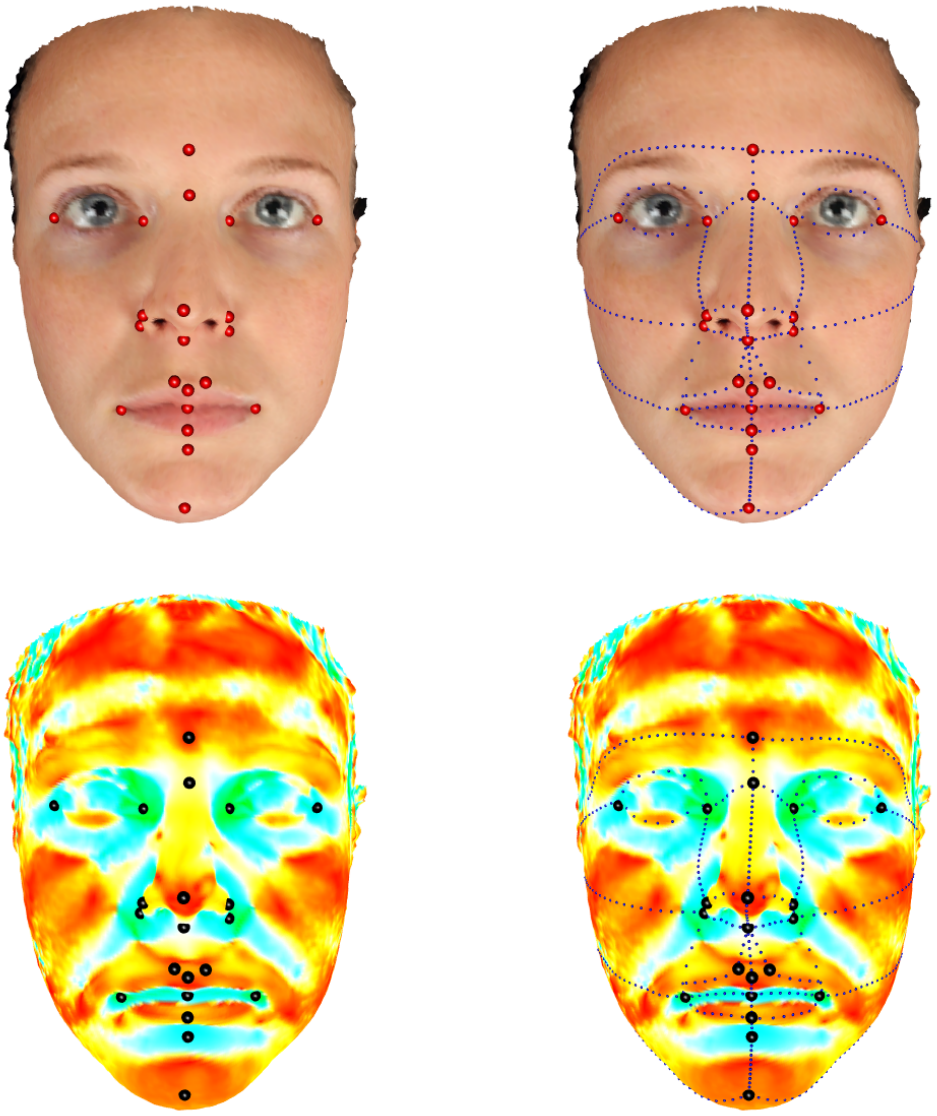

FIGURE 4.1: 3D facial image with new defintion of landmarks (red) and anatomical curves (blue) and the same 3D facial image coloured by shape index with the corresponding landmarks and anatomical curves

Table 4.1: Anatomical Curves for Landmark Definitions

Curve Name	Definition
brow ridge	ridge points at the supra-orbital region of the forehead
inferior orbital	rut points immediately below the lower eyelids
lower/upper eye lid	the superior and inferior edges of the palpebral fissure
alar	ridge points on the lateral extension of the nasal cartilage
philtrum ridge	ridge points immediately lateral to the mid-line philtrum
labial seal	rut points where the upper and lower lips meet
lower/upper lip	ridge points along the lower/upper lip
ear rim	ridge points on the peripheral boundary of the ear cartilage, constituting the *helix* and the ear lobe
tragus	ridge point on the rim of the *tragus*, terminating with the superior and inferior points of maximum curvature at the margins of the tragus
mandible	ridge points across the entire mandible (lower jaw)
mid-line nasal profile	ridge points from the nasal root along the dorsum of the nose and the columella
mid-line philtrum	rut points between the columella and the upper lip
mid-line upper lip	the continuation of the philtrum curve to the closest point on the labial seal curve
mid-line lower lip	the continuation of the mid-line upper lip curve to the closest point on the lower lip curve
mid-line mento-labial	the continuation of the mid-line lower lip curve to the closest point of the *mentolabial sulcus* (rut)
mid-line chin	the continuation of the mid-line mentolabial curve to the closest point on the mandible curve

Table 4.2: Landmarks on Single Curves

Landmark Name	New Definition
sellion	the point of maximal curvature of the mid-line nasal profile curve at its nasal root end
subnasale	the point of maximal curvature on the mid-line curve at the base of the nasal septum
alare	the point of maximal curvature along the alar curve
alate crest	the point of maximal curvature on the alar curve where this meets the paranasal area
cheilion	the point of maximal curvature at the lateral end of the labial seal curve
sublabiale	the point of maximal curvature in the mid-line curve as it passes through the *mentolabial suclus*
tragion	the point of maximal curvature at the superior end of the tragus curve
otobasion inferus	the final point at the preauricular end of the ear rim curve

Table 4.3: Landmarks at the crossing of two curves

Landmark Name	New Definition
exocantion	the crossing of the lateral ends of the lower and upper eye lid curves
endocanthion	the crossing of the medical ends of the lower and upper eye lid curves
nasion	the point where the brow ridge curves meet the superior extension of the mid-line nasal profile curve
pronasale	the crossing of the mid-line nasal profile and alar curves
crista philtri	the crossing of the upper lip and philtrum ridge curves
labiale superius	the crossing of the upper lip and mid-line philtrum curves
stomion	the crossing of the mid-line upper lip and labial seal curves
labiale inferius	the crossing of the lower lip and mid-line lower lip curves
gnathion	the crossing of the mid-line chin and mandible curves

Table 4.4: Standard Deviation (mm) of random effects, averaged over all landmarks and dimensions

Random Effect	Curvature	Orientation
Observer	0.361	0.553
Day	0.288	0.323
Image	0.103	0.086
Repeat	0.562	0.587
Subject	1.645	1.670

4.3 Methods of Curve identification

Many different disciplines such as mathematics, statistics, computer science, and biology have an interest in the comparison of different 3-dimensional shapes. Curve identification is not a new concept and several different procedures to determine ridges and valleys (ravines) of shape surfaces are available. Belyaev et al. [1998] use the extrema of the principal curvatures along curvature lines in order to describe the bending of surfaces, where the valleys are the local negative minima of the minimal principal curvatures along the designated curvature line and the ridges are defined in the same manner. Ohtake et al. [2004] take a similar approach by using the first and second order curvature derivatives on triangulated mesh surfaces. Then, by combining multi-level implicit surface fitting and finite difference approximations, an estimation of high-order surface derivatives is computed. For every mesh vertex (of the triangulated mesh), the curvature tensor and curvature derivative can be estimated. Next, every mesh edge is checked for a ridge vertex by determining the angle difference between the principal directions. The ridge vertices are then connected and the strength of the ridge line is determined by the integral of the curvature along the found ridge line using the trapezoid approximation of the integral. Other methods have involved using the inherent vector field of smooth 2-manifold surfaces to extract the ridges. The methods of Ohtake et al. [2004] are used but then Che et al. [2011] produced a projection procedure to ensure that the ridge does not diverge at any point, optimising a ridge guess to lie on a ridge line precisely.

Srivastava et al. [2009] use a Riemannian framework to produce a new facial coordinate system for these 3D surfaces, allowing for both comparison and deformation using a single elastic metric. By introducing the Darcyan Curvilinear Coordinate system the geodesic distance function from a fixed reference point defines the facial surface instead of conducting arbitrary parametrisations of the face. This means that each facial shape is represented as an indexed collection of level curves. This coordinate system is invariant to rotation and translation and deforms with any change in facial expression. It is shown that the Darcyan system allows for a more robust elastic matching of the curves and curve points of facial surfaces, providing a simpler computational implementation. Geodesic paths are found between corresponding, elastically matched, level curves. This then provides a set of optimal elastic deformations between faces and an elastic metric for facial shape analysis and comparison. The main argument for this method is that it compares shapes, not curves. For curves there is a canonical coordinate system that allows study and comparison. The points along a curve have a fixed ordering, allowing for a clear parametrisation. However, there is no set, nor natural ordering of points as there is with curves and therefore no canonical coordinate system that allows for a parametrisation. It is important to note that the Darcyan system relies completely on

the calculated reference point (the tip of the nose), so while there is less reliance on a larger amount of landmarking, the *pronasale* is still used for reference.

4.4 Isolation and Description of Manifold containing desired curve information

Assuming the landmarks are correctly fixed on the 3D facial surface, there is a desire to describe the curve that lies between these two landmarks, thereby isolating anatomical curves on the 3D facial surface. Given a 3-dimensional manifold (in this case with application to a 3-dimensional facial representation) with accurately placed landmarks, there are multiple methods of isolating the desired facial feature area. Mangan and Whitaker [1999] suggest using a type of partitioning of 3D surface meshes using watershed segmentation in order to isolate a desired feature based upon the total curvature of the surface. The surface is then segmented into different surface meshes based upon relative consistency of the strength of curvature throughout that piece, bounded by areas that have a radical change in curvature.

The facial area of interest is isolated given two manually marked landmarks which define the region about which the information is located. A tubular boundary or 'cigar shape' is created by these chosen landmarks and a boundary. The boundary is defined by choosing proportions of the Euclidean distance between the landmarks (pre-determined to be 20 percent in width and 50 percent in height). A projection is taken of all the points that comprise the shape, those which fall within the boundary are kept and those outside of this pre-determined boundary are excluded (Figure 4.2).

Given a 3-dimensional manifold, two landmarks x_1 and x_2, and a boundary distance D, a new 3-dimensional manifold results by assuming a directionality from x_1 to x_2 and subsetting the manifold from the projected x_1 to x_2.

There are a few different starting points to consider when identifying the curve information of this specific manifold. First, a simple, shortest distance path which lies on the surface can be drawn between these two landmarks. A plane cut is taken at every angle (the angle around the two points can be specified from 0 to π) and the shortest distance between the two points is chosen from the optimal angle as illustrated in Figure 4.3. The final curve, using this method (Figure 4.4), does not take into account any curvature information, but is simply optimising on the minimum distance $\int 1ds$, where s denotes arc length.

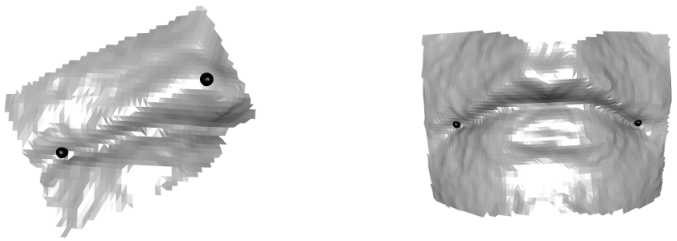

FIGURE 4.2: 3-dimensional manifolds (Ridge-Left and Valley-Right) with two manually marked landmarks

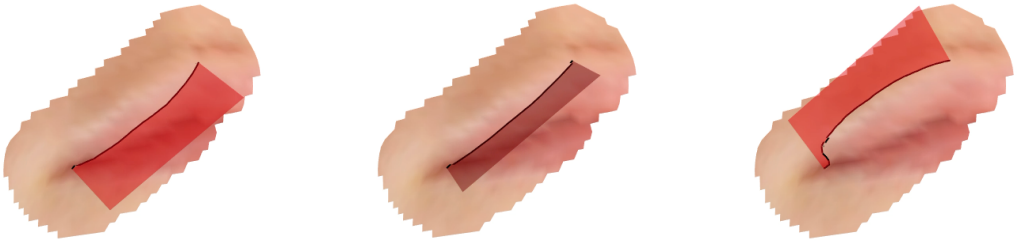

FIGURE 4.3: Plane Cut to determine shortest path

4.4.1 Optimised Planepath By Curvature

Surface information can be used to determine the type and strength of curvature on a surface. Given the manifold M with points p_i where $i = 1, \ldots, m$, any point $p_i \in M$ with a value of shape index SI not equal to 1 for a ridge and -1 for a valley within a set tolerance, is discarded. This leaves only points p_i with the appropriate shape index defining the manifold (Figure 4.4).

Shape index illustrates whether there is a 'ridge' or 'valley' where a point lies, but it does not illustrate the strength of the curvature. Therefore, weights are used to describe the strength of the curvature along the ridge as discussed in Chapter 1. Each point of the manifold is assigned this specific weight. The weights are obtained using the maximum κ, principal curvature. This then leaves a 3-dimensional manifold described by a fixed number of points and two fixed landmark points, where each point has an associated weight value based upon maximum (positive or negative) curvature (Figure 4.5).

This leads to the second method of estimating the curve which lies between the two fixed landmark points on the manifold. Again, a plane cut is taken of the surface at every angle between the two landmarks just as with optimising on shortest distance, but instead optimisation takes place on the values of the shape index curvature (giving a path with the highest curvature Figure 4.6) by maximising $\int v(s)ds$. This gives a more

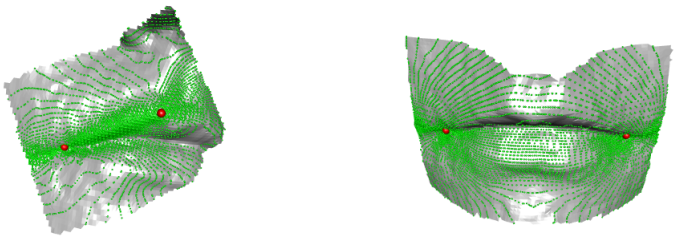

a

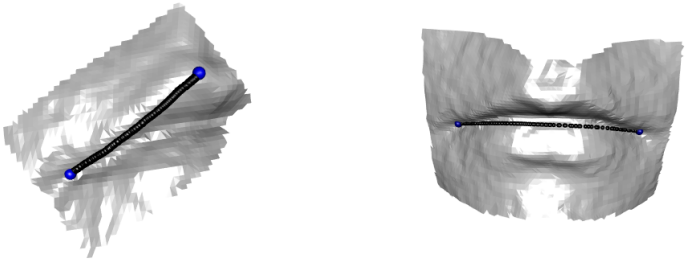

b

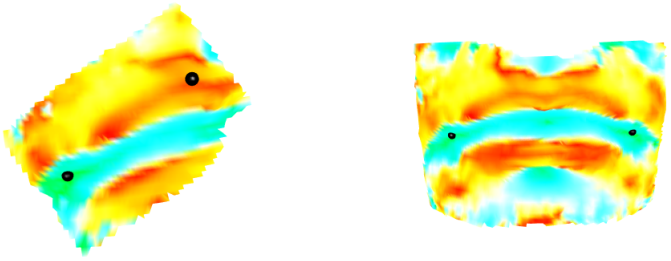

c

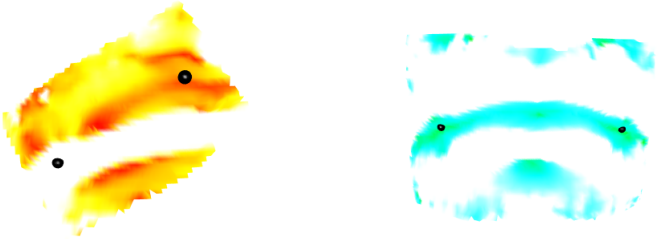

d

FIGURE 4.4: 3-dimensional manifolds (Ridge- Left and Valley-Right) with two manually marked landmarks optimised over distance (a), final distance-optimised curve (b) Shape index (c) and only determined Shape Index (d)

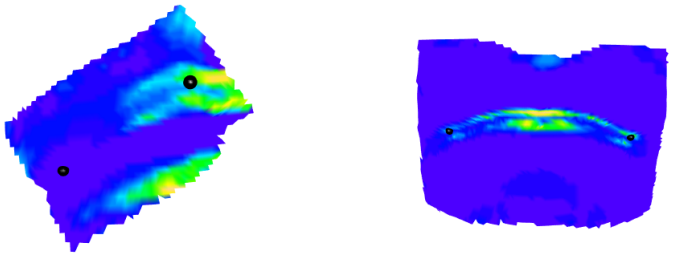

FIGURE 4.5: 3-dimensional manifolds (Ridge-Left and Valley-Right) with two manually marked landmarks

precise definition of the curve that lies between the two manually marked landmarks x_1, x_2 defined as either a ridge or valley. Using the notation of Eberly [1996], given $U \subset \mathbb{R}^n$ an open set where $f : U \leftarrow \mathbb{R}$ is smooth. Given $p_0 \in U$ then $\nabla_{p_0} f$ is the gradient of f at p_0. Recalling definitions from Chapter 1, let $H_{p_0}(f)$ be the Hessian matrix of f at p_0 such that $\lambda_1 \leq \lambda_2, \leq \ldots \leq \lambda_n$ are the ordered eigenvalues and e_i is a unit eigenvector. This then allows for the definition of point p_0 to be a point on the ridge of f if both the following conditions are met such that $\lambda_{n-1} < 0$ and $\nabla_{p_0} f \cdot e_i = 0$ for $i = 1, 2, \ldots, n-1$. Essentially, for this particular analysis, a ridge is the set of points that comprise the specific local maxima curvature value in a quadratic surface patch within a radius of 10mm of the point of interest on the manifold.

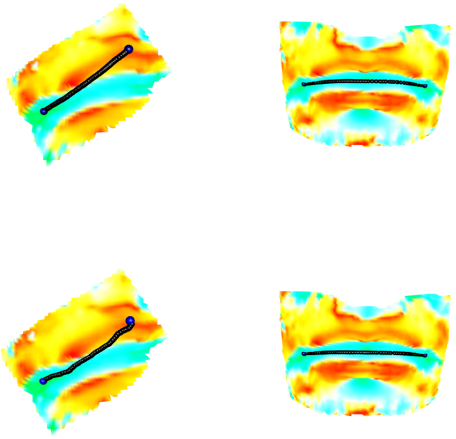

FIGURE 4.6: 3-dimensional manifolds (Ridge- Left and Valley-Right) with two manually marked landmarks coloured by Shape Index: Optimised over shortest distance (top) - Optimised over greatest curvature (bottom)

4.4.2 Optimised Planepath on Curvature with Smoothing

Optimised plane path on curvature values is a constrained estimate, only allowing the path to be on a specific plane. Smoothing is introduced in order to give a more flexible approach. However, the curve must remain on the surface of the manifold. Projecting the manifold onto a 2-dimensional subspace is the most viable method. Following the smoothing procedure which is now carried out on this 2-dimensional subspace, an interpolation function is constructed which easily translates the 2-dimensional information back into its original 3-dimensional space. Most importantly, the curve remains on the manifold.

There are a few different procedures for projecting a 3-dimensional object into two dimensions. Using the first two principal components to interpolate between 3D and 2D (a reduction in dimensionality) is one method. The data are characterised by the value of the first two eigenvalues (of the first two principal components) and therefore the axes can be arranged to be along the eigenvectors rather than using the x, y, and z axes [Dryden and Mardia, 1998]. Implicitly, given a matrix D, $d \times 3$, the set of points are translated to the origin, the covariance matrix Σ is calculated and a single value decomposition is performed on the covariance matrix giving the optimal rotation matrix V. The 2 dimensions correspond to the first two columns $(d \times 2)$ of DV. However, this process can lead to a loss of information where the surface is folded or bends strongly. The procedure used below redefines the axes in two dimensions as the Euclidean distance along the fixed curve and the Euclidean distance to the closest point on the curve from each of the describing points of the manifold (Figure 4.7). This procedure should use the distance along the surface instead of the Euclidean distance, but that process is highly time consuming computationally and there is little difference between the two.

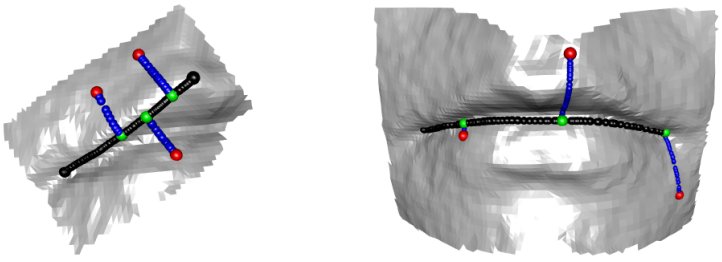

FIGURE 4.7: 3-dimensional manifolds (Ridge- Left and Valley-Right) with reference curve (black), describing points (red), and closest (perpendicular) distance to the reference curve (blue)

It is necessary to understand the distribution of the points and their associated curvatures in order to potentially perform a smoothing process. Viewing the data in two dimensions, coloured topographically by curvature value, it is clear that the standard pattern is that the weights decay as the describing points of the manifold lie further from the curve. Exploring this idea further, the describing points of the manifold are plotted in two dimensions given their perpendicular distance to the curve and their distance along the curve, topographically coloured by each point's respective weight or curvature value (Figure 4.8). There is a clear decay shown as the describing points are further from the curve on either side in an approximate quadratic trend.

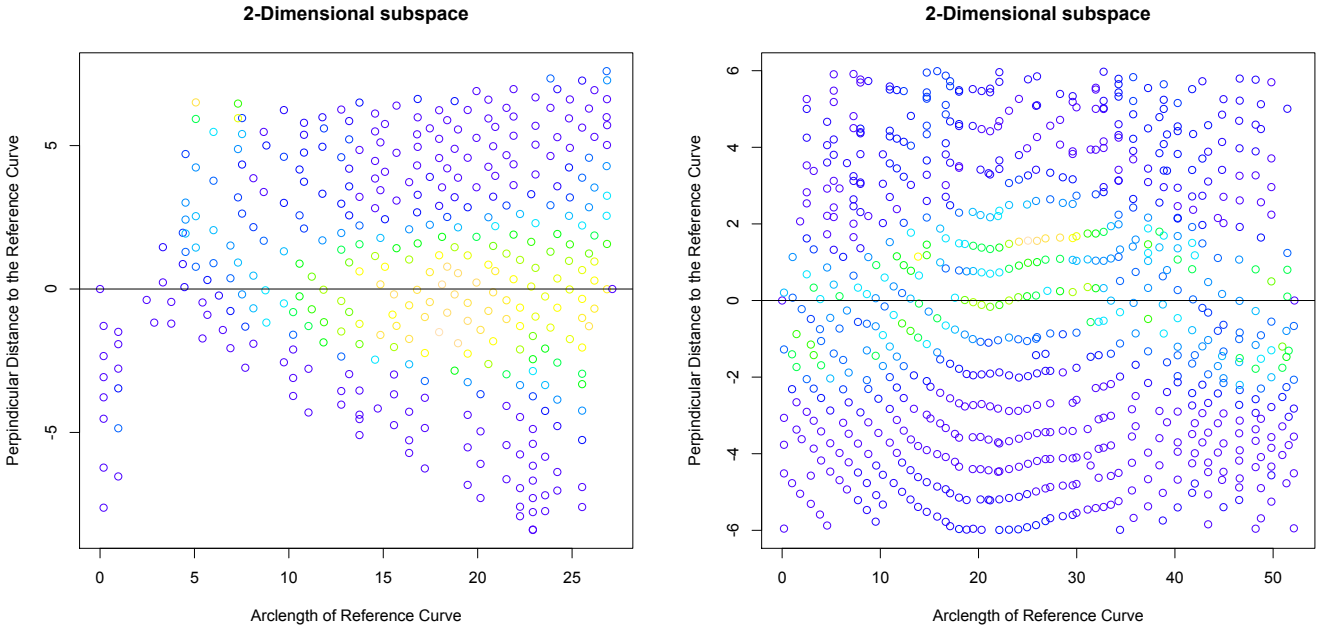

FIGURE 4.8: 3-dimensional manifold plotted in 2-dimensional space (black horizontal line is the reference curve)

Given this, the weights of the describing points are modelled in relation to the perpendicular distance the describing points are from the fixed curve. There are three different methods presented here for smoothing in the 2-dimensional subspace.

In the first approach a scaled exponential pattern is reformulated below into a quadratic regression;

$$W_i = \beta e^{\frac{-1}{2}\frac{z_i^2}{\lambda_i^2}} \epsilon_i$$

$$log(W_i) = log(\beta_i) - \frac{1}{2}\frac{z_i^2}{\lambda_i^2} + \epsilon_i$$

$$log(W_i) = \alpha_i + \gamma_i z_i^2 + \epsilon_i$$

where W_i is the weight for every point p_i, $z_i = d_i - m_i$, ϵ is the error $N(0, \sigma^2)$, α,γ are parameters for weight decay, d_i is the perpendicular distance of the point from the curve and m_i the maximum location. Given this quadratic regression, a smoothing procedure is examined which would allow the rigid optimised curve to be modelled more flexibly. The two coefficients of the quadratic are then smooth functions of the arc length such that $\alpha_i = a(x_i)$ and $\gamma_i = b(x_i)$. Solving this exponential as a quadratic, it is possible to say that the form for this data would be

$$\sum_j \alpha_j \phi_j(x) + \sum_i \beta_j \phi_j(x) m + cm^2,$$

where m is the perpendicular distance and x, the arc length of the curve. Solving the quadratic at any particular arc length gives the maximum at any point. Splines are then used to force smoothness in the quadratic shape. This would mean that for a fixed x, the 1^{st} derivative is

$$Q'(m) = \sum_i \beta_j \phi_j(x) + 2c * m$$

therefore,

$$m_{max} = \frac{-1}{2c} \sum_i \beta_j \phi_j(x).$$

This will be used as the linear constraint, knowing that c must be negative for m to be a maximum.

Splines seem to be an inherently good method of smoothing for this particular case. The following notation is used by Eilers et al. [Eilers and Marx, 1996] where a B-spline is a piecewise polynomial function of degree t . Knots are the break points in ascending order. The spline is only non-zero in the range between the first and the last knot. For any given set of knots, any spline function of degree m can be derived as a linear combination of B-splines such that

$$S_t(x) = \sum_i \alpha_i B_{i,t}(x).$$

P-splines are essentially the B-spline representation, but where the coefficients are determined partly by the data to be fitted and partly by a penalty function. An issue that commonly arises when using B splines is that if a small number of basis functions are used, the positioning of the knots can have a large effect on the fitted model. Penalised splines instead use a roughness penalty as opposed to the number of basis functions in order to control the smoothness of the estimate. The penalty term can be represented by including it into an expanded design matrix. Given that B is the design matrix corresponding to the imposed B-spline basis, D is a second order difference penalty, and

penalty term $\lambda\|D\beta\|^2$, the new design matrix to be solved is

$$\left[\begin{pmatrix} y \\ 0 \end{pmatrix} - \begin{pmatrix} B \\ \sqrt{\lambda D} \end{pmatrix} \alpha \right]^2.$$

Therefore the design matrix for the B-splines (B-spline basis) will simply be

$$B = \begin{bmatrix} \phi_1(x_1) & \dots & \phi_t(x_1) & \phi_1(x_1)m & \dots & \phi_t(x_1)m & m^2 \\ \dots & \dots & \dots & \dots & \dots & \dots & \dots \\ \phi_1(x_n) & \dots & \phi_t(x_n) & \phi_1(x_n)m & \dots & \phi_t(x_n)m & m^2 \end{bmatrix}.$$

Therefore,

$$B; \underline{\theta} = \begin{pmatrix} \underline{\alpha} \\ \underline{\beta} \\ c \end{pmatrix}$$

with the usual penalties on the α's and β's.

This means there will need to be two penalty matrices ($P_{t\times t}$) (one for each parameter).

The two fixed, manually marked landmarks must be integrated into the B spline design. Assume that the B-spline basis with fixed points is

$$A^* = \begin{pmatrix} \phi_1(x_1^*) & \dots & \phi_p(x_1^*) \\ \phi_1(x_2^*) & \dots & \phi_p(x_2^*) \end{pmatrix}$$

and given the linear constraint of $m_{max} = 0$, then

$$A\underline{\theta} = 0.$$

The usual adjustment is then made given that

$$A = \begin{pmatrix} 0 & \dots & 0 & A^* & 0 \\ 0 & \dots & 0 & & 0 \end{pmatrix}$$

such that $B^{-1}A^T(AB^{-1}A^T)^{-1}(\text{fixed points} - A\beta)$ is used in addition to adjust.

The data are fitted using the model above using B-spline smoothing with fixed points (the landmarks) in this 2-dimensional subspace. However, there tended to be some anomalies with this approach, especially when there was not enough information (or describing points) about the manifold. The curve would look for a quadratic, and when one was not found or it was too slight, the curve would go off to infinity. A

second approach to smoothing in the 2-dimensional subspace is simply to use a P-spline smoothing approach (Figure 4.9). A question arises that initiates a fair discussion of why smoothing is an appropriate choice for finding the maximum curvature. The smoothing used simply looks for the mean of the data, but the definition of a ridge or valley is not the mean curvature, but rather, the points along the surface of maximal curvature. However, by Taylor's theorem [Anderson et al., 1958] it can be said that any surface, at any given point can be estimated by a quadratic surface. This algorithm looks at sufficiently small surface patches, so in trying the find the mean curvature by targeting the perpendicular curvature across the ridge, the smoothing process is really finding the mode, or maximal curvature. The difference between the quadratic spline smoothing and simple p-spline smoothing is relatively insignificant in most cases.

The final approach to be considered is fitting a principal curve as defined by Hastie and Stuetzle [1989] to this 2-dimensional subspace. Principal curves are defined as smooth one dimensional curves which pass through the 'middle' of a multidimensional data set (a nonlinear generalization of the first principal component). Previous work has been done on fitting principal curves in 3 dimensions; however, the same issue arises of not lying on the surface of the manifold. If the principal curve is fitted in 2D though, there will be no such problem. This could be potential for further investigation, although an initial query saw the same issue as the quadratic smoothing process with anomalies arising with a lack of information.

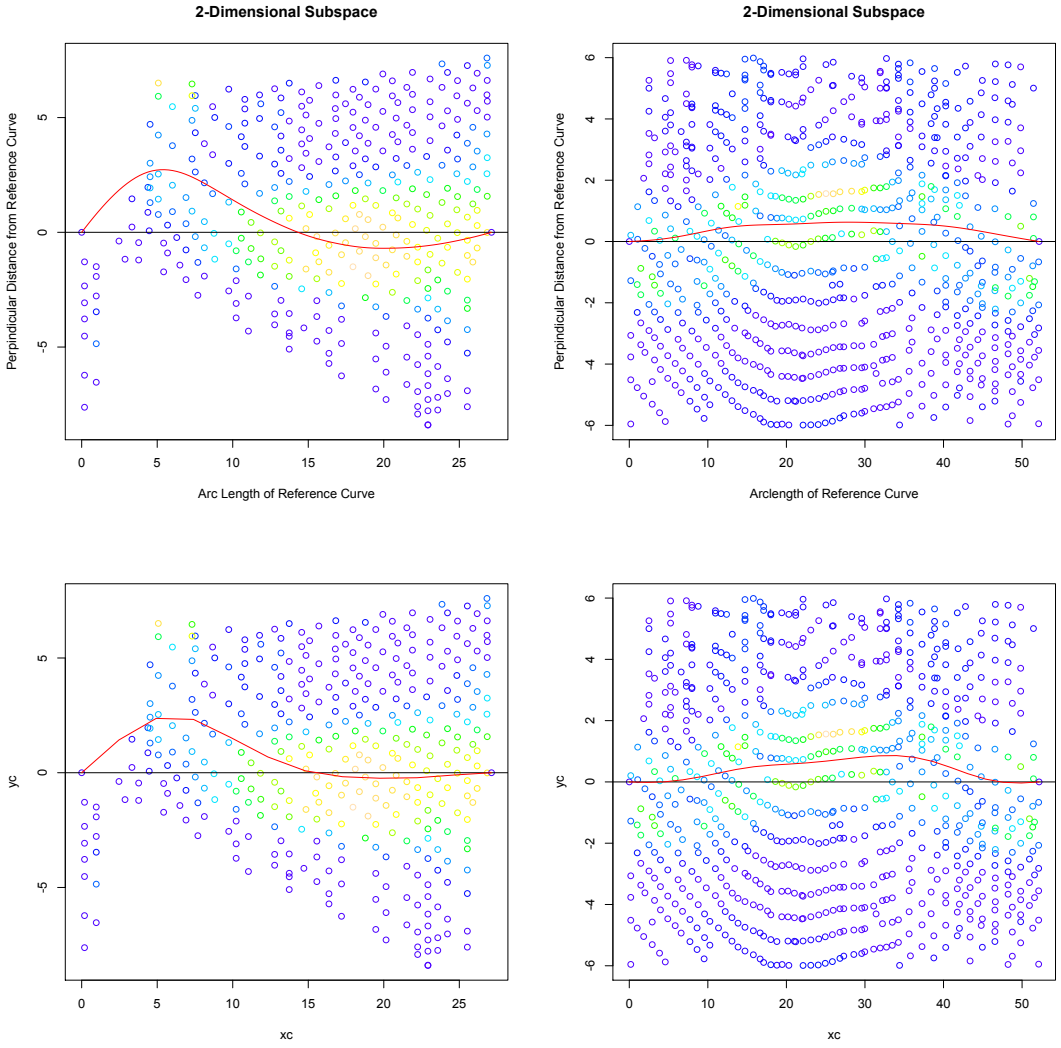

FIGURE 4.9: 3-dimensional manifolds (Ridge- Left and Valley-Right) projected onto a 2-dimensional subspace (black horizontal line is the reference curve) - Quadratic Spline Smoothing (top), Simple Spline Smoothing (bottom)

4.4.3 Numerical Evaluation of Curve Identification in Practice

Shape index is calculated by defining a local surface patch around a specified point. However, this could mean that the actual 'ridge' is potentially blurred by the shape index and gradients of the surrounding, neighbourhood points. This section investigates a method of determining what level of error is involved in estimating the ridge or valley of the surface. Taking a slice of the surface in x and y (Figure 4.10) shows the true ridge point in red and a calculated ridge point in blue having been 'blurred' by the fitting of the quadratic patch when calculating the shape index. Tu et al. [2008] use this concept when trying to recover 3D shape of local planar surface patches from two defocused images (camera system concept). The concept closely follows the issue presented for the curve identification algorithm given that shape there, at each pixel, is specified by the distance and slopes of a local planar surface patch which approximates the surface at that specific pixel. The blurring is considered shift-variant blurring and uses a Taylor series approximation of the pixel distance to determine shape parameters to correct this image imperfection.

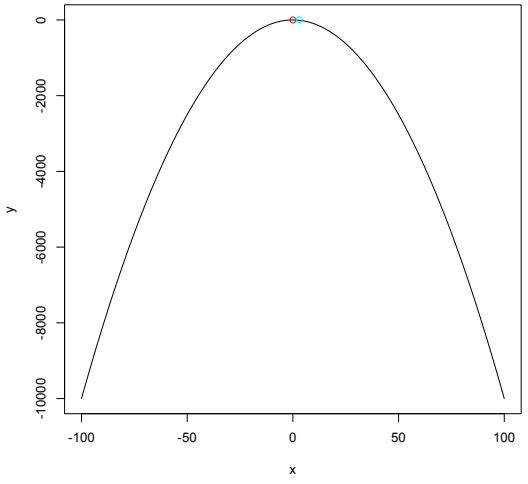

FIGURE 4.10: Quadratic plot slice of surface where the red point marks the true ridge and the blue dot marks the observed ridge

For simplicity, consider the case of two dimensions (x,y). Given a curve $y = f(x) = Bx^2$, twice differentiable, the curve can be parametrised in terms of parameter t such that $x = x(t) = t$ and $y = y(t) = Bt^2$. By definition, the arc length of the curve s is defined as

$$s(t) = \int_a^b \sqrt{\frac{dx}{dt}^2 + \frac{dy}{dt}^2}\, dt,$$

given that $a \leq t \leq b$. Curvature at any point t can also be defined as the rate of change of the tangential angle, Φ, with respect to the arc length s such that

$$
\begin{aligned}
K &= \frac{d\Phi}{ds} \\
&= \frac{\frac{d\Phi}{dt}}{\frac{ds}{dt}} \\
&= \frac{\frac{d\Phi}{dt}}{\sqrt{\frac{dx}{dt}^2 + \frac{dy}{dt}^2}} \\
K(t) &= \frac{x^{'}y^{''} - y^{'}x^{''}}{(x'^2 + y'^2)^{\frac{3}{2}})}.
\end{aligned} \tag{4.1}
$$

This means that both the curvature and arc length can be defined through the auxiliary parameter t (Figure 4.11).

FIGURE 4.11: Quadratic plot slice concept of curvature and arc length values

In order to understand the ability of a quadratic patch to fit a non-quadratic surface, a numerical calculation of the properties of curvature under different settings and neighbourhood sizes was undertaken, but with no noise. It can be assumed that the no noise surface is simply the mean of data that does have noise. Given the simple function $y = f(x)$ the curvature is

$$
K = \frac{|y^{''}|}{(1 + y'^2)^{\frac{3}{2}}},
$$

which was then used to calculate the true curvature for a varying set of curves. This was then compared against the curvature that was calculated from fitting a quadratic patch [Koenderink and Doorn, 1992] to the surface, given different curves, neighbourhood sizes, and mesh sizes. Figures 4.12, 4.13, 4.14 clearly show the 'blurring' that can occur when the curve of interest is progressively steeper. This is due to the patch size capturing not only the ridge of the surface but also some part of the surrounding area that is not quite as 'ridged', giving a lower value. Figure 4.12 show the surfaces, coloured by curvature values, illustrating the effect of simply fitting a quadratic patch (the top figures) versus calculating the curvature values directly (bottom). Figure 4.13 shows plots of the arc length versus curvature of quadratic curves with different neigbourhood (mesh) sizes,

different coefficients and different radii of quadratic patch fitting. It is clear that there is significant blurring at the ends, but the ridges look sufficiently commensurate. However, this figure is quadratic and a quadratic patch is being fit, so it should be the same curvature values. Figure 4.14 reviews a cubic curve in the same states of change as the quadratic. The true calculated curvature is clearly greater than the curvature found from fitting a quadratic patch, meaning that there is blurring that occurs when fitting a quadratic patch to a non quadratic surface.

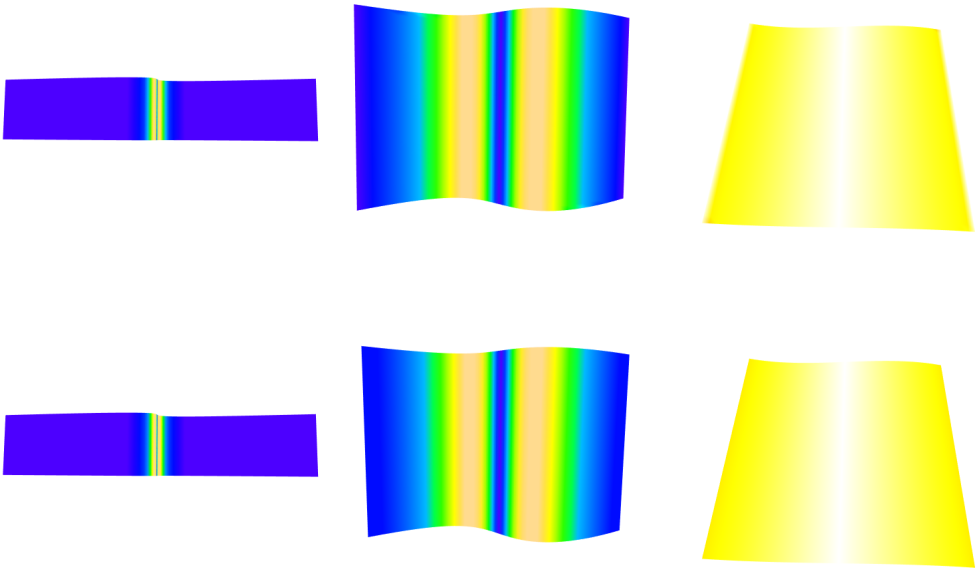

FIGURE 4.12: Values calculated by fitting a quadratic patch (top) and corresponding values calculated directly for a cubic equation (bottom) of varying steepness levels ($y = 5x^3, y = 1x^3, y = .1x^3$, respectively)

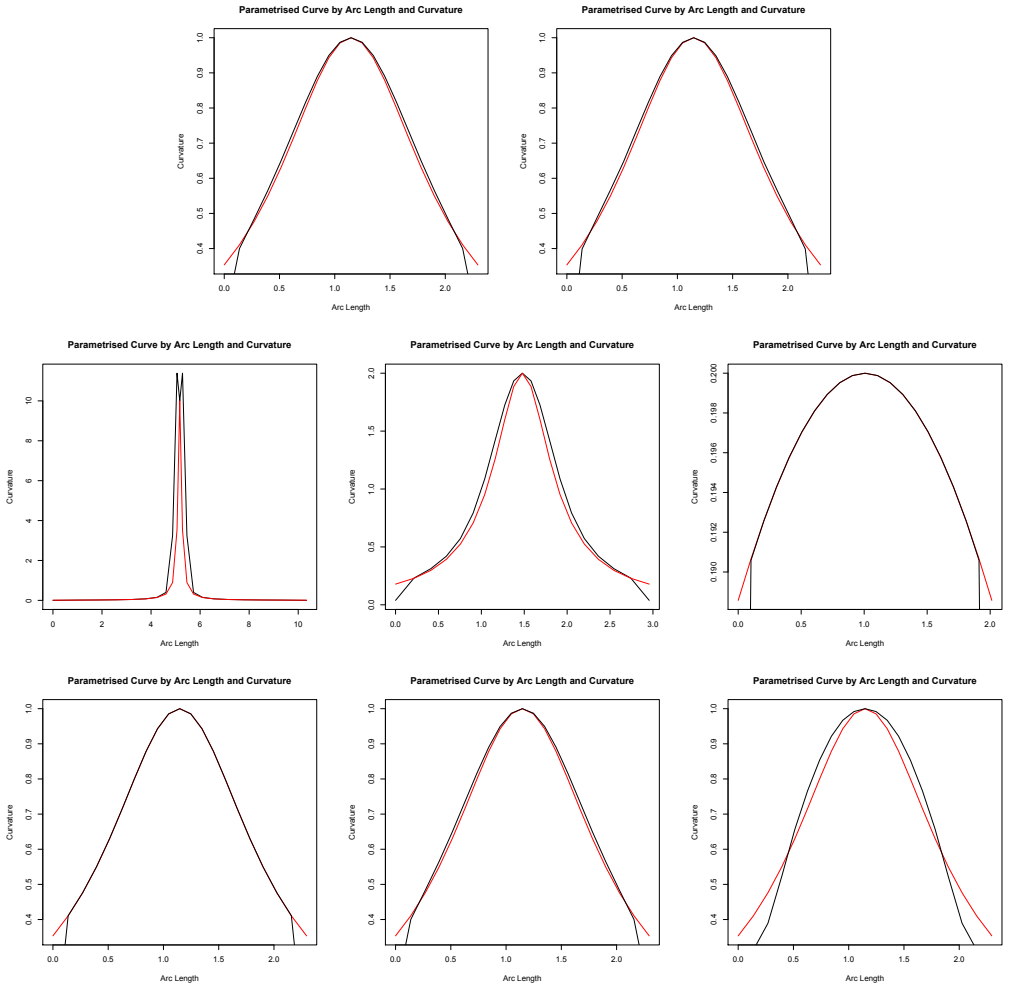

FIGURE 4.13: Plots of arc length and curvature for $y = -\frac{1}{2}x^2$ with mesh sizes 0.05 and 0.10 respectively (top), plots of arc length and curvature for $y = -Bx^2$ with $B = 5, 1, .1$ respectively (middle), and plots of arc length and curvature for $y = -\frac{1}{2}x^2$ with neighbourhood fits of .1, .5, and 1 respectively (bottom) where the black line represents the quadratic patch fit curvature values and the red line represents the true, calculated curvature

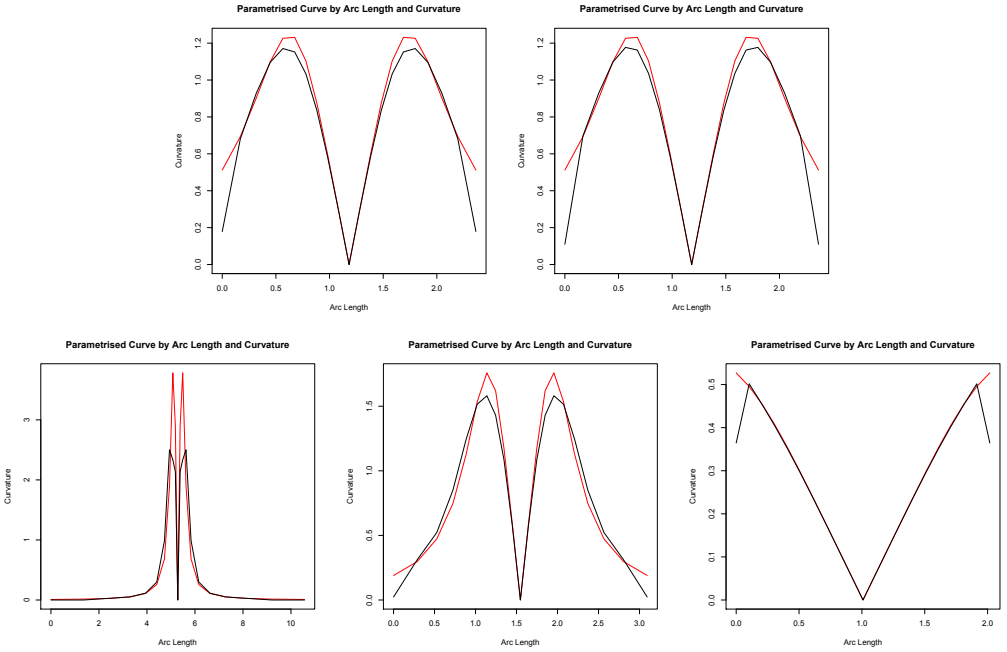

FIGURE 4.14: Plots of arc length and curvature for $y = -\frac{1}{2}x^3$ with mesh sizes 0.05 and 0.10 respectively (top) and plots of arc length and curvature for $y = -Bx^3$ with $B = 5, 1, .1$ respectively (bottom) where the black line represents the quadratic patch fit curvature values and the red line represents the true, calculated curvature

4.4.4 Interpolation - Two Dimensions to Three Dimensions

Once the smoothing process has been performed it is necessary to move back into the 3-dimensional space. When using thin-plate spline smoothing to interpolate the 2-dimensional information back into its original 3D space the curve points are not always interpolated correctly and are, much of the time, off the surface, partly due to whether or not there is an abundance of descriptive points. Due to the failure of this method, barycentric interpolation is implemented. Barycentric interpolation generalises linear interpolation to any dimension. It is not generally used on smooth functions but in this case the method is applicable, as the underlying data correspond to a polygonal (linear) mesh. The algorithm observes the values in a neighboring grid, returns a weighted average of these values and then based upon those averages returns an interpolation [Meyer et al., 2002].

First, a Delaunay triangulation (dividing the convex hull of the grid below into triangles) is built from the 'random' fixed points. Each triangle defines the neighbourhood which is used in interpolation.

For any triangle in Figure 4.15, if an interpolation is carried out at any location within that triangle, the measured value of the three vertices of the triangle will be used. The relative weights of the three vertices are defined by barycentric coordinates. Given a point p on the interior of one of the triangles formed by the describing points x_1,x_2, and x_3, then point p is defined as

$$p = \sum_{i=1}^{3} \alpha_i x_i$$

where the $\alpha_i's$ are the barycentric coordinates of point p with $\alpha_i > 0$, $\sum \alpha_i = 1$. The barycentric coordinates of point p are now used as weights in the interpolation such that

$$f(p) = \sum_{i=1}^{3} \alpha_i f(x_i).$$

Figure 4.16 shows the interpolated data, topographically coloured. The points retain their weight values as shown.

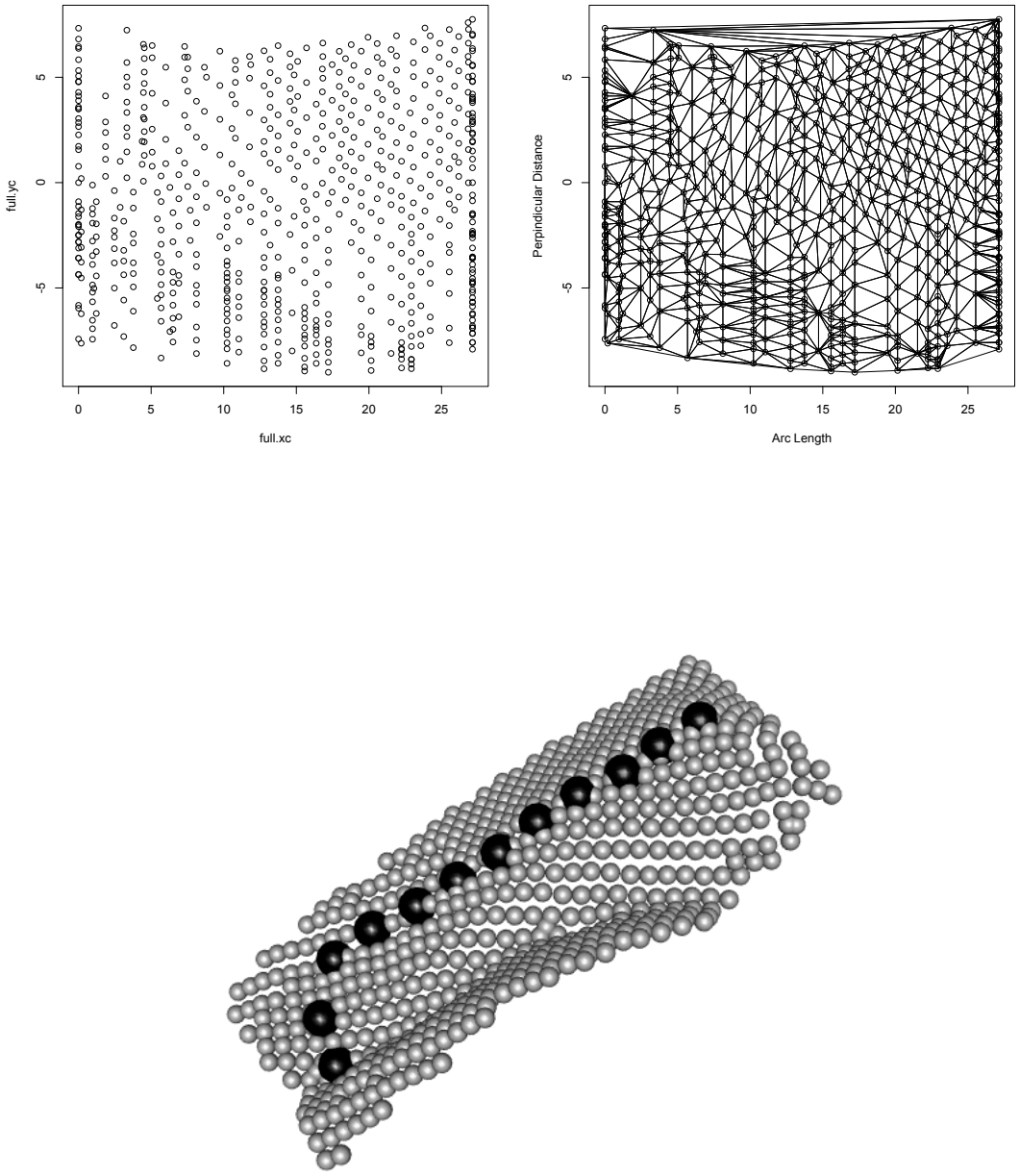

FIGURE 4.15: Barycentric Interpolation

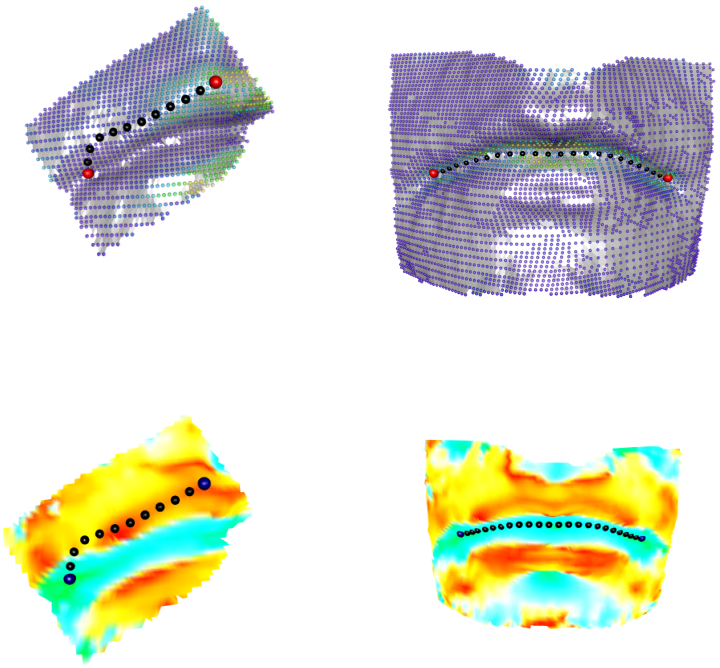

FIGURE 4.16: Topographic 2-dimensional to 3-dimensional interpolation (top) and Smoothed Final Curve referencing Shape Index (bottom)

To summarise, there are three methods of manifold curve identification. The first is an optimised shortest distance curve (shown in green in Figure 4.18). The second is an optimised curvature curve shown in red. Lastly, the optimised curvature curve is used as a reference for a smoothed curve (shown in black).

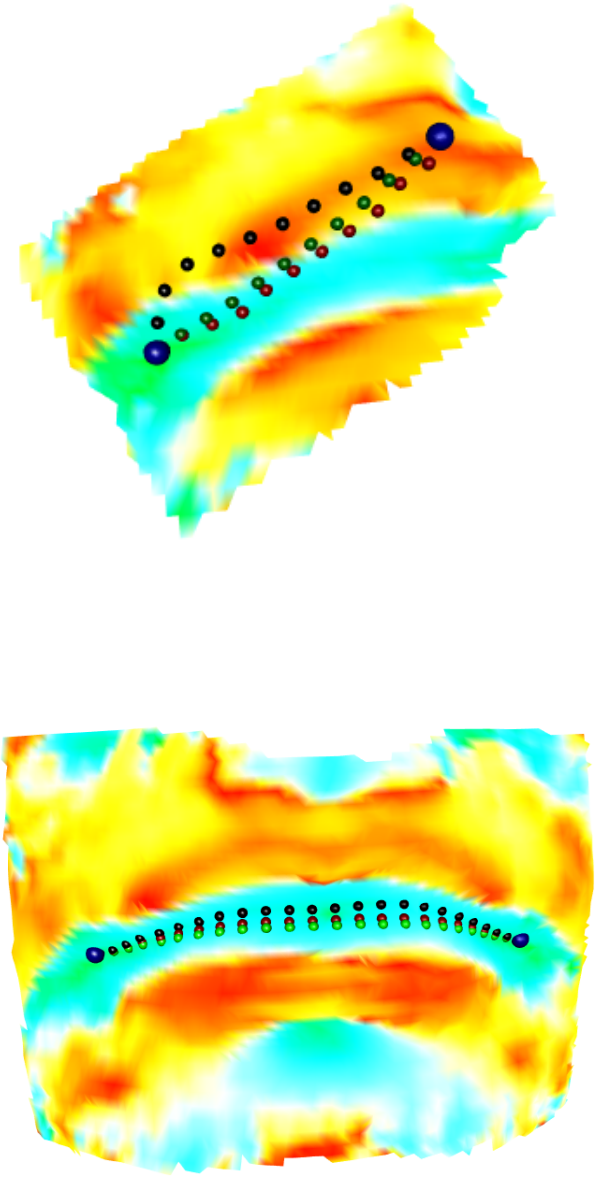

FIGURE 4.17: 3-dimensional manifolds (Ridge- Left and Valley-Right) with optimised distance curve (green), optimised value curve(red) and smoothed curve (black)

The same process is replicated for all the anatomically defined curves of the face between the set of manually identified landmarks. Figure 4.18 illustrates the full set of facial

curves found using the described method.

FIGURE 4.18: 23 manually marked landmarks to Automatic Curve Identification (467 green describing points)

4.4.5 3-dimensional Facial Mesh

In order to realise a full facial mesh from this set of automatically found anatomical curves, there are several steps that must occur. First, intermediary curves are found between the anatomical curves. These points are then made into a surface using a triangulation. Then the mesh must be slid against a facial template in order to minimise bending energy due to the resampling of points along the curves. Lastly, a few curves that are not captured using the curve finding algorithm described before must be warped on the facial surface using a facial template. These steps are described in this section in order to automatically create a full facial mask for each individual image.

From the set of 3-dimensional facial curves, intermediary curves are found in between these using the method of optimised planepath by distance discussed in Section 4.4. There is then a simple triangulation between these points, producing a fully rendered facial mesh. However, there are a number of processes that are performed to ensure an appropriate production. In order to have an even sampling along each curve so that the meshes line up along with the intermediary curves, there must be a resampling of the curve points.

The process of 3D-2D-3D for the smoothing process in Section 4.4.4 is performed such that the curve stays directly on the surface of the manifold, so the resampling must be realised carefully so as to remain congruent. This resampling is achieved using a type of cubic spline interpolation, given that a linear or constant interpolation would not be sufficient. Explicitly, given a curve C in matrix form such that the rows are the

semi-landmarks $p_1 \dots x_n$ and the columns are the dimensionality x, y, z, a cubic spline interpolation is performed for each dimensionality based upon the cumulative Euclidean distance along the curve using splines. This gives a new set of interpolated values for each dimensionality that is assured to be on the manifold surface. This is an iterative process until the cumulative Euclidean distance of the interpolated values reaches a set threshold (Figure 4.19).

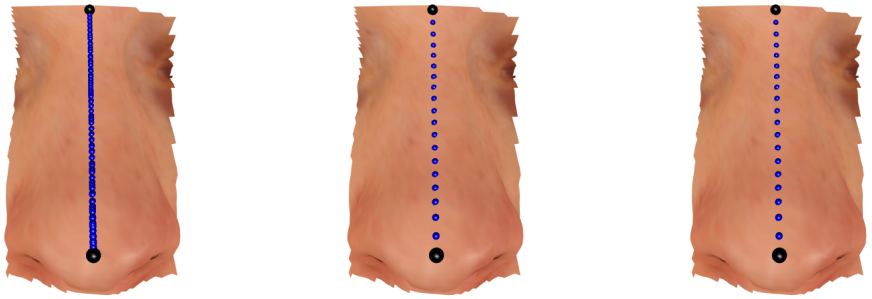

FIGURE 4.19: Resampling of mid-line nasal profile curve - original plane cut (left), after first iteration (middle), final resampled curve(right)

Once all the anatomical and intermediary curves have been sufficiently resampled, the process of sliding, the minimisation of bending energy occurs, requiring a template mesh. A template is a completely symmetric and highly dense 3D facial surface with exactly symmetric curves and meshes already processed, run by the same algorithm as the facial images (Figure 4.20) for both a male facial shape and a female facial shape. The template is created using both a Procrustes mean shape (average of facial shape from about 150 cases) and a single example case. The curves from the Procrustes mean shape for both males and female separately are used by warping an example case's mesh onto the mean curve shape (in order to produce a highly dense surface). This is then triangulated appropriately and used as the warping and sliding surface. Only the Procrustes mean shape curves are used because in order to create a full mesh, a surface path is required, therefore the 'filled in' intermediary curves are warped from an example case.

Sliding is the process of minimising the bending energy of curves between a completely symmetric surface (the template) and a non-symmetric surface (the facial image). This step is necessary due to the lack of definition that arises with simply resampling the semi-landmarks points on a curve to be equidistant. Examining Figure 4.21 bottom a) the thin-plate spline deformation grid shows a substantive pattern of gradients and bending. However, this can be combatted by re-spacing the semi-landmarks. Gunz et al. [2005] suggest that the spacing should be found instead by a by-product of the analysis itself. In general, landmarks are defined as homologous points across specimens, and semi-landmarks (the points in between them that make up the curve) are not necessarily explicitly defined and hence need further examination in order to assign these

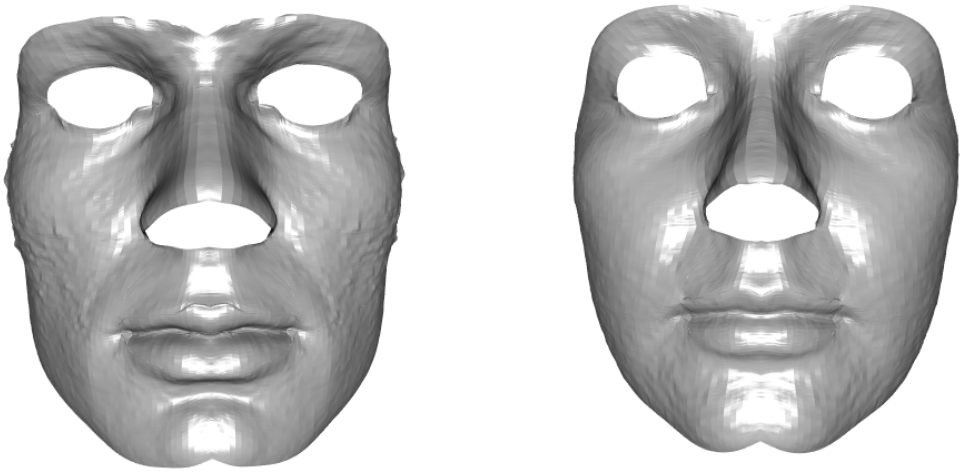

FIGURE 4.20: Template Male (left) and Template Female (right)

semi-landmarks the same level of accuracy across specimens as landmarks. There is an argument that Procrustes distance can be used instead of bending energy as both are simply convenient numeric tools; however, bending energy is invariant under all operations of Procrustes superposition [Bookstein, 1996] and therefore allows for the general geometric morphometrics application seen in Chapter 6.

The following notation follows Bookstein [1997]. Assume a template T with k landmarks $T_i = (x_i, y_i, z_i)$ and a target shape Y with k landmarks $Y_i = (x_i, y_i, z_i)$. Given this, assume U is the function $U(\vec{r}) = |r|$

$$K = \begin{pmatrix} 0 & U_{12} & \dots & U_{1k} \\ U_{21} & 0 & \dots & U_{2k} \\ \dots & \dots & \dots & \dots \\ U_{k1} & U_{k2} & \dots & 0 \end{pmatrix},$$

$$Q = \begin{pmatrix} 1 & T_{x_1} & T_{y_1} & T_{z_1} \\ 1 & T_{x_2} & T_{y_2} & T_{z_2} \\ \dots & \dots & \dots & \dots \\ 1 & T_{x_k} & T_{y_k} & T_{z_k} \end{pmatrix},$$

$$L = \begin{pmatrix} K & Q \\ Q^t & 0 \end{pmatrix},$$

where $O_{4\times4}$ is a matrix of zeros. The thin plate spline $f_k(T)$ has values h_i where at all points T_i is the function $f(T) = \sum_{i=1}^{k} w_i U(T - T_i) + a_0 + a_x x + a_y y + a_z z$, where $W = (w_1, \dots, w_k, a_0, a_x, a_y, a_z)^t = L^{-1}H$ where $H = (h_1, \dots, h_k, 0, 0, 0, 0)^t$ [Bookstein, 1989].

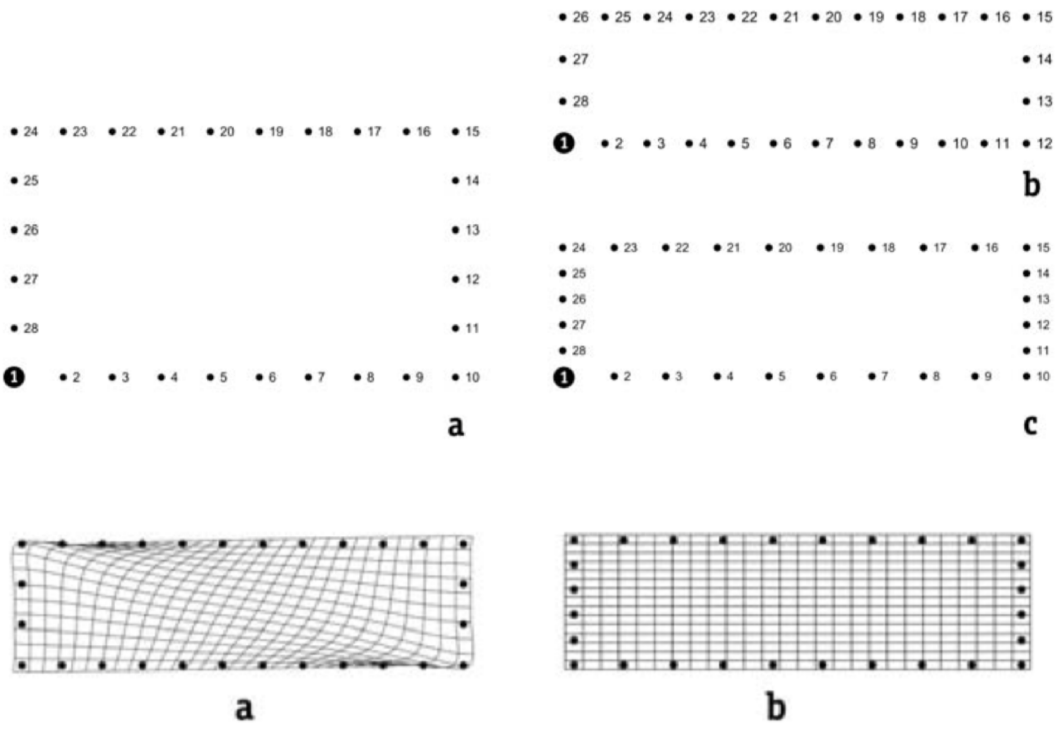

FIGURE 4.21: Top a), A fixed landmark with 27 equally spaced points around it Top b), an elongated rectangle with a fixed landmark and 27 equally spaced points around it Top c), an elongated rectangle with a fixed landmark and 27 optimised bending energy points around it Bottom a), the thin-plate splines corresponding to the deformation grid of top a. to top b., Bottom b) deformation grid of top a. to top c [Gunz et al., 2005]

Therefore, $f(T_i) = h_i$ or f interpolates the function heights h_i at the landmark T_i and the function f has minimum bending energy corresponding to the minimum of

$$\int\int\int_{R^3} \sum \sum_{i,j=1,2,3} \frac{\delta^2 f}{\delta x_i \delta x_j}^2$$

which is approximate to saying that $-W^t H = -H_k^t L_k^{-1} H_k$ where L_k^{-1} is the bending energy matrix that comprises the $k \times k$ matrix as the upper left submatrix of L^{-1} and H_k is the corresponding vector of heights. This is the same as taking the Moore Penrose Generalised Inverse of L, and then the generalised Kronecker product of a 1's diagonal 3×3 matrix and the upper left $k \times k$ submatrix of the Moore Penrose Generalised Inverse.

In seeking the spline of template landmarks $T_1, \ldots, T_k$ onto the target landmarks $Y_1, \ldots, Y_k$, the semi-landmarks are allowed to slide but the landmarks themselves must stay fixed. Say, the original target landmarks are arranged in vector form as

$$Y^0 = (Y_1^x, Y_2^x, \ldots, Y_k^x, Y_1^y, Y_2^y, \ldots, Y_k^y, Y_1^z, Y_2^z, \ldots, Y_k^z)$$

and the positions of the landmarks after sliding are defined as $Y_ij = Y_{ij}^0 + M(v_{ij}^x, v_{ij}^y, v_{ij}^z)$ and this bending energy is

$$-Y^t \begin{pmatrix} L_k^{-1} & 0 & 0 \\ 0 & L_k^{-1} & 0 \\ 0 & 0 & L_k^{-1} \end{pmatrix} Y = -Y^t L_k^{-1} Y.$$

This is then minimised over the hyperplane $Y = Y^0 + UM$ and the solution to this least squares problem is simply

$$M = -(U^t L_k^{-1} U)^{-1} U^t L_k^{-1} Y^0).$$

This is equivalent to calculating the optimal bending energy for every point in the target landmarks Y and choosing the absolute minimum bending energy between each. Many processes allow sliding along the tangent curve to the landmarks; however, for purposes of facial analysis, it is preferable to have the semi-landmark remain on the previously decided curve. This is achieved by using the dense surface given by the camera system. A sufficiently dense surface (for resampling for smoothness) of the facial image is given from the raw data. Therefore using the raw data points that are on the previously decided curve, this is then resampled to be a sufficiently large number in order to satisfy smooth requirements as proposed by Katina [2015a]. The semi-landmarks are then allowed to slide along that resampled curve, but not along the tangent curve. Sliding is performed on all curves, and then the intermediary curves that compose the full facial mesh.

Two curves are difficult to identify in the curve identification algorithm: the upper and lower eye socket curves. For the upper eye socket curves, the eye lashes cause noise in the image capture and the image capture protocol is not designed to aid in the capture of the upper eye socket. The subject is asked to look up at the ceiling so that the camera can fully capture the jaw. However, this means that the subject's eyes are caught at such an angle that it is difficult to capture the well of the upper eye socket. The lower eye socket is problematic, again sometimes due to the eyelashes, but mostly due to the facial image capture algorithm of the eye balls where sharp peaks and valleys occur, instead of a round globe. Using warping methods, the best possible matching for the upper and lower eye socket curves is found. Figure 4.22 illustrates these effects.

The use of thin plate splines provides a smooth interpolation between the set of control points (template) and the corresponding set of target points (the facial image) as described earlier in sliding.

In particular, let L $k_1 \times 3$ be the target landmarks without the warping area of interest, T $k_1 \times 3$ be the template without the warping area of interest, and let V $k_2 \times 3$ be the warping area of interest on the template T. S_ϕ a $k_1 \times k_1$ matrix is the Euclidean distance from every point on T to itself and Z a 4×4 matrix of 0's . Then Γ^{-1} is the Moore Penrose Generalised Inverse matrix of $\Gamma = \begin{pmatrix} S_\phi & 1 & T \\ 1 \dots 1 & 0 \dots & 0 \\ T^T & 0 \dots & 0 \end{pmatrix}$. The thin plate spline coefficients are then simply $C = \Gamma^{-1} \begin{pmatrix} L \\ Z \end{pmatrix}$. The new set of landmarks for the target configuration are comprised of the affine and non-affine contribution of the thin plate spline coefficients such that $V_L = VC_{k_1:k_1+4} + \phi^T C_{1:k_1}$ where ϕ is the square root of the sum of the distances from every landmark in T to V. A full description of this process can be found in Katina [2015a]. This allows both the lower eye curve and the upper eye curve to be interpolated from the template to the facial images.

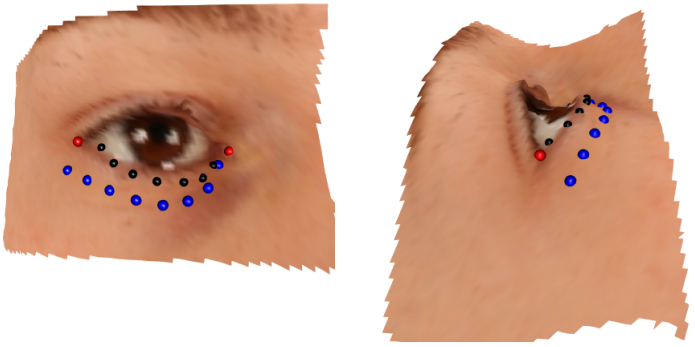

FIGURE 4.22: Warped eye with manual landmarks (red), original curve (black) and warped lower eye socket curve (blue)

Given the full set of curves and intermediary curves between, a full facial mesh is produced (Figure 4.23) and then a simple triangulation of the surface produces a full facial mask (Figure 4.23).

FIGURE 4.23: Automatic Rendered Mesh (922 blue describing points) and Facial 'Mask' (bottom)

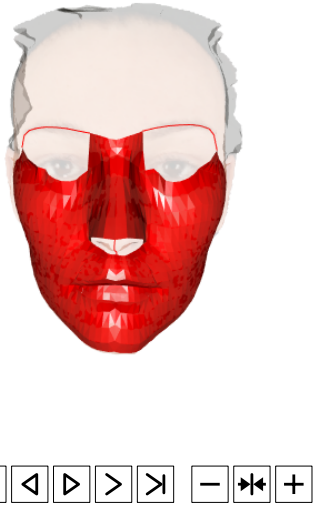

4.4.6 Simulation Study for Curve Identification

Simulation studies are performed to determine the efficacy of using this method of curve identification. Surfaces are created and rendered with known ridges. The determining factors studied are noise (uniform noise added to the height function), curvedness (movement of the curve), steepness (quadratic coefficient), landmark placement (distance the fixed landmarks are moved away from the ridge), and mesh size (patch size of triangulation) over 500 simulations with a surface of 1×1 unit size. The simulation clearly shows that the results are as expected. With an increasingly complex manifold i.e. noise and a flat surface or an extreme ridge, there is more deviation, but at an expected and clearly acceptable level. Figure 4.24 illustrates the levels of factors investigated. Table 4.5 as compared to Table 4.6 illustrates the curve simulation results using steepness of the curve and noise with mesh size factors. Clearly, as the mesh size increases, there is more variability in the observed ridge as the noise and steepness factors increase. The comparison of Table 4.7 and Table 4.8 illustrates the change in observed ridge as the landmarks move further away from the ridge. Clearly as the landmark movement away increases, the observed ridge deviation also increases, as well as with the increase of the other factors (noise, steepness, and curve movement).

These results give a brief snapshot of the findings, with the full simulation study results found in Appendix B. The results show a trend for a larger deviation when the surface is noisy and flat and again a larger deviation when the surface is noisy and very steep. This is consistent with the hypothesis that this algorithm is not yet appropriate for extreme shapes, but has been optimised for facial features. Note that in the following tables "Dev" refers to the deviation from the true ridge given the stated parameter changes.

TABLE 4.5: Ridge Identification Simulation Study - Constant Landmarks - Mesh Size 0.05- Noise-Steepness

Steep	0.250	0.500	0.750	1.000	1.250	1.500	1.750	2.000	2.250	2.500
	Dev	Dev	Dev	Dev	Dev	Dev	Dev	Dev	Dev	Dev
Noise										
0.000	0.000	0.000	0.000	0.000	0.000	0.000	0.000	0.000	0.000	0.001
0.006	0.006	0.003	0.002	0.002	0.002	0.001	0.001	0.001	0.001	0.001
0.011	0.012	0.006	0.004	0.003	0.003	0.003	0.003	0.003	0.002	0.002
0.017	0.015	0.007	0.006	0.005	0.004	0.004	0.004	0.004	0.004	0.004
0.022	0.019	0.009	0.008	0.006	0.005	0.005	0.005	0.005	0.005	0.005
0.028	0.019	0.012	0.008	0.007	0.007	0.007	0.006	0.005	0.006	0.006
0.033	0.021	0.013	0.010	0.008	0.008	0.007	0.007	0.007	0.007	0.007
0.039	0.025	0.016	0.011	0.009	0.009	0.008	0.008	0.008	0.008	0.007
0.044	0.029	0.015	0.012	0.011	0.010	0.010	0.009	0.009	0.009	0.008
0.050	0.034	0.017	0.014	0.012	0.010	0.010	0.010	0.010	0.009	0.009

TABLE 4.6: Ridge Identification Simulation Study - Constant Landmarks - Mesh Size 0.10- Noise-Steepness

Steep	0.250	0.500	0.750	1.000	1.250	1.500	1.750	2.000	2.250	2.500
	Dev	Dev	Dev	Dev	Dev	Dev	Dev	Dev	Dev	Dev
Noise										
0.000	0.000	0.000	0.000	0.000	0.000	0.000	0.000	0.000	0.000	0.000
0.006	0.012	0.005	0.003	0.002	0.002	0.001	0.026	0.017	0.020	0.013
0.011	0.023	0.010	0.005	0.003	0.003	0.003	0.024	0.020	0.016	0.017
0.017	0.028	0.013	0.009	0.005	0.005	0.004	0.022	0.016	0.019	0.016
0.022	0.031	0.016	0.010	0.007	0.006	0.006	0.022	0.019	0.018	0.018
0.028	0.046	0.022	0.013	0.008	0.007	0.007	0.024	0.022	0.017	0.016
0.033	0.052	0.022	0.015	0.009	0.009	0.008	0.022	0.019	0.015	0.023
0.039	0.051	0.025	0.016	0.011	0.010	0.011	0.022	0.022	0.019	0.018
0.044	0.057	0.034	0.019	0.013	0.011	0.013	0.026	0.021	0.018	0.021
0.050	0.061	0.032	0.023	0.014	0.012	0.015	0.026	0.022	0.025	0.020

TABLE 4.7: Ridge Identification Simulation Study - Constant Mesh Size - Landmark Movement 0.01- Noise-Steepness

Steep	0.250	0.500	0.750	1.000	1.250	1.500	1.750	2.000	2.250	2.500
	Dev	Dev	Dev	Dev	Dev	Dev	Dev	Dev	Dev	Dev
Noise										
0.000	0.001	0.002	0.002	0.002	0.002	0.002	0.002	0.002	0.002	0.002
0.006	0.008	0.004	0.004	0.003	0.003	0.003	0.002	0.002	0.002	0.002
0.011	0.011	0.007	0.005	0.004	0.004	0.004	0.004	0.004	0.003	0.003
0.017	0.017	0.010	0.007	0.006	0.005	0.005	0.005	0.005	0.005	0.005
0.022	0.020	0.011	0.008	0.007	0.007	0.006	0.006	0.006	0.006	0.006
0.028	0.020	0.013	0.010	0.008	0.008	0.007	0.007	0.007	0.006	0.007
0.033	0.023	0.015	0.011	0.010	0.009	0.008	0.008	0.008	0.008	0.008
0.039	0.026	0.017	0.012	0.011	0.010	0.009	0.009	0.009	0.009	0.008
0.044	0.031	0.018	0.014	0.012	0.010	0.010	0.010	0.010	0.009	0.009
0.050	0.032	0.017	0.015	0.013	0.011	0.011	0.011	0.010	0.010	0.010

TABLE 4.8: Ridge Identification Simulation Study - Constant Mesh Size - Landmark Movement 0.10- Noise-Steepness

Steep	0.250	0.500	0.750	1.000	1.250	1.500	1.750	2.000	2.250	2.500
	Dev	Dev	Dev	Dev	Dev	Dev	Dev	Dev	Dev	Dev
Noise										
0.000	0.046	0.046	0.051	0.051	0.051	0.046	0.051	0.051	0.051	0.046
0.006	0.052	0.051	0.051	0.051	0.051	0.051	0.051	0.051	0.051	0.051
0.011	0.053	0.052	0.051	0.051	0.051	0.051	0.051	0.051	0.051	0.051
0.017	0.055	0.053	0.052	0.051	0.052	0.051	0.051	0.051	0.051	0.051
0.022	0.057	0.052	0.052	0.052	0.052	0.052	0.052	0.051	0.051	0.052
0.028	0.057	0.053	0.052	0.053	0.052	0.051	0.051	0.052	0.052	0.052
0.033	0.057	0.054	0.052	0.052	0.052	0.052	0.052	0.052	0.051	0.052
0.039	0.059	0.054	0.053	0.051	0.052	0.052	0.052	0.052	0.052	0.052
0.044	0.064	0.055	0.054	0.053	0.053	0.053	0.052	0.051	0.052	0.052
0.050	0.063	0.056	0.054	0.053	0.053	0.053	0.052	0.052	0.052	0.052

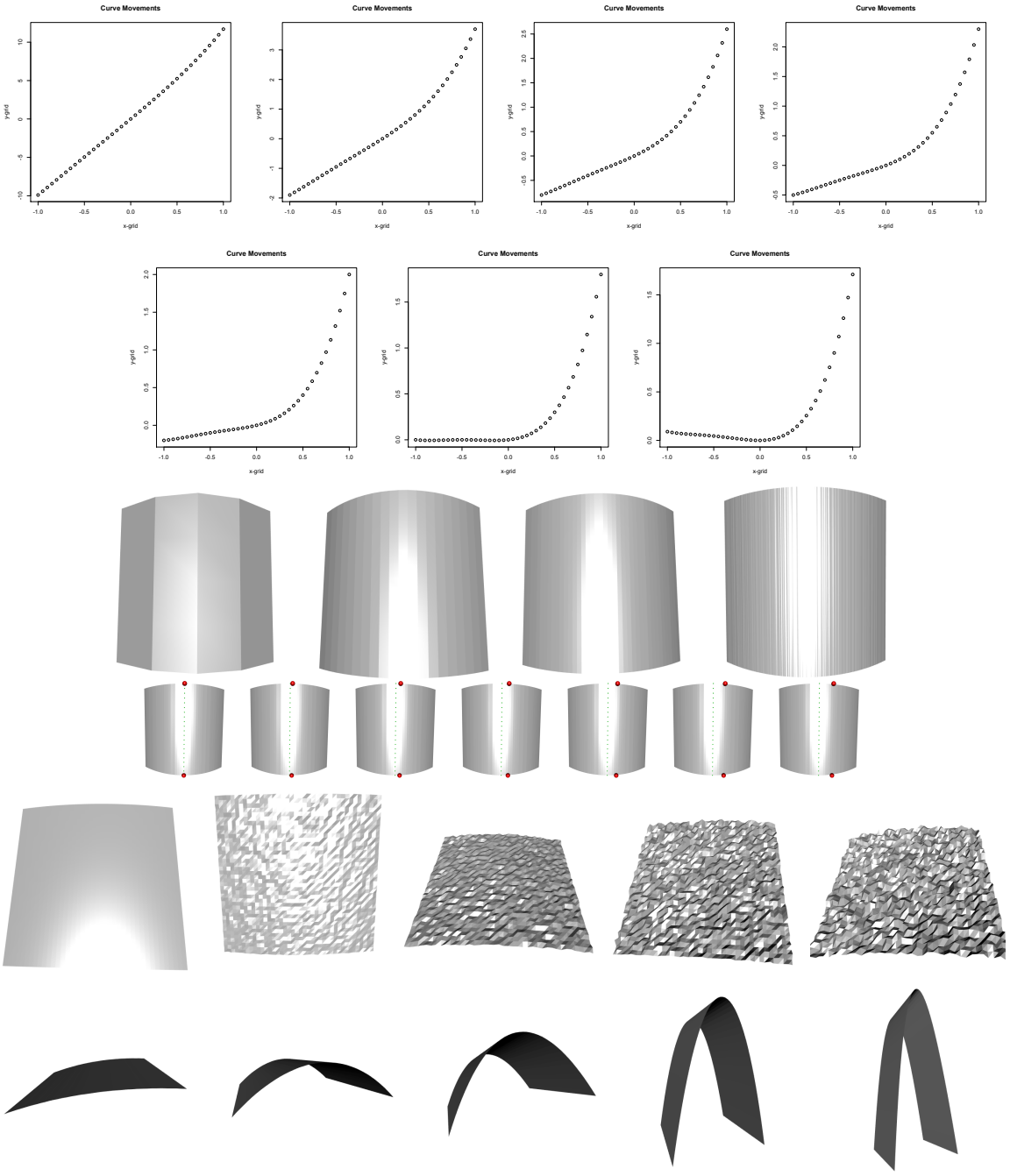

FIGURE 4.24: X, Y plots for different curve movements (top two rows), Mesh size differences (middle top), Landmark Movement (middle-middle), Noise (middle bottom), Steepness (bottom)

4.5 Manual Curve Comparison

While manual landmarking has clear drawbacks and inaccuracies associated with it, it has been the 'gold standard" of production for analysing 3D data. Therefore, the automatically found curves are compared to the manually landmarked curves. These same curves were manually marked in Landmark software ©IDAV. Using 55 cases, the automatically identified curves and the manually marked curves were Procrustes matched giving an overall root mean square distance of 1.70mm. There were particular areas (the lips and the nasal bridge) where there was a significantly increased difference between the manual marker's observation and the automatic ridge procedure. Without these regions of discrepancy, the overall root mean square distances was 0.60 mm.

Looking at these problematic regions more closely will give potential reasons for this discrepancy. For the lips, the manual observer follows the vermillion border exclusively; however, this is not the *upper lip curve* by definition, but the colour of the lips provides an inherent, yet incorrect, guideline for a manual observer. The automatic ridge algorithm simply looks for the area of greatest curvature and ignores any colour change, which gives the true ridge of the upper lip curve. For the nasal bridge, the manual observer always tends to mark behind the actual ridge of the nose, i.e. further up the face toward the eye. It is necessary to rotate the face significantly to tell where the true ridge is whereas the algorithm simply searches for the area of most curvature. While the manual curves may look more precise and symmetric around the lips, Figure 4.26, in fact, the ©IDAV system only allows for certain freedom of movement, giving a falsely symmetric curve. The automatic landmarks, shown in black, follow the true ridge, which is clearly not symmetric when viewing a person's facial features.

4.6 Further study and Use of Curves and Meshes

There are many different methods for identifying curves automatically, but the method described in this chapter is a novel method that uses the surface's intrinsic curvature information to determine and compare between shapes. Given this new method of defining shape and especially facial shape, new methodological analysis tools must be developed in order to fully comprehend and utilise the richer information given by curves and meshes. The tools discussed in Chapter 5 are traditional tools that have been extended in order to fully encompass the additional detail in facial shape. These are novel ways to use these traditional tools.

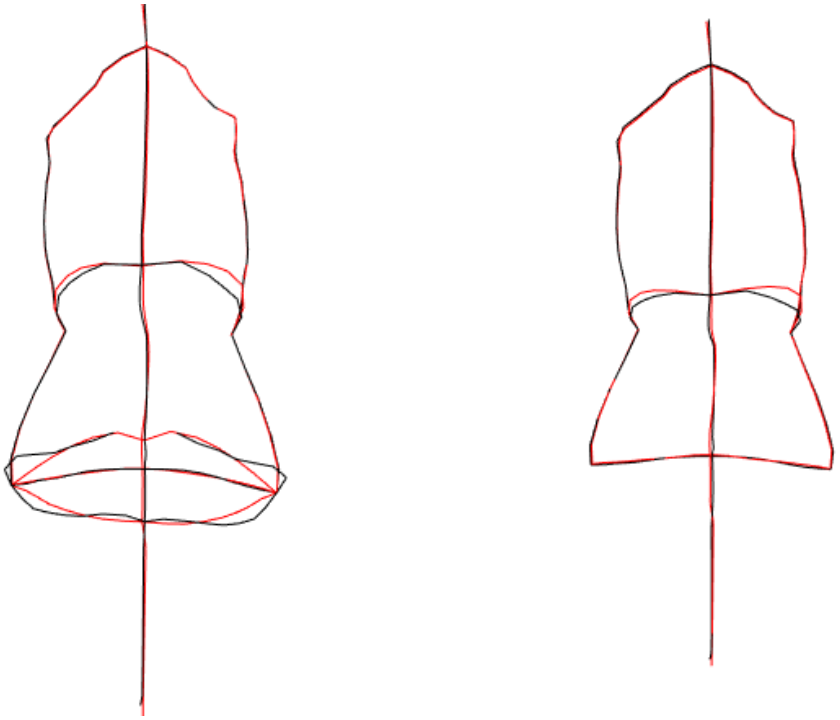

FIGURE 4.25: Example case of Manual curves (red) and Automatic curves (black) comparison with a OSS of 1.61mm (left) and without the upper and lower lip curves OSS of 1.03mm

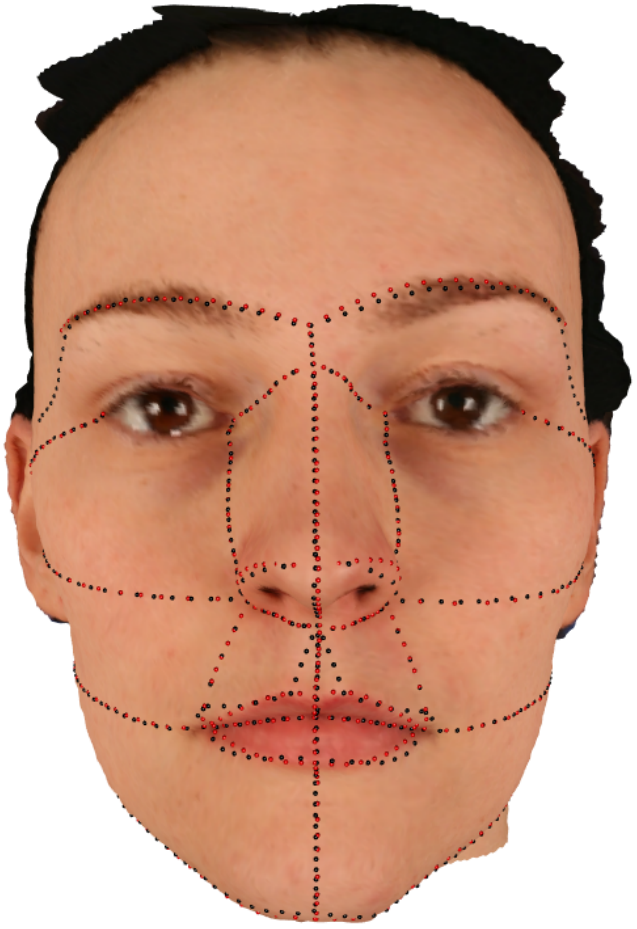

FIGURE 4.26: Example case of Manual curves (red) and Automatic curves (black) comparison

Chapter 5

Analytical Tools

5.1 Introduction

With the creation of these automatic curve and subsequent facial meshes described in Chapter 4, the analysis tools derived for manual facial landmarks must now be extended to include this much richer information. A variety of tools are developed in order to fully take advantage of these facial meshes for the discussion of the differences and similarities between different populations as well as individuals within these populations. Some of these following methods have been previously developed, but all are expanded upon in a novel way. Traditionally, facial anthropometry (measurement of the face) and cephalometry (measurement of the head) have been the common, objective techniques for analysing facial abnormality. Multiple studies document characteristic features and the change that occurs in a face over time with different races, genders, ethnic groups, dysmorphic syndromes, etc. But, with the invention of 3D photogrammetry systems, there are clearly many more tools to be included. Dryden and Mardia [1998] synthesise multiple bodies of work for analysis of configurations of landmarks. In the same vein Ramsay [2006] compiles a set of tools for functional data analysis of curves as opposed to landmarks.

A key characteristic in determining differences in facial shape is asymmetry. Hartmann et al. [2007] created a facial symmetry plane finder using key, manual anatomical landmarks, and then finding a mean deviation angle between symmetry planes to determine varying degrees of asymmetry in facial features. Hammond et al. [2004] use a type of cross-validation with dense surface models with different pattern recognition algorithms in order to determine differences between populations. Simpler approaches such as Lefevre et al. [2012] measure the facial width-to-height ratio (fWHR) to determine characteristic differences between genders and ethnic groups. In general, for all analyses,

geometric morphometrics must first be applied to the sets of shape configurations. In order to compare 3-dimensional facial images the coordinates must be transformed to remove size, location and orientation [Dryden and Mardia, 1998].

5.2 Geometric Morphometrics

Landmark coordinate configurations are independent, not sharing a common origin, and are therefore not comparable to each other. In order to begin comparing these shapes, Procrustes methods must be applied that standardise these 3D configurations to be oriented, rotated, and resized. A *centred* configuration according to Dryden and Mardia [1998] is a configuration with location removed i.e. all the configurations share the same shape origin. Using a transformation matrix derived from a Helmert matrix, location is removed by centring a configuration to the origin. Size is standardised by rescaling the configurations to unit centroid size where the centroid size is the square root of the sum of squared Euclidean distances from each landmark in the configuration to the centroid. Lastly, rotation is removed using a rotation matrix Γ in $S0(m)$, a special orthogonal group of rotations. After these effects have been removed, the shape can be described by the set

$$X = \{Z\Gamma : \Gamma \in SO(m)\},$$

where Z is called the pre-shape of X denoting the configuration after scaling and translating. Generalised Procrustes Analysis (GPA) is applied to optimally superimpose a set of objects to some optimally determined mean shape. The basic algorithm for GPA is to choose some arbitrary reference shape, superimpose all the configurations onto the reference shape, and then compute the mean of all the superimposed configurations. If the Procrustes distance between the computed mean shape and the original arbitrary reference shape is above some set threshold, then set the mean shape as the reference shape. Following Dryden and Mardia [1998]'s notation, given n configurations $X_1, \ldots, X_n$ where $X_i \in R^{k \times m}$, consider the pertubation model

$$X_i = \beta_i(\mu + E_i)\gamma_i + \alpha_i$$

where μ is the unknown mean shape configuration, E_i describes the deviation from μ associated with the particular configuration X_i, and $\beta_i, \gamma_i, \alpha_i$ are the nuisance parameters for scale, rotation and translation, respectively.

For the full method of GPA, all configurations are translated, rotated, and rescaled relative to each other in order to minimise the total sum of squares. The Generalised Procrustes matching equation is such that a quantity proportional to the sum of squared

norms of pairwise differences is minimised;

$$G\left(X_1, ..., X_n\right) = \frac{1}{n}\sum_{i=1}^{n-1}\sum_{j=i+1}^{n}\left\|\left(\beta_i \mathrm{X}_i\Gamma_i + \mathbf{1}_k\gamma_i^T\right) - \left(\beta_j X_j\Gamma_j + \mathbf{1}_k\gamma_j^T\right)\right\|^2 \tag{5.1}$$

by translating, rescaling and rotating the configurations $X_1, ..., X_n$ relative to each other. To avoid a degenerate solution, a constraint

$$\overline{X} = \frac{1}{n}\sum_{i=1}^{n}\left(\beta_i X_i\Gamma_i + \mathbf{1}_k\gamma_i^T\right) = 1 \tag{5.2}$$

is used to ensure that the size of the configuration average is equal to 1.

There is no reference object upon which to project because the objects have not yet been rotated or scaled. Due to the lack of a defined target, the algorithm described above is iterative such that the mean of the registered shape at the $(i-1)^t h$ iteration is the target object. Therefore, when the algorithm converges the *full Procrustes coordinates* for each X_i can be defined by the minimising parameters such that

$$X_i^P = \hat{\beta}_i X_i\hat{\Gamma}_i + \mathbf{1}_k\hat{\gamma_i}^T, i = 1, ..., n \tag{5.3}$$

where $\hat{\beta}_i > 0$ is the scale parameter, $\hat{\Gamma}_i \in SO(m)$ is the rotation matrix and $\hat{\gamma_i^T}$ denotes the location parameters.
The transformed data are now denoted as $X_1^P, X_2^P, \ldots, X_n^P$ and the point in the shape space corresponding to the arithmetic mean of the Procrustes fits

$$\bar{X} = \frac{1}{n}\sum_{i=1}^{n} X_i^P$$

is in the same shape space as the full Procrustes mean, giving an estimate of the unknown mean shape. This is the quantity which minimises

$$[\hat{\mu}] = min_{\alpha^T,\beta,\gamma}\frac{1}{n}\sum_{i=1}^{n}\|\mu - (\beta_i X_i\gamma_i + 1_k\alpha_i^T)\|^2$$

subject to the constraint that the mean is of size 1.

The dimensionality of the shape space is very high after transforming these sets of configurations via Generalised Procrustes Analysis, therefore Principal Components Analysis (PCA) is often used to reduce this dimensionality. PCA is an orthogonal transformation which converts a set of observations of possibly correlated variables into a set of values

of linearly uncorrelated variables, each called a principal component. The transformation is defined in such a way that the first coordinate (principal component) holds the greatest variance of any projection and that the succeeding coordinates also hold the greatest variance given that each is orthogonal to the proceeding coordinate.

In order to fully understand PCA in this setting, it is necessary to discuss tangent space. The tangent space is the linearised version of the shape space in the space of the pole of the tangent projection. In this case, the pole is the mean shape of the data. Continuing with Dryden and Mardia [1998]'s notation, for a matrix $X_{n\times p}$ of tangent co-coordinates, PCA finds the linear combinations of the columns of X that explain the maximal variance of the data. The sample covariance matrix is given by

$$S = \frac{1}{n}(X - n^{-1}\mathbf{1}\mathbf{1}^T X)^T(X - n^{-1}\mathbf{1}\mathbf{1}^T X) = \frac{1}{n}(X^T X - n\bar{\mathbf{x}}\bar{\mathbf{x}}^T) \tag{5.4}$$

where $\bar{\mathbf{x}} = \mathbf{1}^T X/n$ is the row vector of means of the variables and $\mathbf{1}$ is a vector of ones.

The sample variance of a linear combination $\mathbf{a}^T\mathbf{x}$ of a row vector $\mathbf{x}$ is $\mathbf{a}^T\Sigma\mathbf{a}$ and this can be used to obtain the required linear combinations of the columns of X. In particular, $\mathbf{a}^T\Sigma\mathbf{a}$ is maximised subject to $||\mathbf{a}||^2 = \mathbf{a}^T\mathbf{a} = 1$. The eigenvectors and eigenvalues of the sample covariance matrix S of X then identify the principal components. The eigen-decomposition of Σ is defined as $\Sigma = C^T\Lambda C$. This is a non-negative definite matrix, where C contains the eigenvectors and Λ is a diagonal matrix of (non-negative) eigenvalues in decreasing order.

For the purpose of shape analysis, PCA is an orthogonal transformation that captures the variability within the shape or set of shapes. In general, the amount of principal components used for analysis is determined by the amount of variability captured, about 85 percent. The meaning of particular principal components can be expressed by retransforming the associated variables into shape space configurations.

5.3 Tests of No Change in Facial Shape

In order to discuss shape fully, it is of interest to investigate how shape changes as some other measured aspect changes, such as age. A variety of tests will be discussed for the analysis of principal components under the assumption of no change. These tests will be the F-statistic with the Randomisation method, the F-statistic with the Chi-squared method, the likelihood ratio statistic with the Randomisation method, and finally Fisher's method.

5.3.1 Multivariate Linear Regression

Given the multivariate regression model,

$$Y = XB + U,$$

$Y_{n\times p}$ is a matrix of n observed values and p response variables, $X_{n\times q}$ design matrix where q is the known independent variables, $B_{q\times p}$ is a matrix of unknown regression parameters with covariance matrix Σ and U is the unobserved random disturbances. The response variables (columns of Y) are dependent variables explained by the covariate (columns of X) q independent variables. This means that $E(y_{ij}) = x_i' B_{(j)}$.

A multivariate linear regression is fitted to the data with the intention of understanding how face shape changes with age, or some other covariate. Specifically, a model is created with the principal component scores as the response variables (i.e. $Y_{n\times p}$, where p are the principal component scores) and age as the covariate ($X_{n\times 2}$, where the first column is the intercept, and the second, age or size, etc.). The fit $\hat{B} = (X^T X)^{-1} X^T y$ will produce the coefficients of the model.

A non-parametric regression can be performed to estimate the effect of age on the first principal component score. A model which will show the shape variability based upon the different principal component scores is described in Arnold [1981]. Considering the principal component scores ($s_1 = \tilde{y^T} p_1$) and how they relate to the overall shape of an object, is paramount. The shape associated with score j is the mean shape ($mshape$) $+s_1\sqrt{\lambda}\tilde{e_j}$. For the regression model, a particular covariate x, produces fitted values from the regression model $\hat{f}_1 \dots \hat{f}_p$. Therefore in order to translate this back to the shape, consider that each new position is the mean shape added to the score multiplied by the squareroots of the eigenvalue of the first principal component eigenvectors of the sample covariance (i.e. the principal components) $mshape + \sum_{j=1}^{p} \hat{f}_j \sqrt{\lambda_j}\tilde{e_j}$. Using the fitted mean values of the model, this can be extended to include multiple principal components. Therefore given the model $Y_{12} = X_{age}B + U$, the new position is given by the mean shape added to the coefficients of the model multiplied by the age vector (with intercept). The general process of recovering shapes from fitted principal component values is applied as in Section 5.2.

5.3.2 Randomisation Test

Another test to determine possible effects of different covariates is the Randomisation test [Odén and Wedel, 1975]. Given the null hypothesis that the covariate has no effect, then randomly permuting the covariate values against the response variable, calculating

the test statistic on this and comparing with data from the original model, provides a test of no effect. The F-statistic is defined as the division of the total sum of squares and residual sum of squares. It should be stated that this F-statistic will not have an F distribution under the null hypothesis; it is simply a sensible test statistic that becomes an F statistic under certain parametric assumptions that are not being made here.

The F-statistic is calculated for both the original data and for the permuted data. An empirical p-value is computed from the proportion of the permutation F-statistics which exceed the observed F-statistic. If there is no significant effect then the null hypothesis should not be rejected.

5.3.3 Likelihood Ratio Test

In order to begin analysing the model, the log likelihood of Y in terms of β and Σ is calculated. Through linear algebra it is found that

$$l(\beta, \Sigma) = \frac{-1}{2} nlog|2\pi\Sigma| - \frac{1}{2} tr[(Y - XB)\Sigma^{-1}(Y - XB)^T).$$

It is easily seen that $\hat{\beta} = (X^T X)^{-1} X^T Y$ and $\hat{\Sigma} = \frac{1}{n}(Y - X\hat{\beta})^T(Y - X\hat{\beta}) = \frac{1}{n} Y^T P Y$, where $P = I - X(X^T X)^{-1} X^T$(the hat matrix) projecting orthogonally onto the columns of X [Loader, 1999]. Therefore the maximum value of the log-likelihood is

$$l(\hat{\beta}, \hat{\Sigma}) = \frac{-n}{2} log|2\pi\hat{\Sigma}| - \frac{np}{2}.$$

Consider the general linear hypothesis where $C_1 B = 0$ with C_1 $(g \times q)$. C is partitioned such that $C^{-1} = (C^{(1)}, C^{(2)})$, where C_2 is a matrix such that $C^T = (C_1^T, C_2^T)$ is a non-singular matrix $q \times q$. Let B_0 be any matrix such that $C_1 B_0 = 0$. This means the new projection is defined as $P_1 = I - XC^{(2)}(C^{(2)T} X^T X C^{(2)})^{-1} C^{(2)T} X^T$ onto the subspace, which is orthogonal to the columns of $XC^{(2}$).

Recalling that the maximum value of the log-likelihood is $l(\hat{\beta}, \hat{\Sigma}) = \frac{-n}{2} log|2\pi\hat{\Sigma}| - \frac{np}{2}$, the maximum likelihood under the null hypothesis is $|2\pi n^{-1}(Y - XB_0)^T P_1 (Y - XB_0)|^{-n/2} e^{\frac{-np}{2}}$ and the maximum likelihood under the alternative hypothesis is

$|2\pi n^{-1} Y^T P Y|^{-n/2} e^{\frac{-np}{2}}$. The likelihood ratio statistic for the hypothesis has test statistic

$$\lambda^{2/n} = \frac{Y^T P Y}{Y^T P Y + (Y - XB_0)^T (P_1 - P)(Y - XB_0)}.$$

Specifically, for the case of age as the covariate and the principal component scores as the response, $C = C^{-1} = \begin{pmatrix} 0 & 1 \\ 1 & 0 \end{pmatrix}$, $C_1 = [0, 1]$, $C_2 = [1, 0]$, $B = \begin{pmatrix} 1 & 1 & \dots & 1 \\ \beta_1 & \beta_2 & \dots & \beta_p \end{pmatrix}$, $B_0 = \begin{pmatrix} 1 & 1 & \dots & 1 \\ 0 & 0 & \dots & 0 \end{pmatrix}$, and $X = \begin{pmatrix} 1 & x_1 \\ \dots & \dots \\ 1 & x_n \end{pmatrix}$.

Now that the test statistic has been calculated, it is transformed using Bartlett's Approximation into a chi-squared distribution:

$$-m - \frac{1}{2}(p - n + 1) \log \Lambda(p, m, n) \sim \chi^2_{np}$$

as $m \to \infty$, where m is the error degrees of freedom, n the hypothesis degrees of freedom, and p the number of regression parameters [Hair et al., 2006].

5.3.4 Nonparametric Smoothing Test

In order to investigate other methods through which to examine model alternatives, a non-parametric smoothing technique approach is discussed due to the diversity of the data. A p-value can be computed given that the F-statistic is in quadratic form [Hair et al., 2006]. Given a simple scenario where $H_0 : E\{y_i\} = \mu$, $H_1 : E\{y_i\} = m(x_i)$, a smooth function of x, the residual sums of squares are easily computed as $RSS_0 = \sum_{i=1}^{n}\{y_i - \hat{y}\}^2$ and $RSS_1 = \sum_{i=1}^{n}\{y_i - \hat{m}(x_i)\}^2$. Using the notation of Bowman and Azzalini [2004] in this section, in order to quantify the differences between the residual sums of squares the statistic $F = \frac{RSS_0 - RSS_1}{RSS_1}$ is of course known to be proportional to the usual F-statistic. Therefore, this is instead the pseudo likelihood ratio test, where H_1 is not of a parametric class and the estimate cannot be fitted by MLE. In order to find the distribution of F under H_0, F is written in quadratic form such that

$$F = \frac{y^T B y}{y^T A y},$$

where A is matrix $(I - S)^T(I - S)$, B is matrix $I - L - A$, L is a $n \times n$ matrix with values $\frac{1}{n}$, and S is a smoothing matrix which creates the vector of fitted values $\hat{m}(x_i)$. Recall that A and B would need to be positive definite for the linear results to apply. However, the p-value can be computed as

$$\begin{aligned} p &= P\{F > F_{obs}\} \\ &= P\{\tfrac{y^T B y}{y^T A y} > F_{obs}\} \\ &= P\{y^T C y > 0\} \end{aligned} \tag{5.5}$$

where $C = B - F_{obs}A$. Clearly, y_i has mean μ under H_0, but it is easy to see that μ drops out of the F-statistic. Therefore $y^T Cy$ is equivalent to $Q = \epsilon^T C\epsilon$. When n is large, it is difficult to directly calculate the numerical value of p. Therefore, p is then approximated by replacing the new distribution of Q by a more convenient distribution with the same first three or four moments. The cumulants can be calculated directly by the cumulant generating function

$$K_n(Q;\lambda;\omega) = logE(e^{\theta Q(\omega)}),$$

where $Q(\omega) = \sum_{i=1}^{n} \lambda_i \omega_i^2$, and $W_i, i = 1 \ldots n$ are mutually independent unit normal variables. In the central case where y_i has mean 0, the s^th cumulant of $Q(\omega)$ is

$$k_s(Q;\lambda;0) = 2^{s-1}(s-1)! \sum_{j=1}^{n} \lambda_j^s,$$

where Λ are the eigenvalues of VC and where V is the covariance matrix of y. It is further seen that $\sum_{j=1}^{n} \lambda_j^s$ is simply the $tr\{(VC)^s\}$, so

$$k_s(Q;\lambda;0) = 2^{s-1}(s-1)!tr\{(VC)^s\}.$$

The moments of $a\chi_b^2 + c$ distribution are matched with the moments of Q. The is due to the use of independent standard normal variables. In other words, with the data being the residual vector represented by the fitted model $e = (e_1, \ldots, e_n)^T$,

$$\begin{aligned} p &= P\{\tilde{\epsilon}^T A\tilde{\epsilon} > 0\} \\ &= P\{a\chi_b^2 + c > 0\} \\ &= P\{\chi_b^2 > \tfrac{-c}{a}\} \end{aligned} \tag{5.6}$$

such that $a = \frac{\|k_3\|}{4k_2}$, $b = \frac{8k_2^3}{k_3^2}$, and $c = k_1 - ab$. The p-value is calculated as $1 - q$ where q is the probability of lying below $\frac{-c}{a}$ in a Chi-squared distribution with b degrees of freedom. Notice that the components of e are correlated, $var(e) = V$, but it is the same computation of the distribution of a quadratic form of normal random variables with mean zero.

In order to understand if the p-value can be derived as the likelihood ratio test the univariate case is examined. Recall that the test-statistic for the likelihood ratio test is simply, $\lambda = \frac{L_u}{L_r}$ where u implies an unrestricted hypothesis and r, restricted. It is easily

seen that the F-ratio is a monotone transformation of the likelihood ratio statistic since

$$\begin{aligned} \lambda &= \frac{L_u}{L_r} \\ &= \frac{\frac{2\pi}{n}^{-\frac{n}{2}} e^{\frac{-n}{2}} RSS_0^{\frac{-n}{2}}}{\frac{2\pi}{n}^{-\frac{n}{2}} e^{\frac{-n}{2}} RSS_1^{\frac{-n}{2}}} \\ &= \left(\frac{RSS_0}{RSS_1}\right)^{-\frac{n}{2}} \end{aligned} \tag{5.7}$$

$$\begin{aligned} F &= \frac{\frac{RSS_1 - RSS_0}{r}}{\frac{RSS_0}{n-k}} \\ &= \frac{n-k}{r}(\lambda^{\frac{2}{n}} - 1). \end{aligned} \tag{5.8}$$

For the multivariate case, assume the model $Y = X\beta + U$, where Y is n by p, n is the sample size and p is the number of response variables. X is a n by q design matrix, where q is the number of independent variables, β is a q by p matrix of unknown regression parameters, and U contains the unobserved random disturbances. Assume a variance-covariance matrix $\Sigma = \sigma^2 I$ where $\hat{\Sigma} = (Y - X\hat{\beta})^T(Y - X\hat{\beta})$, unrestricted estimator $\hat{\beta} = (X^T X)^{-1} X^T y$, and log likelihood $l = \frac{-n}{2} log\hat{\Sigma}$. Assuming the same variance, $\hat{\Sigma}_{ii} = (\tilde{y_i} - X\tilde{\beta_i})^T(\tilde{y_i} - X\tilde{\beta_i}) = RSS_1$. It follows simply that $\|\hat{\Sigma_1}\| = \prod_{j=1}^{p} RSS_{j1}$, and $\|\hat{\Sigma_0}\| = \prod_{j=1}^{p} RSS_{j0}$. The test-statistic can be written as

$$\lambda^{2/n} = \frac{\|\hat{\Sigma_0}\|}{\|\hat{\Sigma_1}\|} = \frac{\prod_{j=1}^{p} RSS_{j0}}{\prod_{j=1}^{p} RSS_{j1}}.$$

While in the multivariate case the F-ratio is no longer a monotone transformation of the likelihood ratio statistic, it yields a feasible form motivated by the likelihood ratio test. However, there are other tests that form a more convenient approach in determining the goodness of fit of the alternate models for principal components analysis.

5.3.5 Fisher's Method

Having originally examined the use of the F-statistic as the Likelihood Ratio Test with an independence amongst all the responses for the flexible regression case, it seemed unreasonable to assume independence. However, if there is no change assumed in the facial shape, then all of the principal components will be independent. Therefore a variation on Fisher's method is appropriate to combine the p-values of independent tests based upon the same null hypothesis into one test statistic

$$X^2 = -2\sum_{i=1}^{k} log_e(p_i),$$

where p_i is the probability that the i^{th} variable (test) exceeds the observed value under the null hypothesis i.e. the p-value for the i^{th} test [Elston, 1991]. Under the null hypothesis, with all $p_i's$ independent, X^2 has a Chi-squared distribution with $2k$ degrees of freedom, where k is the number of independent tests combined. For the combined analysis, the null hypothesis is that all individual null hypotheses are true, and the alternative hypothesis assumes that at least one of the individual null hypotheses is not true.

Doing a simulation of Fisher's method using generated data from the normal distribution, the Bowman and Azzalini [2014] is utilised for calculating p-values. For the current purposes, independence can be assumed for the special case of principal component scores as the response variable and a covariate such as age. Having generated data, the p-value is extracted from a nonparametric regression on a single response variable with one covariate, with the assumption that there is no effect. This process is repeated on all the response variables and the Fisher statistic is then calculated.

Comparing this to the Chi-squared distribution with $2k$ degrees of freedom, Figure 5.1 shows that it does closely follow a uniform distribution. This is expected due to the probability of all tests regardless of the number of response variables being the same. For 10 response variables and 100 response variables the situations are similar where the empirical p-value (the percentage of p-values below .05) is 0.054 for 10 response variables and 0.057 for 100 response variables.

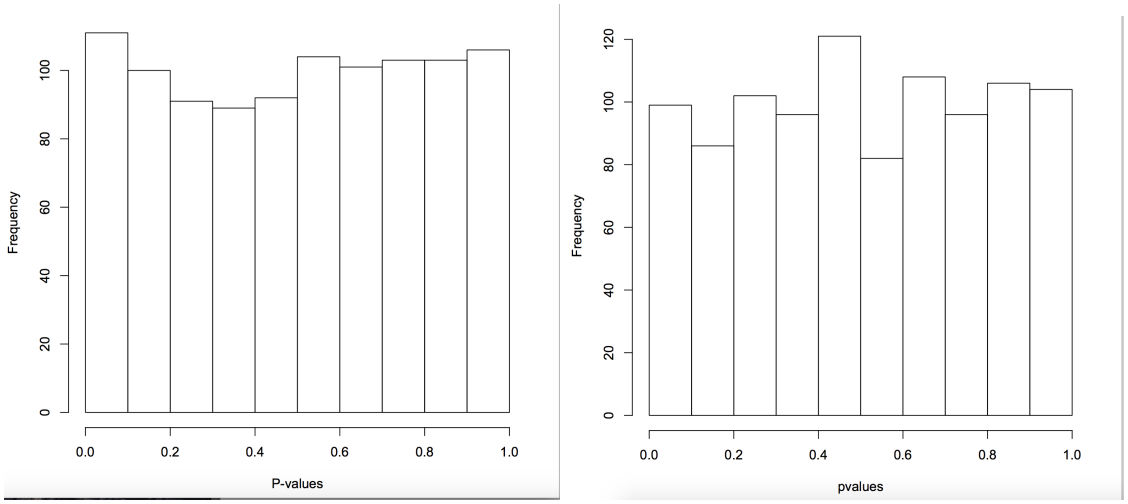

FIGURE 5.1: Fisher's Method Simulation for 100 response variables (left plot) and 10 response variables (right plot)

If there is dependence that is not accounted for and there is a small p-value, the evidence for the alternative hypothesis could be overstated. There is a modification required to approximate the null distribution of X^2 when the variables (i.e. tests) are not jointly

independent. Brown's method includes combining dependent p-values with known covariance, and Kost's method involves combining dependent p-values with unknown covariance.

For Brown's method [Gay, 1975], assume a joint multivariate Gaussian density amongst all the variables (tests). Under the null distribution, the covariance between $-2log_e p_i$ and $-2log_e p_j$ is a function only of the correlation between the i^{th} and j^{th} variables (tests). The covariance is then evaluated and tabulated using numerical integration giving an arbitrary correlation matrix. Then the first two moments of X^2 can be calculated which are then equated to those from the chi-squared distribution and an approximate distribution for X^2 can be derived adequate to a wide range of correlations. If the variables (tests) are not jointly independent then X^2 has mean

$$E(X^2) = 2k$$

and variance

$$\begin{aligned} \sigma^2(X^2) &= \textstyle\sum_i \sum_j cov(-2log_e(p_i), -2log_e p_j) \\ &= 4k + 2\textstyle\sum_{i<j} \sum cov(-2log_e(p_i), -2log_e p_j), \end{aligned} \tag{5.9}$$

where the $cov(x, y)$ represents the covariance between x and y. Since the p-values are invariant under the group of affine transformations, it is clear that the covariance between $-2log_e p_i$ and $-2log_e p_j$ is a function only of the correlation between the i^{th} and j^{th} variables (tests). The covariances can be computed by a Gaussian quadrature. It can then be shown that X^2 can be approximated by cX_f^2 where X_f^2 is a chi square variate with f degrees of freedom. When the first two moments of X^2 and cX_f^2 are equated,

$$E(X^2) = cf$$

$$\sigma^2(X^2) = 2c^2 f.$$

Clearly, c and f can be easily computed and evaluated where

$$f = 2E(X^2)^2/\sigma^2(X^2)$$

and

$$c = \sigma^2(X^2)/2E(X^2).$$

Data are simulated with correlated responses with an uncorrelated covariate in Figure 5.2.

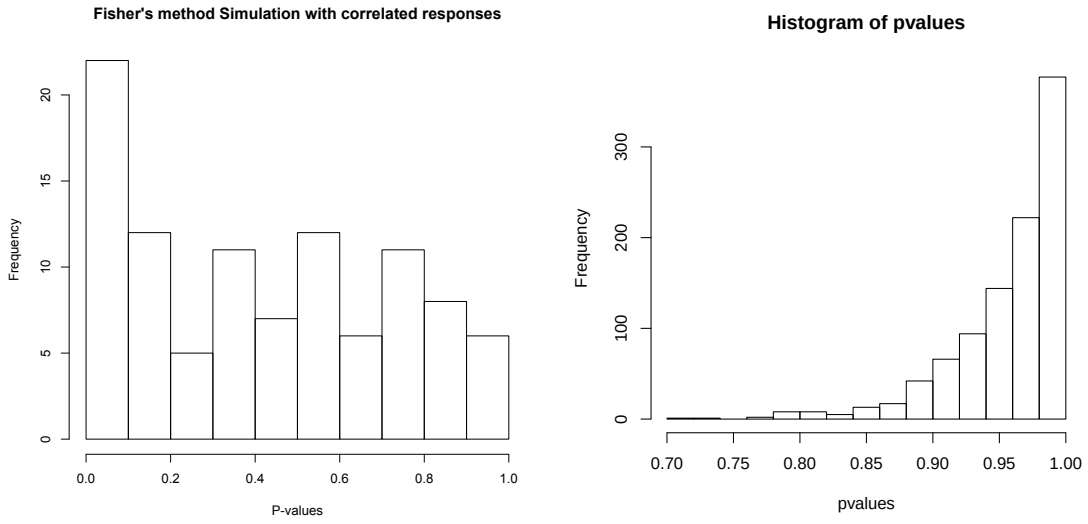

FIGURE 5.2: Fisher's Method Simulation for 100 correlated response variables (left) and the same with an uncorrelated covariate (right)

However, if there is an unknown covariance, there is a a slight difference which can be mitigated using Kost's method of combining dependent p-values. For Kost's method proposed by Kost and McDermott [2002], assume that the tests $X_1 \ldots, X_k$ have distribution $N_k(\mu, \sigma^2 E_0)$ where σ^2 is unknown and E_0 is a singular matrix with known covariance structure and $\sum diag E_0 = 1$. The null distribution of the statistic can be approximated using the same methodology as in Brown's method for known variance. Saying

$$P_i = T_v \frac{(X_i - \mu_i 0)}{S},$$

where T_v is the cdf of the t distribution with v degrees of freedom and S^2 is an estimate of σ^2 that is independent of the tests with $\frac{xS^2}{\sigma^2} \sim \chi^2_v$. Using the bivariate distribution given by Johnson and Kotz, $(T_i, T_j)', i \neq j$, then

$$R = \begin{pmatrix} 1 & p_{ij} \\ p_{ij} & 1 \end{pmatrix},$$

where $p_{ij} = corr(X_i, X_j)$. It then follows the same as the known covariance case where computing

$$E[(-2logP_i)(-2logP_j)] = E[W_i W_j] = \int_0^\infty \int_0^\infty w_i w_j f_{w_i,w_j}(w_i, w_j) dw_i dw_j$$

requires numerical integration as shown. The parameters for c, f are then computed by the same method as with Brown's method.

The last method discussed is Stouffer's Method (also referred to as Whitlock's inverse normal method) proposed by Whitlock [2005] where using the Z-score is possibly a

TABLE 5.1: Table of Errors for m tests

	H_0 True	H_1 True	Total
Declared Significant	V (false discoveries)	S	R (observed R.V.'s)
Declared Non-Significant	U	T(false negatives)	m-R
Total m_0	$m - m_0$	m	

more definitive method of combining p-values and can account for the issues that arise with Fisher's test. Let $Z_i = \phi^{-1}(1 - p_i)$ where ϕ is the standard normal cumulative distribution function such that the Z score for the combined tests is

$$Z = \frac{\sum_{i=1}^{k} Z_i}{\sqrt{k}}.$$

The combined tests' Z-score can then be used for one-sided, right-tailed p-values with modifications for two-sided or left-tailed.

It is clear that the power of Stouffer's and Fisher's method are almost identical since both are based on the average of the Z_i values and the $-log(p_i)$ values respectively, recalling that $-log(p) = -log(1 - \phi(z))$.

The known advantage of Stouffer's over Fisher's method is that introducing weights is quite straightforward following a standard normal distribution under the null hypothesis. This is unlike Fisher's method where the null distribution becomes a weighted sum of independent chi-squared statistics, which is more complicated.

There also exists another method of combining p-values by Tippett and Sime, which is especially powerful when there is one or very few false individual H_0's. However, through simulation, it is clear that Fisher's method is most powerful when there are many false, individual H_0's, which is assumed in the following facial shape analysis Chapter 6. This can be determined using the FDR (approximate false discovery rate) method which corrects for multiple comparison in a multiple hypothesis testing environment. It controls the expected proportion of incorrectly rejected null hypotheses i.e. false discoveries. As mentioned previously, the FDR can potentially play a role in the analysis using Fisher's method. With Fisher's method, if positive dependence is not accounted for and the combined analysis p-value is small, then the evidence for the alternative hypothesis can tend to be overstated. In this situation the approximate false discovery rate $\frac{\alpha(k+1)}{2k}$, where k is the number of positively correlated tests, can adjust α sufficiently. The advantages of using FDR is that it is less strict than other methods such as family-wise error. It is adaptable and scalable, producing the same value even if the sample size is cut in half.

Q is defined as the proportion of false discoveries among all the discoveries

$$Q = \frac{V}{R}$$

such that

$$FDR = Q_e = E[Q] = E\left[\frac{V}{V+s}\right] = E\left[\frac{V}{R}\right],$$

where $\frac{V}{R} = 0$ when $R = 0$. Therefore the analogous q-value to the p-value is the minimum FDR at which the test may be significant. The controlling procedure for Fisher's Method is the Benjamini-Hochberg procedure (or step-up method), controlling the FDR at level α when m tests are independent (Table 5.1). First, for a given α, find the largest k such that $p_k \leq \frac{k}{m}\alpha$, then reject (i.e. declare positive discoveries) all H_i for $i = 1, \ldots, k$. Therefore the mean α for m tests is $\frac{\alpha(m+1)}{2m}$, meaning an α adjusted for m independent tests.

For the following analysis in Chapter 6, Fisher's method will be used to analyse change in the populations.

5.4 Asymmetry

The asymmetry between populations and for individuals is a source of great interest. 3D-CT scans are used to evaluate patient asymmetry in studies such as Maeda et al. [2006]. Hartmann et al. [2007] analyse the reliability of a landmark-independent method for calculating facial asymmetry as well as a facial symmetry plane. That study found that it is a reliable method given a non-significant difference in the mean angular deviations of the computed symmetry planes. For the purposes of these 3D facial images, for an individual analysis there is no set size, but when comparing within a population, a standardised centroid size will be assigned for the full set of images in order to have a comparable analysis.

The process of assessing the asymmetry within a singular configuration, be it a set of landmarks, curves, or a facial mesh, is precisely the same. Given a configuration matrix X which is m landmarks in p dimensions, k paired landmarks (those that do have a right and left) and l singular landmarks (those which do not have a right and left namely the mid-line landmarks) the landmarks are reflected and relabelled in order to give a global asymmetry score of average distance between corresponding landmarks. The reflected landmarks are found by changing the signs of the the x-coordinates of X. After relabelling, this gives a new reflected, relabelled matrix Y configuration. An Ordinary Procrustes Analysis (Chapter 1) is performed of X onto Y in order to find the optimal rotation matrix (R) to allow the original set of landmarks to be in the

same shape space as the reflected, relabelled version. The final reflected, relabelled version is $B = YR + \delta$, where δ is the centroid distance. The symmetric landmarks can be calculated as $S = \frac{B+X}{m}$ and lastly, the global asymmetry score, simply the sum of squares between the reflected, relabelled version, and the original set of landmarks. Figure 5.3 displays a set of 23 anatomical facial landmarks in black with the reflected version in red and the fully symmetric face shown in green. This can also be decomposed into scores for particular features given a full set of curves or a facial mesh mask.

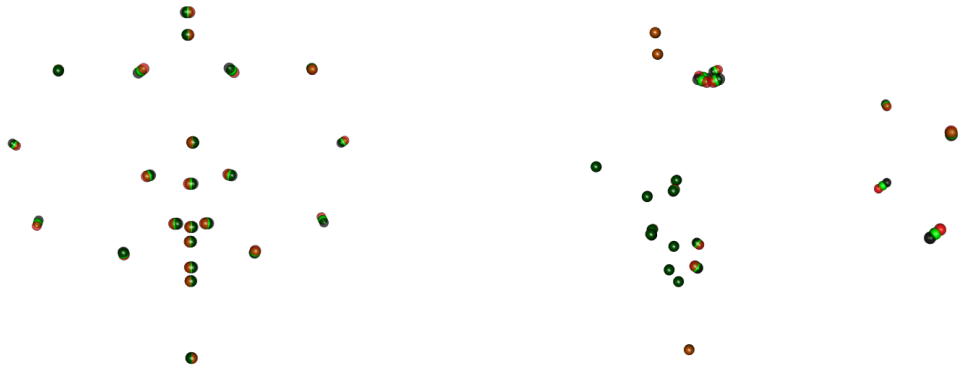

FIGURE 5.3: Asymmetry of Landmarks frontal view (left) and profile view (right) with the original landmarks(black), symmetric landmarks (green), and reflected and relabelled landmarks (red) with a global asymmetry score of 1.9mm

5.5 Mean on Surfaces

A very valuable tool in determining surface structure is finding the mean curvature value on a surface. This allows for a potential initial placement of a landmark on the surface or possibly determining correspondences between different facial structures. To begin, the mean curvature point was found using the first two principal component scores of the surface to move from a 3D space into a 2D space. The mean of the x and y curvature values are found and then translated through barycentric interpolation (Chapter 4) into the same 3D space. Figure 5.4 depicts the upper right lip coloured both by its shape index (middle top), curvature values (middle right), the 2D plot of the surface points coloured by curvature values (Chapter 4) and the mean 2d point, as well as the point interpolated back into 3 dimensions.

However, a potentially more informative mean is the Frechet Mean, a generalisation of the mean (or expected probability distribution) on a Euclidean space [Le, 2001]. The Frechet mean of probability measure w on a metric space (M) is defined as the global

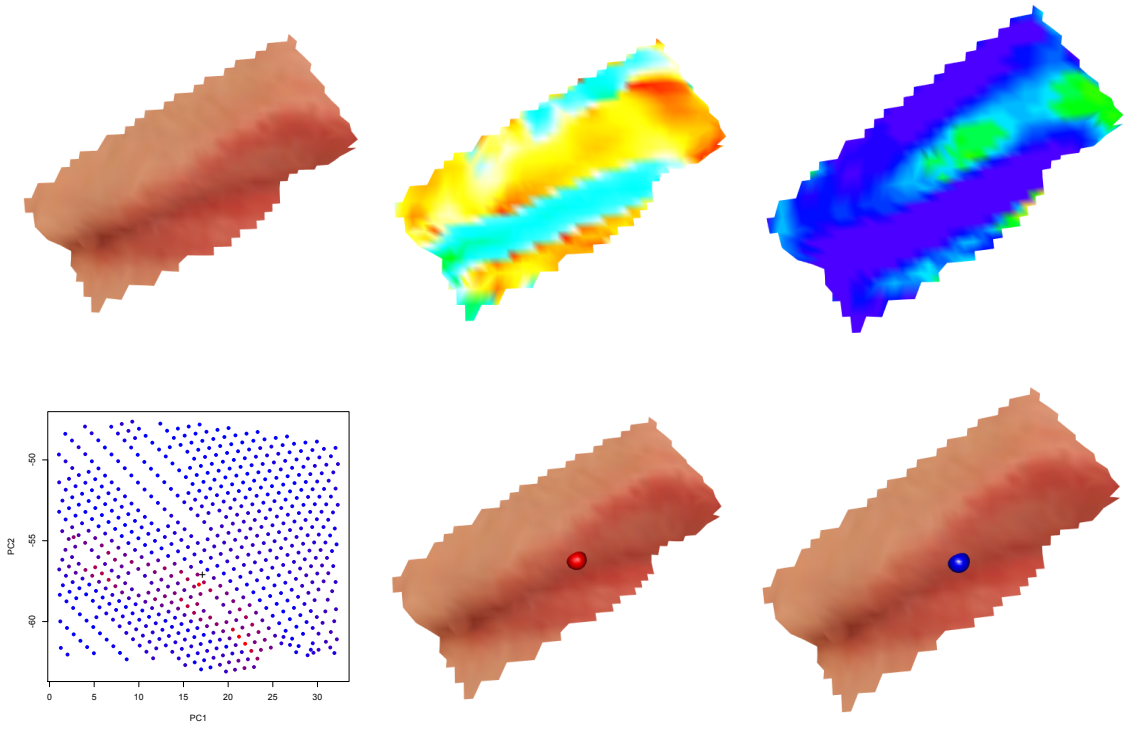

FIGURE 5.4: Absolute Mean Curvature Values on a Surface- upper lip (top left), upper lip coloured by shape index (top middle), upper lip coloured by curvature values (top right), 2-dimensional plot with mean point (bottom left), interpolated mean value (bottom middle red), frechet mean value (bottom right blue)

minimum of the function

$$F(x) = \int_M dist(x,p)^2 d(w)(p). \tag{5.10}$$

The aim is to find the point x that minimises the Frechet function 5.10. This is equivalent to computing the expected squared distance from any point p_j on the surface to the random points x_i such that the Frechet mean point

$$f_m = argmin_{p \in M} \sum_{i=1}^{N} w_i d^2(p_i x_i), \tag{5.11}$$

where w represents some weighting function.

In the case where $d = d_{Euclidean}$, then $f_m = \sum w_i x_i$ assuming $\sum w_i = 1$. The gradient of F at the minimum f_m must be zero. In particular, for any $x \in R^3$

$$\sum w_i \|x - p_i\|^2 = 0. \tag{5.12}$$

Therefore, $\sum w_i \|x - p_i\|^2 = \|x - f_m\|^2 + \sum w_i \|f_m - x_i\|^2 \geq \sum w_i \|f_m - x_i\|^2$.

In this analysis, w can represent the curvature values of the surface, giving a mean surface value based on curvature.

5.6 Closest Controls

Most tools compare populations, but what is also of particular interest in facial shape analysis is comparing one individual case of a specific population with an entire population. For example, the specific differences between a control population and a post-surgical patient could inform on ways to either improve the surgery or indicate different methods that could be used to improve surgical outcomes. Consider the tangent coordinates for a control population as characterised by a confidence ellipsoid, such that the majority of control cases, with all their individual variation, fall within that space. A shape that does not fall within the 'accepted range' of a control shape would then be lying somewhere outside of this confidence ellipsoid. If an affected population case is corrected to the point of being 'normal' then it will fall inside this 'ellipsoid'. However, if it is still too far off in shape, then it will lie somewhere outside this 'ellipsoid'.

In particular, a 'normal' range is not available for facial shape surfaces due to the deficiency of data in relation to the dimensionality. Bowman and Bock [2006] suggest using a selected number of principal components to define the subspace in which to characterise normality in order to greatly reduce the dimensionality of the problem while capturing the majority of the variation in the selected data.

Using the notation of Bowman and Bock [2006], let $x_1 \dots x_n$ be vectors such that x_i contains the f principal component scores of the tangent coordinates of the cases, which are assumed to be described by a normal distribution. The distance between an observation x and the control mean $\hat{x}_c$ (called the Mahalanobis distance) is

$$d(x) = (x - \hat{x}_c)^T \hat{\Sigma}^{-1} (x - \hat{x}_c) \tag{5.13}$$

where $\hat{\Sigma}$ is the covariance matrix of the control cases. Given that the Mahalanobis distance has a chi-squared distribution in this f-dimensional space, it can be determined that when $d(y_i, \hat{x}_c) > \chi^2_f(0.95)$, where y_i is a non-control case and $\chi^2_f(0.95)$ is the upper 5 percent point of the chi-squared distribution. Then the local limit of the normal space is constructed by projecting onto the contour hypersurface. This contour hypersurface is defined by the point where the Mahalanobis distance is equal to the upper 5 percent point of the chi-squared distribution.

Moreover, the point p between $\hat{x}_c$ and y that is cut by the interpolating line $py+(1-p)\hat{x}_c$ is found through solving the Mahalanobis equation

$$p(y-\hat{x}_c)^T\hat{\Sigma}^{-1}p(y-\hat{x}_c) = \chi^2_f(0.95).$$

The solution that defines the proportion of distance it is necessary to move between the mean shape and the non-control shape in order to lie on the contour hypersurface is found to be $p = \sqrt{\frac{\chi^2_f(0.95)}{d(y)}}$.

Figure 5.5 illustrates this process where the black line represents the closest control or reference curve (i.e. what is 'wrong' with the affected case) and the blue line is the actual affected case. While clearly there is little difference between these curves, it is imperative to realise that the reference curves are not the typical or average case but rather the extremity.

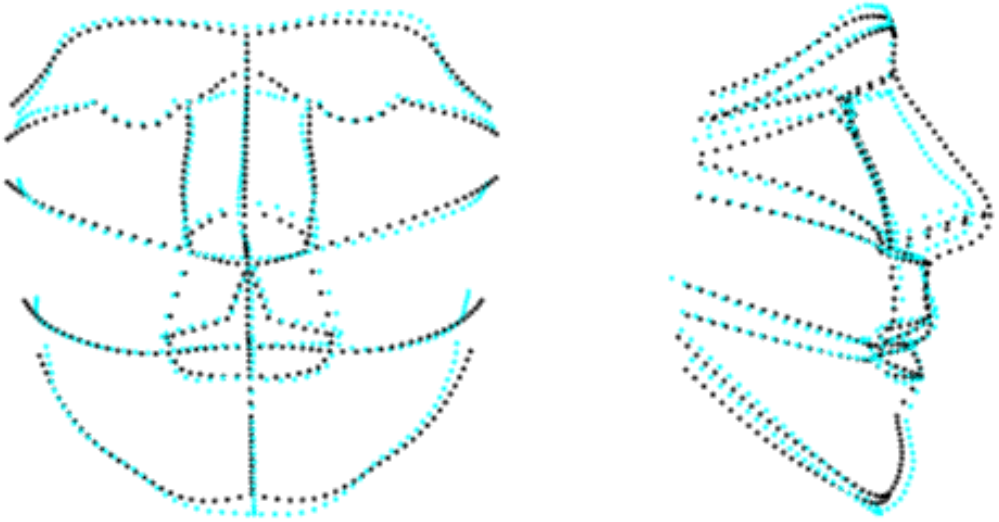

FIGURE 5.5: Closest showing Control - Curves

5.7 Using tools for Analysis

Overall, there now exists a quite comprehensive guide for analysing differences between populations, but also methods to identify abnormalities in one individual compared to a population, as well as tools to simply identify and quantify an individual's characteristics. However, facial shape is not the only type of object that can be compared using these methods and tools; in Chapter 6 it will be shown that these tools are applicable to other types of shape objects as well. Some tools described in this chapter will not be used in the following case studies. These tools were developed in order to showcase all possible options of using the enriched facial shape description, but the following studies were not

designed, but rather data was given as is. Therefor, some tools will be used, but others developed in this chapter will be used for future work.

Chapter 6

Analysis- Cases Studies

6.1 Introduction

As previously discussed, stereophotogrammetry is a 3D surface imaging technique with a rapidly expanding range of applications in diverse medical and scientific fields. Its use in craniofacial imaging has improved surgical planning, assessment of outcomes, and the study of pathologic and normal morphology as well as growth and development. The ©Di3D dimensional imaging camera system was used to capture all subjects used in the forthcoming analysis as discussed in Chapter 1. Given the methods developed in Chapters 4 and 5, Chapter 6 will look at using those tools to infer information about human populations and other applications.

Using the Di3D 3-dimensional surface-imaging device, facial images were systematically collected from volunteer subjects in the local community. Subjects were asked to give basic demographic information including age, sex, ethnic background, and any history of craniofacial condition, surgery, or trauma. Subjects were then stratified by this information, generating representative data from neonatal to mature adult populations. They were also stratified by race, with the ultimate goal of obtaining sufficient data to statistically represent norms for multiple racial groups.

However, for the purposes of this analysis, the chosen studied population was confined to the age group of young adult to mature adult, and with a White British Isles ethnicity through all sets of grandparents. In order to compare these faces across age and sex, methodology using regression and flexible regression are thoroughly investigated. The most obvious classification with which to begin is the differences between the male and female populations. There is an enormous amount of information on the discriminating features between men and women. Different factors such as distances between anatomical landmarks, texture of skin, and the number of anatomical landmarks all heavily

impact the classification of key features. There is a large amount of work in two dimensions, but not nearly as much as in three dimensions (where this analysis is carried out).

Much of the work carried out on this research area falls into the field of psychology where subjects are asked to identify if an image is that of a male or a female [Armann and Balthoff, 2012]. The aim of this type of analysis is simply to identify key features between the two populations. Bruce et al. [1993] examine both the key facial features differentiating males and females, as well as identify which of those features people use to make gender classification judgements. It compares distances, angles and ratios from two dimensional images as well as three dimensional measurements. It is found that the computer models are estimated to be 94 percent accurate when combining the two and three dimensional information. However, the misclassified faces by the automatic system are not the same faces as were misclassified by the subjects. Kramer et al. [2012] use 2-dimensional photographs, 3-dimensional scans and measure anthropometry to determine the facial width-to-height ratio between men and women, but found no evidence of sexual dimorphism in the facial features. However, the measurements went from above the upper lip, to below the brow, potentially losing information should the brow or jaw be associated with sexual dimorphism.

How to best properly measure and analyse the different images is an important question. Claes et al. [2012] discuss the inaccuracies which arise when landmarking (the predominant method of facial modelling), such as a lack of information in specific regions. However, this analysis is centred around an automatic curve identification process where a spatially dense sampled facial shape is decomposed into components of symmetry and asymmetry, whereby the two components are used to determine sexual dimorphism. A comparable amount of subjects to the analysis in this thesis (although restricted to 18-25 years of age) are used with an anthropometric mask mapped onto the collected three dimensional images and their reflections, then compared using permutational statistical methods. Their results show a significant size difference in the male features compared to females, but that the differences stopped simply at magnitude, without any shape change. Srivastava et al. [2011] find the geodesic paths (optimal deformations) between level curves that describe facial shape. This allows for optimal elastic deformation between faces giving an elastic metric between which to compare facial shapes. Clearly, there have been many studies conducted on 3-dimensional facial shape, but none which take into account the intrinsic curvature information in the shape as the means of deriving a facial mask.

6.2 Capturing Data

The process of capturing the data is based upon the protocols of the *Face3D* project, funded by the Wellcome Trust, a consortium of several institutions including the University of Glasgow (Statistics, Computing Science, Dental School), the Royal College of Surgeons in Ireland, Dublin City University, the University of Limerick and the Institute of Technology in Tralee, with aims to pursue research into developing methods of extracting information about facial shape from 3D images.

6.2.1 Process of Creating a Facial Database

Over 600 individuals were captured for control database construction purposes, with more than a further 1000 individuals' images obtained from Alex A. Kane, M.D., Division Director of Pediatric and Craniofacial Surgery at Children's Medical Center and Professor of Plastic Surgery at the University of Texas Southwestern Medical Center. Dr. Kane's data was collected using the ©$3dMD$ three-dimensional surface-imaging device, where whole-head images were systematically collected from volunteer subjects in the local community. For both data collection sources, subjects are asked to give basic demographic information including age, sex, ethnic background, and any history of craniofacial condition, surgery, or trauma. Subjects are then stratified by age and sex, generating representative data from neonatal to mature adult populations. They are also stratified by race, with the ultimate goal of obtaining sufficient data to statistically represent norms for multiple racial groups.

A number (approximately 70) of surgical patient images (pre- and post- surgical intervention) were captured at the University of Glasgow Dental School. In addition, to the database of facial images, information was collected about the patients and controls in order to establish whether or not the participant met the *Face3D* project criteria. In order to address the specific research questions of the *Face3D* project as well as adhere to the reasonable concept of comparing facial shape amongst specific ethnic groups, criteria for control data for this study includes:

1) All parents and grandparents must be of *White British*, *White Scottish*, or *White Irish* origin. Note White Scottish is not a subset of White British.

2) There can be no history of cleft lip/palate in the individual or a first degree relative.

3) There can be no history of facial surgery, facial accidents, or an interest in seeking facial surgery in the individual.

4) There can be no history of psychotic disorders in the individual or a first degree relative.

For each participant, this information is collected and then the image capture process is conducted. Question 4 is used for another study not discussed in this thesis that investigates if there exists a difference in facial shape for individuals with psychotic disorders.

FIGURE 6.1: ©*Di3D* Imaging Camera System

For each participant, multiple images are sometimes taken and the best set is selected. There are potential issues/loss of detail with the data capture. First, is the so-called 'orange peel effect'. This occurs when an individual's skin is transparent, or 'thin'. In infants and older individuals, light can easily penetrate the skin and bounces off causing subsurface artifacts. Whereas young adult individuals tend to have thicker skin, so a smoother surface is created in the image capture. The 'orange peel effect' also occurs with a flatter surface that has little to no variation in texture. The area that is most difficult to capture is the ear region. With the angle of the four cameras (Figure 6.1), the ears tend to be 'smeared' backwards, not being able to capture the full dimension of the head. The error associated with this issue was investigated in Chapter 3.

TABLE 6.1: Summary Profile

	Male	Female	Total
Controls	82	133	215

Using 215 controls (all who fit the criteria of the study and had no apparent image quality issues), sexual dimorphism between male and female controls and the shape change with age for all cases is examined.

Overall, there is a well-rounded group of ages for the controls. However, there are more control young adults, than mature cases (Figure 6.2).

Age of Female Controls

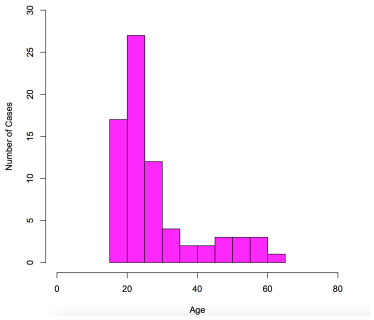

Age of Male Controls

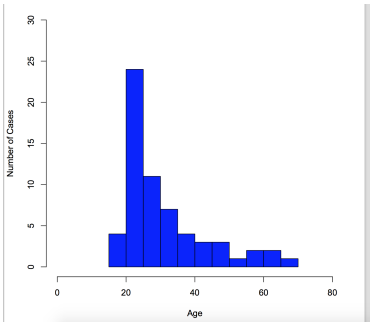

FIGURE 6.2: Histograms Showing the Distribution of Control Ages

6.2.2 General Analysis Method

All subjects are landmarked with the standard anatomical 23 landmarks in *Landmark* software IDAV (Figure 6.3 (top left)). Then a full set of facial curves is produced using the *Face3D* package in *R* where the curves (green) shown in Figure 6.3 (top right) are generated between landmarks, and then, slid, warped, and resampled to be a standard number of points for all cases (Chapter 4). The full mesh (black) is then constructed between the automatically generated curves (Figure 6.3 (bottom)). This method of curve identification was discussed in Chapter 4.

The reliability study, which studies the validity of the ©Di3D dimensional imaging camera system, shows that the camera can create distortions of up to 2 centimeters around the ear area (3). The ears are removed for the purpose of this analysis. While the ear effect is still present (the curves continue around the brow, cheeks and mandible toward the ear), the actual ear landmarks which pull in or out of the face in the x− direction, are not present, as well as a partial (regular) amount of the connected curve.

6.3 Control Analysis

6.3.1 Glasgow Controls - Sexual Dimorphism

Before understanding what the precise differences are between the male and female populations, it is important to state that in this study a two sample t-test found the difference in size of the male and female facial shape to be statistically significant with a p-value of .011, meaning that male facial shape tends to be larger than female. A Hotelling's T^2-test based on re-sampling (with 1000 permutations) of the mean facial shape between men and women (based upon principal component scores) found a significant difference of $p = .048$, or about 5 percent. However, note that this is marginally significant, and cannot be considered a strong result. In order to have a basic examination of the initial differences between the male and female populations, the mean shape of each is produced and rendered with scaling. Noting Figure 6.4 the cheek protrusion on females is particularly noticeable, not just from the nose region back toward the rear of the face, but also from the vermillion line back toward the rear and from the *exocanthions*. There is also a definite protrusion of the mid-sagittal line, in the male population, clearly from the *nasion* to the *gnathion*. This suggests that the male face is narrower with a stronger protrusion in the z− direction and the female face is wider/puffier and more concave in the z− direction. The males seem to have more of a protruding jaw line, with the mandible protruding under and further out from the females. Also, the brow ridge seems to be another place of particular difference. The females tend to have a higher and more recessed brow line, whereas the males seems to have a lower and again, more protruding, ridge.

In order to have better viewing capability, the male mean was turned into the blue rendering (a simple triangulation of all 922 semi-landmarks comprising the mesh) and the female mean mesh (magenta) was laid over it, with a transparency value so that recession and protrusion can be clearly seen (Figure 6.5). Most clearly identified is the protrusion of the male chin and frontal-viewing mandible. The magenta (female) shows

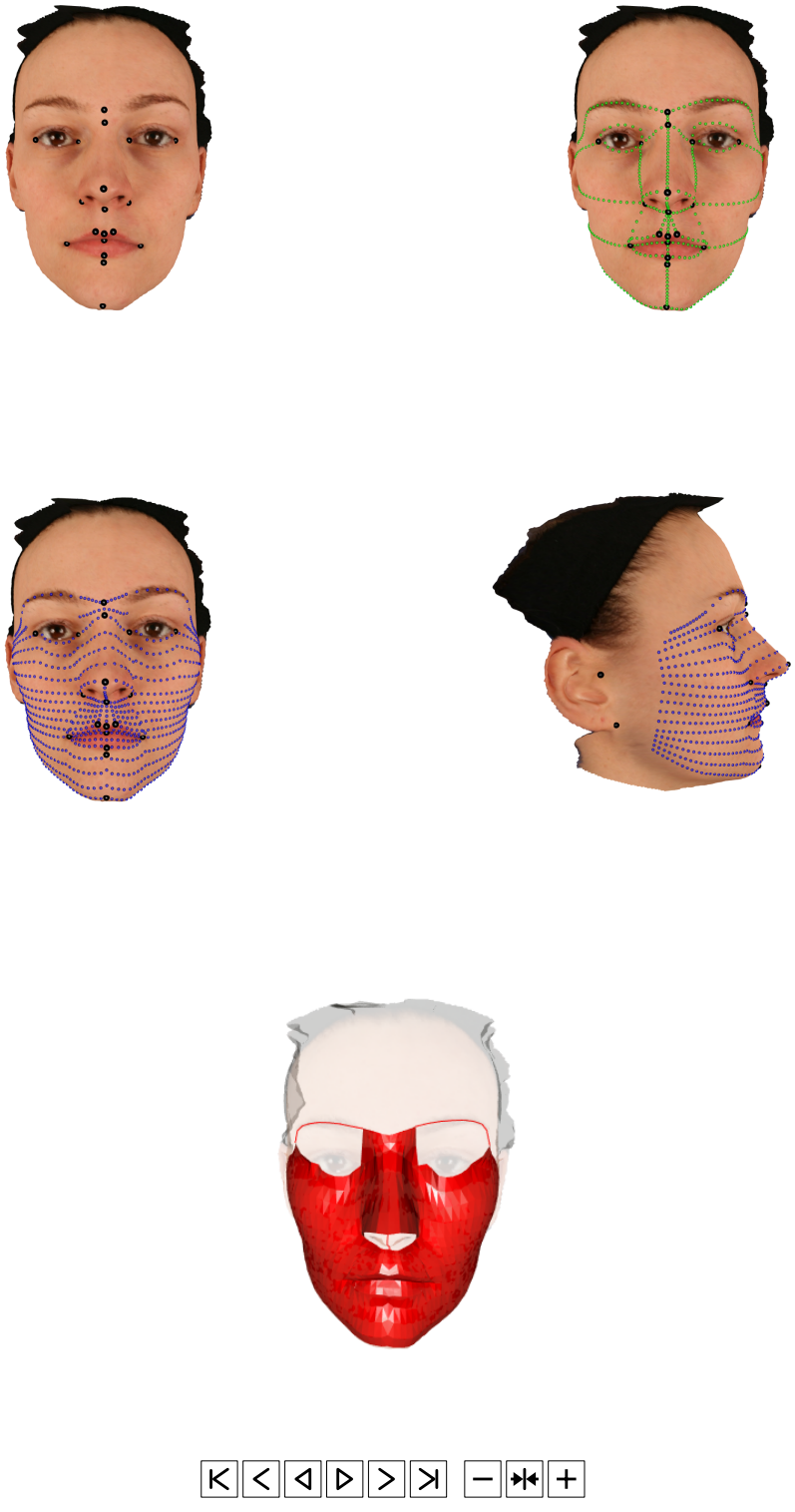

FIGURE 6.3: Manually marked set of 23 landmarks (top left) producing Automatic Curves (467 describing points) (top right), Automatically produced Mesh (922 describing points) (middle), Final rendered mesh (bottom)

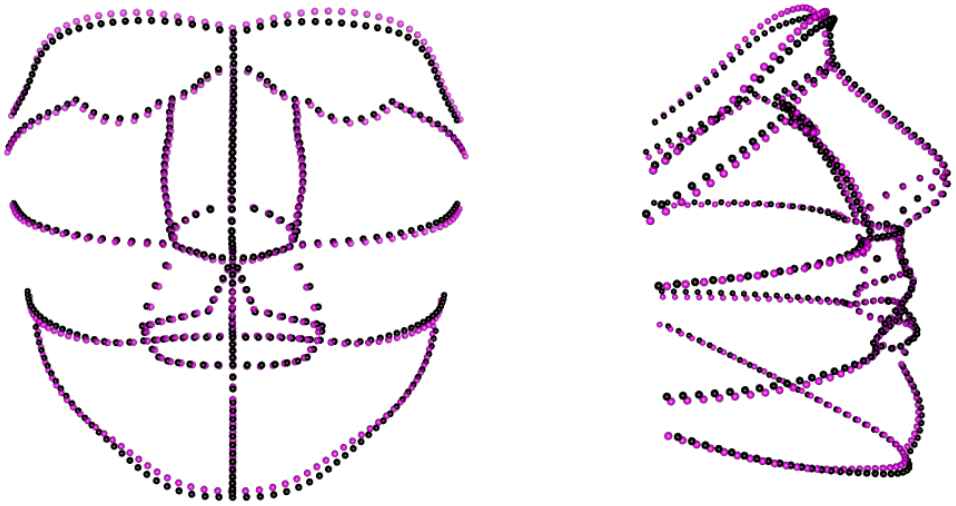

FIGURE 6.4: Glasgow controls sexual dimorphism: Mean shape of males (blue) and Mean shape of females (magenta) - Curves

definite puffier cheeks and cheek bones. As well as the male brow protrusion, the sizeable increase in height of the female brow is stark.

Inferences can be made about where the protrusions and recessions of the facial structure begin. It seems as though the cheeks, all the way from the eye sockets, down to just the cheek-lip curve (created between the *chellion* and the *otobasion*), shows a constant protrusion for the female population. The eye sockets seem to be very similar between the populations; however the sockets show a quick rise in the female brow, recessed and higher than the males. There exists a very clear protuberance of the both the lips and nasal region by the male population, and a recession of the mandible in the female populations as compared to the male counterparts.

Using both the curves and the full meshes as the comparison configurations, General Procrustes Analysis (GPA) is carried out on all cases, with a scaling adjustment for size in order to compare the shape, not size, of the male and female population. Size is an adjustment in scale for the actual width and height of the face in order to match all configurations as closely as possible. Principal Components Analysis (PCA) is then performed in order to evaluate the differences and variations between the two populations.

When viewing Figures 6.6 there does seem to be a slight difference again between males (black) and females (red), but not necessarily a discernible difference.

Referring to Figure 6.7 there is a slight difference between the two populations in reference to the first two principal component scores which make up about 50 percent of the change according to Figure 6.6 .

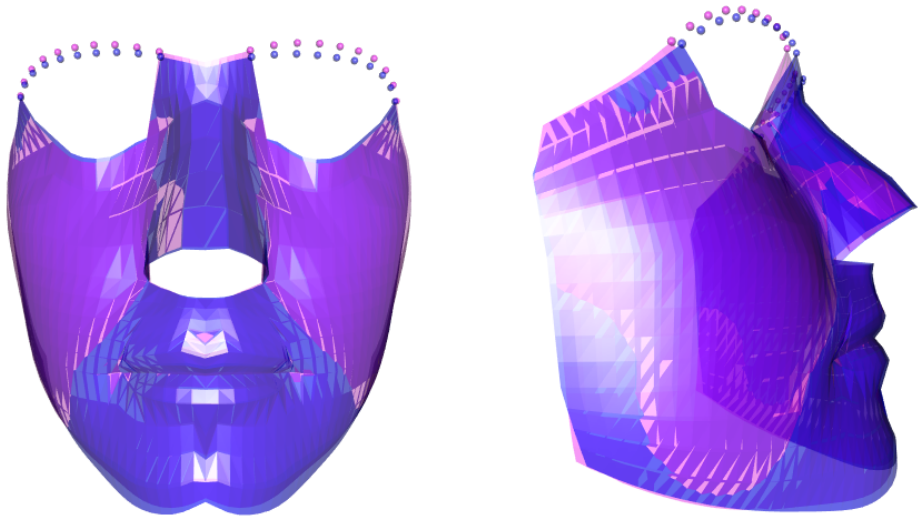

FIGURE 6.5: Glasgow controls sexual dimorphism: Mean shape of males (blue) and Mean shape of females (magenta) - Meshes Rendered

However, the comparison between the two populations when using the full meshes generated from the curves, Figure 6.7, seems to show less of a difference between the two populations, while at the same time, reflecting the same trend in terms of principal component variation. This may suggest that the differences are present in the less significant principal components.

6.3.2 Age Effects in Glasgow Controls

In order to examine how shape changes with age, using a variation of Fisher's test, a nonparametric regression is performed on the first 10 principal components of both the male and female control population against age. This assumed the principal components as the response variables and age as the covariate as discussed in Chapter 5. The degrees of freedom for smoothing are chosen by experimentation. The relationship is not linear, but is not expected to be highly complex and rough, so the degrees of freedom for this test is set to four [Hastie and Tibshirani, 1990] using non-parametric regression. Males and females are modelled separately due to an intense interest of understanding the very slight changes that could occur between populations. A further study modelling both together could be of interest in future work.

Figures 6.8, 6.9 show the shape change with age for the male population (all ages and age restricted) and with an overall empirical p-value of $p = 0.016$, this illustrates a significant change in shape over time. The blue band has width which represents two standard errors of the difference between the smooth curve and a 'no change' model at each point, so any deviation from this reference band indicates a significant change

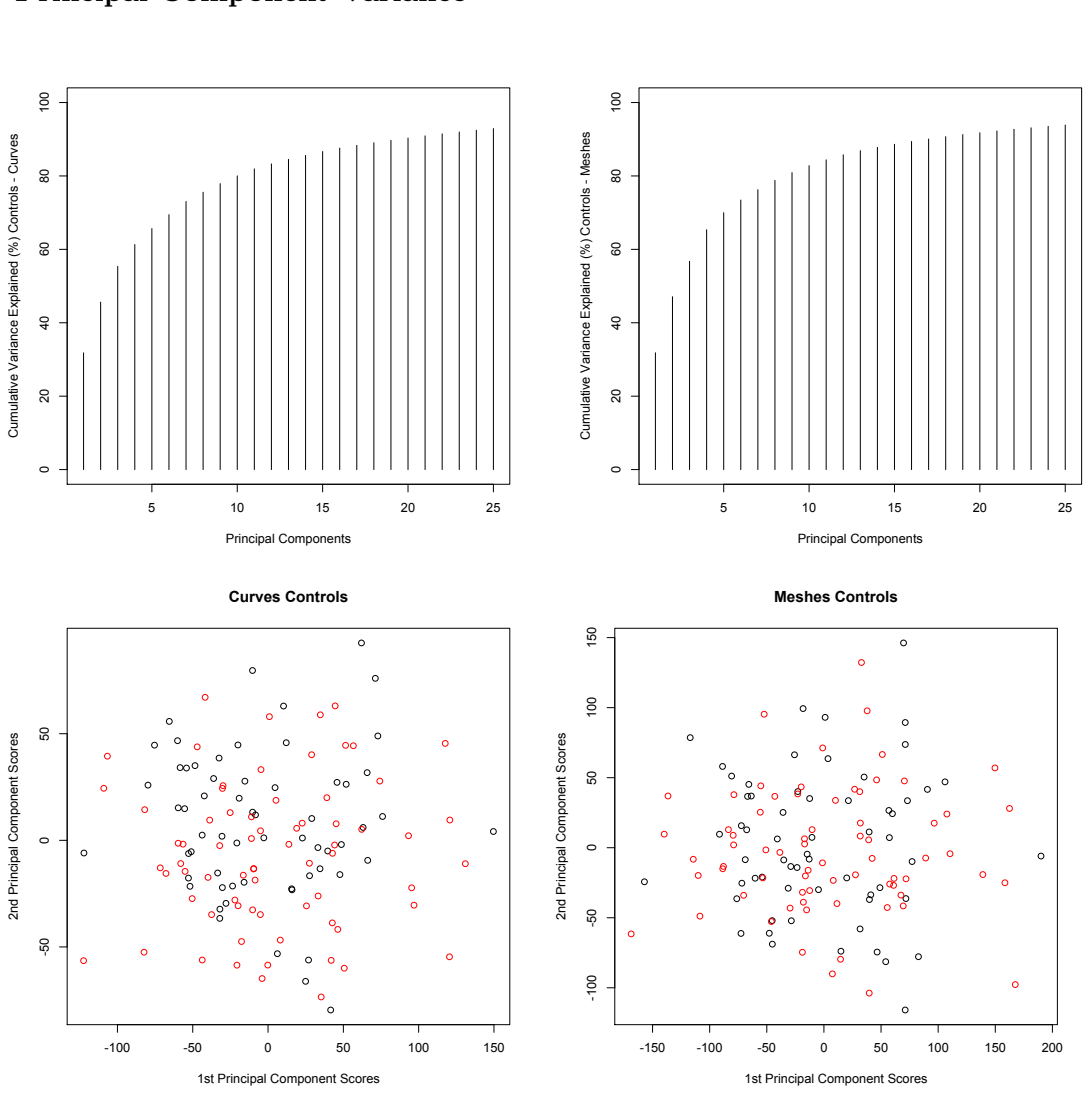

FIGURE 6.6: Cumulative Percentage of Principal Component Variance and Plot of 1^{st} and 2^{nd} Principal Component with respect to Sex of Controls - Curves and Meshes

from the shape. Note that Figure 6.8 (bottom left) only examines the curves of the face. Looking at principal component 3 there is a very significant difference (which represents about 10 percent of the variation).

Examining Figure 6.10, the first principal component (approximately 30 percent of the variation) tends to be a lengthening of the face where the brow rises, and the chin drops. There seems to also be a slight recession of the cheeks (giving a more drawn look as the individual ages).

The 2^{nd} principal component (accounting for 15 percent) clearly shows a widening/flattening of the face with age. The chin drops down and the cheeks flatten out. Again this can account for the 'drawn' look seen as the tightened skin begins to sag as individuals age. The nose also tends to protrude more, giving a more bulbous look. However, this

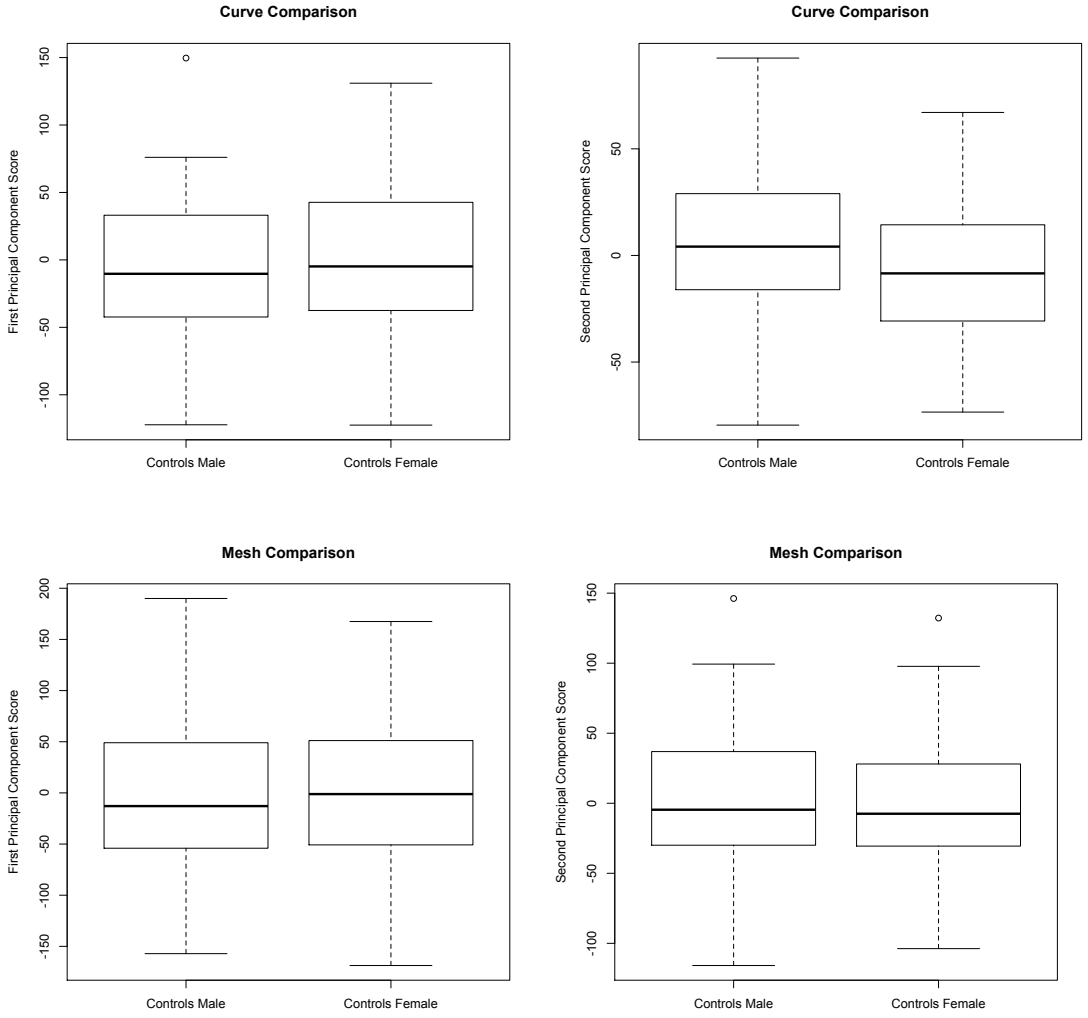

FIGURE 6.7: Boxplots of 1^{st} and 2^{nd} Principal Components with respect to Sex of Controls - Curves and Meshes

is not a significant change given that the regression line remains within the reference range.

Figure 6.10 illustrates principal component 3 (accounting for about 10 percent of the variation) which has a significant change with age. The lips begin to pucker significantly; the chin recedes. This seems to be a result of the lengthening and broadening of the face, suggesting that the lips do not move, but as a result of the other changes, seem to be further puckered over the chin (which drops and recedes considerably).

However, when examining shape change with age using the meshes of the male controls (empirical p-value of $p = 0.021$), there are some slight differences to notice (Figure 6.8). First, notice that the 1^{st} principal component (lengthening of the chin and rising of the brow) tends to follow the same pattern as the curve analysis. However, the 3^{rd} principal component is not as significant as in the curve analysis. In the mesh analysis,

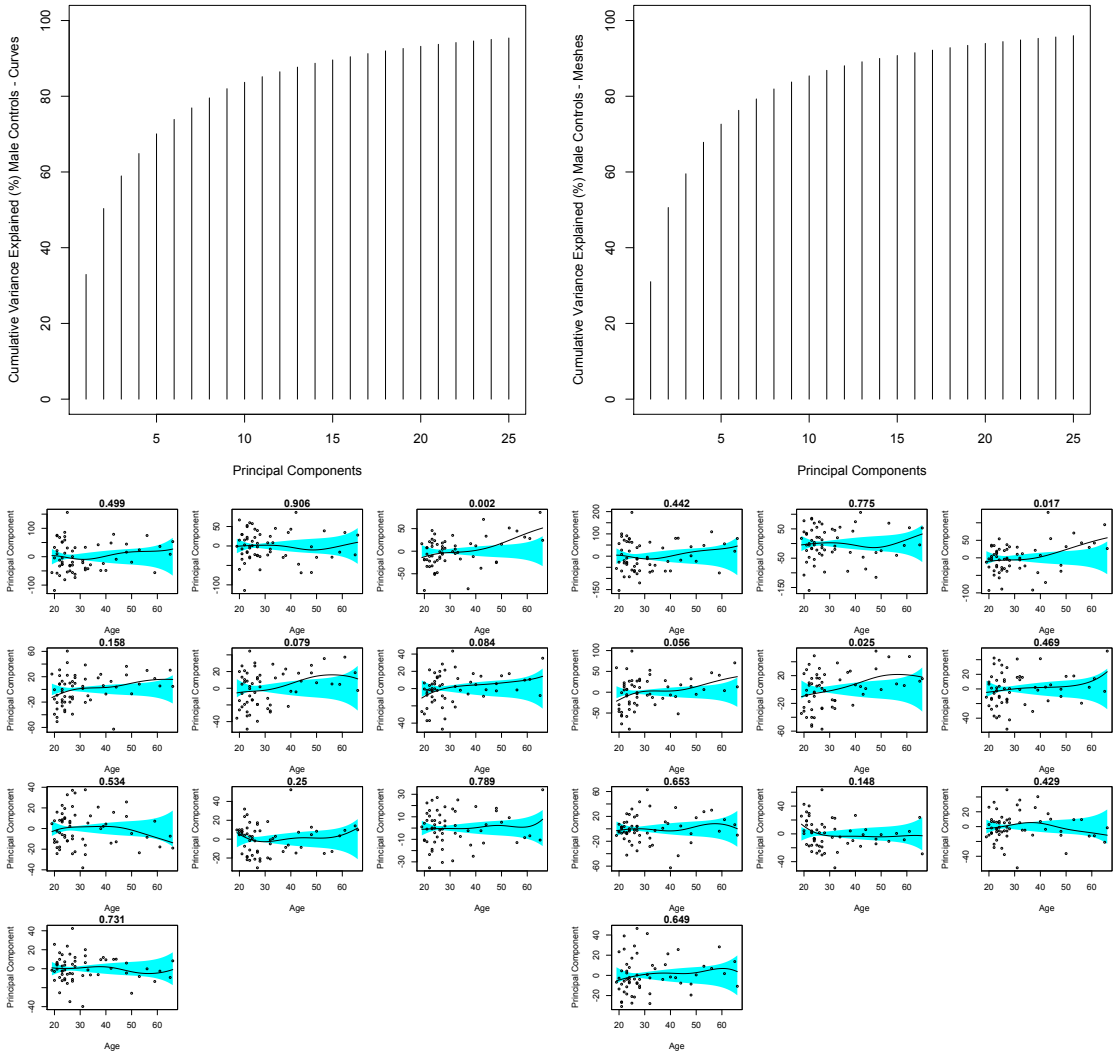

FIGURE 6.8: Male Shape Change with Age - Cumulative Percentage of Principal Component Variance Male Controls - Curves (top left) and Meshes (top right) - Fisher's Method for Male Glasgow controls with the 1^{st} 10 principal components against Age with corresponding p-values for each component at top - Curves [Empirical P-Value 0.0358] (bottom left) and Meshes [Empirical P-Value 0.0423] (bottom right)

the 3^{rd} principal component (9 percent) tends to be a protrusion of the nose, but the 4^{th} principal component (8 percent) accounts for the recession of the chin and puckering of the lips just as with the 3^{rd} component of the curve analysis (also showing a significant change with age). This would suggest that the extra information given by the mesh (significantly more information around the nasal region) caused by the nose protrusion is enough to change the meaning of the principal component.

Overall, there is a clear lengthening of the face in males as they age, with the chin showing a significant drop down and back and the brow receding up and back, creating a lengthening in the nose and puckering of the lips. Figure 6.10 clearly illustrates the

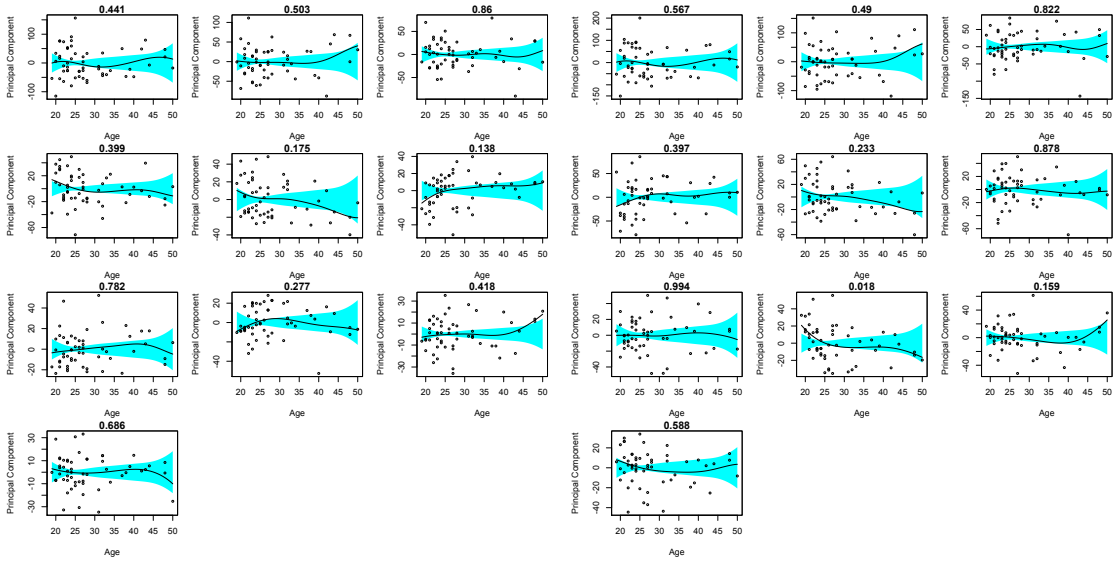

FIGURE 6.9: Male Shape Change with Age - Fisher's Method for Male Glasgow controls Age restricted to 50 and under with the 1^{st} 10 principal components against Age with corresponding p-values for each component at top- Curves [Empirical P-Value 0.5766] (left) and Meshes [Empirical P-Value 0.4091] (right)

extremes of the first three principal components: a strong chin drop and brow recession for the 1^{st} principal component and a flattening and nose broadening for the 2^{nd} principal component.

The female control population has an even stronger change with age where Figures 6.11, 6.12 show the significant empirical p-value of .0001 (all ages and age restricted). The 1^{st} component has a very strong effect and comprises almost 35 percent of the variation as well does the 2^{nd} component, which together account for over 50 percent of the total change.

Figure 6.13 illustrates the change for the 1^{st} principal component which clearly has an effect with age. There is a very definite narrowing of the face with the female population. The chin drops, like the males and the cheeks sag slightly. Also similar to the males, the face tends to get longer, and narrower. The lower lip also shows a very significant sag down.

The 2^{nd} principal component shows a clear dropping of the cheeks, but interestingly, a protrusion, or almost lifting, of the cheekbones. This could perhaps be a loss of 'baby fat' or 'chubby cheeks' that occurs from the teenage years onwards, but again a very slight change with age. In direct opposition to the male population, there is no flattening of the face, but instead a protrusion.

The 3^{rd} principal component, about 9 percent of the variation shows a puckering of the lips quite like the male population. Again this seems to be a consequence of the

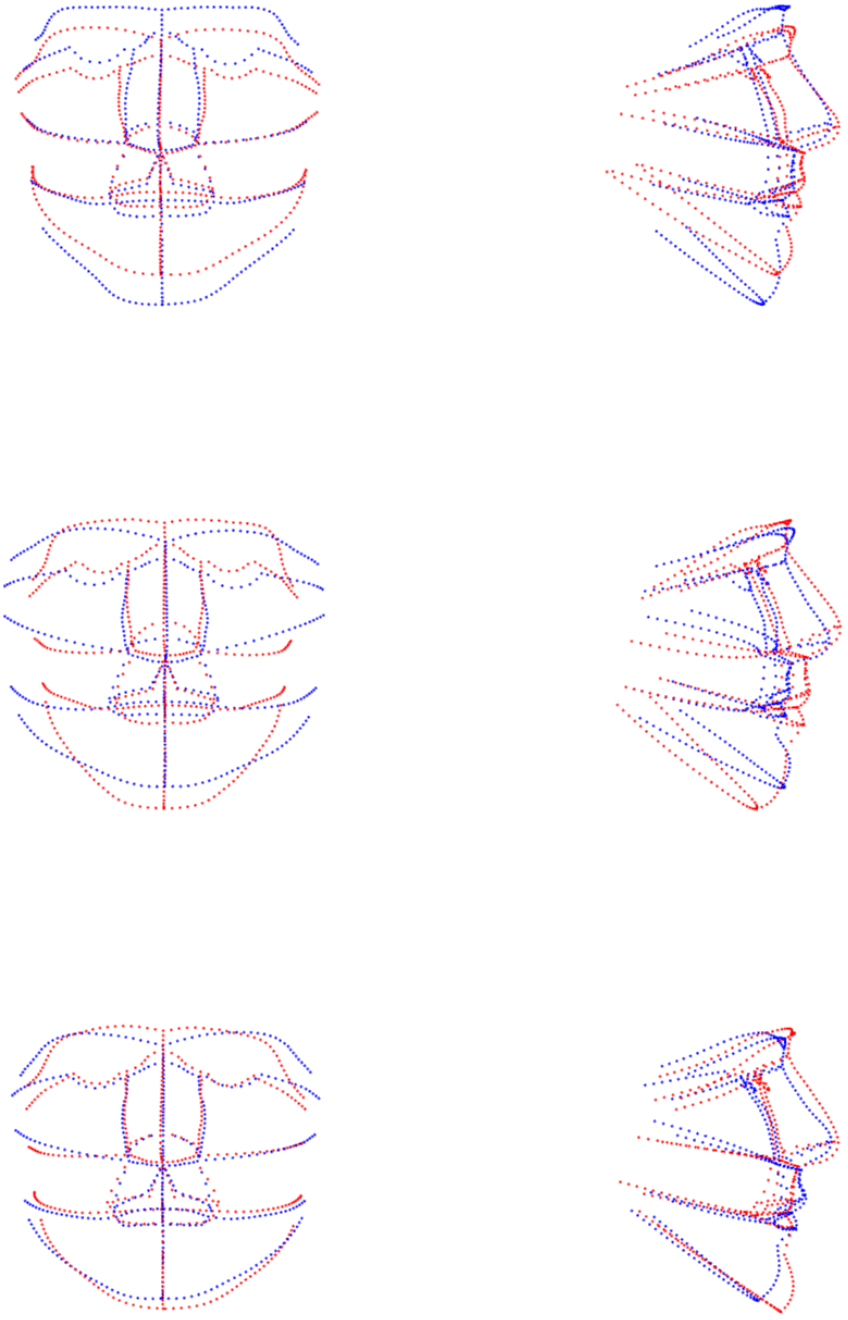

FIGURE 6.10: Male Control Extremes 1^{st} (top), 2^{nd} (middle), and 3^{rd} (bottom) Principal Components

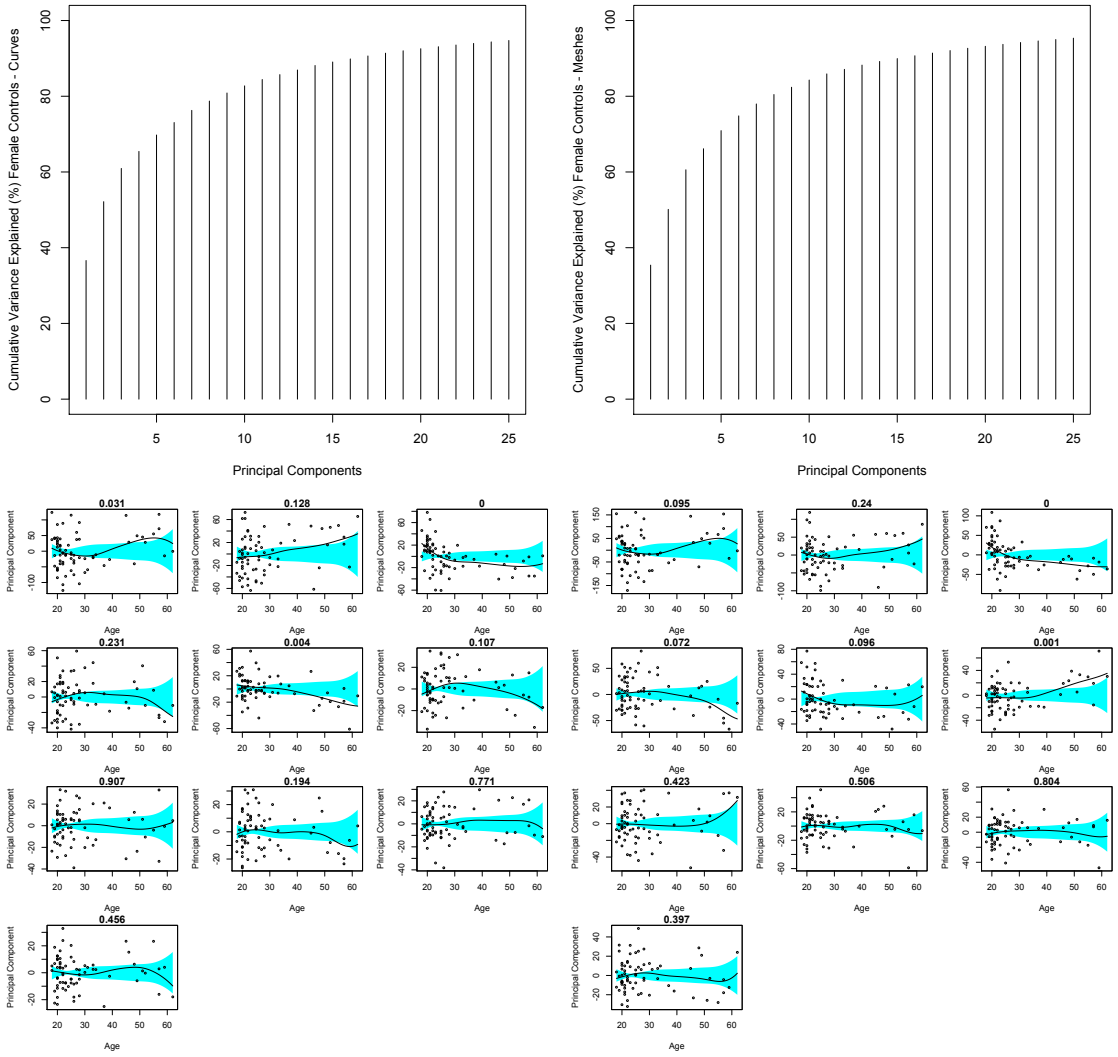

FIGURE 6.11: Female Shape Change with Age - Cumulative Percentage of Principal Component Variance Female Controls - Curves (top left) and Meshes (top right) - Fisher's Method for Female Glasgow controls with the 1^{st} 10 principal components against Age with corresponding p-values for each component at top - Curves [Empirical P-value 0.0002] (bottom left) and Meshes [Empirical P-value 0.00009] (bottom right)

lengthening of the face and a dropping of the chin, making the lips pucker out over the chin, again a non-significant change. However, the 4^{th} principal component shows a very significant change with age. Accounting for about 5 percent of the variation, there is a marked movement of the cheekbones with a drawing-in of the lower cheeks. This suggest a definite sagging of the cheeks giving the 'drawn look' of age. There is also a definite puckering of the lips, just as with the males. The additional information given by mesh analysis tends to not give anything more definite than the curve analysis in this case. Figure 6.13 shows the extremes of the principal components, commensurate with the findings above.

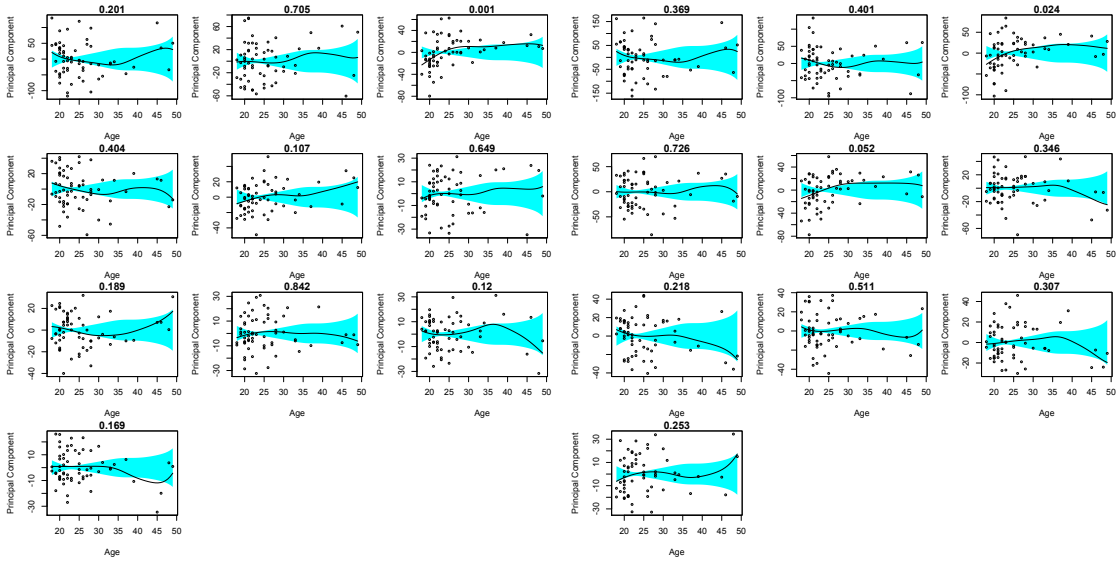

FIGURE 6.12: Female Shape Change with Age - Fisher's Method for Female Glasgow controls with the 1^{st} 10 principal components against Age with corresponding p-values for each component at top - Curves [Empirical P-value 0.0147] (left) and Meshes [Empirical P-value 0.0791] (right)

The overall change that seems to occur with the female population is a lengthening and narrowing of the face with a significant chin drop, and the cheek bones begin to protrude in contrast to the sagging of the cheek skin. Again this would account for the 'drawn' look that can occur with age, in accordance with the male population.

Examining the differences with an age restriction (excluding any case not in the age range of $20 - 35$ years old) shows discrepancies which are almost exactly commensurate with the sexual dimorphism seen with no age restriction. As forensic reconstruction expert, Professor Caroline Wilkinson, [Wilkinson, 2004] explains, in the forensic reconstruction field the largest differences between the male and female populations are over the brow region (with males having a significant brow protrusion) and the jawline. Here the findings are consistent with those accepted findings.

Multiple comparison effects were not taken into account during the principal components analysis. Bonferroni adjustment as described by Bonferroni [1936] could be used to control the overall Type I error when carrying out these multiple tests. Some of the effects documented above are sufficiently strong to remain significant after an adjustment of this type. However, the individual p-values are quoted in unadjusted form in order to provide a complete description of the effects. Fisher's method has also been used to provide a global assessment. Overall, principal components seem to be a valid method of discussing broad differences in facial shape, but future work could involve a new method in which to analyse the more nuanced changes that occur between populations in aging, sexual dimorphism etc. There are definite limitations that occur in using principal

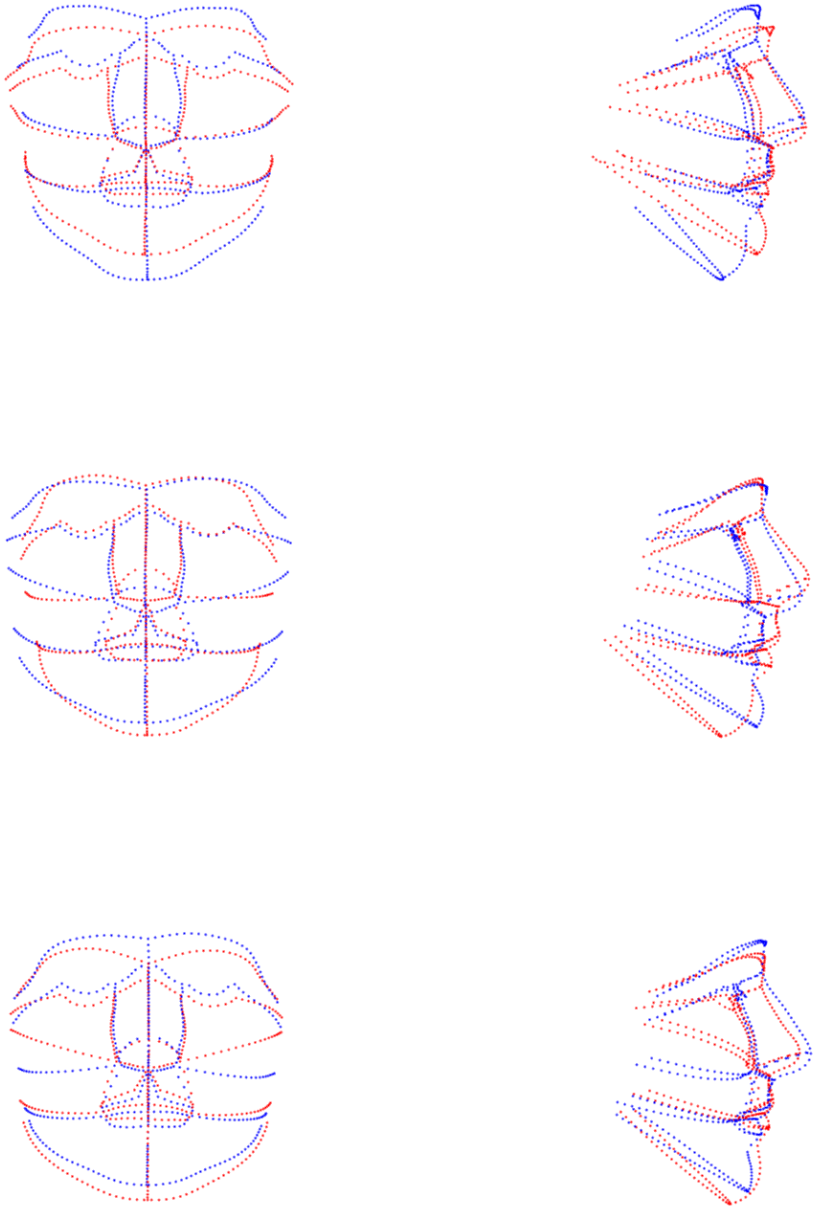

FIGURE 6.13: Female Control Extremes 1^{st} (top), 2^{nd} (middle), and 3^{rd} (bottom) Principal Components

components. Not all methods discussed in Chapter 5 were used due to the design of the analysis. Body fat would have been a very interesting addition to this study, and could be looked at in the future as a portion of the questions left unanswered could be due to differences in body fat. A small study did take place that included body fat, but the cohort became self selecting due to a hesitancy to give such personal information.

An analysis of the asymmetry over a specific control case's face can be investigated. Figure 6.14 shows the overall asymmetry differences between the populations. No significant differences are observed.

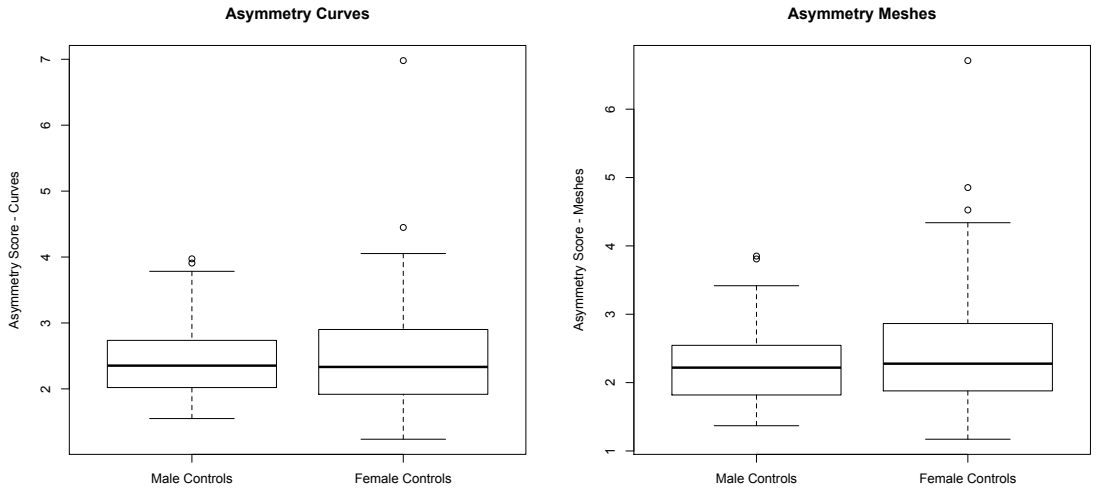

FIGURE 6.14: Asymmetry Box Plots comparing the Female and Male populations

As an example of how asymmetry can be shown, Figure 6.15 shows a male control case (asymmetry score 1.8mm) with the difference between the the asymmetric version, and the original face, painted topographically by difference. A blue colour represents a recession of the face, green a very close approximation, and yellow a protrusion.

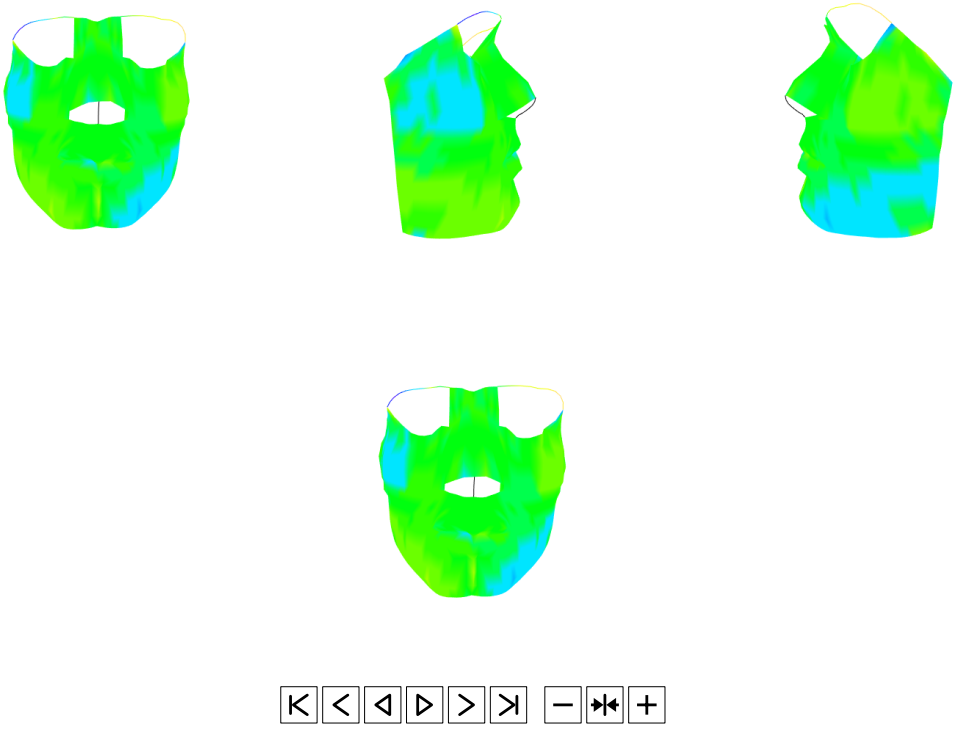

FIGURE 6.15: Asymmetry Rendering

6.4 Post-Orthognathic Analysis

This analysis aims to discuss the pre- operative and post-operative facial shapes of three different types of orthognathic surgical intervention. A group of approximately 50 patients are analysed by statistically examining their pre-orthognathic and post-orthognathic 3-dimensional images. These cases are compared against the group of control cases discussed previously (those who have not had any facial injuries or surgeries). Comparisons between controls and pre-/post-orthognathic cases, the shape change with age for all cases, and asymmetry between the populations will be examined.

The post orthognatic cases are collected from the multi-disciplinary dentofacial planning clinic led by Professor Ashraf Ayoub and Dr. Sunny Khambay. All patients are diagnosed with maxillary deficiency biased on a comprehensive clinical and radiographic assessment. The final position of the maxilla is determined by conventional 2D profile prediction methods and model surgery. None of the patients require any change in the vertical position of the maxilla or have facial asymmetry requiring surgical intervention. A cinch stitch is applied if the alar base width is increased more than 3 mm peri-operatively. The images are taken 1 year post-surgery.

The post-orthognathic patients are further split by the type of surgical procedure. In general, The Lefort I surgery is where the maxilla (upper jaw) is separated at the level of the nasal opening and moved either forward, up, or down, but specifically not backwards movement. The Mandible BSSO surgery occurs when the mandible is separated at a specific angle on both sides and then moved in any direction. Lastly, the Bimax combined surgery is a combination of the previous two.

The quality of life of patients following a cosmetic or reconstructive surgical procedures is directly related to improvement in physical appearance [Cunningham et al., 1996], an increased self-confidence and ability to mix socially. Evaluating the difference and relative change compared to control patients (those who have no need for surgery) illustrates the success of the surgery. The purpose of this study was to apply a novel method to evaluate surgical outcomes at 1 year after surgery for patients undergoing orthognathic surgical protocols.

Research evaluating surgical outcomes by comparing post-surgical patients and a set of control patients is not as rich as that which evaluates pre-/post-surgical patients. However, there are some techniques used to evaluate the control cases versus the post surgical patients. These usual methods include assessment of patients using cone beam computed tomography (CBCT) [de Paula et al., 2013]. CBCT scans are taken prior to surgery and at some pre-determined time post-surgery. In order to assess the differences in the scans, an automatic cranial base superimposition method registers the scans and

then shape correspondence is applied to assess the changes. Many studies make use of laminagraphic X-rays to monitor mandible displacement [WORMS et al., 1980] as well as 3-dimensional facial morphological values measured from facial CT images [Kim et al., 2013]. In this study, a curve comparison analysis is used instead, with General Procrustes analysis and asymmetry correspondences. In general, it has been found that most patients have maxilla adaptations of greater than 2mm post-surgery vertically. However, compared to a control population, there was still about a 1.5 mm difference [de Paula et al., 2013].

In the following analysis, the differences in shape between the control population and the post-orthognathic surgery population are thoroughly investigated in order to determine how close the the post-surgical population is to control shape. Differences in asymmetry between the populations based both upon the entire facial structure as well as specific facial features are also discussed. Analysis of the difference between pre- and post-surgical patients as well as pre-surgical and controls is examined. Lastly, individual comparisons of patients (pre-intervention and post-intervention) are shown. Figure 6.16 shows the overall distribution of the age of the populations discussed. While the pre- and post-surgical patients numbers differ, for the pre-/post-analysis, only matching pairs (complete cases of pre- and post- images) were used. However, when investigating the pre-/post-surgical population against controls separately, the full data set is used.

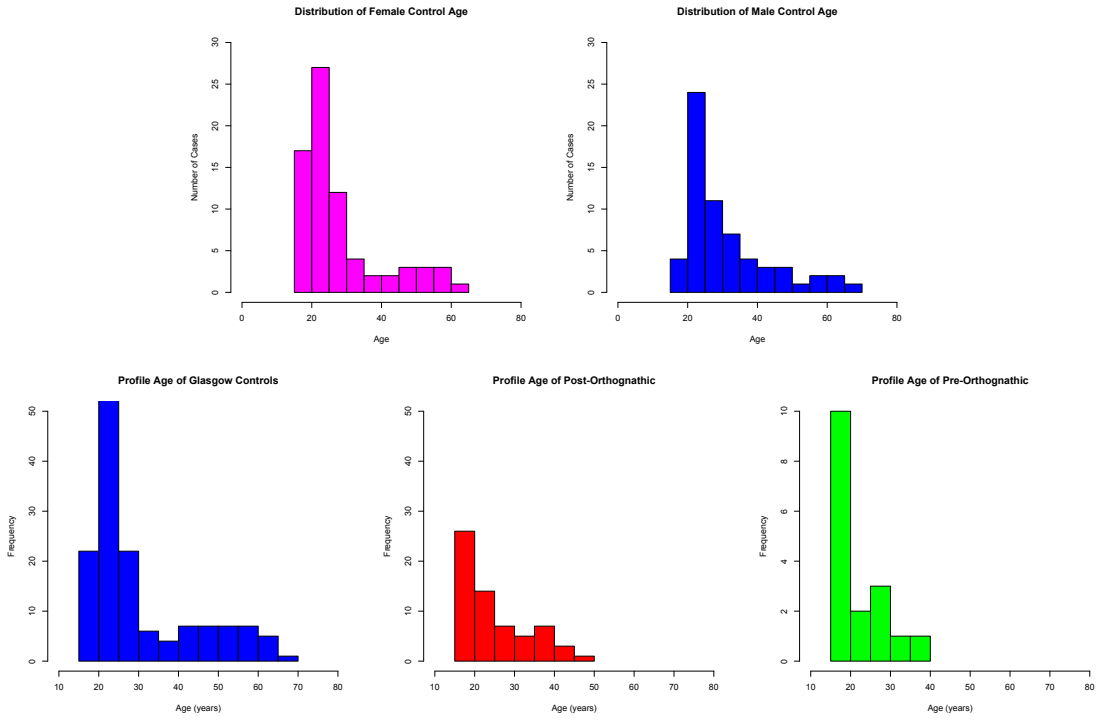

FIGURE 6.16: Histogram of M/F Control Age Distribution (top) and Control/Pre/Post-Orthognathic Age Distribution (bottom)

TABLE 6.2: Summary Profile - Subjects

		Male	Female	Total
Orthognathic Cases				
	Maxilla Lefort	4	16	20
	Mandible BSSO	4	4	8
	BIM - Combined	5	7	12
	Not Used	3	6	9
	Total	16	33	49
Control Cases		83	132	215

6.4.1 Glasgow Controls and Orthognathic Shape Differences - Mean Shape

In order to assess the level of success of orthognathic surgery, the Glasgow controls are compared against the post-orthognathic surgery population. If the orthognathic cases show the same general facial shape as the control cases, then it can be said that the surgery made the individual's face 'normal' in relation to the general population. Here an examination of what exactly is different in the facial shape between the two populations is conducted.

TABLE 6.3: Hotelling T^2 Test P-Values Summary for Principal Component Analysis (Post-Orthognathic cases against Controls)

	Male	Female
Maxilla Lefort	0.049	0.666
Mandible BSSO	0.877	0.103
Bimax - Combined	0.695	0.347
All	0.06	0.001

The differences between control and orthognathic cases can begin to be seen by comparing the mean shapes. Due to previous study done which showed clear differences in facial shape between males and females, the populations have been further separated by sex. A Hotelling two sample t-test was performed on the individual surgical populations as opposed to the control groups as shown in Table 6.3.

Examination of the differences between male controls and post-orthognathic Maxilla Lefort surgical patients (Figure 6.17) shows a recessed upper face of the post-orthognathic cases. Recall, that Maxilla Lefort I surgery is a movement forward, up, or down of the upper jaw. It would appear as though the surgery under-corrects by not bringing the upper jaw adequately forward. This flaw is demonstrated by a recessed upper face and a protruding lower face. However, in females there seems to be over-correcting. This could make sense given the differences in male and female facial shape. Females tend to have a less pronounced lower face and jaw, the opposite of males. Potentially, the surgery

under-corrects for males and over-corrects for females, since the same procedure is performed on both. On both the males and females, the Maxilla Lefort post-orthognathic cases do have a more pronounced mandible.

Male

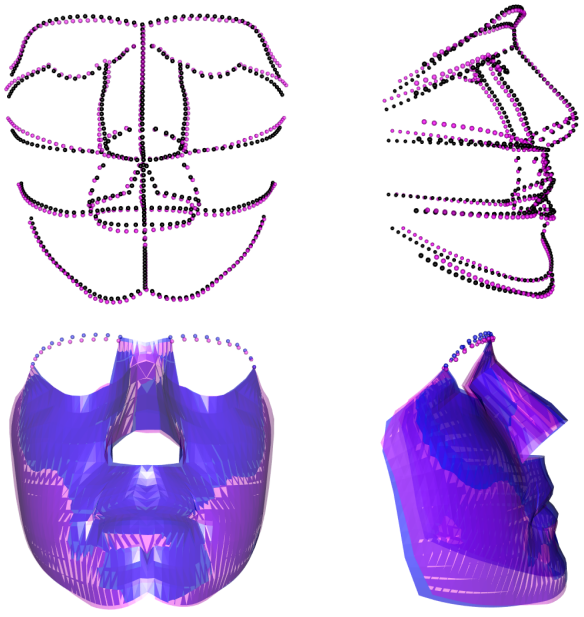

Female

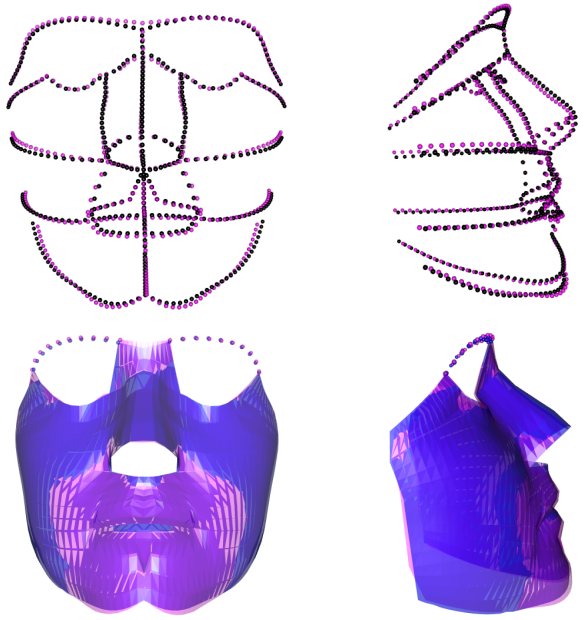

FIGURE 6.17: Mean shape of Controls (blue) and Mean shape of Maxilla Lefort Orthognathic cases (magenta)- Curves and Rendered Meshes

When examining the mean shape comparison of the control population and the post-orthognathic Mandible BSSO patients (Figure 6.18), it is clear the the orthognathic cases have very pronounced mandibles in both males and females. Recall, that Mandible BSSO surgery is a correction of the mandible (lower jaw) in any direction. It is possible

that in both cases there has been an over-correction. Interestingly, males seem to tend toward a lower lip puckering as well, but this is much less significant than that of the mandible curve.

Clearly, in both the male and female populations, the orthognathic cases tend to have a recessed nose; this is also true in the Maxilla Lefort I surgery. The mandible is seemingly recessed, but it also tends to be lower, giving the orthognathic individual a 'longer looking' face.

Male

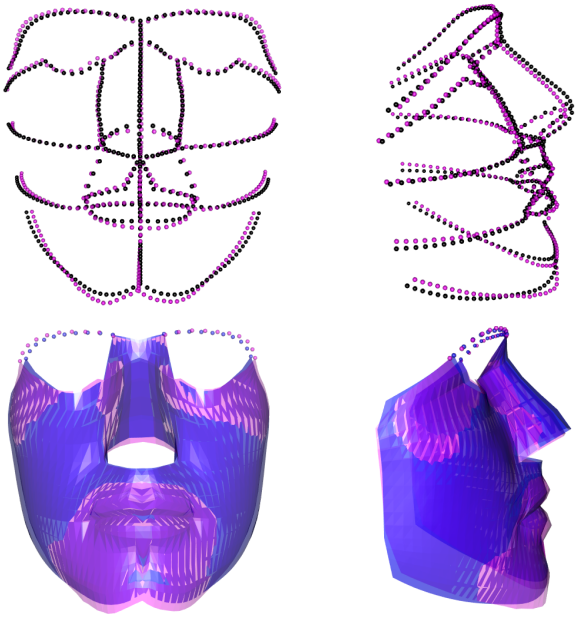

Female

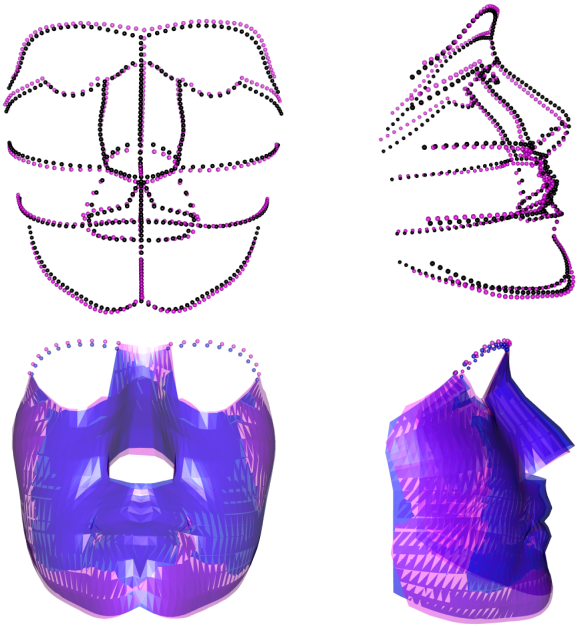

FIGURE 6.18: Mean shape of Controls (blue) and Mean shape of Mandible BSSO Orthognathic cases (magenta)- Curves and Rendered Meshes

Lastly, the mean shape of the control population is compared to that of the Post-Orthognathic Bimax Combined surgical patients (Figure 6.19). Recall that the Bimax Combined surgery is a combination of both the Maxilla Lefort I and the Mandible BSSO surgeries. Due to this, the mean shape could be considered less informative for this situation. Different patients would have undergone different jaw corrections leading to heterogeneous results. However, what is clear throughout is that there is a protrusion of the lower mandible curve for both males and females.

Overall, what must be considered is what type of surgery the orthognathic patients went through as this could cause the mean shape to not be fully inclusive of all information. For some patients the jaw is moved forward, some back, and some both. This could cause some lack of conformity when viewing the mean shapes as a method of comparing the two populations. While the populations are further separated into groups based upon the type of surgery, two issues still remain; the number of patients per group and differences in surgical procedure for individuals. However, in general it is clear that the mandible curve for surgical intervention patients is more pronounced and longer than the control population, giving the orthognathic patients a protruding jaw with a 'longer face'.

Male

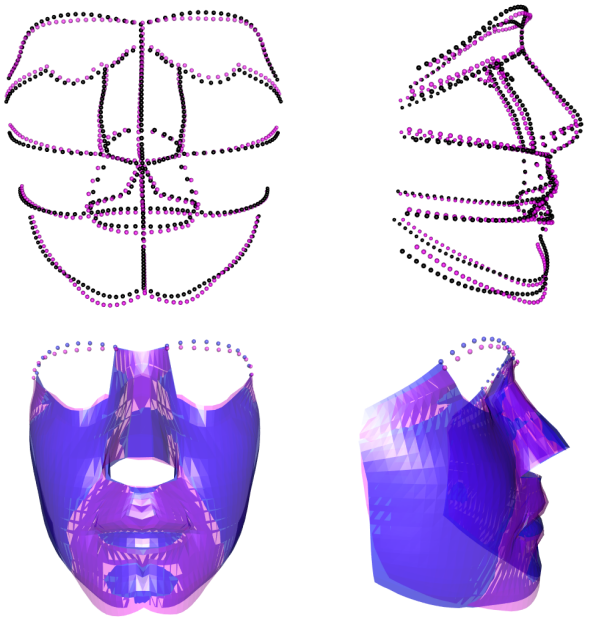

Female

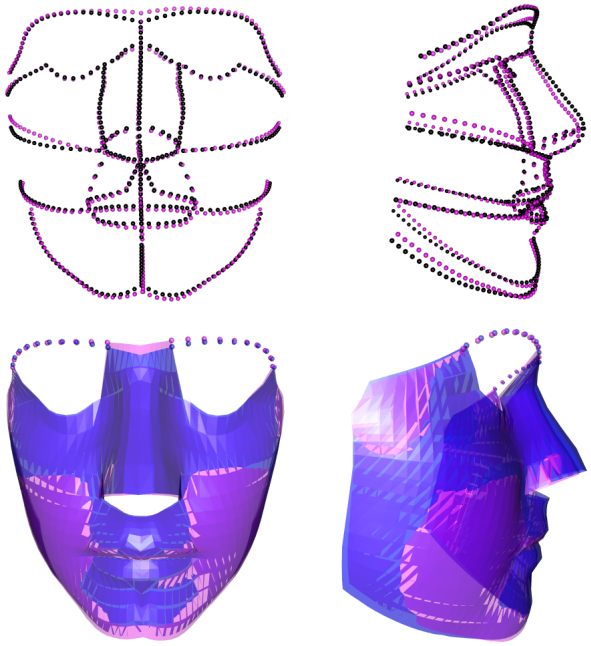

FIGURE 6.19: Mean shape of Controls (blue) and Mean shape of Bimax Combined Orthognathic cases (magenta)- Curves and Rendered Meshes

6.4.2 Glasgow Controls and Orthognathic Shape Difference - Principal Components

Using curves and meshes as the comparison configurations, General Procrustes Analysis (GPA) is applied to all cases, with scale effects removed, in order to compare the shape, not size, of the populations. Principal Components Analysis (PCA) is then performed in order to evaluate the differences between the populations, respectively.

The Maxilla Lefort I cases are examined first, with Figure 6.20 clearly showing the differences between the control and post-orthognathic populations, further separated by sex. There seems to be a clear difference between the controls and post-orthognathic population for the 1^{st} principal component and slightly less so, yet still significant for the 2^{nd} principal component.

While the groups are separated by sex, the same principal component is being viewed for all groups (i.e. the principal components align in terms of meaning). Thus, there are clearly similarities in the controls cases versus the orthognathic, regardless of sex. The extremes of the first two principal components are shown in order to illustrate what movement each is describing.

The 1^{st} principal component is a clear dropping of the mandible, whereas the 2^{nd} principal component is a clear protrusion of the mandible. This follows precisely from the mean shape differences that are seen between the populations of a more protrudent and longer lower jaw for post-orthognathic cases.

For the Mandible BSSO patients and the controls (Figure 6.21), there is certainly a smaller difference shown in the principal components than for the Maxilla Lefort I surgery. On the other hand, the principal components are precisely the same with the first being a lowering of the mandible and the 2^{nd} being a protrusion of the mandible. Perhaps, because the mandible is being concentrated on in this surgery (not the maxilla) there is less of a difference between the populations.

Lastly, the Bimax combined surgical patients are seen in relation to the controls (Figure 6.22). There is again, very little difference in principal components between the two. However, the principal components are the same as both the Mandible BSSO and Maxilla Lefort I patients. Clearly, the mandible dropping and protruding is most evident in the Maxilla Lefort I male patients (also evidenced by the Hotelling T-squared Test shown in Table 6.3), whereas the Mandible BSSO and Bimax combined patients have much less significant movement.

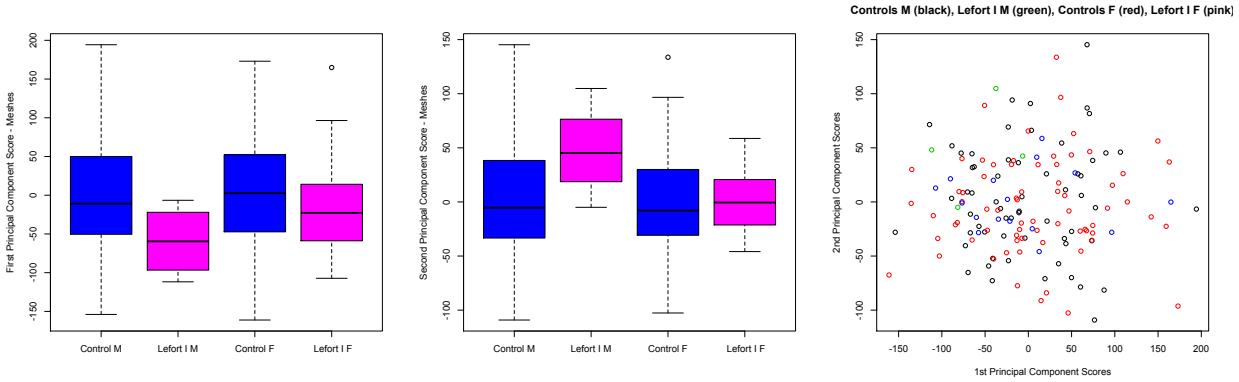

1^{st} principal component Extremes - 32 percent

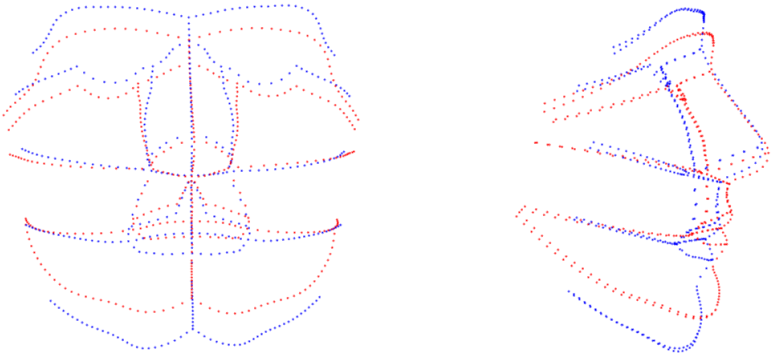

2^{nd} principal component Extremes - 13 percent

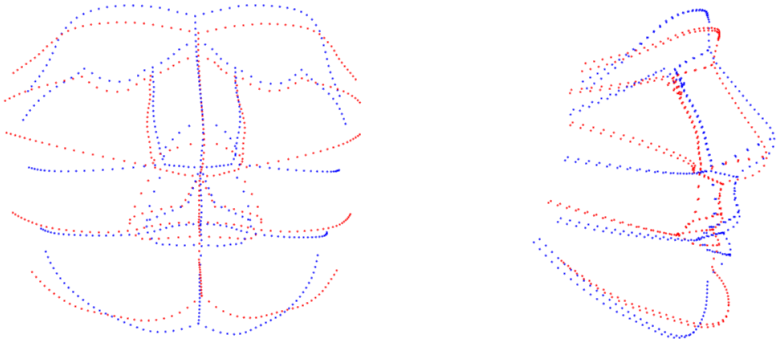

FIGURE 6.20: 1^{st} and 2^{nd} Principal Components Controls and Maxilla Lefort I Post-Orthognathic Cases

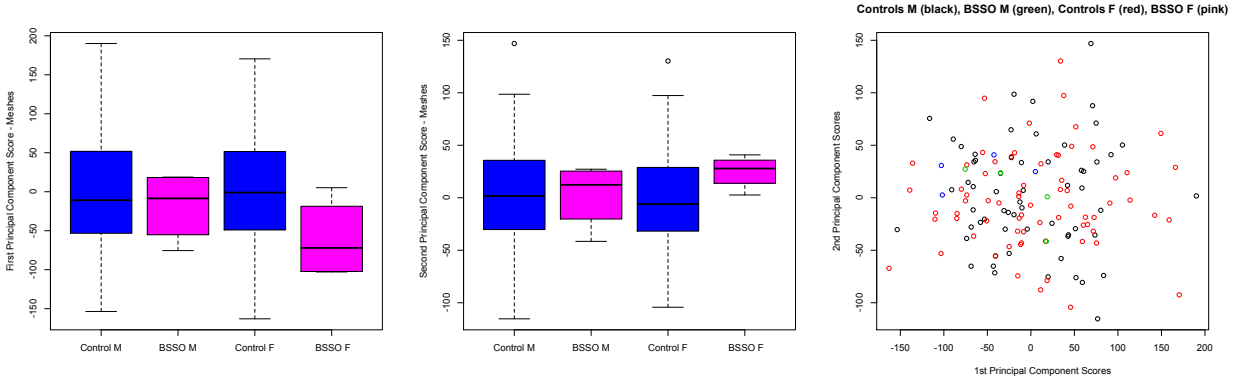

1^{st} principal component Extremes - 31 percent

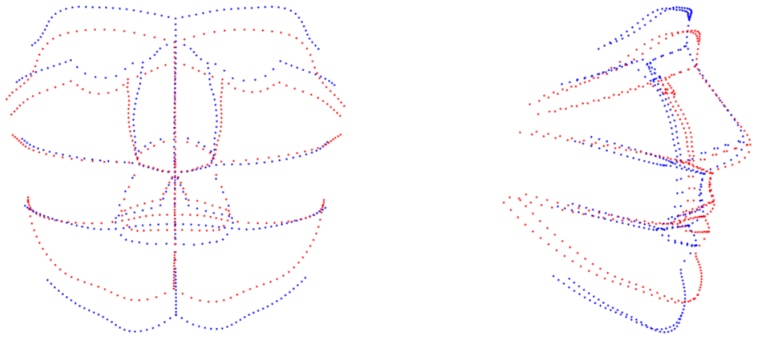

2^{nd} principal component Extremes- 13 percent

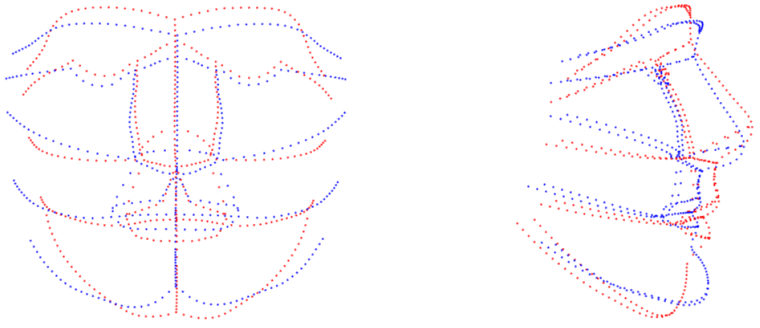

FIGURE 6.21: 1^{st} and 2^{nd} Principal Components Controls and Mandible BSSO Post-Orthognathic Cases

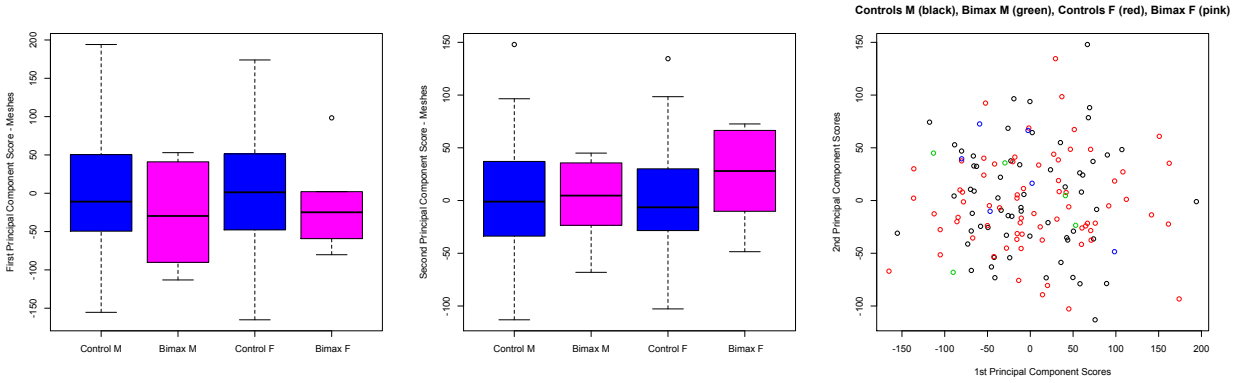

1^{st} principal component Extremes - 31 percent

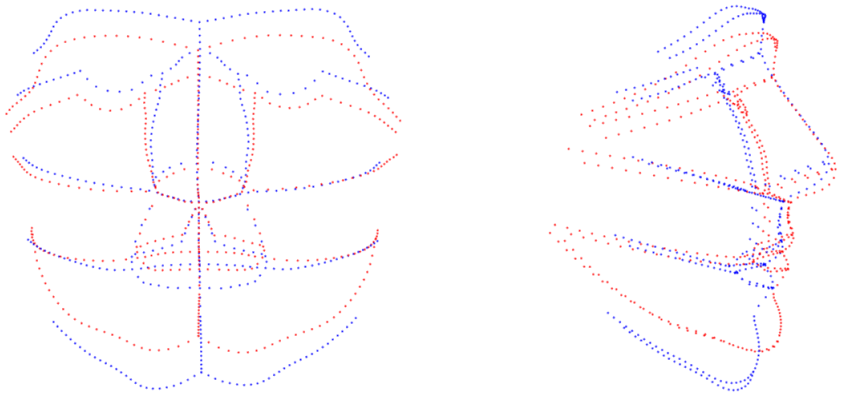

2^{nd} principal component Extremes- 13 percent

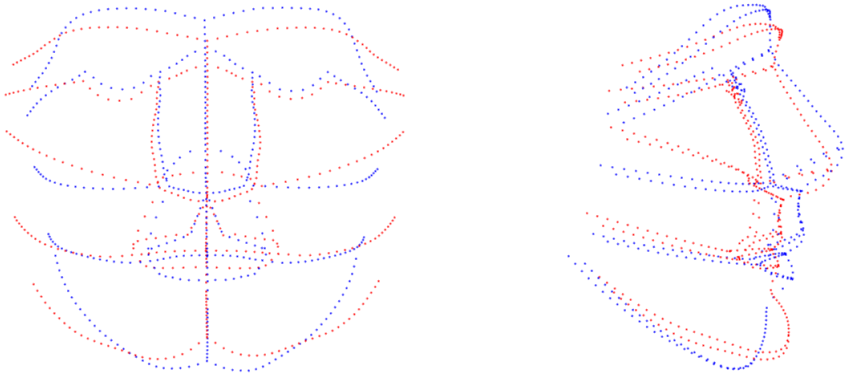

FIGURE 6.22: 1^{st} and 2^{nd} Principal Components Controls and Bimax Combined Post-Orthognathic Cases

6.4.3 Glasgow Controls and Orthognathic Shape Change with Age

Using the same methodology as described with the Glasgow controls with respect to shape change with age, the shape changes in age of controls and orthognathic cases is investigated. Recall that the reference bands correspond to two standard deviations of difference between the curves at each point. The age is restricted to 40 years old and younger in order to have the same age range for both groups. Examining the differences between the two populations (control and orthognathic), the principal component movement is viewed. The 1^{st} principal component (40 percent of the total variation - Figures 6.23, 6.24) for the males tends to be the lowering of the chin, creating what almost looks like a 'longer face' for the cases. Interestingly, the upper chin (mid-line mentolabial, from the lower lip curve to the *mentolabial curve*) seems to protrude but then drops sharply at the lower chin as compared to the control cases. Notice that the controls and orthognathic males start off very differently but as they age, the facial shape becomes highly similar. The controls have only a slight change with age, but the orthognathic males begin with a significantly larger drop in the chin than the controls and then age similarly.

The 2^{nd} principal component (15 percent of the total variation) for males shows a high recession of the chin. A very definite recession is seen, not just the *pronasale*, but the entire midline nasal profile. This is the most stark difference between the two populations where the orthognathic males have a much more significant lengthening of the face and a large recession of the chin, but the control males have significantly less chin recession and nose protrusion.

Principal Component 3 (about 10 percent of the variation) shows a puckering of the lips and flattening of the face. However, the additional information added by the meshes (Figure 6.23), shows a difference in the 3^{rd} principal component as to the curves. This would suggest that the protrusion of the nose which is seen in both the male orthognathic cases and control cases, has a stronger effect when seen with the meshes. The meshes add a significant amount of information to the nasal region, producing this effect.

Overall, there seems to be a clear dropping of the chin for both populations with the orthognathic cases starting with a more protruding chin but aging in the same way as the control cases. However, the controls cases tend to have less recession of the chin than the orthognathic cases.

There is a high correlation in the 1^{st} principal component between the female and male populations (Figures 6.25, 6.26). The control and orthognathic cases start off very differently, but follow a similar pattern as they age with a lengthening of the chin and rising of the brow, giving a very clear narrowing of the face.

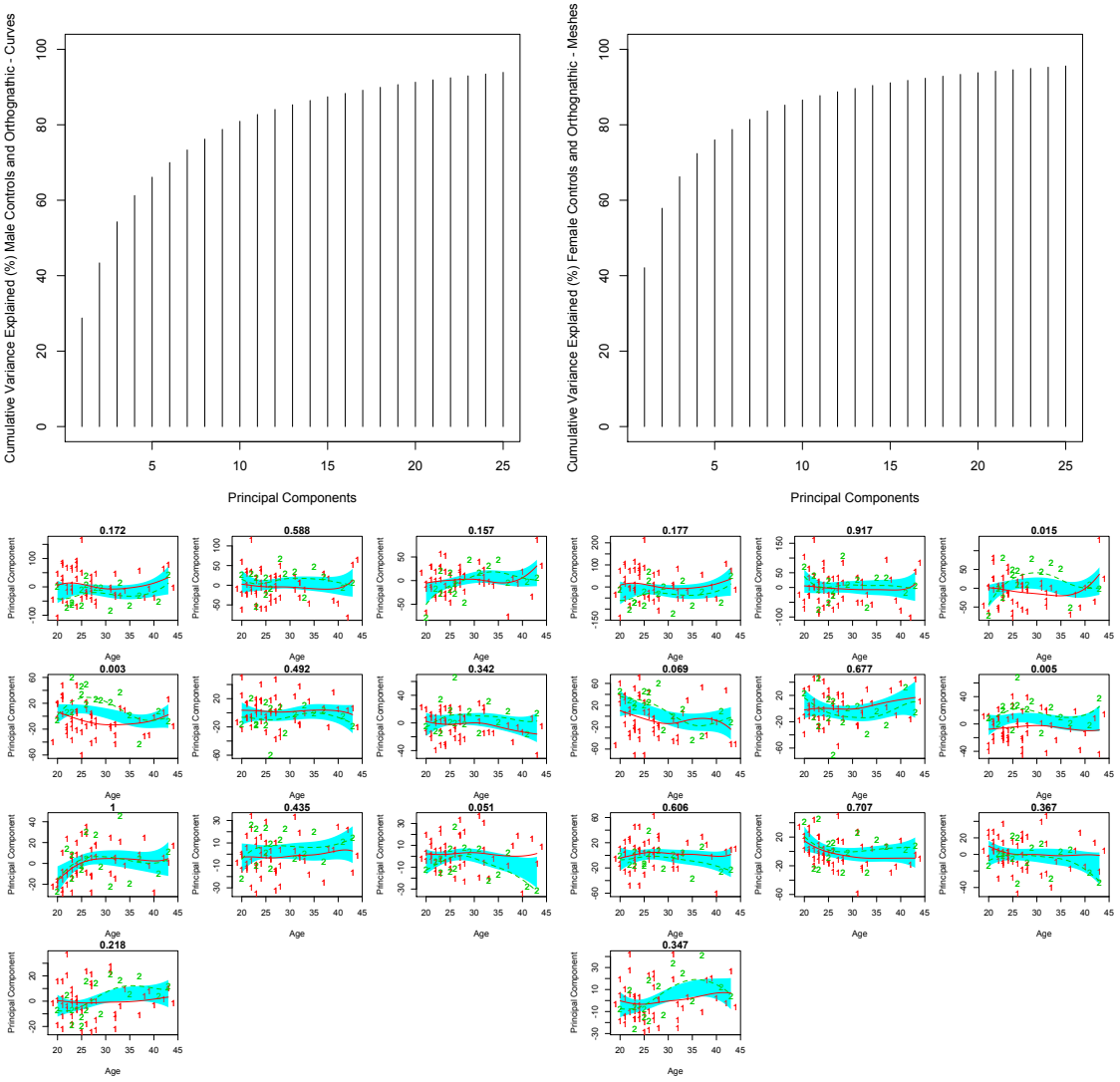

FIGURE 6.23: Cumulative Percent of Principal Components Control (red 1) and Orthognathic Males (green 2) Curves (top left) and Meshes (top right) and Fisher's Method for Male Glasgow controls with the 1^{st} 10 principal components against Age - Curves [Empirical P-Value 0.02346] (bottom left) and Meshes [Empirical P-Value 0.0216] (bottom right)

Again, the two populations are highly similar in the 2^{nd} principal component with a clear dropping of the cheeks and protrusion of the cheek bones. The 3^{rd} principal component shows a puckering of the lips.

Lastly the 4^{th} principal component (8 percent) shows a significant change, with a highly representative movement of the cheekbones with a drawing-in of the lower cheeks. This suggest a definite sagging of the cheeks giving the 'drawn' look of age. The additional information given by mesh analysis tends to not give anything more definite than the curve analysis for the females.

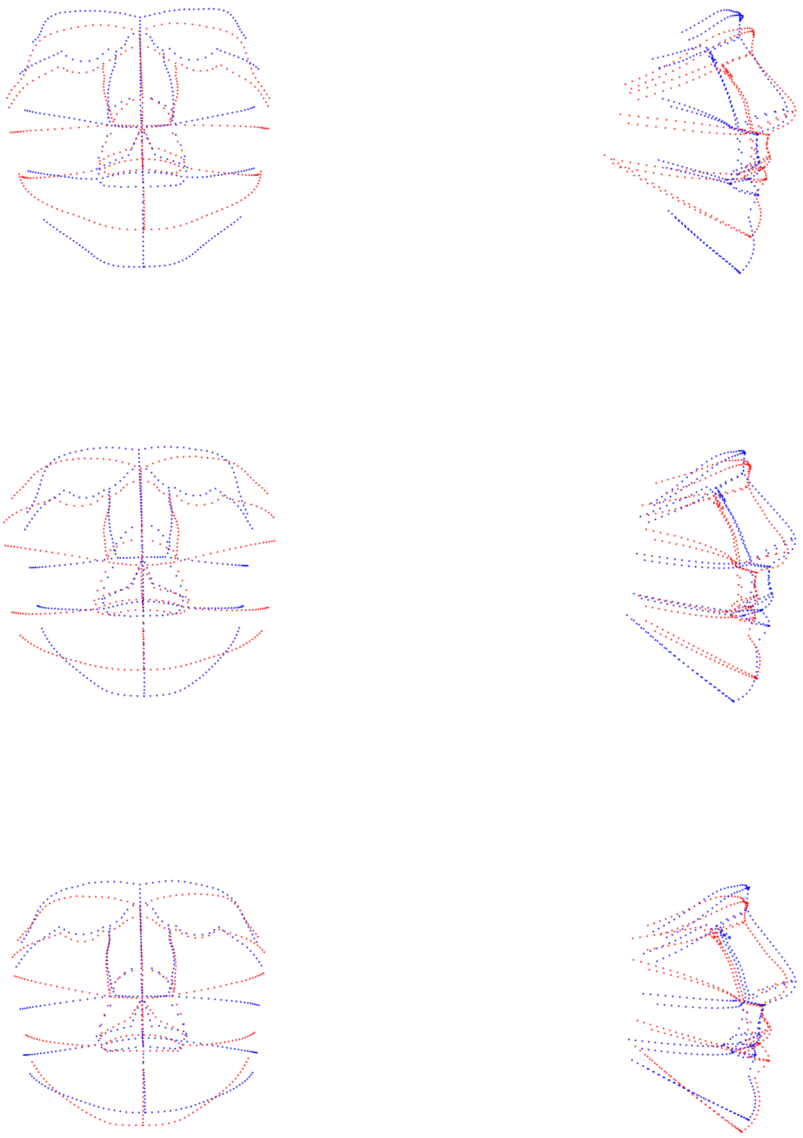

FIGURE 6.24: Male Control and Orthognathic Extremes 1^{st} (top), 2^{nd} (middle), and 3^{rd} (bottom) Principal Components

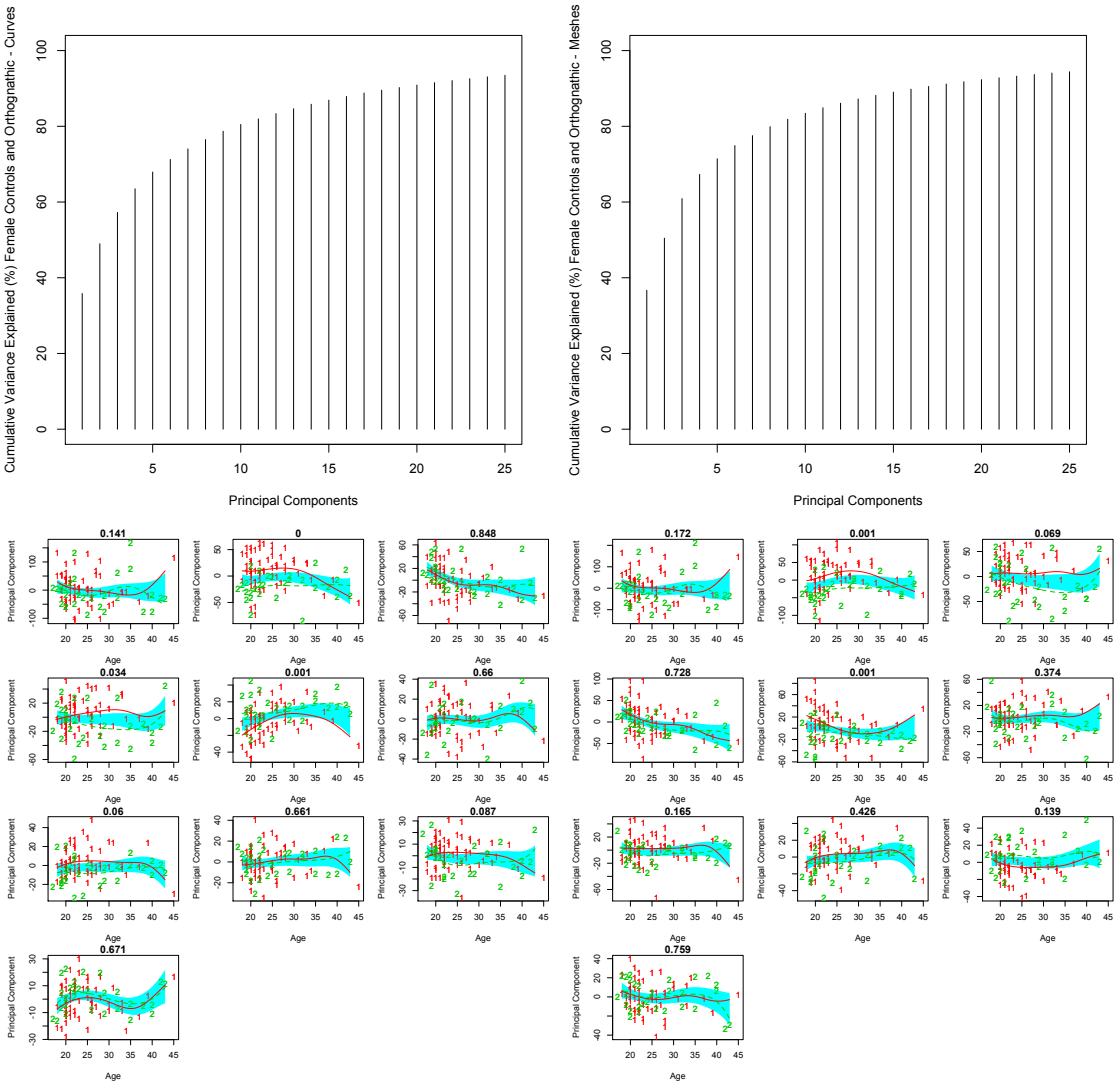

FIGURE 6.25: Cumulative Percent of Principal Components Control (red 1) and Orthognathic Females (green 2) and Fisher's Method for Female Glasgow controls with the 1st 10 principal components against Age - Curves [Empirical P-Value 0.00006] (left) and Meshes [Empirical P-Value 0.0002] (right)

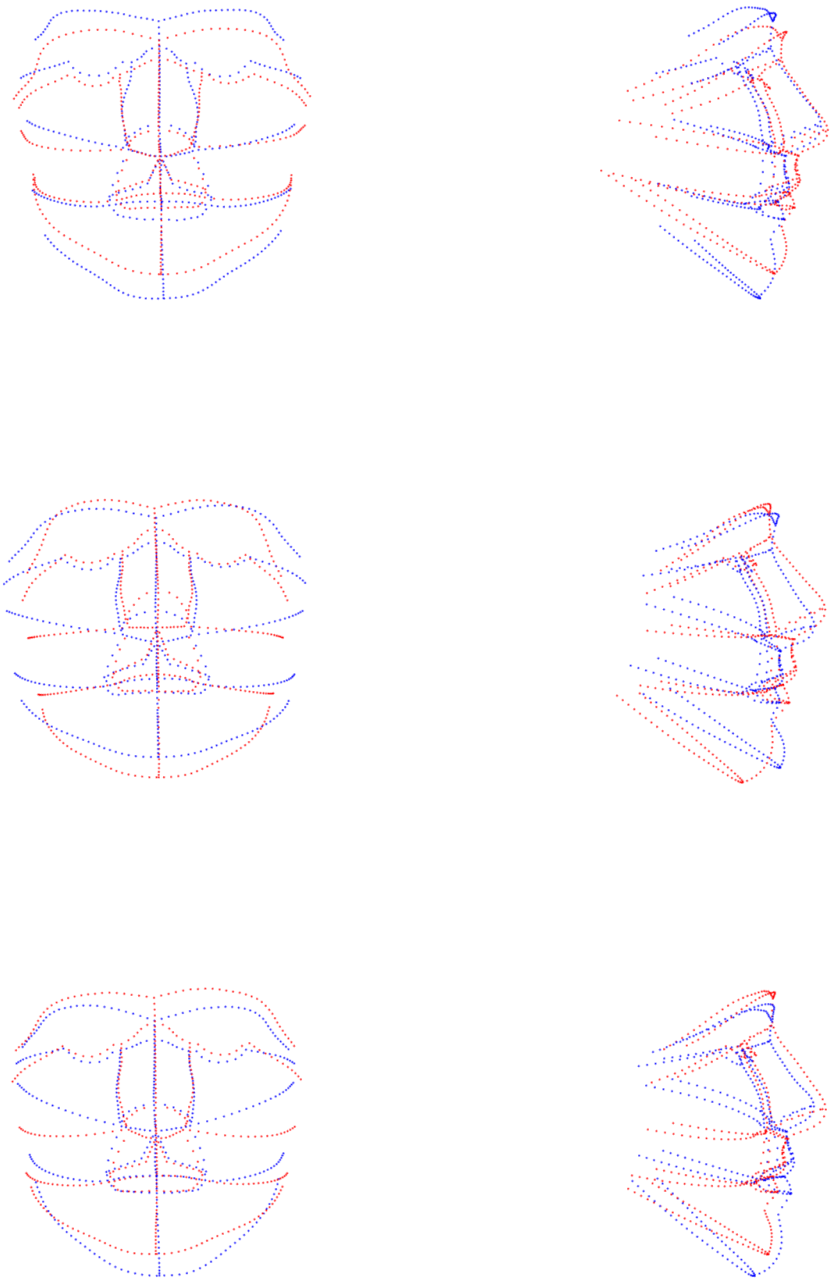

FIGURE 6.26: Female Control and Orthognathic Extremes 1^{st} (top), 2^{nd} (middle), and 3^{rd} (bottom) Principal Components

6.4.4 Glasgow Controls and Orthognathic Shape difference - Closest Control

Consider the shape space under which controls lie to be a confidence ellipsoid, such that the majority of control cases, with all their individual variation, fall within that space. A shape that does not fall within the 'accepted range' of a control shape would then be lying somewhere outside of this confidence space. If a post-orthognathic surgery case was corrected to the point of being 'normal', then it would fall inside this 'ellipsoid'. However, if it was still too far off in shape, then it would be lying somewhere outside of this ellipsoid.

It is informative to view the 'closest control' to a specific orthognathic case that does not lie within this ellipsoid. In layman's terms, it finds a control shape (made up of all the multiple variations that exist inside the control shape ellipsoid) that is closest to the orthognathic case, that if the orthognathic case was changed just that amount, then it would lie within the "accepted range" of normality.

The black line represents the closest control (i.e. what is 'wrong' with the orthognathic case) and the blue line is the actual orthognathic case. As seen in Figure 6.27, the male Maxilla Lefort I cases shows clearly that the nose recesses along the entire nasal profile, with a protrusion and dropping of the mandible and an equal or potential recession on the mid-line mentolabial. For the Mandible BSSO case, almost the exact same differences are evidenced. This follows from the previous analysis that post-orthognathic cases that are not fully corrected have a clear lowering and protrusion of the mandible.

6.4.5 Glasgow Controls and Orthognathic Shape Asymmetry

In the process of evaluating surgical outcomes, there is particular interest in asymmetry. Here, using asymmetry analysis, it is possible to tell exactly how asymmetric a specific (and collective) group of post-orthognathic surgery patients are in relation to the control patients. The difference in the overall asymmetry scores for the full meshes tend to be quite slight in Maxilla Lefort surgery and Maxilla BSSO, but the change in asymmetry for the Bimax Combined surgery is quite significant. However, since surgery only affects certain regions of the face, different parts can be isolated. Looking at the populations split by surgery type, specific regions on the face of interest can be isolated.

Figure 6.28 shows an overall asymmetry of the face, as well as specific regions based upon the pre- and post-surgical asymmetry scores of the three types of surgical groups. The control score is also displayed for comparison. The curves and full facial mesh scores

Closest showing Maxilla Lefort

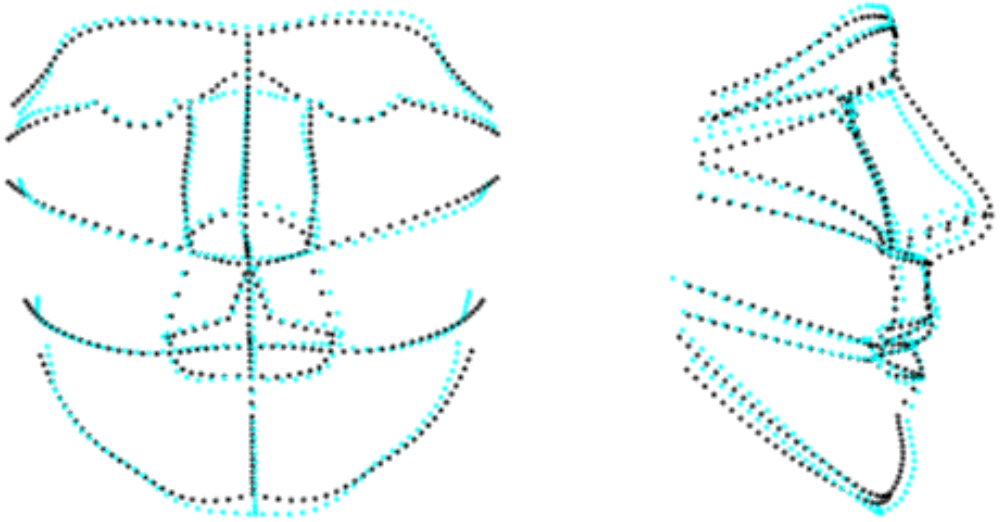

Closest showing Mandible BSSO

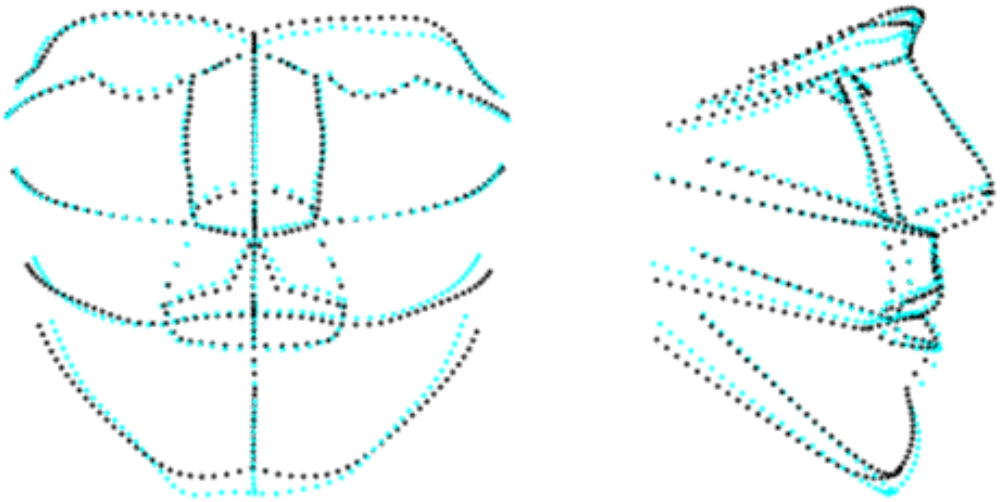

FIGURE 6.27: Closest showing Control - Curves

show almost precisely the same thing (as expected), with the controls having the lowest overall asymmetry score.

For the Maxilla Lefort I patients, asymmetry clearly decreases across the upper lips, lower lips, and nose; however the lower face is unaffected. Considering this is a maxilla (upper jaw) surgery, those results seem reasonable. Overall the asymmetry is largely unaffected.

The Mandible BSSO patients actually tend to increase a little in asymmetry. This surgery affects such a large part of the face (moving the mandible in any direction), that

a slight difference in asymmetry post surgery is possible. However, the change is small, if not negligible.

Lastly, the Bimax Combined patients have a clear decrease in asymmetry. Considering the surgery affects both the upper jaw and lower jaw these conclusions follow promptly. This surgery sometimes aims not only to improve the jaw direction but also to correct asymmetry. In all parts of the face there is a clear drop in asymmetry. In relation to the controls, this population has the highest asymmetry, which again follows from it being a surgery that actually corrects specific asymmetry.

Overall, asymmetry (Figure 6.29) does not seem to be a particularly important part of the Mandible BSSO or Maxilla Lefort I surgery. Clearly, if a data point lies below the line of equality, then the pre-surgical asymmetry score was higher than the post-surgical score i.e. a reduction in asymmetry. However, for Bimax Combined there is a significant decrease in asymmetry post surgical intervention. However, it is still not completely on par with the level of control asymmetry, whereas the other post surgical patients are.

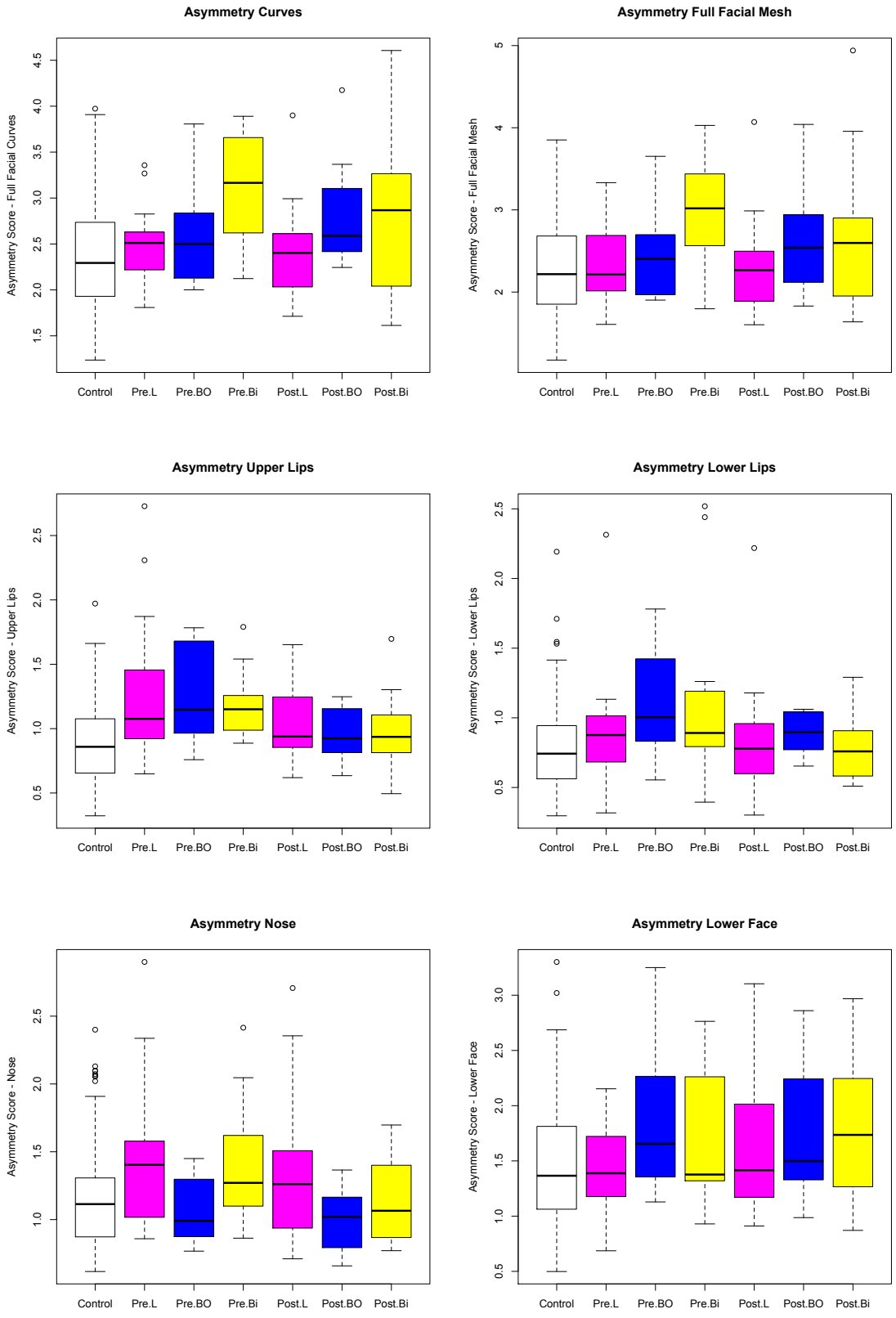

FIGURE 6.28: Asymmetry Scores for Controls, Pre-Orthognathic, and Post-Orthognathic Populations separated by surgery type

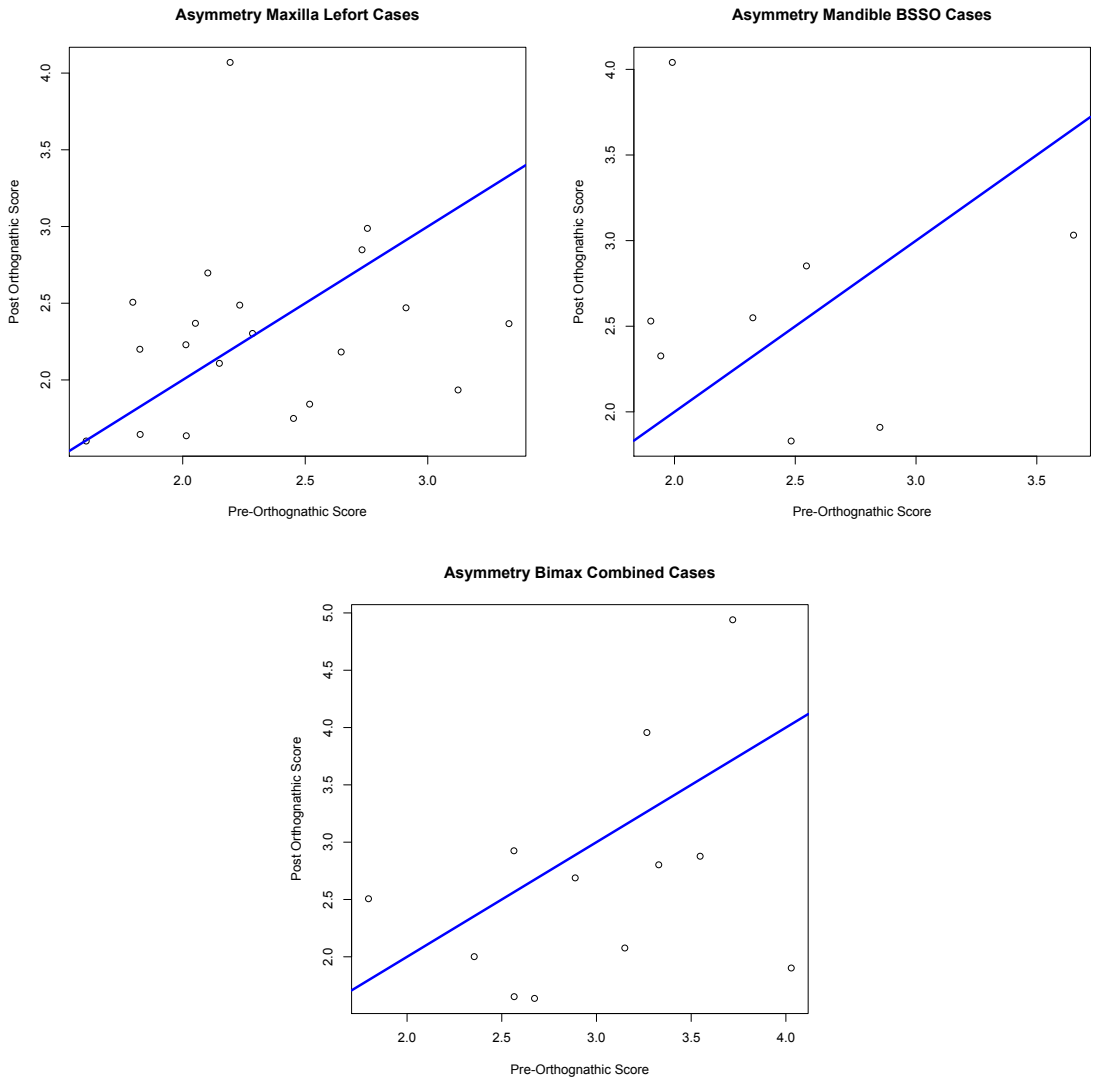

FIGURE 6.29: Asymmetry Matching Pre/Post-Orthognathic Cases

6.4.6 Individual Comparison

The previous discussion focuses on comparing populations and groups within those populations, but when thinking of a surgical patient, an individual analysis can also aid in discussing the overall needs of an individual. Below are several different patients all having undergone different surgical interventions. For each patient, his or her before and after pictures are shown as well as two movies. One movie topographically colours the post-orthognathic image of where changes have been made from the pre-orthognathic image. For example if the lower jaw is yellow, then the surgery pushed the lower jaw forward significantly. The second movie topographically colours the post-orthognathic image compared to perfect symmetry.

Each patient also has a scorecard and table listing pre- and post-asymmetry scores. The scorecard has different features' (as well as overall) asymmetry shown. The black/grey strip is a density estimate strip showing where the control asymmetry scores lie. Where it is the 'blackest', most of the controls lie, and then it tapers off grey on either end where only few controls lie. The red line indicates where that individual patient is, in comparison to the controls. So if the red line sits way to the left, then the patient's asymmetry is less than that of the average controls, and if the red line sits to the right, then the patient's asymmetry is more than that of the average controls.

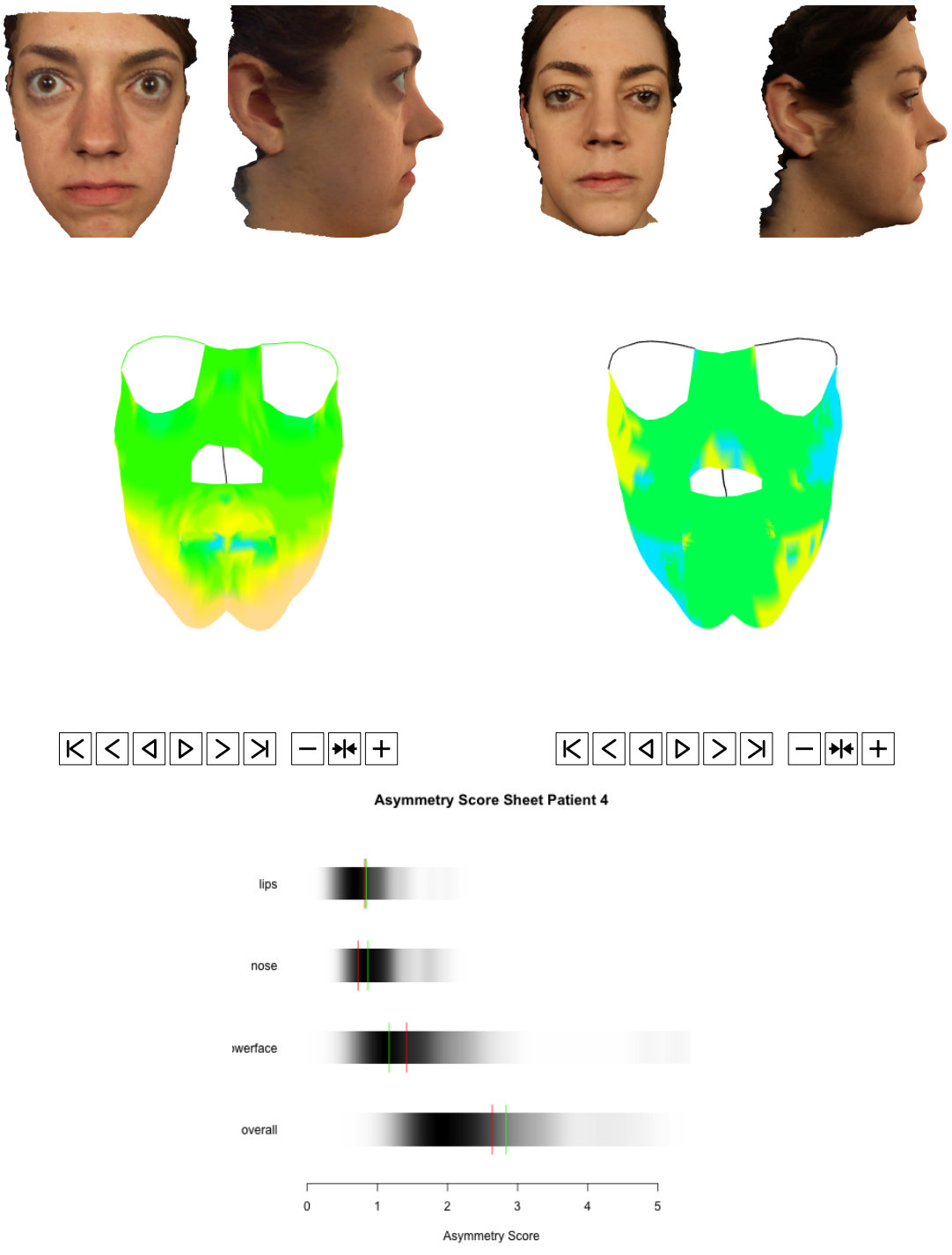

FIGURE 6.30: Patient 4 Pre-Orthognathic image (top left) and Pre-Orthognathic image (top right) - Maxillary Advancement 3mm Post-Orthognathic [Post-Orthognathic rendered with topographic colouring of where that face is compared to Pre-Orthognathic (left)] [Post-Orthognathic rendered with Topographic colouring compared to Symmetry (right)] - Asymmetry Score Sheet (Pre-Ortho - red, Post-Ortho - green)

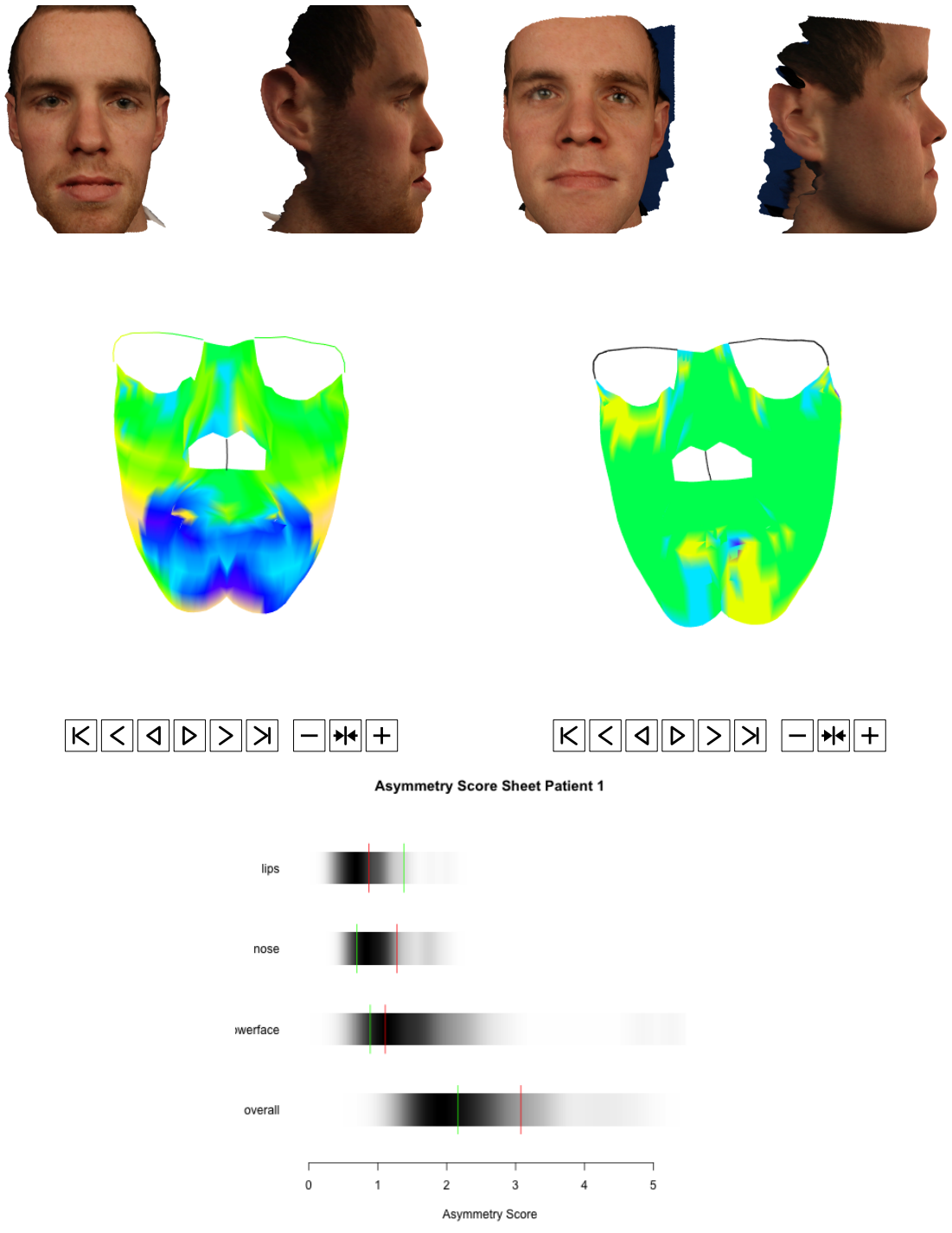

FIGURE 6.31: Patient 1 Pre-Orthognathic image (top left) and Post-Orthognathic image (top right) - Maxillary Advancement 6mm Post-Orthognathic [Post-Orthognathic rendered with Topographic colouring compared to Pre-Orthognathic (left)] [Post-Orthognathic rendered with Topographic colouring compared to Symmetry (right)]- Asymmetry Score Sheet (Pre Ortho - red, Post-Ortho - green)

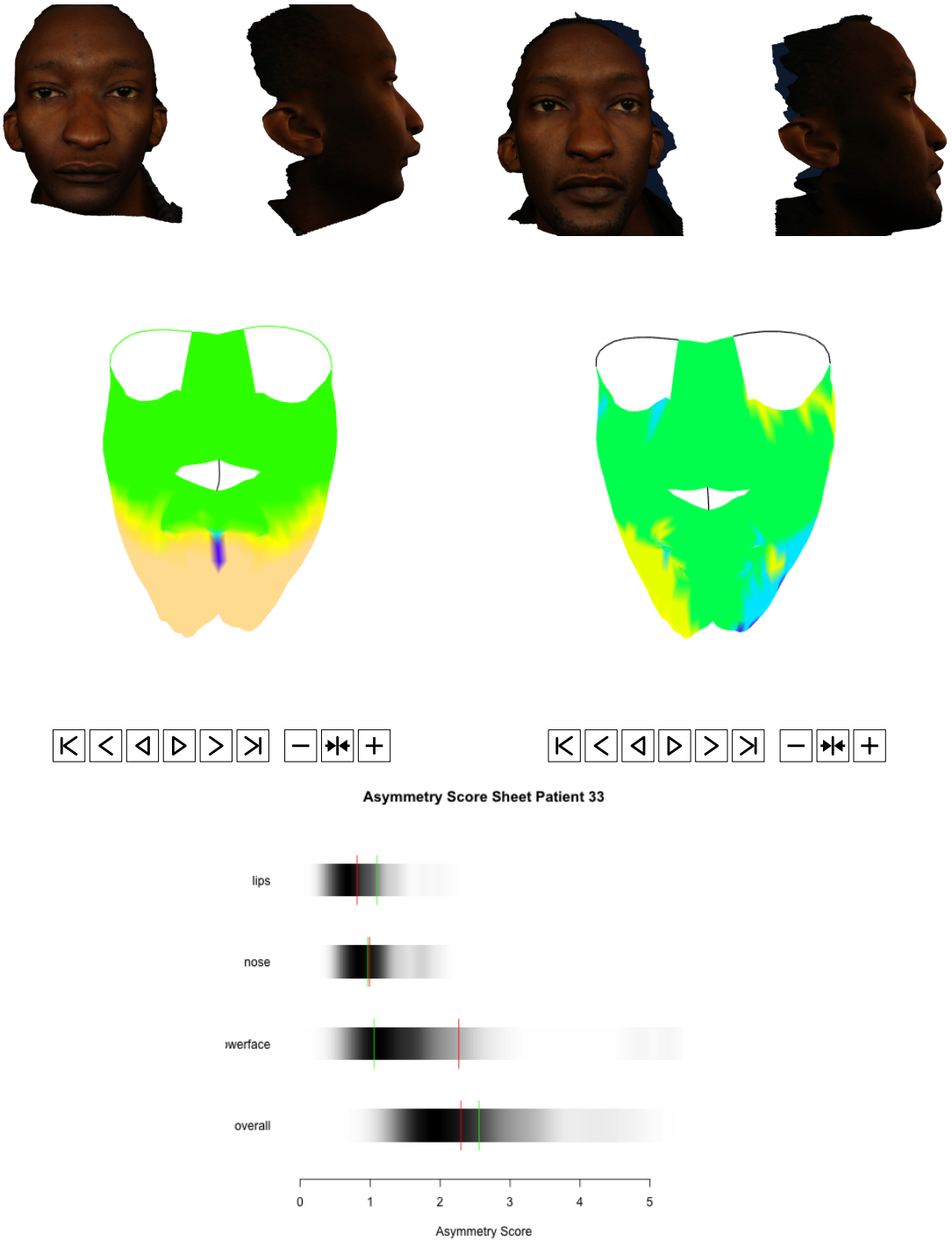

FIGURE 6.32: Patient 33 Pre-Orthognathic image (top left) and Post-Orthognathic image (top right) - Mandibular Advancement 11mm and 3 mm shift Post-Orthognathic [Post-Orthognathic rendered with topographic colouring of where changes were made from the Pre-Orthognathic image](left)] [Post-Orthognathic rendered with Topographic colouring compared to Symmetry (right)] - Asymmetry Score Sheet (Pre Ortho - red, Post-Ortho - green)

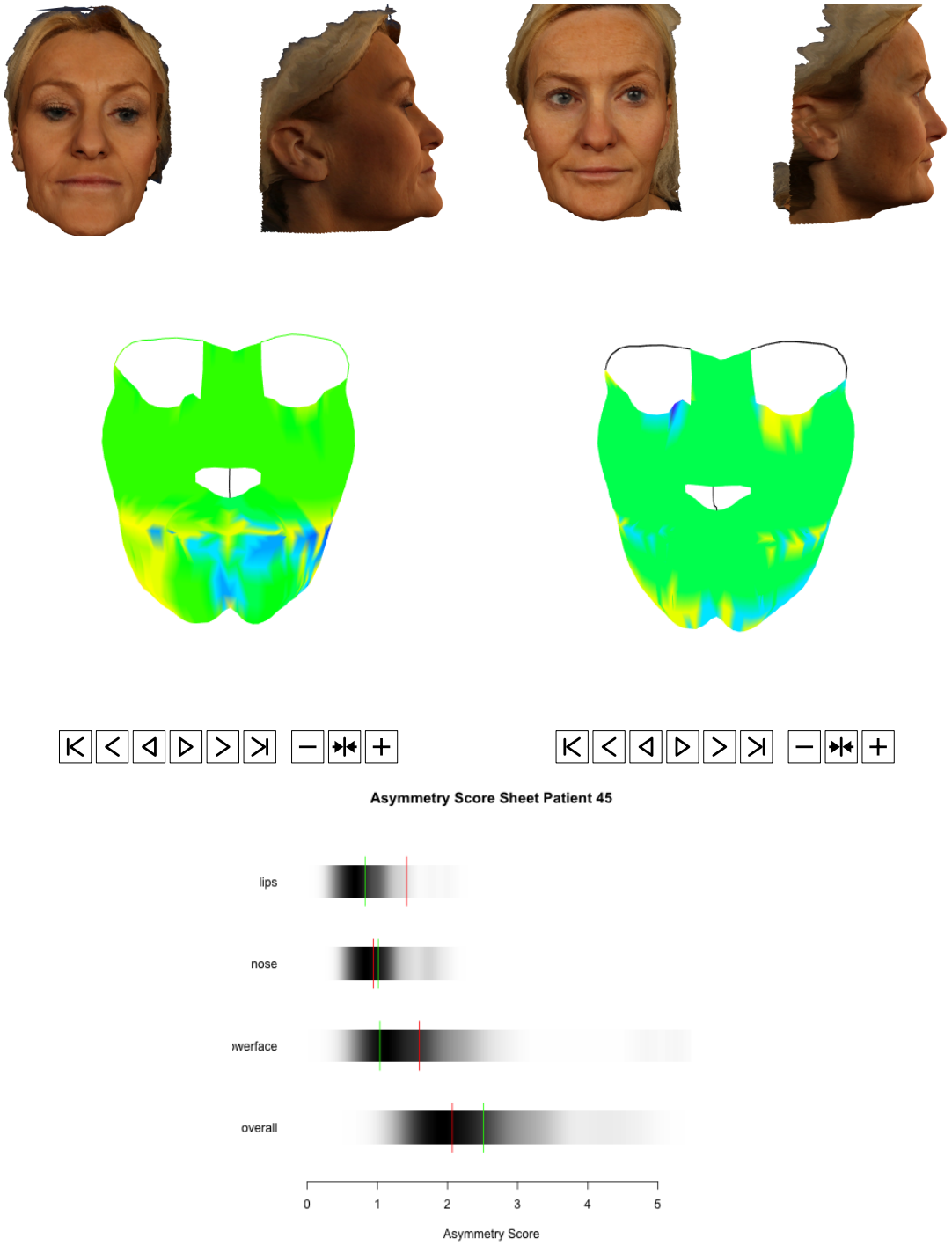

FIGURE 6.33: Patient 45 Pre-Orthognathic image (top left) and Post-Orthognathic image (top right) - Mandibular setback of 4mm [Post-Orthognathic rendered with topographic colouring of where changes were made from the Pre-Orthognathic image] (left)] [Post-Orthognathic rendered with Topographic colouring compared to Symmetry (right)] - Asymmetry Score Sheet (Pre Ortho - red, Post-Ortho - green)

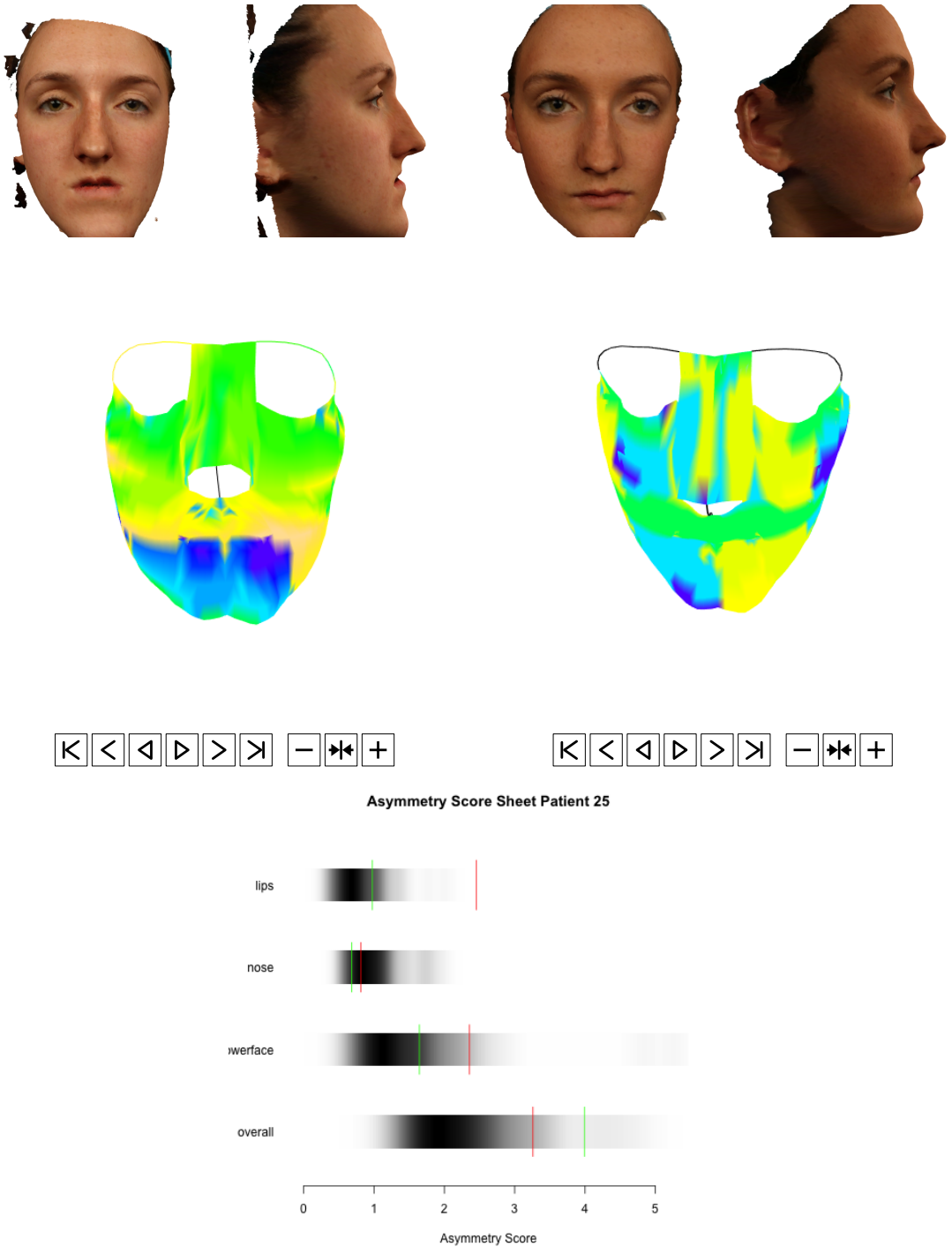

FIGURE 6.34: Patient 25 Pre-Orthognathic images (top left) and Post-Orthognathic images (top right) - Maxillary advancement 6.5mm, mandibular advancement 2mm Post-Orthognathic [Post-Orthognathic rendered with topographic colouring of where changes were made from the Pre-Orthognathic image (left)] [Post-Orthognathic rendered with Topographic colouring compared to Symmetry (right)] - Asymmetry Score Sheet (Pre Ortho - red, Post-Ortho - green)

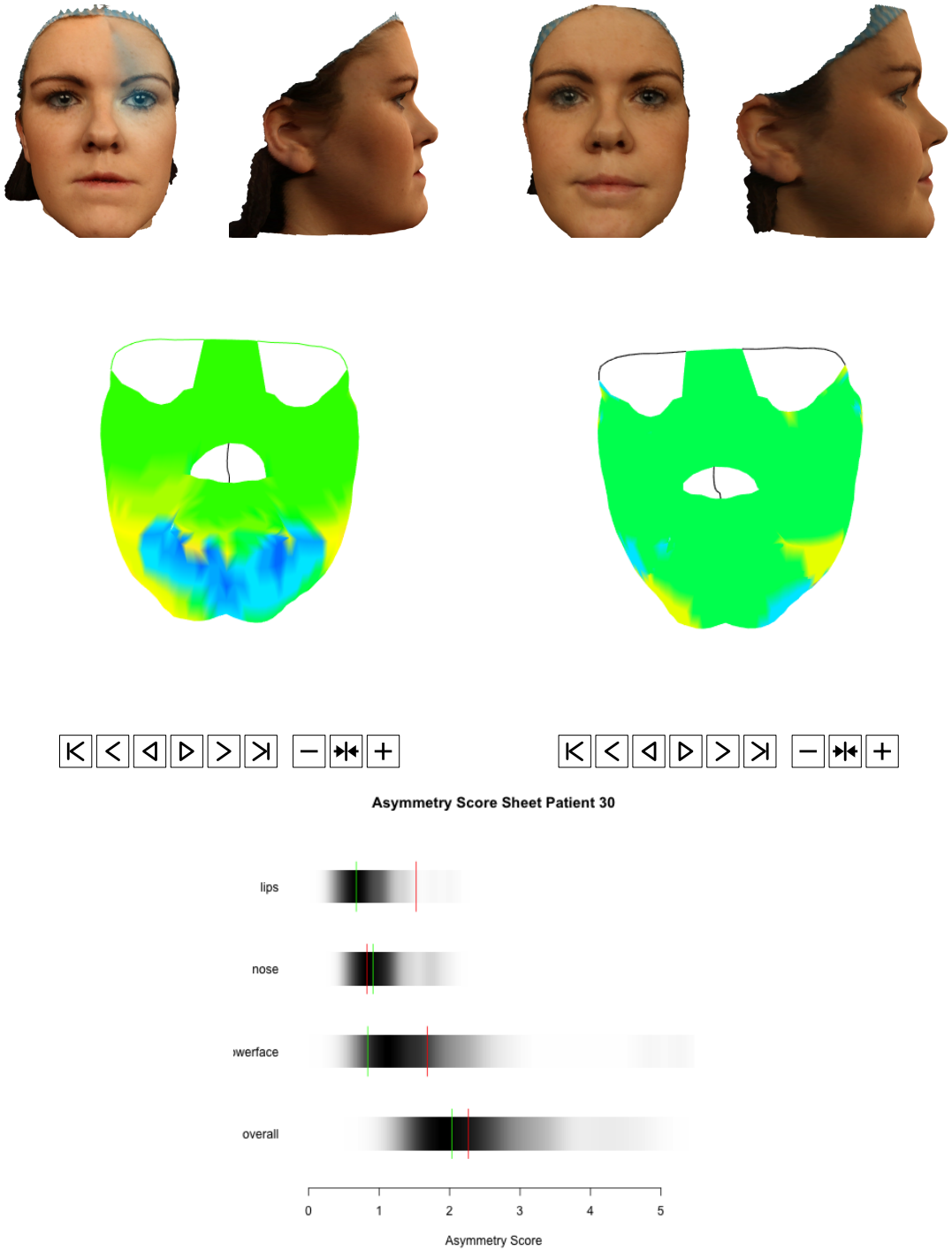

FIGURE 6.35: Patient 30 - Pre-Orthognathic Images (top left) and Post-Orthognathic images (top right) - Maxillary advancement 6mm mandibular setback 4mm [Post-Orthognathic rendered with topographic colouring of where changes were made from the Pre-Orthognathic image (left)] [Post-Orthognathic rendered with Topographic colouring compared to Symmetry (right)]- Asymmetry Score Sheet (Pre Ortho - red, Post-Ortho - green)

6.4.7 Glasgow Pre-Orthognathic/Control Analysis

In order to assess the need for orthognathic surgery, the Glasgow controls are compared against the pre-orthognathic surgery population. If the pre-orthognathic cases show a significant difference in shape to the general facial shape of the control cases, then it can be said that surgery might be necessary to make the individual's face 'normal' in relation to the general population. An examination is conducted to determine the difference in facial shape between the two populations.

Using the meshes as the comparison configurations, General Procrustes Analysis (GPA) is carried out on all cases with the scaling to size effect in order to compare the shape, not size of the male and female populations. Principal Components Analysis (PCA) is then performed in order to evaluate the differences between the two populations, respectively. First, the female controls and female pre-orthognathic populations and the male controls and the male pre-orthognathic cases are reviewed. From Figure 6.36, there seems to be a significant difference between the two female populations, but not with the male populations.

Examining the 2^{nd} principal component again shows a significant difference between the two female populations (control and orthognathic) but not the same for the male population.

When plotting the first two principal components against each other, it is clear that while the male populations do have some slight difference (Figure 6.38) they are distinctly more integrated than the female populations who seem have a much more significant difference.

The actual differences between the control and pre-orthognathic cases can begin to be seen by looking at the mean shapes against each other. The male pre-orthognathic cases (magenta) (Figure 6.39) tend to have a recessed nose, and a more protruding lower lip and lower chin. Interestingly, the area along either side of the nose tends to be less protruding in the pre-orthognathic cases, as is the cheek from the *alar base* around to the rear of the face. Not only is the mandible seemingly recessed, but it also tends to be lower, giving the orthognathic individual a 'longer looking' face.

The full meshes are also compared (Figure 6.39). The same differences are obviously seen, but the additional information displays significantly more about how the overall shape difference appears. The male pre-orthognathic cases have a largely recessed nasal region and longer nasal base continuing through the philtrum and upper lip. However, there is a general switch at that point on the face, giving a more protrudent lower lip and chin area, with a lower jaw line. Interestingly, the cheeks from the cheek-lip curve

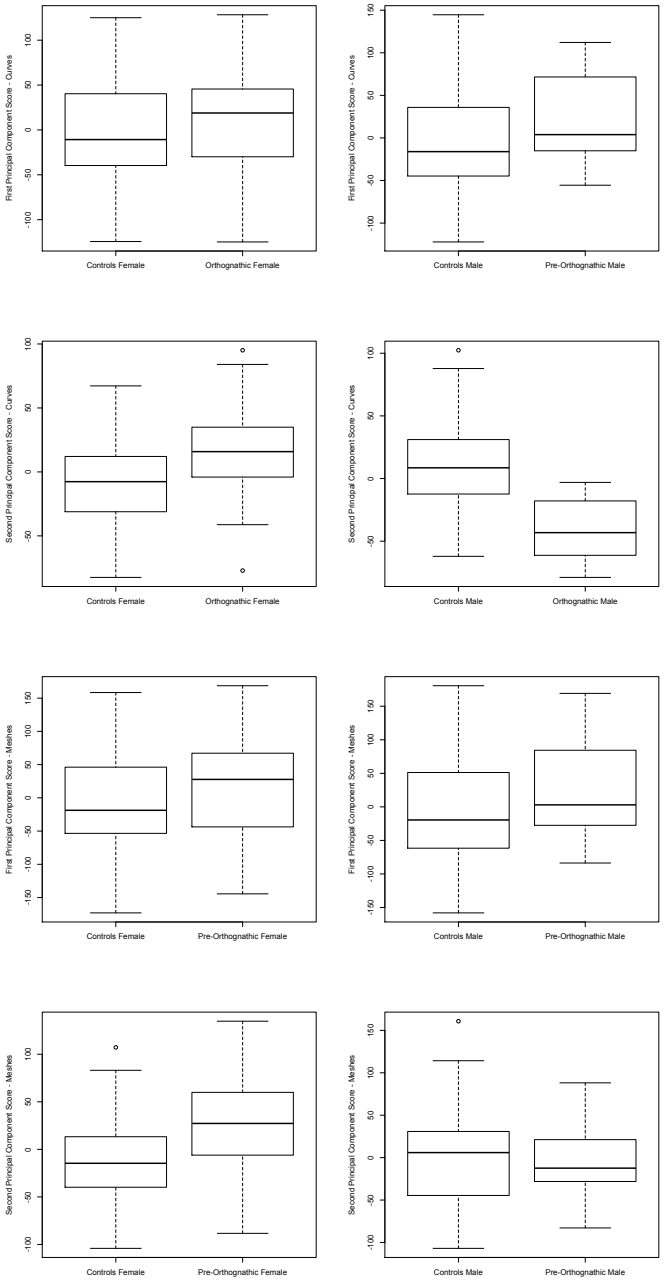

FIGURE 6.36: 1^{st} and 2^{nd} Principal Component Boxplot of Pre-pre-orthognathicOrthognathic and Control cases - Curves (top two rows) and Meshes (bottom two rows)

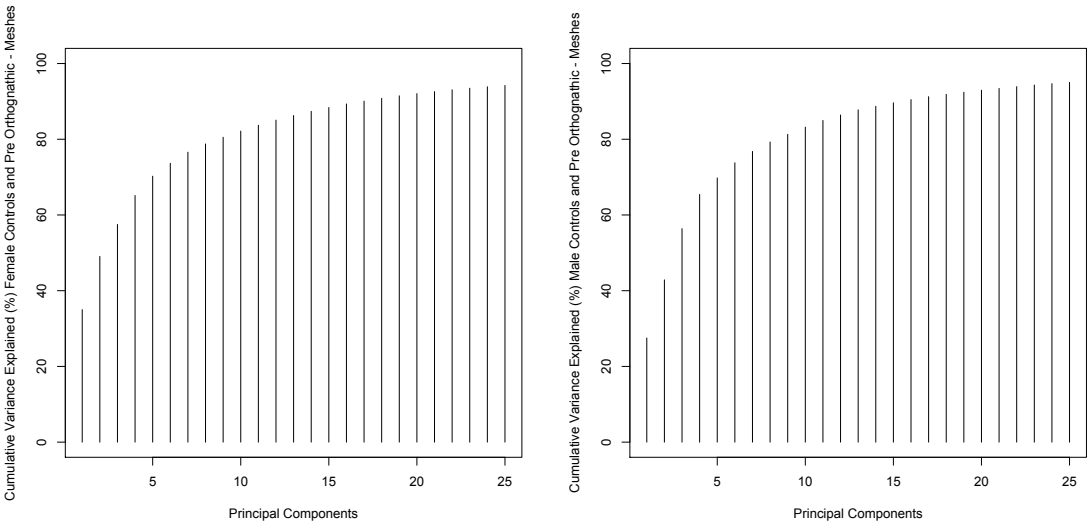

FIGURE 6.37: Cumulative Percentage of Principal Component Variance of Controls and Pre-Orthognathic cases

(*chellion* to *otobasion*) up through the face to the cheek-eye curve (*exocantion* to *tragion*) tend to be more recessed in the orthognathic cases.

The female orthognathic cases (Figure 6.40) have very similar differences to the female controls as the male population did. There is a definite recession of the nose, as well as a protrusion of the lower lip and lower chin. The area along either side of the nose shows a clear difference in protrusion, as does the cheek from the *alar base* around to the rear of the face as in the male cases. However, there does seem to be less of a difference in the mandible curve than in the male populations.

The type of surgical procedure the patients experience must be considered as the mean shape may not be fully inclusive of all information. For some patients the jaw was moved forward, some back, and some both. This could cause some discomformity when viewing the mean shapes as a method of comparing the two populations.

When viewing the full meshes (Figure 6.40), again the philtrum area as well as the nasal region shows a clear recession of the female orthognathic cases, just as in the male populations.

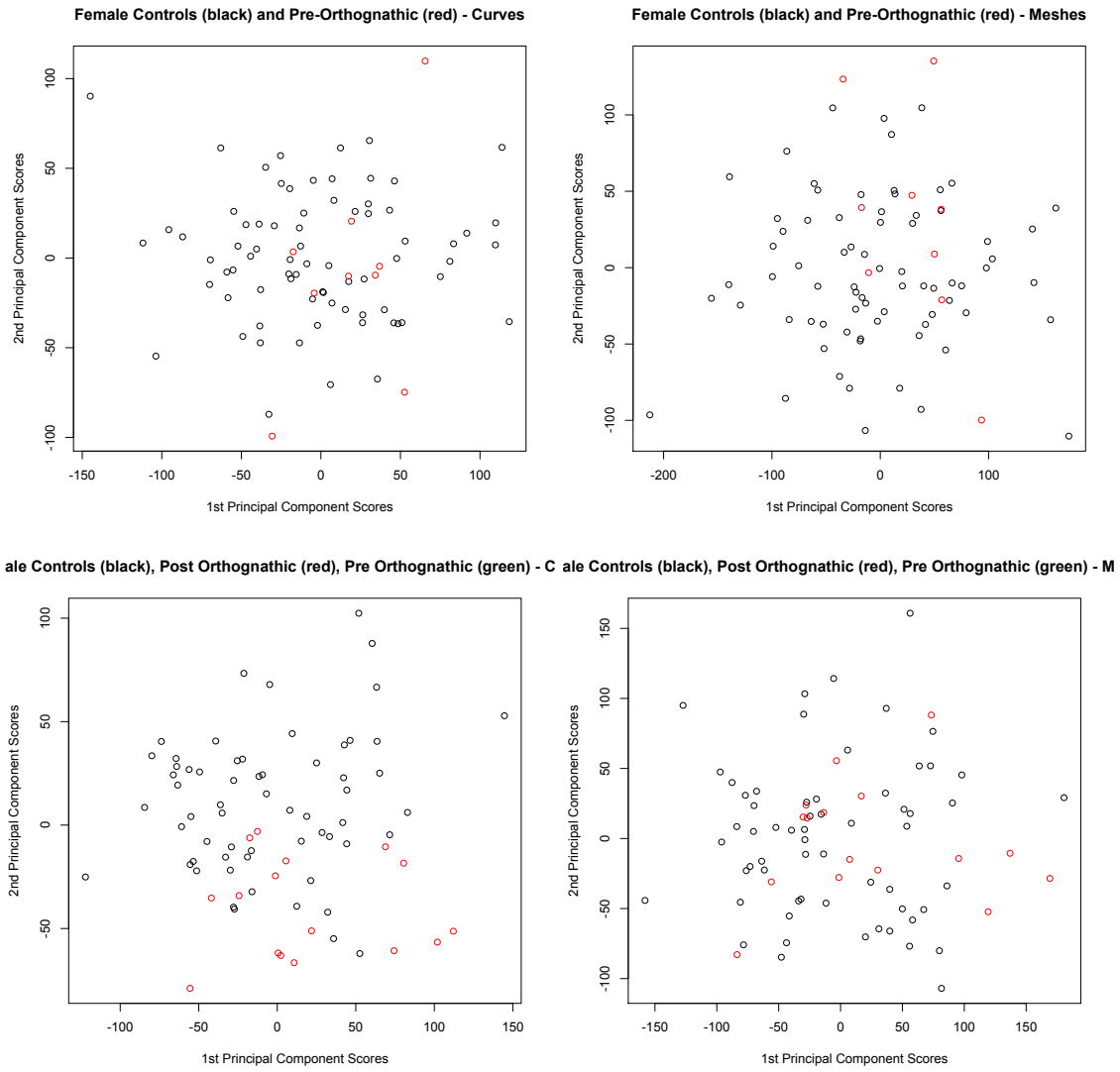

FIGURE 6.38: 1st and 2nd Principal Component Scores for Female Controls (black) and Pre-Orthognathic (red) cases - Curves (top left) and Meshes (top right) and for Male Controls (black) and Pre-Orthognathic (red) cases - Curves (bottom left) and Meshes (bottom right)

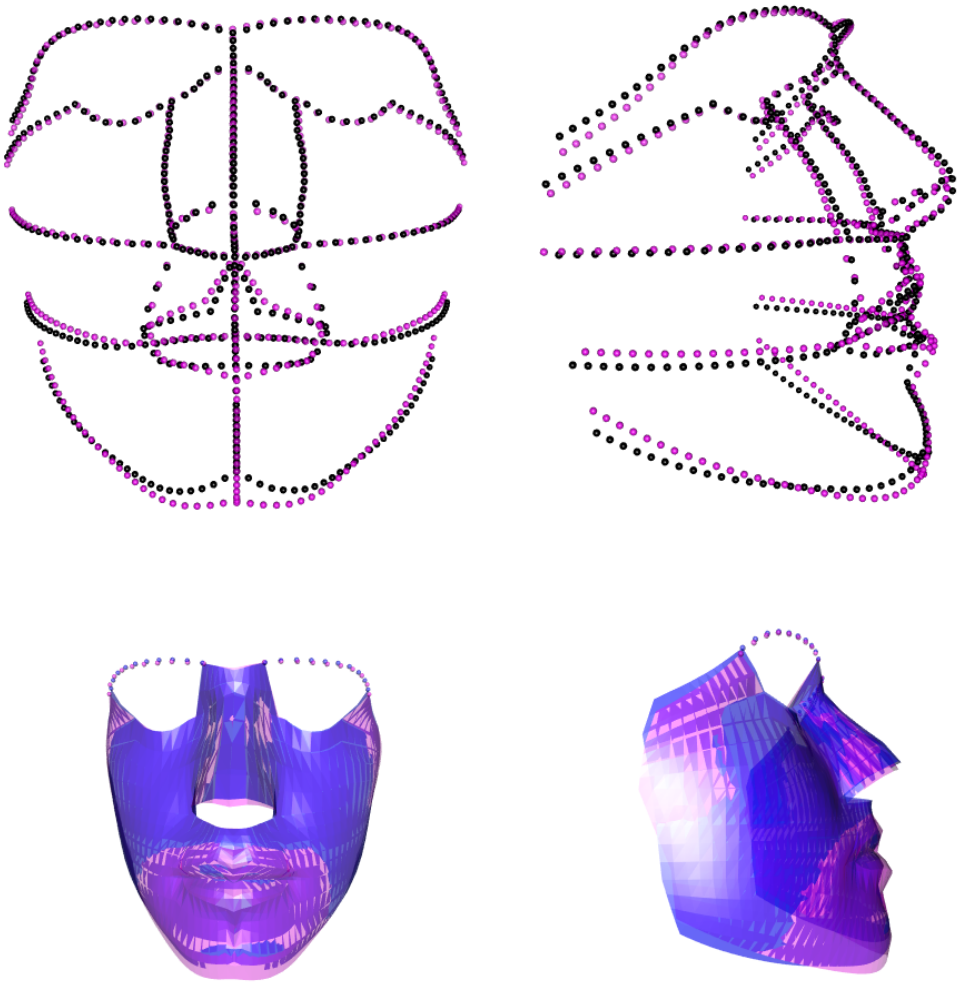

FIGURE 6.39: Mean shape of Male Controls (black) and Mean shape of Male Pre-Orthognathic cases (magenta)- Curves (top) and Rendered Mesh (bottom

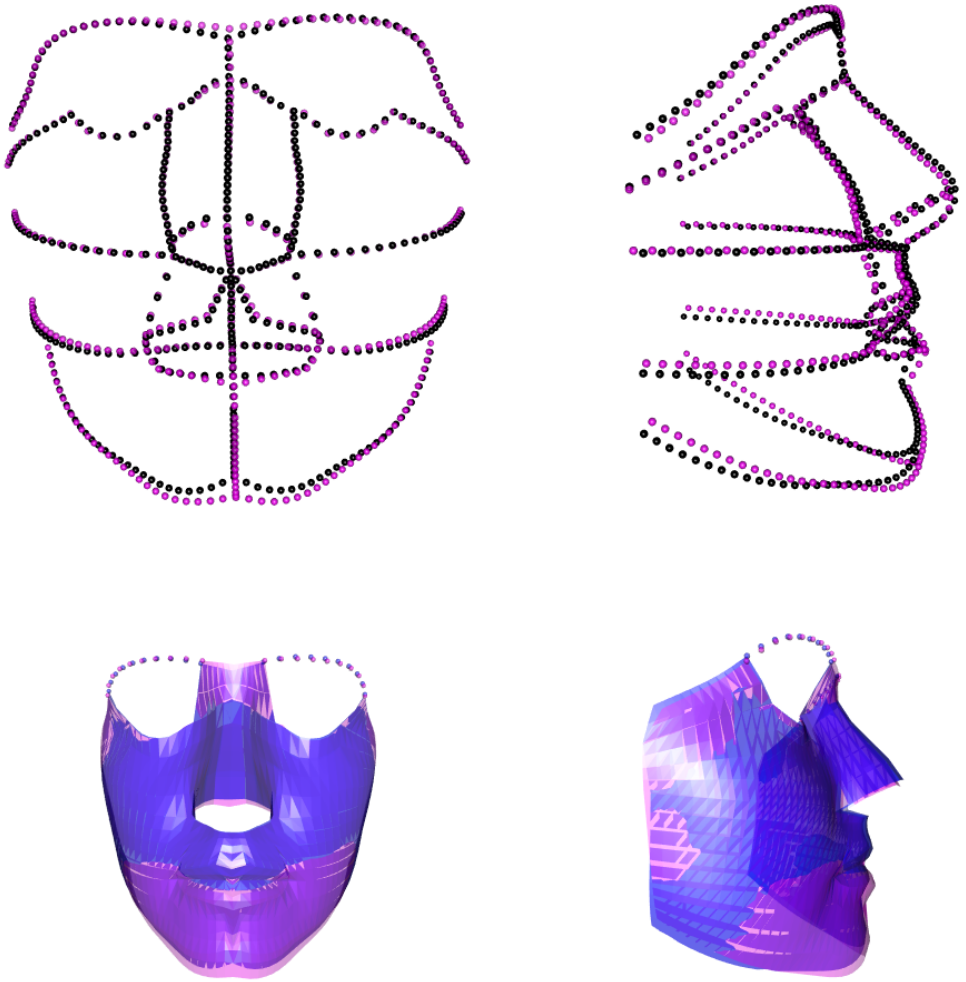

FIGURE 6.40: Mean shape of Female Controls (black) and Mean shape of Female Pre-pre-orthognathicOrthognathic cases (magenta)- Curves (top) and Rendered mesh (bottom)

6.5 Braces Intervention

Considering the number of surgical patients undergoing orthodontic bracket correction, a study is undertaken to understand potential changes in lip morphology with bracket intervention. There is not a large amount of literature available for determining the effect of brackets on facial structure; however two different analyses (one in 2D and one in 3D), both determine that there is no effect pre- and post-bracket removal. In the 2-dimensional study [Abed et al., 2009] profile photographs are taken (pre- and post-bracket removal) of 33 patients. A reference line is created between the center of the tragus and the outer canthus. Angles are then used to evaluate the prominence of the lips by way of analysis of variance (ANOVA) and t-tests for paired differences. There are no significant differences noted using this method.

In the 3-dimensional study [Eidson et al., 2012], images of 50 subjects were taken in repose and maximum intercuspation before and after bracket removal with a stereo camera. Using 6 standard anatomical landmarks (only 4 on the lips themselves), the images (pre and post) are registered (with some type of iterative closest-point algorithm) by proprietary software created by the stereocamera company. The mean landmark differences all show significant differences from 0 mm after the braces are removed; however a clinical threshold is set at 1.5mm, meaning there is no significance. There is considerable individual variability where over 50 percent of patients have greater than 1.5mm differences at the commissures. Almost 20 percent have greater differences of the lower lips. A recent study undertaken by Kim et al. [2015] uses a white light scanner to image subjects to determine any possible soft tissue changes around the lips after bracket debonding. They find no significant pre-/post-changes in either the horizontal or vertical axes of the lips; however, of the 15 soft tissue landmarks used, those in the oral commissures and the lower lip show statistically significant retrusion in the anterior-posterior axis post-debonding.

6.5.1 Method of Data Collection

In this study, 10 patients were imaged using a ©Di3D stereo camera system on the same day both pre- and post-orthodontic bracket debonding by Anas Almukhtar at the Glasgow Dental School. Each patient formerly underwent orthognathic surgery to correct for various facial deformities. All have successfully completed a combined surgical and orthodontic treatment and were at the stage of orthodontic fixed appliance debonding. A 3D photograph consent form was signed by each participant prior to image capture. The procedure was explained to the patient in detail before the first capture. In order to establish a standardised facial posture, patients were asked to gently close

the teeth together with the lips in a totally relaxed posture. They were also asked to memorise this posture and try to replicate it in the next capture session. Patients were seated in a comfortable upright position with a natural head position. The patient was asked to look straight forward at a point on the main panel at the same level as the patient's head. Three images were captured for each patient to ensure the capture of the relaxed position. The three images were then viewed on DI3D software and the best capture was considered. After the bracket debonding procedure, the patients were immediately recalled to the imaging room to perform the post-debonding imaging session. The same protocol was followed as for the pre-debonding session. The data could potentially be compromised by a skin stretching or muscle memory issue with the lips, which could potentially show a false negative in terms of significance of change. Of these patients two have open mouths; however, the results are similar to the patients with closed mouths.

6.5.2 Analysis

All patients are manually landmarked with the standard 25 landmarks and subsequent automatic curves are produced as standard. Each patient's pre- and post-debonding landmark configuration are matched using Procrustes analysis on all curves except the lips. If the images are matched on the lip curves, then the algorithm matches the lip curves as closely as possible. However, what is desired is to understand the difference in the lip curves from pre- and post-removal. No other curves should be altered between pre- and post-removal so that the Procrustes matching occurs only on non-lip affected curves. Table 6.4 below shows the root mean square distance between landmarks (i.e. all curve points) post-procrustes matching. All are within accepted levels of error in terms of landmarking correctness.

TABLE 6.4: Summary Profile - Landmarks RMSD Procrustes Matched only on Lip Landmarks (mm)

	RMSD
Patient 1	1.73
Patient 2	1.26
Patient 3	1.64
Patient 4	1.12
Patient 5	1.42
Patient 6	1.09
Patient 8	1.45
Patient 9	1.12
Patient 10	0.97

In order to compare this study with similar studies, there is an initial analysis on just the lip landmarks (not the curves). Figure 6.41 (top) shows the x,y, and z movement for each landmark, colour-coded by subject. Each configuration is oriented such that the x-direction is across the face, the y-direction is up and down, and the z-direction is coming out of the page. The *chellions* show a significant level of movement in the x direction. There does not seem to be a significant level of movement in the y and z movement. However, the curves should give a further understanding of the movement. When all lip curves are analysed there is a clear difference in the x-direction of certain landmarks; however, due to the number of semi-landmarks within the curves it is difficult to differentiate. Those curves with the largest difference are then further isolated for comparison, namely the mid-line lip (Figure 6.41 (bottom)). From the table it is clear that the mid-line lip curves have a large difference between the pre- and post-images in the x-direction. A few patients in the y-direction have large differences as well. Mid-line lip 1 is the landmark *stomium*, directly in the middle of the midline of the lip. Mid-line lip right and left 9 is the *chellion R/L* respectively. Clearly, the difference increases as the curve moves from mid-line lip 1 (stomium) to mid-line lip 9 right(chellion right) and to mid-line lip 9 left (chellion left).

A simple paired t-test is performed on the differences of the mid-line lip curve with results shown in Table 6.5. Given 2mm of potential error, the analysis illustrates a significant difference pre- and post-bracket removal with a significant decrease in x-direction lip size post bracket removal.

TABLE 6.5: Summary Profile - P-values of differences between mid-line lip semi-landmarks

(Semi-) Landmark	P-value Left	P-value Right
Chellion	0.00068	0.00072
Mid-line lip 2	0.00084	0.00041
Mid-line lip 3	0.00363	0.00134
Mid-line lip 4	0.08732	0.00092
Mid-line lip 5	0.45725	0.00102
Mid-line lip 6	0.75405	0.00074
Mid-line lip 7	0.83383	0.00209
Mid-line lip 8	0.62963	0.03762
Stomium	0.28795	0.28795

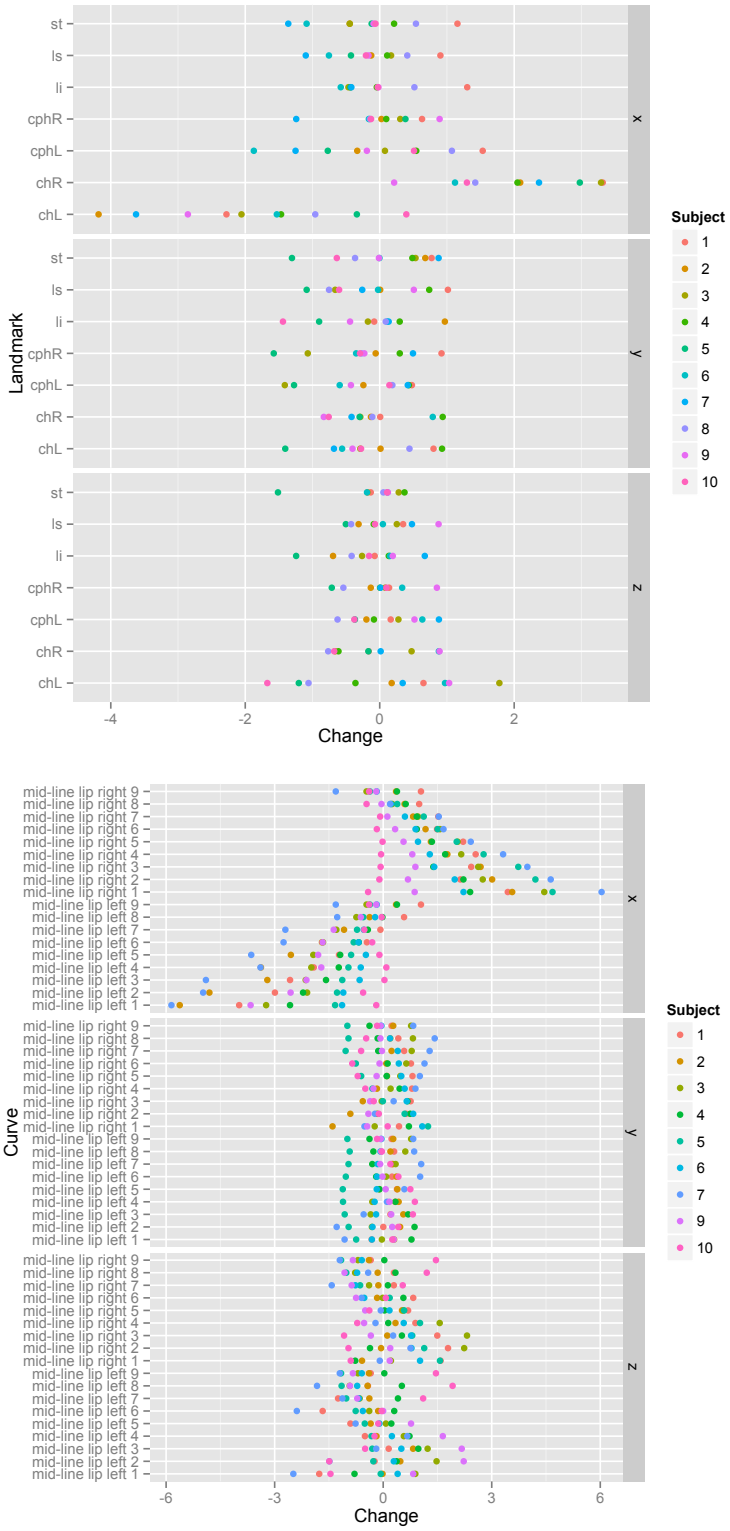

FIGURE 6.41: Changes in 7 Lip Facial Landmarks (top) and Mid-line Facial Curves (bottom)

6.6 Mussels - Environmental Evidence of Shape Change

Earlier studies show that organisms with calcium carbonate shells such as mussels, are at great risk from ocean acidification (Doney et al. [2009]), which can cause reduced calcification and growth which could potentially lead to shell dissolution (Kamenos et al. [2013]). When the structural integrity as well as shape (inability to close efficiently and effectively) is subject to change due to changing environments, there could be a gross impact on the ability of these organisms to survive. With ocean acidification and increasing climate temperatures, there are significant questions about the survivability of organisms with calcium carbonate shells to survive. This concern prompts a study in the common blue edible mussel *M. edulis* (an economically important mussel type) and the impact of rising temperatures and acidification on shell growth, thickness, shape, and durability. The mussels are collected from Loch Fyne Oysters Ltd and cultured under specific experimental conditions for 9 months with different levels of ocean acidification (550, 750, 1000 atm pCO2), as well as ambient pCO2 (380 atm pCO2). Two groups are further studied under 750 uatm and 1000 uatm but those concentrations are grown in seawater that is 2 degrees higher in temperature in order to simulate combined global climate increases in CO2 and in temperature by the year 2100.

Using statistical shape analysis, the shape change (not size, specifically) is discussed throughout the different concentrations. The stereocamera described in Chapter 1 is used to image one valve of the bivalve shell which is attached to an imaging board with a pastel coloured background. Figure 6.42 (top left) shows the 3D image of the shell and (top right) the same shell with manually place landmarks around the perimeter of the shell. These landmarks are assigned where the ridge meets the perimeter of the shell and approximately halfway in between those two locations. The aim is to find the ridge and perimeter of the mussel. The shape index of the mussel (Figure 6.42, middle left) is coloured topographically, as is the ridge curvature values (middle middle) and the perimeter curvature values (middle right). The same algorithm of curve identification, both the ridge and perimeter of the mussel are found. These two curves pass through the areas of greatest curvature (negative and positive respectively) of the mussel surface. These curves are shown (bottom left) as well as the fully rendered 'mask' or 3-Dimensional surface representation, of the mussel (bottom right) done by regular triangulation between the automatically identified curves and intermediary curves. This process is replicated for every mussel (six experimental groups with four mussels per group) and then used to compared their shapes.

The ridges and perimeters are now examined to determine if there is any significant different between the two shapes. A Generalised Procrustes analysis is applied, with a scaling adjustment for size in order to compare the shape, not size, which matches the

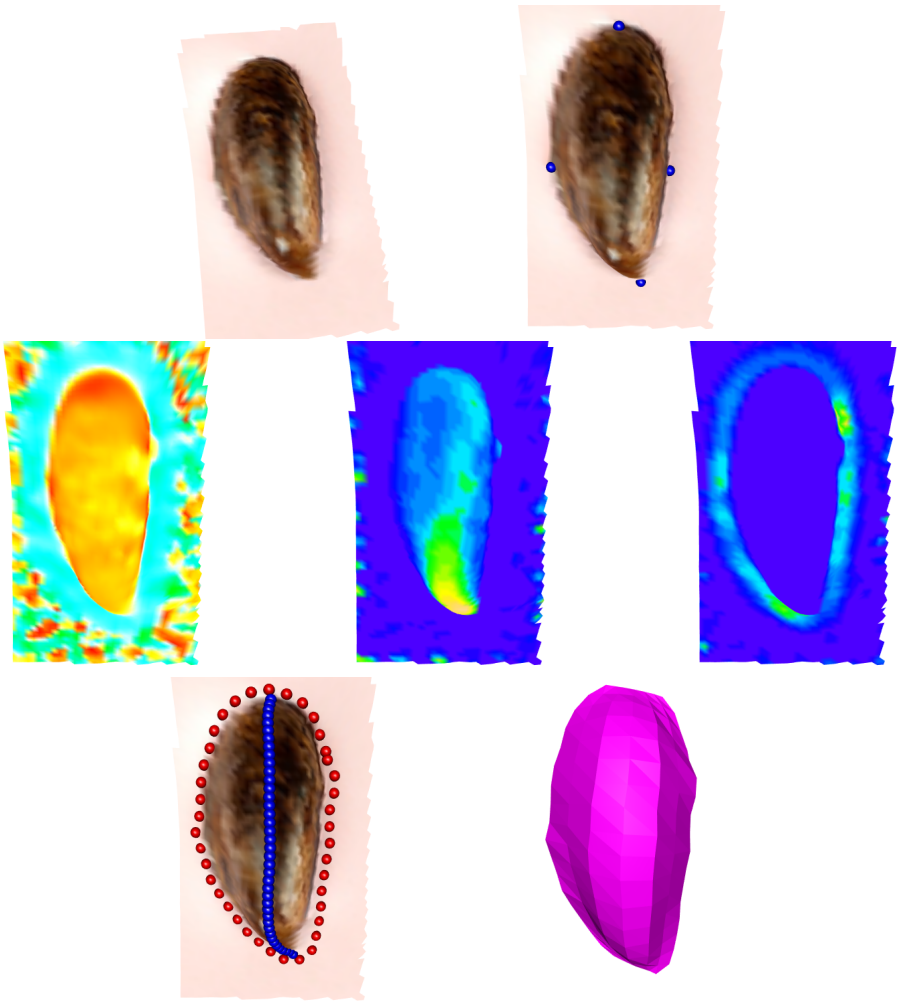

FIGURE 6.42: Locating Mussels Ridge and Perimeters - 3D image of Mussel (top left), Manual Landmarks (top right), Shape Index of Mussel (middle left), Ridge Curvature Values (middle), Perimeter Curvature Values (middle right), Ridge and Perimeter (bottom left), Rendered Mesh of Mussel (bottom right)

curves to each other. This means that all curves are in the same shape space, allowing a more abundant analysis.

Visually, (Figure 6.43) there is no discernible difference between the curves, either ridges or perimeters. Note that the curves are coloured topographically by CO2 concentration (380 uatm - dark blue, 550 uatm - light blue, 750 uatm - green, 750 uatm + 2C - yellow, 1000 uatm - orange, 1000 + 2C -red).

For further investigation, a Principal Components Analysis (PCA) is performed in order to evaluate the differences and variations between the ridges, perimeters and meshes of the populations of mussels grown under experimental conditions (380, 500, 750, 1000 atm pCO2, 750 and 1000 atm pCO2 + 2C). Figure 6.44 shows very little discernible difference between the concentrations except in the 3^{rd} principal component of the meshes and the 2^{nd} principal component of the perimeters. The former has to do with a rise and fall of

the ridge of the mussel, yet only accounts for 6 percent of the variation; however, the p-value is significant at 0.020. This suggests that as the concentration increases, the strength of the ridge of the mussel decreases, i.e. flattens out. The perimeter tends to become more circular as the CO2 concentration increases. At a lower level concentration the perimeter is very ellipsoidal in shape and spreads as the concentration increases with a significant p-value of 0.021.

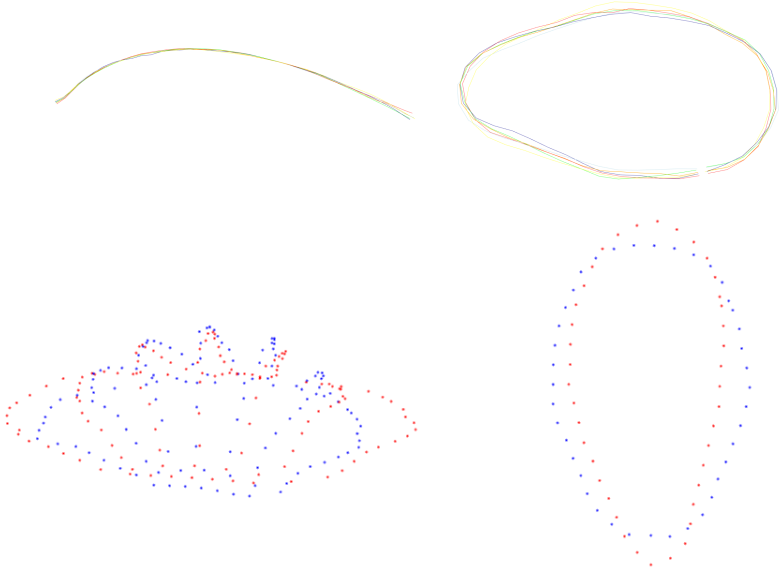

FIGURE 6.43: Mean of Ridges (top left) and Perimeter (top right) Extremes of Mesh 3^{rd} principal component (bottom left) and Extremes of Perimeter 2^{nd} principal component (bottom right)

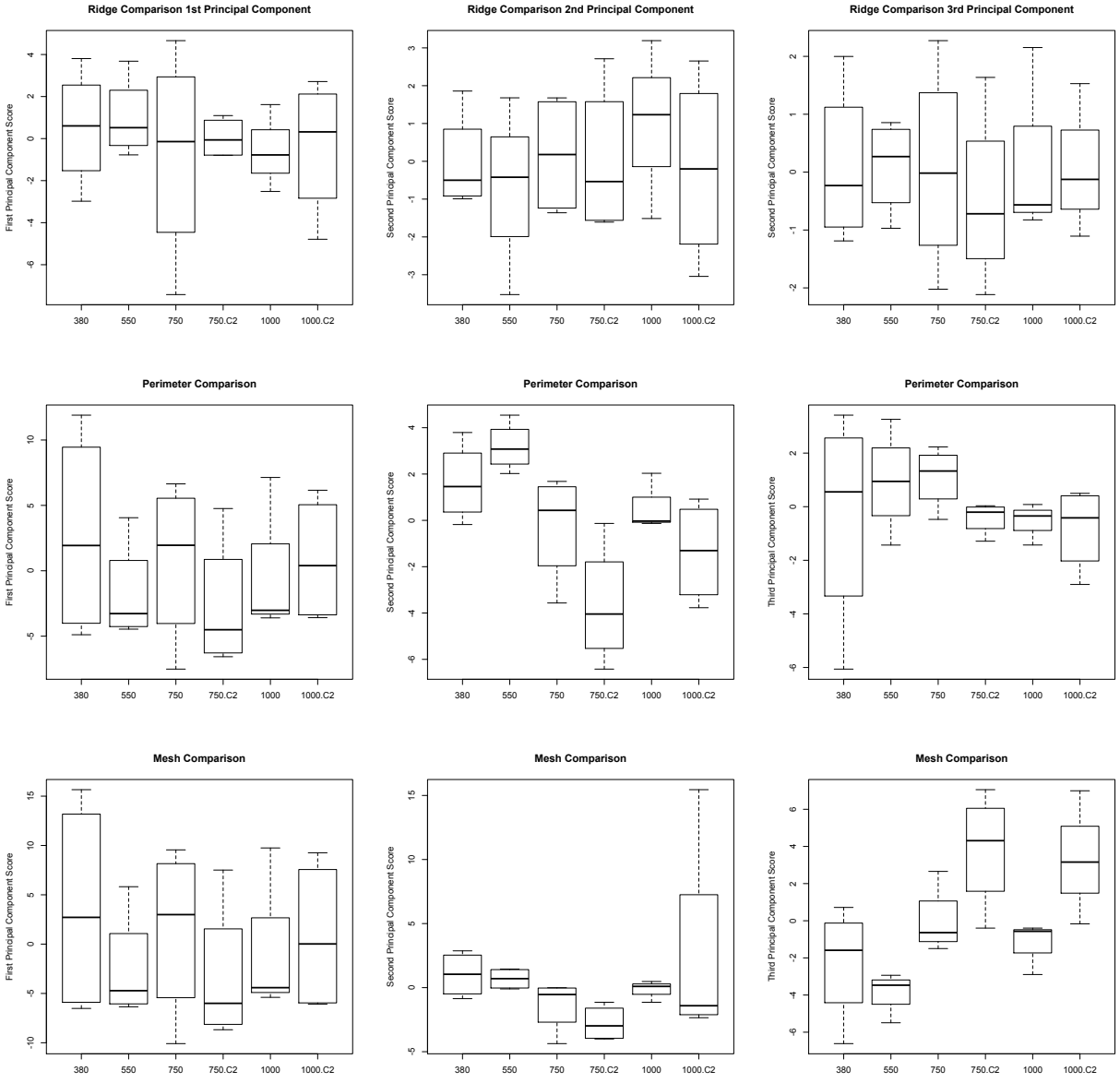

FIGURE 6.44: Box Plots of Principal Components - Ridges (top), Perimeters (middle), Mesh (bottom) [1^{st} principal component (left), 2^{nd} principal component (middle), 3^{rd} principal component (right)]

A regression analysis determines if an increase in C02 concentration changes the shape of the mussel (Figure 6.45). The shaded area represents a region of no change. If the line stays within the boundary of the shaded area, then there is no significant change between the mussel concentrations. The overall p-value for the ridges is 0.835; perimeter 0.107; and the meshes 0.288 showing no significant change. The only discernible difference is the 3^{rd} principal component of the mesh analysis and the 2^{nd} principal component of the perimeter, as discussed previously.

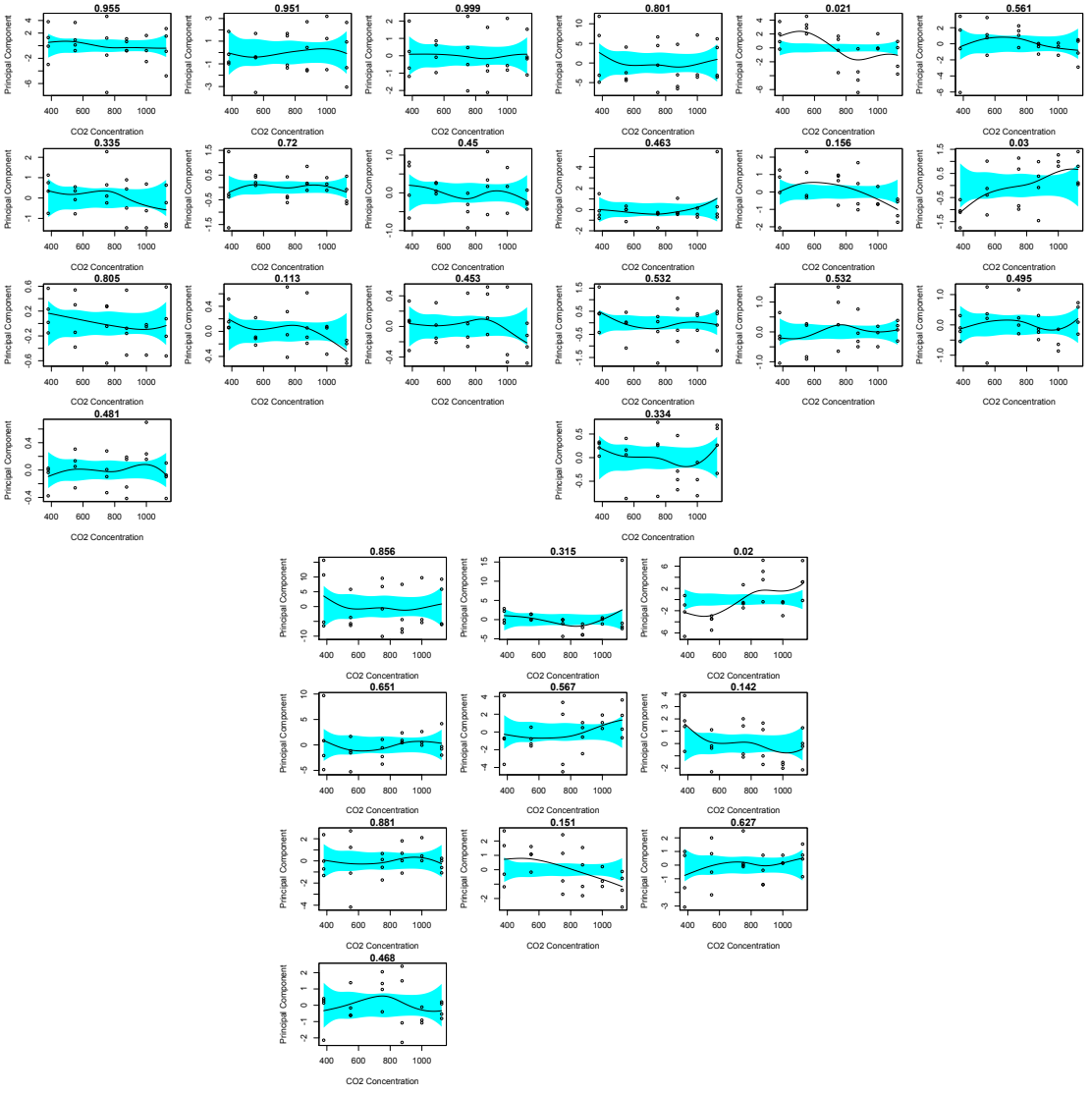

FIGURE 6.45: Regression Analysis on CO2 concentration against Shape Change - Ridges (top left), Perimeters (top right), Mesh (bottom)

The other area of interest on the mussel, beside the ridge, perimeter, and mask, is the splay of the lip of the mussel, or how much the lip is 'turned upwards' instead of tightly sealed downwards. In order to examine this relatively small section of the ridge, a General Procrustes Analysis is carried out, but only matching on about 90 percent of the ridge (leaving the area that could be splayed out of the matching process). The matching process aligns the curves, which can sometimes hide changes like splay. Figure 6.46 (top left) shows the curves matched, allowing for splay. Clearly, there is a difference in the end lines of the curves. The best way to understand the change in these curves, at the lip of the mussel, is to examine the gradients. Table 6.6 shows a possible difference between the gradients in the z direction (that is the up and down movement of the curve at the lip of the mussel). Performing a regression analysis on the concentrations versus the splay in the x, y, and z directions shows no clear evidence of change in the z direction as pCO2 increases, but certainly some indication of it (Figure 6.46).

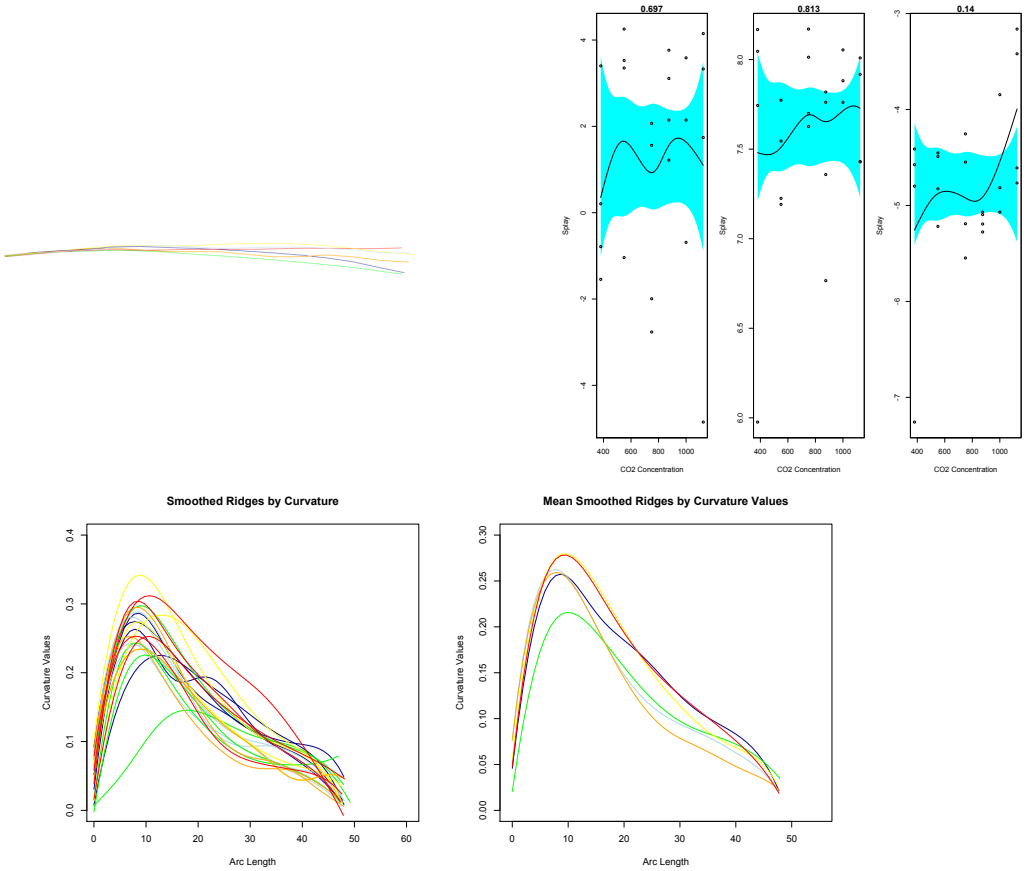

FIGURE 6.46: Splay Analysis - Mean ridge splay in 3D (top left), Regression Splay (top right- x, y, z directions), 2d arc length and plots (bottom)

Overall, there is no clear evidence that as the concentration of pCO2 increases (and temperature as well), that the gradient becomes less steep, i.e. the mussel shell does not close as sharply. However, if the indication is true, which would potentially be seen in a larger sample size, this could lead to inadequacies with the shells closing properly or

TABLE 6.6: Summary Profile - Z-direction Gradients of Splay

C02 concentration	380	550	750	750+2C	1000	1000+2C
	-4.25	-4.40	-5.12	-4.76	-4.64	- 3.32
	-4.04	-4.17	-4.66	- 4.86	- 3.48	- 4.28
	-4.43	-4.15	-4.24	- 4.67	- 4.43	-3.10
	-6.63	-4.84	-3.95	-4.64		-4.21

sealing tightly. Shell edge separation during low tide in tidal estuarine habitats cause difficulty for desiccation since a looser seal can allow air to enter the shell. However, there is evidence of significant differences with increasing pCO2 in the 3^{rd} principal component of the rendered mussel shell mesh ($p = 0.020$) and in the 2^{nd} component of mussel shell perimeters ($p = 0.021$). The significant difference in the 3^{rd} components of the rendered mussel surfaces is due to a rise and fall of the mussel shell ridge, suggesting that the intensity of the mussel shell ridge decreases or flattens out with increasing pCO2. The 2^{nd} component of the mussel shell perimeter describes a distinct trend toward becoming rounded as the pCO2 increases as compared to a more elliptical shape in ambient conditions (380 μatm pCO2). Morphological shell disparities, like this, could be due to predator cues as a type of defensive mechanism. Considering the shells tend to become more circular and flatter could suggest that the mussels grown under ocean acidification and increasing temperature alter shape to compensate for reductions in shell thickness for survival (Fitzer et al. [2015]). According to Brönmark et al. [2011], a more circular and rounder shell has been found to reduce predator efficiency.

6.7 Analysis Conclusions and Further Discussion

As shown, the method and tools discussed in Chapters 4, 5 can be applied to many different aspects of shape. Whether it be control populations as compared to post-surgical patients (orthognathic surgery or otherwise), as well as pre- and post-surgical outcome patients, the methods of facial shape description are very reliable. Clearly, these methods work on other shape objects such as the mussel population in Section 6.6. Objects that have clear curvature information in the form of ridges and valleys can be robustly explained and defined by this curvature information.

The orthognathic analysis yielded many further questions and potential areas of future work. It is difficult to say anything definitive or precise about the differences in facial shape, but it certainly raised many thoughts about the process of surgical intervention and potential methods that could be used to improve it. The lack of patient numbers created significant difficulty in making determined conclusions. Potentially more data

will be available in the future and then the same analysis could be completed on that augmented group in order to yield further results.

The braces intervention analysis had an extreme limitation due to sample size. With only 10 patients, there are very little results that can be concluded unequivocally. The same limitation apply in the mussel study. Using only four samples per experiment group in a principal components analysis is not fully appropriate. Not all methods developed in Chapter 5 are used in these analyses due to constraints on the design. This data was given as is, these experiments were not designed for perfect conditions.

The main objective of this thesis is to take a 3D facial image and develop a novel method of characterising it and forming it into an analysable dataset. This was clearly accomplished and these case studies give rise to interesting questions about future work that could be undertaken.

Chapter 7 gives a novel proof of principle of the final manual piece of the methodology discussed in Chapter 4. With a reliable system of quantifying facial shape, the last manual aspect is the initial manual landmarking of the 23 anatomical points. If this process could be automated, then the process from receiving the camera image, to the analysis would be complete.

Chapter 7

Bayesian Methods for the Identification of Landmarks

7.1 Introduction

Bayesian Methods have become very popular in 3-dimensional facial recognition. Prior information is readily available for facial images. Human recognition knows what facial shape is basically composed of; where the nose is relative to the lips, the ears relative to the eyes, etc. Bayesian methods are also used to reconstruct 3-dimensional shapes from 2-dimensional images. Han and Zhu [2003] exploit the concept that human vision can extrapolate 3-dimensional shape from a single 2-dimensional image whereby the occluded parts are filled in by prior human visual knowledge. This prior knowledge is represented by probabilistic models built on a graph representation for a single object and the second model built on the relation graphs of all objects in the scene. Given this use of a Bayesian framework for 3-dimensional facial image work, using the prior information given by a database of facial images to predict landmark and curve placement for a new facial image follows. An initial investigation into a Bayesian framework for curve identification uses a Bayesian process of choosing the smoothing parameter as implemented in the 2-dimensional aspect of the algorithm (Chapter 4).

7.2 Choosing A Smoothing Parameter

Recall that within the curve identification algorithm, a step occurs where the reference curve path on the surface is taken from 3D into 2D for the smoothing process (Figure 7.1). Currently, experimentation with different curves sets a fixed smoothing parameter,

but a new Bayesian method is investigated to determine the optimal level of smoothing for each curve on each individual face. The posterior of this smoothing parameter λ can be derived as shown in Evers et al. [2014]. This gives an optimal level of smoothing for each individually located curve on each individual facial image. The process is also computationally efficient, which is shown below.

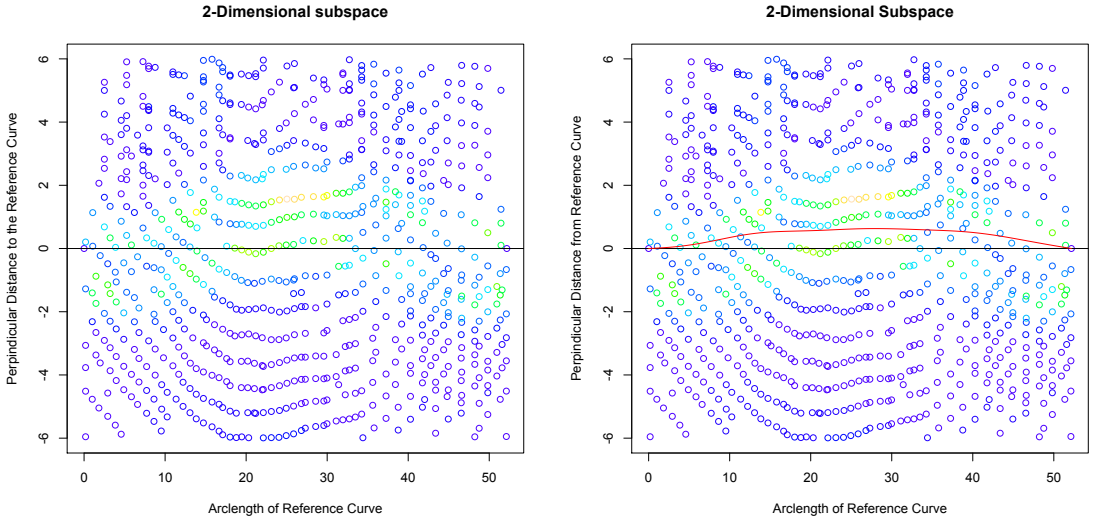

FIGURE 7.1: 2D mid-line lip plot with the reference curve (black) and the non-optimal smoothed curve (red)

Recall the model $Y = B\alpha + \epsilon$ where B is the design matrix, α the parameters, Y the responses, and ϵ the error $N(0, \sigma^2 I_n)$. Fit the above model ($Y|\alpha, \sigma^2, \lambda \sim N(B\alpha, \sigma^2 I_n)$) using Eilers and Marx [1996]'s P-splines. A P-spline is a 'penalised B-spline' using the B-spline representation where the coefficients are determined by both the data to be fitted and by a penalty function that aims to impose smoothing. Eilers and Marx [1996] penalties proposal based on finite differences

$$S(x) = \sum_{i-1}^{m} \left(y_i - \sum_{j=1}^{n} \hat{\alpha_j} B_j(x) \right)^2 + \lambda \sum_{j=k+1}^{n} \left(\delta^k \hat{\alpha_j} \right)^2$$

can be written as

$$\|y - B\alpha\|^2 + \lambda \|D^\alpha\|^2.$$

P-splines now choose the value of α such that

$$min_\alpha \left[\|Y - \beta\alpha\|^2 + \lambda \|D\alpha\|^2 \right].$$

From a Bayesian perspective, this is equivalent to the assumption of a normal prior for α with a covariance matrix $(D^TD)^{-1}$. Going further and including a prior distribution for σ^2 and λ, a natural choice is $\alpha, \sigma^2|\lambda \sim NIG(0, \lambda(D^TD)^{-1}, a, b)$ and $\lambda \sim f(\lambda) \sim 1$

The posterior distribution on the penalty parameter λ from Evers et al. [2014] can be shown to be

$$f_{M_\lambda|Y} \propto \lambda^{\text{rank}\frac{(D^TD)}{2}} \frac{|B^TB + \lambda D^TD|^{\frac{-1}{2}}}{\{2b + y^T\left[I_n - B(B^TB + \lambda D^TD)^{-1}B^T\right]y\}^{a+\frac{n}{2}}} f^{\text{prior}}_{M_\lambda}.$$

A key part of this is

$$\hat{\alpha} = (B^TB + \lambda D^TD)^{-1}B^Ty, \tag{7.1}$$

where the trace of matrix $B(B^TB + \lambda D^TD)^{-1}B^T$ which creates the fitted values from data y is the effective degrees of freedom. Computation efficiency is an integral part of this smoothing solution. The penalised least-squares estimator and the determinant must be recomputed for ever value of λ. Detailed in Evers et al. [2014], the problem is rewritten in such a way that the involved linear algebra operations are performed independently of λ, giving a much more computationally efficient procedure.

The weights (curvature values at every describing point) must be accounted for in this smoothing process. The weights are simply added into the B-spline basis such that B^TB is $B^T\Sigma B$, where Σ is a diagonal matrix constructed from the vector of curvature values. Figure 7.2 shows the smooth path based upon a set degree of smoothness and the same path based upon an optimal level of smoothing. Lastly, the fixed points (manually marked landmarks) must be accounted for in the B-spline design in terms of fixing the ends of the smoothed path. The first method to do this is by simply assigning a very large weight value to the fixed points. Another approach is to find the optimal degree of smoothing and use that at the set constraint in the previously discussed 2-dimensional smoothing process. Initial testing using this algorithm shows that the original estimate of approximately 4 degrees of freedom during the smoothing process was a suitable choice.

7.3 Bayesian Methods - Automatic Landmarks

Automatic landmarking is a highly attractive method of characterising facial shape due to the high level of human error associated with manual landmarking, as well as the time involved. There is a significant amount of work on the question of automatically landmarking 2D images, but not nearly as much on landmarking 3D images. As discussed

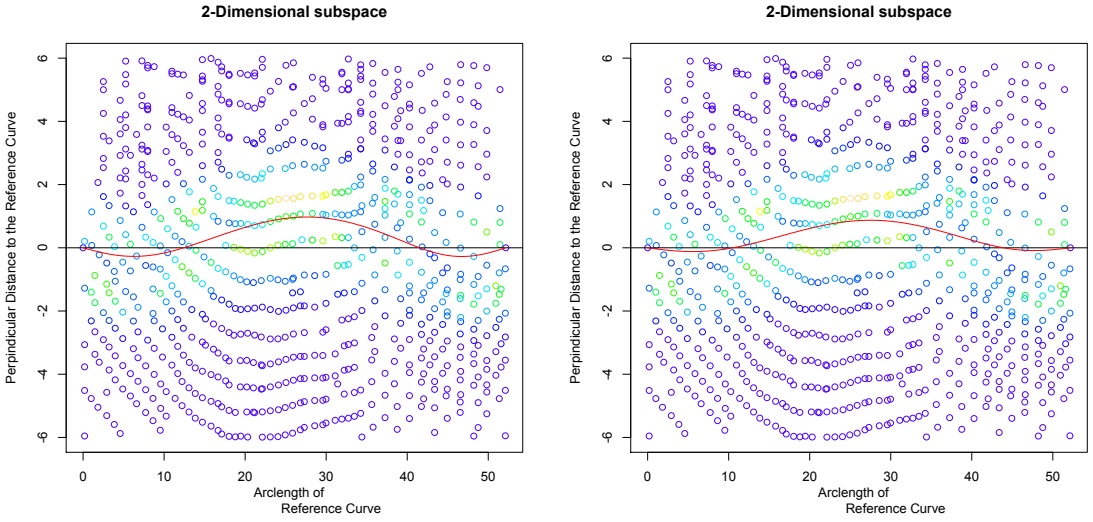

FIGURE 7.2: Set degree of smoothness (5) curve in 2D (left) and Optimal degree of smoothness (4.2) curve (right)

previously one of the most common methods is registering the facial shape to a template [Irfanoglu et al., 2004]. Colbry et al. [2005] register facial landmarks using a 2.5D image (a simplistic representation of a 3D image where there exists at most one height point (z), for any point in the $x - y$ plane). Using a frontal image based approach, the nose tip is determined (*pronasale*) by choosing the point on the face closest to the camera system. A simple model is created using the Euclidean distances from the *pronasale* to other landmark areas (from about 1000 scans) giving 'bounding boxes' in which the model states that a landmark must lie. After calculating the shape index at every point (since it is invariant to orientation), that information is used to pinpoint the area of maximal curvature within the bounding box. Sukno et al. [2014] created a method for automatic landmarking that integrates non-rigid deformation with the ability to handle missing points. Using a flexible shape model, a set of candidate points is generated from a feature detecting system and then a combinatorial approach is performed.

The concept of Bayesian methods in automatic landmarking and curve detection creates a clear avenue toward creating a fully automatic process that is quite stable and potentially more informative. If there could be a method to take the manually marked landmarks or curves that have already been painstakingly produced and use that information to create a prior distribution, it would be possible to use a Bayesian framework for landmark/curve prediction. Proposed in this thesis is a proof of concept exploration. This concept is not yet a fully robust method of automatically landmarking a facial image.

In the absolute sense, this Bayesian framework would allow for the creation of a prior for all landmarks of interest simultaneously, a likelihood for all landmarks simultaneously,

and then choose the landmark positions simultaneously that would maximise this global posterior. However, this would be a highly multivariate problem and quite difficult to solve. Therefore, the proof of concept explored here begins by looking at how a Bayesian framework could be utilised for four initial landmarks, the *pronasale* (tip of the nose), *sellion* (valley between the eyes), and *endocathion L/R* (inner corners of the eyes).

7.3.1 Initial Identification Method and Likelihood

Starting with a facial image, with no information other than the mesh points, it is not straightforward as to how an initial estimate of any landmarks could be placed. Therefore, an initial orientation must be made on the facial image in order to achieve this first estimate. The landmark that has the most readily available and easily discernible information assigned to it is the *pronasale*, which can also be determined as the most prominent feature on the face. If the facial image is oriented in the z-direction (assuming the x-axis is from ear to ear, the y-axis from forehead to chin, and the z-axis from the back of the head to the front) then the sum of the surface normals in the z-direction should be at a maximum. Once this is maximised, it is necessary to ensure that the face is approximately vertical in the x-y plane i.e. an optimisation step over the rotation angle around the z-axis must occur. A set of horizontal strips are created across the face and the most prominent points in the z-direction are found across these strips such that the standard deviation in the x-direction is the set of nearest points of the strip, which is then minimised, giving a face that is very nearly looking straight ahead (Figure 7.4 top).

Once the facial image has been oriented, an initial estimation of the landmarks can be made. The surface area around an estimated landmark has intrinsic curvature information at any point that is calculated by fitting a quadratic patch to the neighbourhood (Chapter 4). The algorithm begins by colouring the area of interest by shape index (a ratio of the principal curvatures). The shape index threshold is determined by the landmark of interest (cap, saddle point, and bowl respectively). The Gaussian curvature is calculated (product of the principal curvatures) and then a quadratic patch is fit to every possible candidate landmark in the thresholded area, which then allows for an evaluation of the residual sum of squares at every point using simply point to point distance with the assumption of an isotropic quadratic. This process is, in fact, finding a likelihood for the landmarks.

In particular, assume that the data X is the mesh which is simply the Euclidean distances between the points along the mesh that defines the connectivity of the mesh points. As a type of re-parametrisation of the mesh information, the full surface can be described

together by shape index (a ratio of the principal curvatures) and the gaussian curvature (the product of the principal curvatures). The landmark θ is the point with the correct shape index and strongest gaussian curvature which lies on the surface of the mesh. This means that the model for observed gaussian curvatures is

$$GC = \alpha + \beta d_i^2 + \epsilon,$$

a simple quadratic fit around the landmark point θ where d_i is based upon the Euclidean distance from the mesh point to the observed landmark point θ such that $d_i^2 = (m_{i1} - \theta)^2$. This model generates a likelihood based upon the residual sum of squares such that

$$SS(\theta, \alpha, \beta) = exp^{\frac{-1}{2}\sigma^2 \sum_{i \in N} [GC_i - \alpha - \beta (m_i - \theta)^2]^2} \tag{7.2}$$

where N is the neighbourhood of interest, GC_i is the observed gaussian curvature, and the error is some correlated process, but it is assumed to be normal and can be ignored.

Figure 7.3 shows the surface of 5 different landmarks coloured topographically by the residual sum of squares given a quadratic fit. It is clear that the minimum residual sum of squares is where the manual landmark has been placed (and is also the location of the greatest curvature).

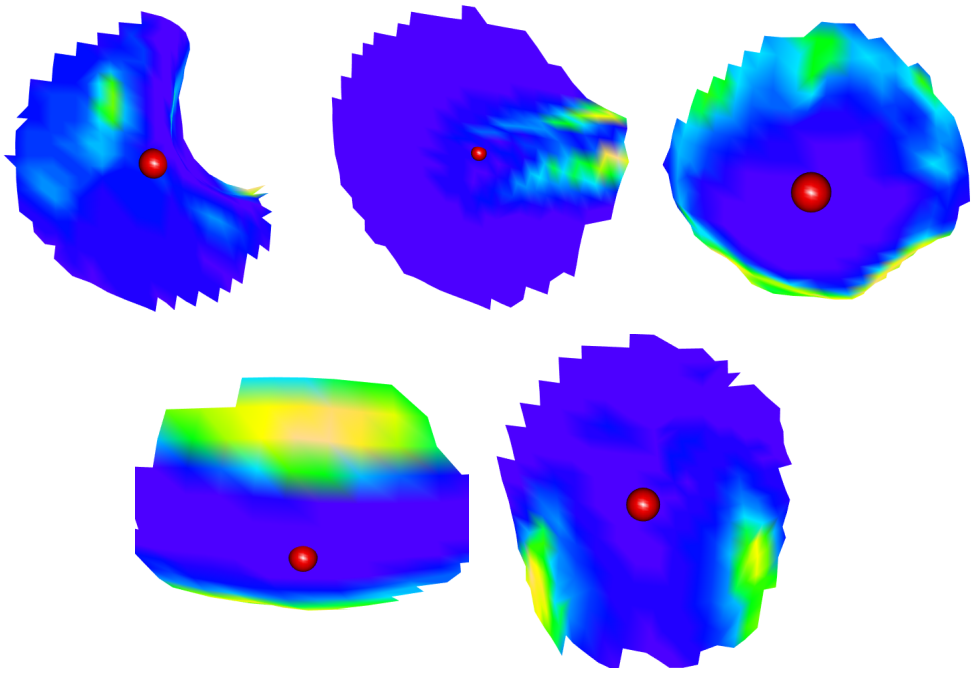

FIGURE 7.3: Residual Sum of Squares of the quadratic patch fit coloured topographically *alare crest*, *chellion*, *pronasale*, *labiale superius*, and *sellion*, respectively

This concept is used for the initial estimate of the *pronasale*. The shape index and curvature values of the most prominent z-direction of the oriented face is calculated

(Figure 7.4 bottom left). This surface is then thresholded by a shape index of 0.75, as that is a non-strict shape index value for a cap, and an initial landmark estimate is made at the minimum residual sum of squares location (Figure 7.4 bottom right).

FIGURE 7.4: Orienting the face (top) and locating the initial estimate of the *pronasale* by taking the shape index, curvature values, thresholded by shape index, and residual sum of squares respectively.

The algorithm then must find an initial estimate for the three other landmarks. The shape index is calculated on the surface a set amount away from the *pronasale* where the *R/L exocanthion* (inner corners of the eye) are located. The same process is used for finding these landmarks as was for the *pronasale*. Lastly, a planepath is drawn between the *endocanthion* and the point with a minimum residual sum of squares is labelled as the *sellion*. This produces four landmarks that are then used for orientation with the Procrustes registered, manually landmarked images (the prior information).

Using this method the initial four landmarks are found and the likelihood of the landmark location is defined. Figure 7.5 shows the patch of each landmark and the new chosen landmark based upon fitting the above quadratic model. However, there is a significant amount of prior information that now can be included.

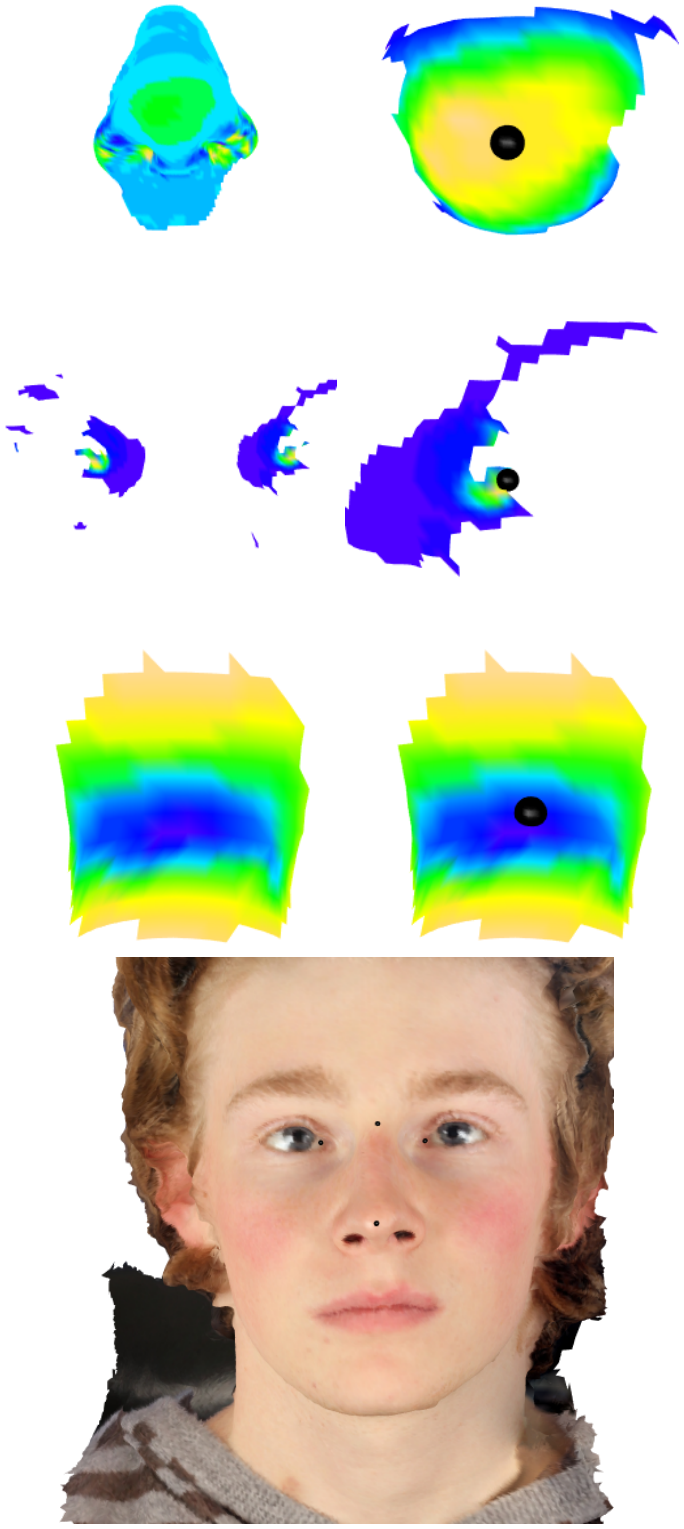

FIGURE 7.5: Initial Identification Algorithm for 4 set landmarks (*pronasale*, *endocathion L/R*, *sellion*, respectively) with the initial minimum sum of squares (L) and new landmark identification (R) and the final set (bottom)

7.3.2 Prior information addition

The entire concept of using a Bayesian framework for this identification process is that there exists a set of control facial images containing landmark configurations of k landmarks in three dimensions. This data can be approximated well by a multivariate normal distribution $N_{3k}(\mu, \Sigma)$ whereby a Procrustes registration forces the centroid to be at the origin and oriented correctly. Surprisingly, this distribution has significantly less variance than one would imagine as faces are generally more similar than expected. Figure 7.6 (left) shows 150 cases of landmark configurations after Procrustes matching and the confidence ellipsoids of the matching of this prior distribution onto a facial image with the four initial landmarks.

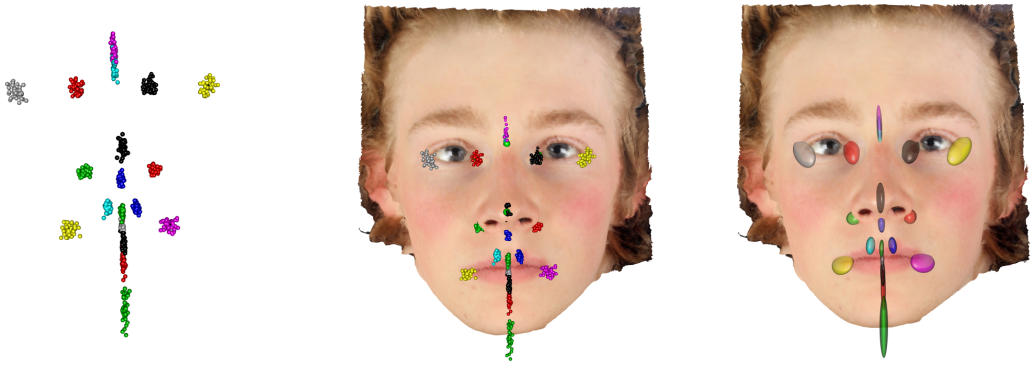

FIGURE 7.6: Prior information (left) and prior distribution translated onto an example face

This illustrates a clear prior on the landmark θ from previously collected and manually marked faces that is multivariate normal. However, the prior on the two parameters α, β from Equation 7.2 is not as clear. There are three methods by which to describe the prior on these parameters. First, an empirical bayesian estimate can be performed that simply fixes or 'plugs in' the estimates giving a uniform prior. Second, since the model is quadratic in terms of α, β, the parameters could be integrated out, requiring a flat prior. Lastly, the priors on the parameters could be recreated from the manually collected landmarks to create an informative or true prior which describes the distribution of the parameters across individuals.

The simplest method is to maximise $SS(\theta, \alpha, \beta)$ w.r.t. the parameters α, β with a flat prior giving θ numerically. Therefore with a flat prior on the parameters and an independent gaussian prior on θ, the posterior simply becomes

$$\min\theta[\frac{-1}{2\sigma^2}\sum_{i\in N}[GC_i - \hat{\alpha} - \hat{\beta}(m_i - \theta)^2 + \log p(\theta)]]$$

The σ term in the minimisation equation constitutes the 'weighting factor' or 'trade-off' between the prior and the likelihood and this must be discussed. There are two methods by which to handle these terms. First, it can be integrated out with some prior Γ. Second, given that there is an estimate of σ from the simple least squares fit, the estimate can itself be used. With experimentation, it was shown that changing the fixed σ term has little practical effect on the minimisation process.

Lastly, the question arises of how to simultaneously minimise over all the landmarks. The prior is on all landmarks but the minimisation is most easily handled on a single landmark conditional on the others. In order to optimise over all landmark simultaneously without creating an enormous optimisation problem, or losing the conditionality, an iterative strategy is taken by systematically minimising over each landmark and Procrustes re-registering to the prior mean after each minimisation iteration for every landmark.

To construct the prior for the four set landmarks, a conditional distribution $p(x_i, x_{-i})$ must be used in order to sequentially determine the conditional prior of each landmark, separately. Here x_i denotes the set of landmarks omitting x_i

Using the notation of Billingsley [2008], given X_1 to be one of the four set landmarks and $X_{2:4}$ to be the other three landmarks,

$$E(X_1|X_{2:4}) = \mu_1 + \Sigma_{1,2:4}\Sigma^{-1}_{2:4,2:4}(X_{2:4} - \mu_{2:4}),$$

$$Var(X_1|X_{2:4}) = \Sigma_{1,1} - \Sigma_{1,2:4}\Sigma^{-1}_{2:4,2:4}\Sigma_{2:4,1}.$$

Given these equations, a conditional prior is set on each landmark using a set Mahalanobis distance. This process is iterative such that after each maximisation of θ over the log sum of the conditional prior and the log likelihood, all four set landmarks are Procrustes re-registered against the mean of the prior and the process is repeated. Figure 7.7 shows the process of the Bayesian algorithm. First, a prior is found using the process described of points which lie on the surface of the mesh (Figure 7.7 top). The shape index, curvature and residual sum of squares of fitting a quadratic are calculated at each point of the set of points that comprises the prior (Figure 7.7 middle) and the new landmark is shown in red which has the maximised posterior (Figure 7.7 bottom).

The only potential failure of this method is if the initial algorithm for finding the four set landmarks places an initial landmark guess far away from the true landmark position. The Procrustes registration step will continually rotate the landmarks incorrectly. A small validation study of this method performed very well. Comparing against the manual landmarks placed by a trained observer on the same set of faces, the average

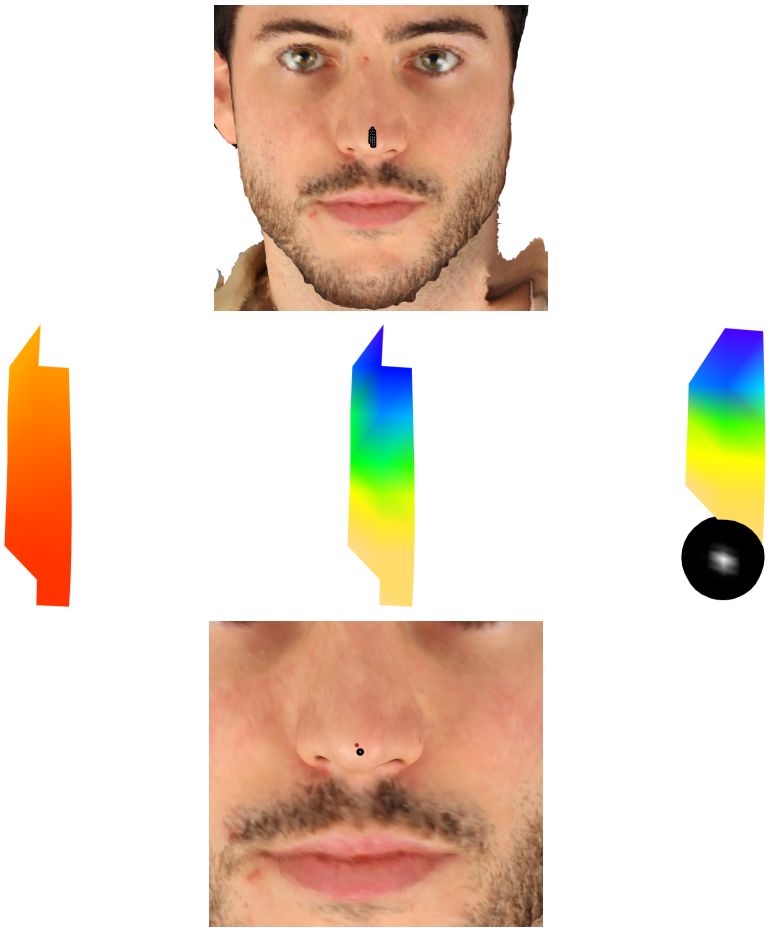

FIGURE 7.7: Process of Producing New Landmark- prior (top), shape index, curvature values and residual sum of squares (middle), and final new landmark in red (bottom)

root mean square distance is 1.13mm. However, this discounted about 20 percent of cases where the landmarks were significantly off and not reflective of the algorithm's principle.

Figure 7.8 illustrates several cases whereby an initial facial image with no other information besides the surface itself is given and the algorithm discussed above locates and optimises over the four initial landmarks.

7.4 Further Discussion

If one landmark is significantly off the mark in the initial approach algorithm, the initial rotation and procrustes registering of these four landmarks onto the mean of the prior can produce poor results. If a new parameter μ is included to define the orientation and location of the face, this problem could potentially be solved. If the $\hat{\mu}$ that maximises

FIGURE 7.8: Bayesian Method of Producing Four Facial Landmarks Automatically

$p(\mu|X)$ is treated as fixed such that

$$p(\mu|X) \propto \int p(X|\mu,\theta)p(\mu|\theta)d\theta,$$

where $p(\mu|\theta)$ has a uniform distribution, then $p(\mu|X)$ is proportionally approximate to the sum of residual sum of squares $(p(X|\mu,\theta))$ and the prior $(p(\theta))$ such that

$$p(\mu|X) \approx \sum_{\theta} p(x|\mu,\theta)p(\theta),$$

maximising over μ. This would allow for the intermediate Procrustes matching step to be removed from the iteration algorithm and allow for a fixed, globally optimised rotation. The same process of locating the new landmark would then be iterative until convergence. Given that these methods are a novel proof of principle, these Bayesian

processes could be explored much further in future work. It seems proper to begin with the process of automatic landmarking and fully understand the concept of likelihood, then continue on to the process of automatic curve identification. With future work these processes seem feasible. Chapter 8 will give an initial exploration of automatic curve identification through Bayesian processes and a full summary of the methods described in this thesis.

Chapter 8

Discussion

8.1 Summary

The initial objective of this thesis was to construct a sound method of describing the human face in order to create analysis tools for the comparison of control and pre-/post-surgical populations. While doing so, an initial investigation of ghost imaging leads to a clear need for a reliability study of the stereocamera system. The reliability study, coupled with a more intense study of facial surface, introduced a novel method of defining traditional anatomical landmarks, allowing, in tandem, a new definition of facial curves. Together, these concepts introduced a method of curve identification, leading to a full facial mesh, implementable across all stereocamera images. A new set of methodological tools were developed, specifically for the curve and facial mesh comparison explorations. Control populations, as well as pre-/post-surgical images were compared and analysed. An investigation was undertaken into pre- and post-bracket removal. The tools created were then used for a very different shape object from a face, a mussel shell. This shows the adaptability and applicability of these tools. Lastly, an investigation was undertaken to use a Bayesian framework for objectively characterising facial images using the concept of prior information from previously manually landmarked individuals. The development of these tools and methods has lead to the creation of a not yet released R package called *Face3D* and the publication of Sun et al. [2013]'s paper on Ghost Imaging, two papers in the second stage of publication (new methods of landmarking and a discussion on mussel shape) and four more papers to be submitted for publication (facial modelling, bracket removal, orthognathic intervention, and a reliability study).

8.2 Limitations in Data (Data and Data Capture)

The process of collecting data, as well as manual landmarking was described at length in Chapters 1, 2. Most of the control participants have been from the University of Glasgow, students and teachers, giving a more narrow age range. The surgical patients also had a more narrow age range, giving no reliable information on individuals under the age of 20 and over the age of 50. There is also a sigificantly higher number of female participants than male. Limitations in the capture of the data itself, the orange peel effect and the issues around the ear region, can sometimes distort the facial images and possibly the curves and landmarks on the surface as well. The small sample size in all the case studies were of great consequence in trying to determine anything conclusively. However, in future work, more data could become available leading to a greater level of conclusive material. The use of principal components in discussing facial shape also comes into question as it could be too broad-brush for such subtle differences.

8.3 Limitation of Curve Identification

Given the manual landmarks used, there is always human error possible in the curve identification. The curves beginning and end points rely solely on the manual landmarks. An enormously high curvature value in some location due to an issue in image capture, can at times, lead a curve to go very much astray. Although this is rare, there were a few cases of this. Future work on the Bayesian processes of prior information could combat this issue.

8.4 Future Work - Bayesian Methods for Automatic Curves

An initial investigation into the concept of prior information is undertaken through the process of warping (Chapter 4). Recalling the facial templates (Male and Female) created from an average control group, produced in Chapter 4, Figure 8.1 illustrates the curves found only with the curve identification algorithm (top right) and the curves found by warping using only the 25 manually placed landmarks for guidance (top left). The warped curves are in surprisingly accurate proportion to the curve identification algorithm curves. This could provide an entirely new method and level of accuracy with which to construct facial masks. The curve identification is not yet able to withstand all high anomalies, and warping could add a new level of confirmation to these identified curves.

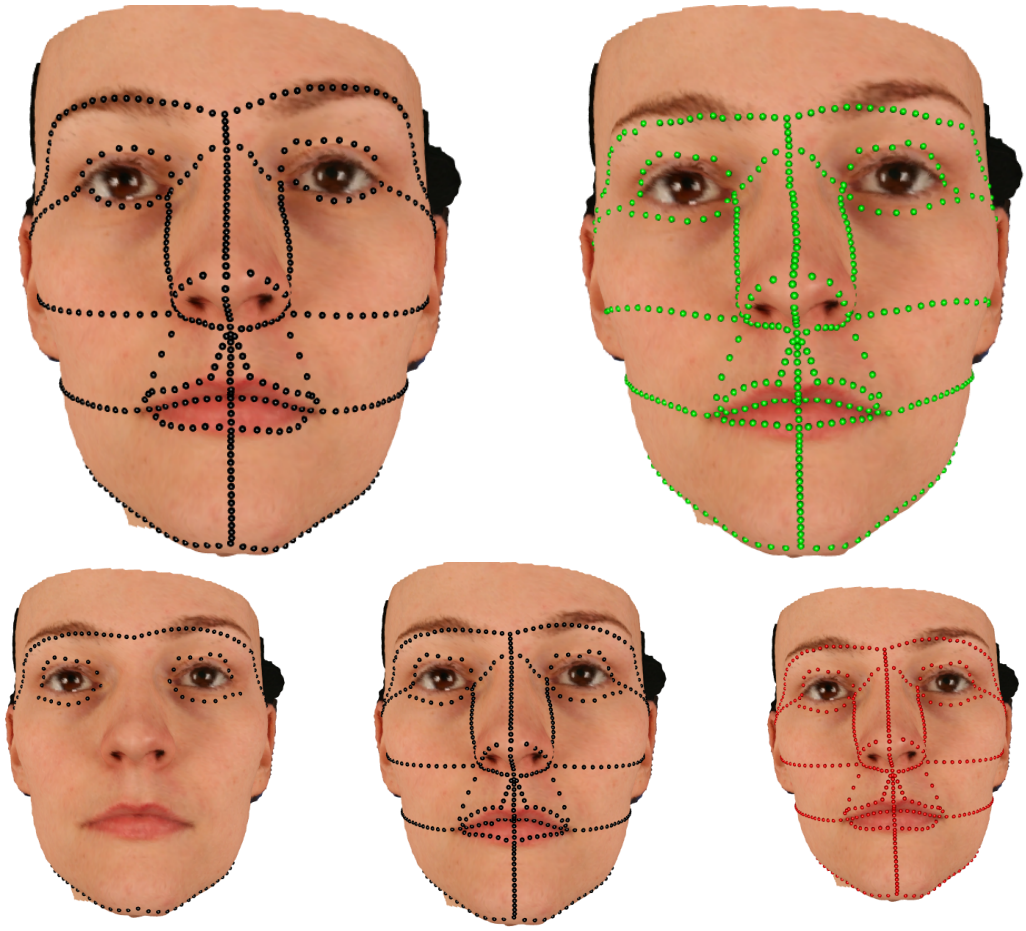

FIGURE 8.1: Top left) Original set of curves found using Chapter 4 methods, Top right) all curves warped using only manual landmarks for guidance, Bottom left) Chosen warped curves, Bottom middle) Warped curves with previous method curves, Bottom right) Final smoothed warped curves and previous method curves

Figure 8.1 gives a clear indication that the concept of 'knowing what a face looks like', prior to finding the curves, is very probably a method for further examining automated methods of landmark and curve identification. This truly motivates an investigation into another method of automatic curve identification, namely a Bayesian framework. A Bayesian framework involves the same concept of having prior information about what a face is supposed to look like. Candidate points for a curve can be calculated as local measures of surface curvature, but a curve must be measured in a specific individual subject using these candidate points. The process in Chapter 4 uses the principal curvatures and an interpolation process to define this curve; however, it could potentially be more informative and stable to use a prior distribution on a large set of manually identified curves to guide the new estimation process and therefore determine the curves on a new facial image. A curve can be parametrised by assuming the manual landmarks are control points and aligning the interested surface by placing these control points on the x-axis, or doing some sort of Procrustes registration. This gives a functional representation of the data in terms of arc length as $x(t)$, $y(t)$ and $z(t)$. A B-spline

representation can be given and therefore the joint distribution of the landmarks and the B-spline coefficients determine a prior distribution on the curve.

The aim is to estimate the B- spline coefficients given the data and the landmarks such that the posterior distribution is

$$p(\beta|X) \propto p(X|\beta)p(\beta),$$

where X is the data (from the mesh) and β represents the parameters of the curve. Now, a distribution must be found for the curvature.

Working in a 2D framework allows easier access given that there will only be one set of basis functions, as well as ensuring that the curve remains on the surface. The β coefficients will use the basis which spans the entire range of the curve, while will clearly be the same number, regardless of size. However, $p(\underset{\sim}{\beta})$ is not a normal prior because of the fixed points constraint of the landmarks which gives a negative correlation between the first and last β coefficients. There must be a change made that somehow negates the effect of the constraints. The first option would be to remove the extra basis coefficients at the ends, but that creates a forced semi-shape. The other method would be to remove the first and last beta coefficients that correspond to the fixed points, and then re-calculate them later. The constraint is linear on the β's so

$$B\underset{\sim}{\beta} = 0$$

is an estimate of the curve at two particular points. If β_1 and β_p are removed then all the prior information is based upon $\beta_2 \dots \beta_{p-1}$. Given the two equations, two unknowns β_1, β_p and solving

$$\begin{aligned} B_{11}\beta_1 + B_{12}\beta_2 + \ldots + B_{1(p-1}\beta_{p-1} + B_{1p}\beta_p &= 0 \\ B_{21}\beta_1 + B_{22}\beta_2 + \ldots + B_{2(p-1)}\beta_{p-1} + B_{2p}\beta_p &= 0 \end{aligned} \tag{8.1}$$

gives

$$\begin{aligned} \beta_1 &= -\frac{B_{12}\beta_2+\ldots+B_{1p}\beta_p}{B_{11}} \\ \beta_p &= \frac{\frac{B_{21}}{B_{11}}(B_{12}\beta_2+\ldots+B_{1(p-1)}\beta_{p-1})-(B_{22}\beta_2+\ldots+B_{2(p-1)}\beta_{p-1})}{-\frac{B_{21}B_{1p}}{B_{11}}+B_{2p}}. \end{aligned} \tag{8.2}$$

Leaving the first and last coefficient, the prior can now be calculated. Fit a normal distribution to the first two coefficients such that variance-covariance matrix is $\hat{\Sigma} = \sum_{i=1}^{2} \lambda_i \underset{\sim i}{\epsilon} \underset{\sim i}{\epsilon}^T$ such that $\underset{\sim}{\hat{\beta}} \sim N(\underset{\sim}{\bar{\hat{\beta}}}, \hat{\Sigma})$. Therefore $p(\underset{\sim}{\beta})$is a normal prior.

Given that both $p(\underset{\sim}{\Gamma})$ and $\underset{\sim}{\beta}p(\underset{\sim}{\beta})$ are both normal, in the multivariate case, the definition for multiplying two normal distributions, $G_1(\mu_1, \sigma_1)$, $G_2(\mu_2, \sigma_2)$, gives mean and variance

for G_3 as

$$\Sigma_3 = (\Sigma_1^{-1} + \Sigma_2^{-1})^{-1} \tag{8.3}$$

$$\mu_3 = \Sigma_3\Sigma_1^{-1}\mu_1 + \Sigma_3\Sigma_2^{-1}\mu_2 \tag{8.4}$$

Beyond this, the likelihood begins to become more confusing. Trying to find a way to relate the shape index and the β coefficients in terms of a prior is proving difficult. However, using the concepts of Chapter 7, potentially a new method could be determined to further the concept of the likelihood and prior in a bayesian framework for automatic curve identification.

These Bayesian processes will be further explored in future work. Given the proof of principle of Bayesian landmark identification in Chapter 7, there is a clear indication that automatic curves in a Bayesian framework are possible. There are two large datasets that have not been manually landmarked, and using the Bayesian methods discussed in Chapter 7 and 8 would completely enhance the accuracy and efficiency of analysis.

Appendix A

Reliability Study

1) *Height*− $y-$direction Euclidean distance between the *gnathion* and *nasion*,

2) *Width*− facial width, the most distant points on the face in the $\hat{x}-$direction distance calculated using a geodesic cut,

3) *Depth*− $z-$direction distance of the mean of the *L/R tragions* and the *subnasale*.

Table A.1: Width−Depth Scaling Glasgow (mm)

Person	RMSD (mm)		
	Rep 1 Camera	Rep 2 Camera	Physical Reconstructed
1	1.510	1.511	1.457
2	1.574	1.561	1.573
3	1.390	1.380	1.384
4	1.602	1.569	1.479

Table A.2: Height−Depth Scaling Glasgow (mm)

Person	RMSD (mm)	
	Rep 1 Camera	Rep 2 Camera
1	1.160	1.151
2	1.188	1.181
3	1.008	1.034
4	1.235	1.217

Table A.3: Height−Width Scaling Glasgow (mm)

Person	RMSD (mm)	
	Rep 1 Camera	Rep 2 Camera
1	0.768	0.762
2	0.755	0.756
3	0.725	0.749
4	0.771	0.776

Table A.4: Width−Depth Scaling Brno (mm)

Person	RMSD (mm)	
	Rep 1 Camera	Rep 2 Camera
1	1.483	1.467
2	1.492	1.502
3	1.390	1.407
4	1.373	1.372

Table A.5: Height−Depth Scaling Brno (mm)

Person	RMSD (mm)	
	Rep 1 Camera	Rep 2 Camera
1	1.068	1.063
2	1.194	1.193
3	1.031	1.047
4	1.198	1.199

Table A.6: Height−Width Scaling Brno (mm)

Person	RMSD (mm)	
	Rep 1 Camera	Rep 2 Camera
1	0.720	0.725
2	0.800	0.794
3	0.742	0.744
4	0.872	0.875

FIGURE A.1: Plane cut Subject 1 (top left), 2 (top right), 3 (bottom left), 4 (bottom right) Glasgow

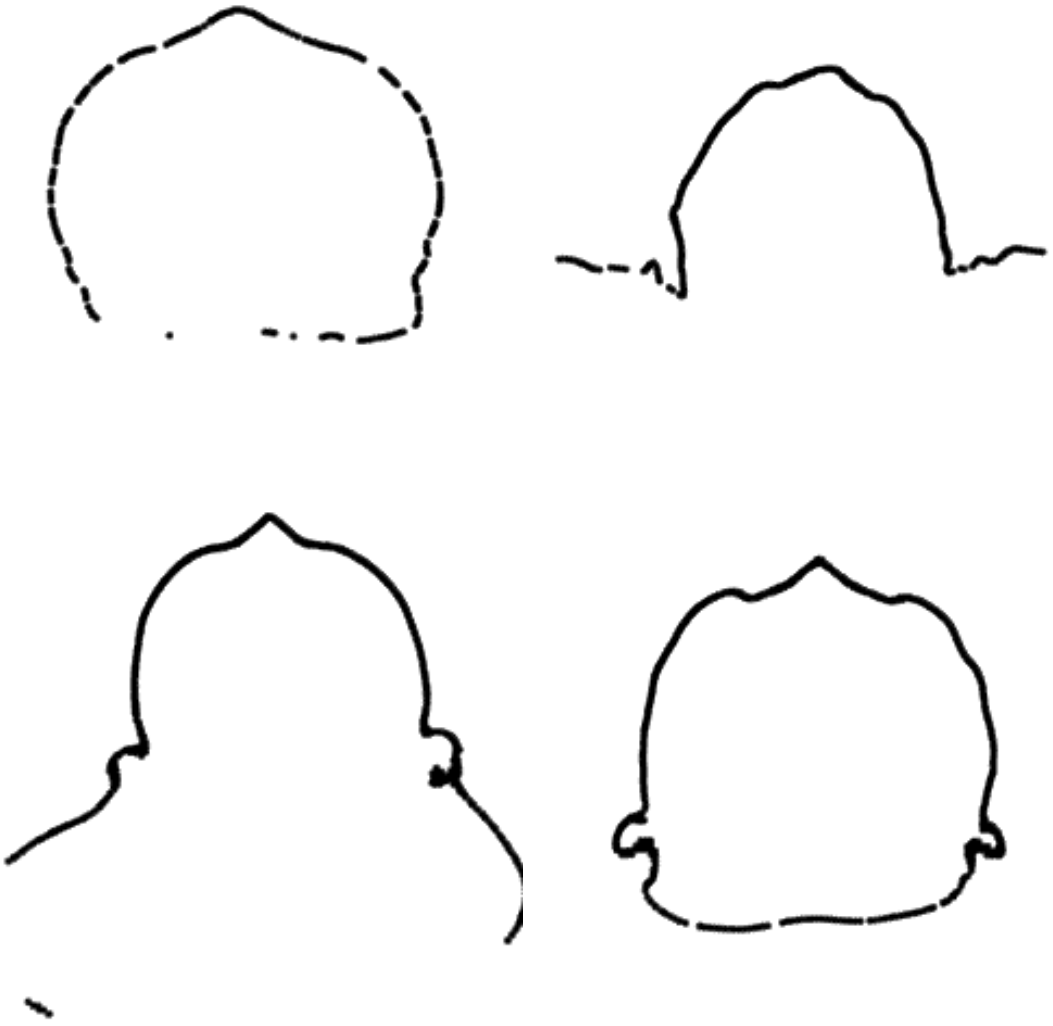

FIGURE A.2: Plane cut Subject 1 (top left), 2 (top right), 3 (bottom left), 4 (bottom right) Brno

Appendix B

Simulation Study

Table B.1: Ridge Identification Simulation Study - Constant Landmarks - Mesh Size 0.05- Noise-Steepness

Steep	0.250	0.500	0.750	1.000	1.250	1.500	1.750	2.000	2.250	2.500
	Dev	Dev	Dev	Dev	Dev	Dev	Dev	Dev	Dev	Dev
Noise										
0.000	0.000	0.000	0.000	0.000	0.000	0.000	0.000	0.000	0.000	0.001
0.006	0.006	0.003	0.002	0.002	0.002	0.001	0.001	0.001	0.001	0.001
0.011	0.012	0.006	0.004	0.003	0.003	0.003	0.003	0.003	0.002	0.002
0.017	0.015	0.007	0.006	0.005	0.004	0.004	0.004	0.004	0.004	0.004
0.022	0.019	0.009	0.008	0.006	0.005	0.005	0.005	0.005	0.005	0.005
0.028	0.019	0.012	0.008	0.007	0.007	0.007	0.006	0.005	0.006	0.006
0.033	0.021	0.013	0.010	0.008	0.008	0.007	0.007	0.007	0.007	0.007
0.039	0.025	0.016	0.011	0.009	0.009	0.008	0.008	0.008	0.008	0.007
0.044	0.029	0.015	0.012	0.011	0.010	0.010	0.009	0.009	0.009	0.008
0.050	0.034	0.017	0.014	0.012	0.010	0.010	0.010	0.010	0.009	0.009

Table B.2: Ridge Identification Simulation Study - Constant Landmarks - Mesh Size 0.06- Noise-Steepness

Steep	0.250	0.500	0.750	1.000	1.250	1.500	1.750	2.000	2.250	2.500
	Dev	Dev	Dev	Dev	Dev	Dev	Dev	Dev	Dev	Dev
Noise										
0.000	0.008	0.006	0.005	0.004	0.004	0.003	0.003	0.003	0.002	0.003
0.006	0.010	0.007	0.005	0.004	0.004	0.004	0.003	0.003	0.003	0.003
0.011	0.014	0.010	0.006	0.005	0.005	0.004	0.004	0.003	0.003	0.003
0.017	0.019	0.012	0.008	0.006	0.005	0.005	0.004	0.004	0.004	0.004
0.022	0.025	0.014	0.009	0.007	0.006	0.006	0.005	0.005	0.004	0.004
0.028	0.024	0.016	0.011	0.008	0.007	0.006	0.006	0.005	0.005	0.006
0.033	0.027	0.017	0.011	0.009	0.009	0.007	0.006	0.006	0.006	0.006
0.039	0.033	0.017	0.013	0.009	0.008	0.009	0.007	0.007	0.006	0.007
0.044	0.039	0.022	0.013	0.012	0.010	0.009	0.008	0.008	0.008	0.007
0.050	0.028	0.022	0.014	0.013	0.011	0.010	0.009	0.009	0.008	0.008

Table B.3: Ridge Identification Simulation Study - Constant Landmarks - Mesh Size 0.07- Noise-Steepness

Steep	0.250	0.500	0.750	1.000	1.250	1.500	1.750	2.000	2.250	2.500
	Dev	Dev	Dev	Dev	Dev	Dev	Dev	Dev	Dev	Dev
Noise										
0.000	0.009	0.006	0.004	0.004	0.003	0.003	0.003	0.003	0.003	0.004
0.006	0.015	0.007	0.005	0.004	0.003	0.003	0.003	0.003	0.003	0.008
0.011	0.017	0.011	0.007	0.004	0.004	0.004	0.004	0.004	0.004	0.009
0.017	0.026	0.013	0.009	0.006	0.005	0.004	0.004	0.004	0.004	0.009
0.022	0.027	0.015	0.009	0.006	0.006	0.005	0.005	0.005	0.006	0.009
0.028	0.035	0.014	0.011	0.009	0.007	0.006	0.006	0.005	0.008	0.010
0.033	0.032	0.019	0.012	0.009	0.008	0.007	0.006	0.006	0.009	0.012
0.039	0.042	0.022	0.014	0.011	0.009	0.008	0.007	0.008	0.010	0.015
0.044	0.056	0.022	0.015	0.012	0.010	0.008	0.008	0.008	0.011	0.020
0.050	0.037	0.025	0.016	0.013	0.012	0.010	0.009	0.009	0.012	0.025

Table B.4: Ridge Identification Simulation Study - Constant Landmarks - Mesh Size 0.08- Noise-Steepness

Steep	0.250	0.500	0.750	1.000	1.250	1.500	1.750	2.000	2.250	2.500
	Dev	Dev	Dev	Dev	Dev	Dev	Dev	Dev	Dev	Dev
Noise										
0.000	0.001	0.001	0.001	0.002	0.002	0.002	0.002	0.002	0.002	0.003
0.006	0.009	0.005	0.003	0.002	0.002	0.002	0.002	0.012	0.011	0.008
0.011	0.014	0.008	0.005	0.003	0.003	0.002	0.002	0.025	0.010	0.009
0.017	0.024	0.011	0.007	0.005	0.003	0.003	0.003	0.022	0.012	0.008
0.022	0.029	0.014	0.009	0.006	0.005	0.004	0.004	0.022	0.012	0.009
0.028	0.029	0.016	0.010	0.007	0.006	0.004	0.004	0.022	0.011	0.009
0.033	0.031	0.019	0.013	0.009	0.006	0.005	0.005	0.023	0.011	0.011
0.039	0.035	0.019	0.014	0.010	0.008	0.006	0.006	0.022	0.011	0.010
0.044	0.045	0.022	0.016	0.010	0.008	0.007	0.007	0.025	0.012	0.012
0.050	0.046	0.024	0.017	0.010	0.008	0.008	0.007	0.020	0.014	0.012

Table B.5: Ridge Identification Simulation Study - Constant Landmarks - Mesh Size 0.09- Noise-Steepness

Steep	0.250	0.500	0.750	1.000	1.250	1.500	1.750	2.000	2.250	2.500
	Dev	Dev	Dev	Dev	Dev	Dev	Dev	Dev	Dev	Dev
Noise										
0.000	0.006	0.007	0.008	0.007	0.008	0.008	0.008	0.009	0.008	0.008
0.006	0.010	0.007	0.008	0.007	0.008	0.008	0.008	0.018	0.014	0.012
0.011	0.017	0.012	0.009	0.008	0.008	0.008	0.008	0.012	0.015	0.012
0.017	0.022	0.013	0.009	0.009	0.009	0.008	0.012	0.014	0.014	0.014
0.022	0.027	0.015	0.009	0.010	0.009	0.009	0.016	0.019	0.014	0.013
0.028	0.029	0.017	0.011	0.011	0.009	0.010	0.025	0.017	0.016	0.014
0.033	0.046	0.022	0.014	0.012	0.010	0.010	0.025	0.017	0.016	0.016
0.039	0.040	0.024	0.018	0.013	0.011	0.011	0.024	0.018	0.016	0.015
0.044	0.044	0.029	0.015	0.015	0.012	0.012	0.024	0.018	0.018	0.018
0.050	0.051	0.031	0.019	0.015	0.012	0.012	0.022	0.020	0.017	0.017

Table B.6: Ridge Identification Simulation Study - Constant Landmarks - Mesh Size 0.10- Noise-Steepness

Steep	0.250	0.500	0.750	1.000	1.250	1.500	1.750	2.000	2.250	2.500
	Dev	Dev	Dev	Dev	Dev	Dev	Dev	Dev	Dev	Dev
Noise										
0.000	0.000	0.000	0.000	0.000	0.000	0.000	0.000	0.000	0.000	0.000
0.006	0.012	0.005	0.003	0.002	0.002	0.001	0.026	0.017	0.020	0.013
0.011	0.023	0.010	0.005	0.003	0.003	0.003	0.024	0.020	0.016	0.017
0.017	0.028	0.013	0.009	0.005	0.005	0.004	0.022	0.016	0.019	0.016
0.022	0.031	0.016	0.010	0.007	0.006	0.006	0.022	0.019	0.018	0.018
0.028	0.046	0.022	0.013	0.008	0.007	0.007	0.024	0.022	0.017	0.016
0.033	0.052	0.022	0.015	0.009	0.009	0.008	0.022	0.019	0.015	0.023
0.039	0.051	0.025	0.016	0.011	0.010	0.011	0.022	0.022	0.019	0.018
0.044	0.057	0.034	0.019	0.013	0.011	0.013	0.026	0.021	0.018	0.021
0.050	0.061	0.032	0.023	0.014	0.012	0.015	0.026	0.022	0.025	0.020

Table B.7: Ridge Identification Simulation Study - Constant Mesh Size - Landmark Movement 0.01- Noise-Steepness

Steep	0.250	0.500	0.750	1.000	1.250	1.500	1.750	2.000	2.250	2.500
	Dev	Dev	Dev	Dev	Dev	Dev	Dev	Dev	Dev	Dev
Noise										
0.000	0.001	0.002	0.002	0.002	0.002	0.002	0.002	0.002	0.002	0.002
0.006	0.008	0.004	0.004	0.003	0.003	0.003	0.002	0.002	0.002	0.002
0.011	0.011	0.007	0.005	0.004	0.004	0.004	0.004	0.004	0.003	0.003
0.017	0.017	0.010	0.007	0.006	0.005	0.005	0.005	0.005	0.005	0.005
0.022	0.020	0.011	0.008	0.007	0.007	0.006	0.006	0.006	0.006	0.006
0.028	0.020	0.013	0.010	0.008	0.008	0.007	0.007	0.007	0.006	0.007
0.033	0.023	0.015	0.011	0.010	0.009	0.008	0.008	0.008	0.008	0.008
0.039	0.026	0.017	0.012	0.011	0.010	0.009	0.009	0.009	0.009	0.008
0.044	0.031	0.018	0.014	0.012	0.010	0.010	0.010	0.010	0.009	0.009
0.050	0.032	0.017	0.015	0.013	0.011	0.011	0.011	0.010	0.010	0.010

Table B.8: Ridge Identification Simulation Study - Constant Mesh Size - Landmark Movement 0.02- Noise-Steepness

Steep	0.250	0.500	0.750	1.000	1.250	1.500	1.750	2.000	2.250	2.500
	Dev	Dev	Dev	Dev	Dev	Dev	Dev	Dev	Dev	Dev
Noise										
0.000	0.003	0.004	0.004	0.004	0.004	0.004	0.004	0.004	0.004	0.003
0.006	0.009	0.006	0.005	0.005	0.005	0.005	0.004	0.004	0.004	0.004
0.011	0.013	0.009	0.007	0.006	0.006	0.006	0.005	0.005	0.005	0.005
0.017	0.018	0.012	0.009	0.007	0.007	0.006	0.006	0.006	0.006	0.006
0.022	0.021	0.014	0.010	0.008	0.008	0.008	0.008	0.007	0.007	0.007
0.028	0.023	0.016	0.011	0.010	0.009	0.009	0.009	0.008	0.008	0.008
0.033	0.026	0.016	0.013	0.011	0.010	0.010	0.009	0.009	0.009	0.009
0.039	0.028	0.017	0.014	0.012	0.011	0.010	0.010	0.010	0.011	0.010
0.044	0.027	0.021	0.015	0.013	0.012	0.011	0.011	0.011	0.011	0.011
0.050	0.034	0.021	0.016	0.014	0.013	0.012	0.011	0.012	0.011	0.012

Table B.9: Ridge Identification Simulation Study - Constant Mesh Size - Landmark Movement 0.04- Noise-Steepness

Steep	0.250	0.500	0.750	1.000	1.250	1.500	1.750	2.000	2.250	2.500
	Dev	Dev	Dev	Dev	Dev	Dev	Dev	Dev	Dev	Dev
Noise										
0.000	0.010	0.010	0.011	0.011	0.011	0.010	0.011	0.011	0.011	0.010
0.006	0.015	0.013	0.012	0.012	0.012	0.012	0.012	0.012	0.012	0.011
0.011	0.020	0.015	0.013	0.012	0.012	0.012	0.012	0.012	0.012	0.012
0.017	0.020	0.016	0.014	0.013	0.013	0.013	0.013	0.013	0.013	0.012
0.022	0.023	0.017	0.015	0.015	0.014	0.014	0.013	0.013	0.013	0.013
0.028	0.025	0.021	0.016	0.015	0.014	0.014	0.014	0.014	0.014	0.014
0.033	0.029	0.021	0.017	0.016	0.015	0.015	0.014	0.014	0.015	0.015
0.039	0.031	0.022	0.017	0.017	0.015	0.015	0.016	0.016	0.015	0.015
0.044	0.027	0.024	0.019	0.018	0.016	0.016	0.016	0.015	0.016	0.017
0.050	0.039	0.024	0.019	0.017	0.017	0.016	0.017	0.017	0.016	0.016

Table B.10: Ridge Identification Simulation Study - Constant Mesh Size - Landmark Movement 0.06- Noise-Steepness

Steep	0.250	0.500	0.750	1.000	1.250	1.500	1.750	2.000	2.250	2.500
	Dev	Dev	Dev	Dev	Dev	Dev	Dev	Dev	Dev	Dev
Noise										
0.000	0.020	0.020	0.023	0.022	0.022	0.020	0.022	0.022	0.022	0.020
0.006	0.025	0.023	0.023	0.023	0.023	0.023	0.023	0.023	0.023	0.023
0.011	0.028	0.025	0.024	0.023	0.023	0.023	0.023	0.023	0.023	0.023
0.017	0.029	0.025	0.024	0.023	0.024	0.023	0.023	0.024	0.023	0.024
0.022	0.031	0.027	0.025	0.024	0.024	0.024	0.024	0.023	0.024	0.024
0.028	0.035	0.026	0.026	0.025	0.024	0.024	0.024	0.024	0.024	0.024
0.033	0.036	0.028	0.026	0.025	0.026	0.025	0.025	0.025	0.025	0.025
0.039	0.041	0.031	0.026	0.026	0.026	0.026	0.025	0.025	0.025	0.025
0.044	0.040	0.030	0.028	0.026	0.026	0.026	0.026	0.025	0.025	0.025
0.050	0.041	0.031	0.028	0.027	0.028	0.025	0.026	0.026	0.026	0.026

Table B.11: Ridge Identification Simulation Study - Constant Mesh Size - Landmark Movement 0.08- Noise-Steepness

Steep	0.250	0.500	0.750	1.000	1.250	1.500	1.750	2.000	2.250	2.500
	Dev	Dev	Dev	Dev	Dev	Dev	Dev	Dev	Dev	Dev
Noise										
0.000	0.033	0.033	0.037	0.036	0.036	0.033	0.036	0.036	0.036	0.033
0.006	0.039	0.037	0.037	0.037	0.037	0.037	0.037	0.037	0.037	0.037
0.011	0.040	0.037	0.037	0.037	0.037	0.037	0.037	0.037	0.036	0.037
0.017	0.043	0.038	0.038	0.037	0.037	0.037	0.036	0.037	0.037	0.037
0.022	0.043	0.038	0.038	0.037	0.038	0.038	0.037	0.038	0.037	0.037
0.028	0.047	0.040	0.038	0.038	0.038	0.037	0.038	0.037	0.038	0.037
0.033	0.047	0.041	0.038	0.037	0.038	0.038	0.038	0.038	0.037	0.038
0.039	0.049	0.042	0.038	0.038	0.038	0.039	0.038	0.038	0.038	0.038
0.044	0.048	0.042	0.041	0.039	0.037	0.039	0.039	0.039	0.038	0.038
0.050	0.052	0.043	0.041	0.040	0.038	0.038	0.040	0.038	0.038	0.040

Table B.12: Ridge Identification Simulation Study - Constant Mesh Size - Landmark Movement 0.10- Noise-Steepness

Steep	0.250	0.500	0.750	1.000	1.250	1.500	1.750	2.000	2.250	2.500
	Dev	Dev	Dev	Dev	Dev	Dev	Dev	Dev	Dev	Dev
Noise										
0.000	0.046	0.046	0.051	0.051	0.051	0.046	0.051	0.051	0.051	0.046
0.006	0.052	0.051	0.051	0.051	0.051	0.051	0.051	0.051	0.051	0.051
0.011	0.053	0.052	0.051	0.051	0.051	0.051	0.051	0.051	0.051	0.051
0.017	0.055	0.053	0.052	0.051	0.052	0.051	0.051	0.051	0.051	0.051
0.022	0.057	0.052	0.052	0.052	0.052	0.052	0.052	0.051	0.051	0.052
0.028	0.057	0.053	0.052	0.053	0.052	0.051	0.051	0.052	0.052	0.052
0.033	0.057	0.054	0.052	0.052	0.052	0.052	0.052	0.052	0.051	0.052
0.039	0.059	0.054	0.053	0.051	0.052	0.052	0.052	0.052	0.052	0.052
0.044	0.064	0.055	0.054	0.053	0.053	0.053	0.052	0.051	0.052	0.052
0.050	0.063	0.056	0.054	0.053	0.053	0.053	0.052	0.052	0.052	0.052

Table B.13: Ridge Identification Simulation Study - Constant Landmarks - Mesh Size 0.05- Noise - Curve Movement

CM	0.000	0.111	0.222	0.333	0.444	0.556	0.667	0.778	0.889	1.000
	Dev	Dev	Dev	Dev	Dev	Dev	Dev	Dev	Dev	Dev
Noise										
0.000	0.000	0.000	0.001	0.002	0.005	0.002	0.002	0.002	0.002	0.002
0.006	0.003	0.003	0.003	0.004	0.006	0.006	0.006	0.005	0.006	0.006
0.011	0.005	0.005	0.006	0.009	0.008	0.009	0.009	0.011	0.010	0.011
0.017	0.007	0.007	0.007	0.008	0.014	0.016	0.017	0.015	0.017	0.017
0.022	0.008	0.009	0.009	0.012	0.014	0.017	0.020	0.022	0.018	0.020
0.028	0.010	0.010	0.010	0.011	0.016	0.030	0.022	0.028	0.022	0.019
0.033	0.012	0.011	0.012	0.014	0.021	0.026	0.031	0.031	0.028	0.026
0.039	0.012	0.012	0.012	0.016	0.019	0.023	0.028	0.025	0.035	0.022
0.044	0.014	0.011	0.014	0.016	0.016	0.022	0.027	0.033	0.041	0.031
0.050	0.016	0.013	0.014	0.019	0.022	0.029	0.035	0.037	0.028	0.044

Table B.14: Ridge Identification Simulation Study - Constant Landmarks - Mesh Size 0.06- Noise - Curve Movement

CM	0.000	0.111	0.222	0.333	0.444	0.556	0.667	0.778	0.889	1.000
	Dev	Dev	Dev	Dev	Dev	Dev	Dev	Dev	Dev	Dev
Noise										
0.001	0.006	0.006	0.005	0.007	0.006	0.007	0.004	0.011	0.006	0.007
0.006	0.006	0.006	0.006	0.007	0.008	0.009	0.009	0.011	0.011	0.010
0.011	0.008	0.008	0.008	0.010	0.010	0.009	0.010	0.014	0.011	0.014
0.017	0.009	0.010	0.009	0.013	0.014	0.016	0.014	0.014	0.015	0.018
0.022	0.012	0.012	0.011	0.012	0.022	0.021	0.019	0.026	0.021	0.016
0.028	0.013	0.014	0.015	0.015	0.018	0.024	0.025	0.024	0.027	0.028
0.033	0.015	0.015	0.014	0.016	0.021	0.025	0.029	0.031	0.025	0.023
0.039	0.016	0.013	0.015	0.020	0.017	0.031	0.027	0.031	0.035	0.040
0.044	0.017	0.018	0.016	0.023	0.025	0.035	0.029	0.037	0.029	0.040
0.050	0.020	0.017	0.018	0.020	0.024	0.038	0.040	0.039	0.034	0.037

Table B.15: Ridge Identification Simulation Study - Constant Landmarks - Mesh Size 0.07- Noise - Curve Movement

CM	0.000	0.111	0.222	0.333	0.444	0.556	0.667	0.778	0.889	1.000
	Dev	Dev	Dev	Dev	Dev	Dev	Dev	Dev	Dev	Dev
Noise										
0.001	0.006	0.005	0.005	0.006	0.006	0.007	0.008	0.009	0.007	0.010
0.006	0.007	0.007	0.006	0.007	0.006	0.008	0.009	0.009	0.011	0.010
0.011	0.008	0.010	0.008	0.009	0.010	0.012	0.011	0.012	0.015	0.011
0.017	0.009	0.011	0.009	0.010	0.010	0.013	0.015	0.014	0.015	0.015
0.022	0.012	0.013	0.012	0.011	0.017	0.019	0.015	0.026	0.018	0.021
0.028	0.014	0.015	0.013	0.019	0.017	0.021	0.027	0.023	0.032	0.024
0.033	0.017	0.015	0.014	0.024	0.021	0.024	0.027	0.025	0.023	0.028
0.039	0.018	0.017	0.018	0.020	0.025	0.031	0.030	0.034	0.027	0.032
0.044	0.020	0.020	0.020	0.019	0.022	0.032	0.028	0.032	0.032	0.034
0.050	0.023	0.020	0.021	0.021	0.024	0.047	0.024	0.040	0.041	0.039

Table B.16: Ridge Identification Simulation Study - Constant Landmarks - Mesh Size 0.08- Noise - Curve Movement

CM	0.000	0.111	0.222	0.333	0.444	0.556	0.667	0.778	0.889	1.000
	Dev	Dev	Dev	Dev	Dev	Dev	Dev	Dev	Dev	Dev
Noise										
0.000	0.001	0.001	0.002	0.003	0.004	0.004	0.004	0.005	0.006	0.005
0.006	0.003	0.004	0.004	0.005	0.006	0.007	0.007	0.007	0.008	0.007
0.011	0.005	0.006	0.006	0.008	0.008	0.010	0.010	0.009	0.010	0.008
0.017	0.009	0.008	0.008	0.010	0.012	0.012	0.014	0.017	0.011	0.012
0.022	0.010	0.010	0.012	0.012	0.017	0.016	0.016	0.013	0.018	0.014
0.028	0.011	0.010	0.013	0.013	0.018	0.019	0.015	0.022	0.016	0.022
0.033	0.014	0.015	0.016	0.018	0.024	0.020	0.020	0.028	0.030	0.019
0.039	0.016	0.017	0.016	0.022	0.022	0.027	0.025	0.033	0.033	0.031
0.044	0.020	0.018	0.016	0.020	0.024	0.030	0.041	0.034	0.041	0.035
0.050	0.021	0.023	0.021	0.022	0.021	0.043	0.027	0.031	0.033	0.034

Table B.17: Ridge Identification Simulation Study - Constant Landmarks - Mesh Size 0.09- Noise - Curve Movement

CM	0.000	0.111	0.222	0.333	0.444	0.556	0.667	0.778	0.889	1.000
	Dev	Dev	Dev	Dev	Dev	Dev	Dev	Dev	Dev	Dev
Noise										
0.000	0.007	0.007	0.007	0.007	0.007	0.010	0.009	0.010	0.009	0.009
0.006	0.007	0.008	0.008	0.008	0.008	0.011	0.010	0.011	0.009	0.011
0.011	0.009	0.009	0.009	0.010	0.010	0.013	0.011	0.015	0.014	0.013
0.017	0.012	0.013	0.011	0.013	0.014	0.017	0.015	0.017	0.017	0.015
0.022	0.012	0.016	0.013	0.016	0.016	0.017	0.018	0.022	0.021	0.017
0.028	0.016	0.014	0.015	0.019	0.021	0.033	0.019	0.023	0.027	0.024
0.033	0.015	0.016	0.017	0.019	0.021	0.030	0.026	0.024	0.026	0.028
0.039	0.017	0.017	0.016	0.025	0.025	0.034	0.029	0.027	0.030	0.029
0.044	0.023	0.021	0.022	0.023	0.026	0.027	0.038	0.035	0.032	0.041
0.050	0.021	0.024	0.024	0.025	0.032	0.034	0.041	0.045	0.031	0.039

TABLE B.18: Ridge Identification Simulation Study - Constant Landmarks - Mesh Size 0.10- Noise - Curve Movement

CM	0.000	0.111	0.222	0.333	0.444	0.556	0.667	0.778	0.889	1.000
	Dev	Dev	Dev	Dev	Dev	Dev	Dev	Dev	Dev	Dev
Noise										
0.000	0.051	0.051	0.050	0.049	0.049	0.047	0.045	0.043	0.042	0.040
0.006	0.051	0.051	0.051	0.050	0.050	0.048	0.046	0.045	0.043	0.041
0.011	0.051	0.052	0.051	0.051	0.050	0.049	0.048	0.046	0.045	0.044
0.017	0.052	0.052	0.051	0.052	0.053	0.051	0.051	0.049	0.045	0.047
0.022	0.052	0.052	0.052	0.053	0.055	0.055	0.056	0.052	0.049	0.053
0.028	0.053	0.053	0.053	0.053	0.057	0.056	0.062	0.056	0.049	0.053
0.033	0.054	0.054	0.052	0.054	0.055	0.059	0.056	0.055	0.056	0.059
0.039	0.054	0.053	0.054	0.054	0.058	0.057	0.059	0.061	0.057	0.052
0.044	0.055	0.054	0.053	0.054	0.055	0.058	0.059	0.059	0.064	0.058
0.050	0.053	0.053	0.055	0.056	0.057	0.058	0.060	0.072	0.066	0.068

TABLE B.19: Ridge Identification Simulation Study - Constant Mesh Size - Landmark Movement .01 - Noise - Curve Movement

CM	0.000	0.111	0.222	0.333	0.444	0.556	0.667	0.778	0.889	1.000
	Dev	Dev	Dev	Dev	Dev	Dev	Dev	Dev	Dev	Dev
Noise										
0.000	0.002	0.002	0.002	0.003	0.006	0.003	0.003	0.003	0.004	0.003
0.006	0.004	0.004	0.004	0.005	0.007	0.006	0.006	0.007	0.006	0.008
0.011	0.006	0.006	0.007	0.009	0.011	0.009	0.012	0.012	0.011	0.011
0.017	0.008	0.008	0.007	0.011	0.019	0.017	0.016	0.015	0.016	0.013
0.022	0.011	0.009	0.010	0.011	0.017	0.022	0.022	0.018	0.021	0.019
0.028	0.011	0.011	0.010	0.014	0.020	0.020	0.027	0.026	0.032	0.019
0.033	0.013	0.012	0.012	0.018	0.021	0.027	0.031	0.029	0.034	0.030
0.039	0.015	0.012	0.015	0.017	0.026	0.031	0.031	0.031	0.032	0.035
0.044	0.015	0.014	0.015	0.016	0.024	0.033	0.031	0.031	0.027	0.032
0.050	0.016	0.015	0.016	0.015	0.022	0.029	0.034	0.031	0.033	0.033

TABLE B.20: Ridge Identification Simulation Study - Constant Mesh Size - Landmark Movement .02 - Noise - Curve Movement

CM	0.000	0.111	0.222	0.333	0.444	0.556	0.667	0.778	0.889	1.000
	Dev	Dev	Dev	Dev	Dev	Dev	Dev	Dev	Dev	Dev
Noise										
0	0.004	0.004	0.004	0.005	0.008	0.005	0.005	0.005	0.005	0.005
0.006	0.006	0.006	0.006	0.008	0.008	0.008	0.008	0.008	0.009	0.008
0.011	0.007	0.007	0.008	0.011	0.012	0.013	0.011	0.014	0.013	0.012
0.017	0.009	0.009	0.009	0.013	0.017	0.014	0.021	0.017	0.016	0.019
0.022	0.011	0.011	0.011	0.015	0.023	0.022	0.028	0.022	0.021	0.018
0.028	0.013	0.011	0.014	0.017	0.028	0.025	0.026	0.027	0.025	0.029
0.033	0.013	0.014	0.014	0.017	0.023	0.036	0.028	0.031	0.031	0.029
0.039	0.016	0.014	0.013	0.021	0.023	0.027	0.028	0.027	0.044	0.029
0.044	0.017	0.015	0.016	0.023	0.020	0.035	0.034	0.040	0.039	0.040
0.05	0.017	0.016	0.017	0.021	0.024	0.030	0.036	0.042	0.036	0.034

TABLE B.21: Ridge Identification Simulation Study - Constant Mesh Size - Landmark Movement .04 - Noise - Curve Movement

CM	0.000	0.111	0.222	0.333	0.444	0.556	0.667	0.778	0.889	1.000
	Dev	Dev	Dev	Dev	Dev	Dev	Dev	Dev	Dev	Dev
Noise										
0.000	0.011	0.011	0.011	0.011	0.013	0.011	0.010	0.010	0.010	0.010
0.006	0.012	0.012	0.013	0.013	0.013	0.014	0.013	0.014	0.013	0.013
0.011	0.014	0.014	0.014	0.016	0.016	0.017	0.018	0.017	0.017	0.017
0.017	0.014	0.015	0.016	0.017	0.019	0.019	0.023	0.019	0.021	0.015
0.022	0.015	0.016	0.016	0.018	0.022	0.027	0.022	0.026	0.031	0.025
0.028	0.017	0.018	0.018	0.019	0.026	0.027	0.025	0.026	0.027	0.034
0.033	0.018	0.018	0.019	0.023	0.023	0.031	0.037	0.039	0.038	0.041
0.039	0.019	0.019	0.019	0.021	0.025	0.026	0.037	0.041	0.031	0.043
0.044	0.021	0.020	0.020	0.022	0.026	0.035	0.037	0.038	0.043	0.040
0.050	0.021	0.021	0.019	0.024	0.028	0.036	0.038	0.033	0.034	0.037

TABLE B.22: Ridge Identification Simulation Study - Constant Mesh Size - Landmark Movement .06 - Noise - Curve Movement

CM	0.000	0.111	0.222	0.333	0.444	0.556	0.667	0.778	0.889	1.000
	Dev	Dev	Dev	Dev	Dev	Dev	Dev	Dev	Dev	Dev
Noise										
0.000	0.023	0.022	0.022	0.022	0.022	0.020	0.019	0.019	0.018	0.017
0.006	0.023	0.023	0.023	0.023	0.023	0.022	0.022	0.021	0.020	0.019
0.011	0.024	0.024	0.025	0.024	0.027	0.026	0.023	0.024	0.023	0.022
0.017	0.026	0.024	0.025	0.026	0.030	0.030	0.029	0.026	0.025	0.027
0.022	0.026	0.025	0.025	0.027	0.033	0.034	0.039	0.034	0.032	0.029
0.028	0.026	0.026	0.026	0.029	0.034	0.031	0.034	0.039	0.040	0.033
0.033	0.026	0.027	0.027	0.030	0.036	0.037	0.036	0.037	0.037	0.038
0.039	0.027	0.026	0.030	0.030	0.030	0.036	0.039	0.045	0.032	0.045
0.044	0.029	0.027	0.030	0.029	0.034	0.045	0.045	0.037	0.035	0.047
0.050	0.030	0.028	0.031	0.033	0.029	0.041	0.044	0.046	0.044	0.052

TABLE B.23: Ridge Identification Simulation Study - Constant Mesh Size - Landmark Movement .08 - Noise - Curve Movement

CM	0.000	0.111	0.222	0.333	0.444	0.556	0.667	0.778	0.889	1.000
	Dev	Dev	Dev	Dev	Dev	Dev	Dev	Dev	Dev	Dev
Noise										
0.000	0.037	0.036	0.036	0.035	0.035	0.032	0.031	0.030	0.029	0.028
0.006	0.037	0.037	0.036	0.036	0.035	0.034	0.033	0.032	0.031	0.030
0.011	0.037	0.038	0.038	0.037	0.038	0.035	0.035	0.033	0.033	0.030
0.017	0.038	0.038	0.038	0.039	0.038	0.038	0.039	0.034	0.034	0.037
0.022	0.039	0.038	0.039	0.040	0.044	0.041	0.046	0.044	0.039	0.038
0.028	0.039	0.039	0.039	0.039	0.045	0.042	0.046	0.044	0.048	0.047
0.033	0.040	0.040	0.040	0.040	0.042	0.047	0.045	0.052	0.042	0.045
0.039	0.040	0.039	0.039	0.043	0.048	0.050	0.053	0.053	0.049	0.045
0.044	0.040	0.038	0.041	0.040	0.046	0.047	0.055	0.044	0.056	0.047
0.050	0.040	0.040	0.041	0.041	0.047	0.051	0.055	0.052	0.053	0.050

TABLE B.24: Ridge Identification Simulation Study - Constant Mesh Size - Landmark Movement .10 - Noise - Curve Movement

CM	0.000	0.111	0.222	0.333	0.444	0.556	0.667	0.778	0.889	1.000
	Dev	Dev	Dev	Dev	Dev	Dev	Dev	Dev	Dev	Dev
Noise										
0.000	0.043	0.043	0.043	0.042	0.042	0.040	0.038	0.037	0.036	0.034
0.006	0.044	0.044	0.043	0.043	0.042	0.040	0.039	0.038	0.037	0.035
0.011	0.044	0.043	0.044	0.043	0.043	0.041	0.041	0.040	0.038	0.036
0.017	0.045	0.044	0.044	0.044	0.046	0.046	0.045	0.042	0.040	0.038
0.022	0.044	0.045	0.044	0.044	0.046	0.047	0.048	0.044	0.044	0.039
0.028	0.045	0.044	0.044	0.045	0.048	0.048	0.047	0.051	0.043	0.043
0.033	0.046	0.045	0.044	0.046	0.049	0.054	0.049	0.049	0.047	0.048
0.039	0.046	0.045	0.045	0.046	0.048	0.052	0.053	0.050	0.049	0.048
0.044	0.046	0.045	0.045	0.045	0.050	0.051	0.051	0.047	0.050	0.049
0.050	0.046	0.046	0.045	0.046	0.050	0.052	0.050	0.049	0.053	0.060

Table B.25: Ridge Identification Simulation Study - Constant Landmarks - Mesh Size .05 - Steepness- Curve Movement

CM	0.000	0.111	0.222	0.333	0.444	0.556	0.667	0.778	0.889	1.000
	Dev	Dev	Dev	Dev	Dev	Dev	Dev	Dev	Dev	Dev
Steepness										
0.250	0.000	0.001	0.001	0.001	0.001	0.001	0.001	0.001	0.002	0.002
0.500	0.000	0.000	0.001	0.001	0.001	0.002	0.002	0.002	0.002	0.002
0.750	0.000	0.000	0.001	0.002	0.004	0.002	0.002	0.002	0.002	0.003
1.000	0.000	0.000	0.001	0.004	0.004	0.002	0.002	0.002	0.002	0.002
1.250	0.000	0.000	0.001	0.002	0.005	0.002	0.002	0.002	0.002	0.002
1.500	0.000	0.000	0.001	0.001	0.003	0.001	0.002	0.002	0.003	0.002
1.750	0.000	0.000	0.001	0.001	0.002	0.002	0.001	0.002	0.002	0.002
2.000	0.000	0.000	0.001	0.001	0.002	0.002	0.001	0.001	0.002	0.002
2.250	0.000	0.001	0.001	0.001	0.001	0.002	0.001	0.002	0.002	0.002
2.500	0.000	0.000	0.001	0.001	0.001	0.001	0.001	0.002	0.002	0.002

Table B.26: Ridge Identification Simulation Study - Constant Landmarks - Mesh Size .06 - Steepness- Curve Movement

CM	0.000	0.111	0.222	0.333	0.444	0.556	0.667	0.778	0.889	1.000
	Dev	Dev	Dev	Dev	Dev	Dev	Dev	Dev	Dev	Dev
Steepness										
0.250	0.009	0.008	0.008	0.007	0.008	0.012	0.008	0.008	0.008	0.009
0.500	0.008	0.010	0.007	0.007	0.011	0.008	0.009	0.008	0.011	0.010
0.750	0.007	0.007	0.007	0.013	0.007	0.008	0.008	0.009	0.010	0.009
1.000	0.006	0.007	0.007	0.011	0.007	0.010	0.010	0.009	0.011	0.008
1.250	0.006	0.006	0.005	0.007	0.006	0.007	0.004	0.011	0.006	0.007
1.500	0.005	0.005	0.006	0.005	0.005	0.007	0.006	0.007	0.004	0.008
1.750	0.005	0.005	0.004	0.004	0.005	0.005	0.005	0.005	0.005	0.005
2.000	0.004	0.004	0.004	0.004	0.004	0.005	0.005	0.004	0.005	0.006
2.250	0.004	0.003	0.004	0.003	0.003	0.004	0.004	0.005	0.005	0.005
2.500	0.004	0.004	0.003	0.003	0.004	0.004	0.004	0.004	0.004	0.005

Table B.27: Ridge Identification Simulation Study - Constant Landmarks - Mesh Size .07 - Steepness- Curve Movement

CM	0.000	0.111	0.222	0.333	0.444	0.556	0.667	0.778	0.889	1.000
	Dev	Dev	Dev	Dev	Dev	Dev	Dev	Dev	Dev	Dev
Steepness										
0.250	0.010	0.009	0.009	0.009	0.010	0.012	0.010	0.011	0.012	0.012
0.500	0.009	0.010	0.009	0.008	0.012	0.011	0.011	0.010	0.011	0.013
0.750	0.008	0.008	0.011	0.010	0.010	0.013	0.009	0.009	0.013	0.013
1.000	0.006	0.007	0.009	0.009	0.007	0.009	0.010	0.013	0.011	0.009
1.250	0.006	0.005	0.005	0.006	0.006	0.007	0.008	0.009	0.007	0.010
1.500	0.004	0.004	0.005	0.004	0.004	0.007	0.007	0.006	0.008	0.007
1.750	0.004	0.004	0.003	0.005	0.004	0.004	0.005	0.008	0.007	0.007
2.000	0.004	0.003	0.003	0.004	0.003	0.004	0.004	0.005	0.006	0.005
2.250	0.003	0.003	0.004	0.003	0.004	0.003	0.004	0.004	0.004	0.005
2.500	0.003	0.003	0.003	0.004	0.003	0.003	0.005	0.004	0.004	0.004

TABLE B.28: Ridge Identification Simulation Study - Constant Landmarks - Mesh Size .08 - Steepness- Curve Movement

CM	0.000	0.111	0.222	0.333	0.444	0.556	0.667	0.778	0.889	1.000
	Dev	Dev	Dev	Dev	Dev	Dev	Dev	Dev	Dev	Dev
Steepness										
0.250	0.001	0.001	0.002	0.003	0.003	0.003	0.002	0.003	0.004	0.004
0.500	0.001	0.001	0.007	0.003	0.004	0.004	0.003	0.004	0.004	0.004
0.750	0.001	0.001	0.002	0.003	0.004	0.004	0.004	0.005	0.005	0.005
1.000	0.001	0.001	0.002	0.003	0.004	0.004	0.004	0.005	0.006	0.005
1.250	0.001	0.001	0.002	0.003	0.004	0.004	0.004	0.005	0.006	0.005
1.500	0.001	0.001	0.002	0.003	0.004	0.004	0.004	0.004	0.005	0.005
1.750	0.001	0.001	0.002	0.003	0.003	0.003	0.003	0.004	0.005	0.005
2.000	0.002	0.002	0.002	0.003	0.003	0.003	0.003	0.004	0.005	0.005
2.250	0.002	0.002	0.002	0.003	0.003	0.003	0.003	0.004	0.005	0.005
2.500	0.002	0.002	0.003	0.003	0.004	0.003	0.003	0.004	0.005	0.005

TABLE B.29: Ridge Identification Simulation Study - Constant Landmarks - Mesh Size .09 - Steepness- Curve Movement

CM	0.000	0.111	0.222	0.333	0.444	0.556	0.667	0.778	0.889	1.000
	Dev	Dev	Dev	Dev	Dev	Dev	Dev	Dev	Dev	Dev
Steepness										
0.250	0.006	0.006	0.006	0.007	0.006	0.007	0.007	0.008	0.008	0.008
0.500	0.006	0.006	0.006	0.007	0.007	0.006	0.008	0.007	0.017	0.008
0.750	0.006	0.007	0.006	0.008	0.008	0.007	0.008	0.007	0.008	0.008
1.000	0.006	0.006	0.007	0.007	0.008	0.007	0.007	0.009	0.012	0.008
1.250	0.006	0.006	0.006	0.007	0.007	0.007	0.007	0.010	0.008	0.008
1.500	0.006	0.006	0.006	0.008	0.008	0.008	0.007	0.008	0.008	0.010
1.750	0.007	0.006	0.006	0.007	0.008	0.009	0.008	0.010	0.008	0.009
2.000	0.007	0.007	0.006	0.007	0.008	0.008	0.008	0.009	0.011	0.008
2.250	0.007	0.007	0.007	0.007	0.006	0.008	0.009	0.008	0.009	0.010
2.500	0.007	0.007	0.007	0.007	0.007	0.010	0.009	0.010	0.009	0.009

TABLE B.30: Ridge Identification Simulation Study - Constant Landmarks - Mesh Size 1.0 - Steepness- Curve Movement

CM	0.000	0.111	0.222	0.333	0.444	0.556	0.667	0.778	0.889	1.000
	Dev	Dev	Dev	Dev	Dev	Dev	Dev	Dev	Dev	Dev
Steepness										

Table B.31: Ridge Identification Simulation Study - Constant Mesh Size - Landmark Movement 0.01 - Steepness- Curve Movement

CM	0.000	0.111	0.222	0.333	0.444	0.556	0.667	0.778	0.889	1.000
	Dev	Dev	Dev	Dev	Dev	Dev	Dev	Dev	Dev	Dev
Steepness										
0.250	0.002	0.002	0.002	0.002	0.002	0.002	0.002	0.003	0.003	0.003
0.500	0.001	0.002	0.002	0.002	0.002	0.003	0.003	0.003	0.003	0.003
0.750	0.002	0.002	0.002	0.003	0.005	0.003	0.003	0.004	0.003	0.004
1.000	0.002	0.002	0.002	0.005	0.005	0.003	0.003	0.003	0.006	0.004
1.250	0.002	0.002	0.002	0.003	0.006	0.003	0.003	0.003	0.004	0.003
1.500	0.002	0.002	0.002	0.002	0.004	0.003	0.003	0.003	0.004	0.003
1.750	0.001	0.002	0.002	0.002	0.003	0.003	0.002	0.003	0.003	0.003
2.000	0.002	0.002	0.002	0.002	0.003	0.003	0.002	0.003	0.003	0.003
2.250	0.002	0.002	0.002	0.002	0.003	0.003	0.002	0.003	0.003	0.003
2.500	0.002	0.002	0.002	0.002	0.003	0.003	0.003	0.003	0.003	0.003

Table B.32: Ridge Identification Simulation Study - Constant Mesh Size - Landmark Movement 0.02 - Steepness- Curve Movement

CM	0.000	0.111	0.222	0.333	0.444	0.556	0.667	0.778	0.889	1.000
	Dev	Dev	Dev	Dev	Dev	Dev	Dev	Dev	Dev	Dev
Steepness										
0.250	0.004	0.004	0.004	0.004	0.004	0.004	0.004	0.004	0.004	0.004
0.500	0.003	0.004	0.004	0.004	0.004	0.005	0.005	0.005	0.005	0.005
0.750	0.004	0.004	0.004	0.005	0.006	0.005	0.005	0.005	0.005	0.006
1.000	0.004	0.004	0.004	0.006	0.007	0.005	0.005	0.005	0.007	0.005
1.250	0.004	0.004	0.004	0.005	0.008	0.005	0.005	0.005	0.005	0.005
1.500	0.004	0.004	0.004	0.004	0.006	0.004	0.004	0.004	0.006	0.005
1.750	0.003	0.004	0.004	0.004	0.004	0.005	0.004	0.004	0.005	0.005
2.000	0.004	0.004	0.004	0.004	0.005	0.004	0.004	0.004	0.005	0.005
2.250	0.004	0.004	0.004	0.004	0.004	0.005	0.004	0.004	0.005	0.005
2.500	0.004	0.004	0.004	0.004	0.004	0.004	0.004	0.004	0.005	0.005

Table B.33: Ridge Identification Simulation Study - Constant Mesh Size - Landmark Movement 0.04 - Steepness- Curve Movement

CM	0.000	0.111	0.222	0.333	0.444	0.556	0.667	0.778	0.889	1.000
	Dev	Dev	Dev	Dev	Dev	Dev	Dev	Dev	Dev	Dev
Steepness										
0.250	0.011	0.011	0.011	0.011	0.010	0.010	0.010	0.010	0.010	0.009
0.500	0.010	0.011	0.011	0.011	0.010	0.011	0.010	0.010	0.010	0.010
0.750	0.011	0.011	0.011	0.011	0.012	0.011	0.010	0.010	0.010	0.010
1.000	0.010	0.011	0.011	0.012	0.012	0.011	0.010	0.010	0.012	0.010
1.250	0.011	0.011	0.011	0.011	0.013	0.011	0.010	0.010	0.010	0.010
1.500	0.011	0.011	0.011	0.011	0.011	0.010	0.010	0.010	0.011	0.010
1.750	0.010	0.011	0.011	0.011	0.011	0.010	0.010	0.010	0.010	0.010
2.000	0.011	0.011	0.011	0.011	0.011	0.010	0.010	0.010	0.010	0.010
2.250	0.010	0.011	0.011	0.011	0.011	0.010	0.010	0.010	0.010	0.010
2.500	0.011	0.011	0.011	0.011	0.011	0.010	0.010	0.010	0.010	0.010

Table B.34: Ridge Identification Simulation Study - Constant Mesh Size - Landmark Movement 0.06 - Steepness- Curve Movement

CM	0.000	0.111	0.222	0.333	0.444	0.556	0.667	0.778	0.889	1.000
	Dev	Dev	Dev	Dev	Dev	Dev	Dev	Dev	Dev	Dev
Steepness										
0.250	0.022	0.022	0.022	0.021	0.020	0.020	0.019	0.018	0.018	0.017
0.500	0.020	0.022	0.022	0.021	0.020	0.020	0.019	0.019	0.018	0.017
0.750	0.023	0.022	0.022	0.022	0.022	0.020	0.019	0.019	0.018	0.018
1.000	0.020	0.022	0.022	0.023	0.022	0.020	0.019	0.019	0.019	0.018
1.250	0.023	0.022	0.022	0.022	0.022	0.020	0.019	0.019	0.018	0.017
1.500	0.023	0.022	0.022	0.021	0.021	0.020	0.019	0.018	0.018	0.017
1.750	0.020	0.022	0.022	0.021	0.021	0.020	0.019	0.018	0.018	0.017
2.000	0.022	0.022	0.022	0.021	0.021	0.020	0.019	0.018	0.018	0.017
2.250	0.020	0.022	0.022	0.021	0.021	0.020	0.019	0.018	0.018	0.017
2.500	0.022	0.022	0.022	0.021	0.021	0.020	0.019	0.018	0.018	0.017

Table B.35: Ridge Identification Simulation Study - Constant Mesh Size - Landmark Movement 0.08 - Steepness- Curve Movement

CM	0.000	0.111	0.222	0.333	0.444	0.556	0.667	0.778	0.889	1.000
	Dev	Dev	Dev	Dev	Dev	Dev	Dev	Dev	Dev	Dev
Steepness										
0.250	0.036	0.036	0.036	0.035	0.033	0.032	0.031	0.030	0.029	0.028
0.500	0.033	0.036	0.036	0.035	0.033	0.032	0.031	0.030	0.029	0.028
0.750	0.037	0.036	0.036	0.035	0.034	0.032	0.031	0.030	0.029	0.028
1.000	0.033	0.036	0.036	0.036	0.034	0.033	0.031	0.030	0.030	0.028
1.250	0.037	0.036	0.036	0.035	0.035	0.032	0.031	0.030	0.029	0.028
1.500	0.037	0.036	0.036	0.035	0.034	0.032	0.031	0.030	0.029	0.028
1.750	0.033	0.036	0.036	0.035	0.034	0.032	0.031	0.030	0.029	0.028
2.000	0.036	0.036	0.036	0.035	0.034	0.032	0.031	0.030	0.029	0.028
2.250	0.033	0.036	0.036	0.035	0.033	0.032	0.031	0.030	0.029	0.028
2.500	0.036	0.036	0.036	0.035	0.033	0.032	0.031	0.030	0.029	0.028

Table B.36: Ridge Identification Simulation Study - Constant Mesh Size - Landmark Movement 0.10 - Steepness- Curve Movement

CM	0.000	0.111	0.222	0.333	0.444	0.556	0.667	0.778	0.889	1.000
	Dev	Dev	Dev	Dev	Dev	Dev	Dev	Dev	Dev	Dev
Steepness										
0.250	0.051	0.051	0.050	0.049	0.048	0.046	0.045	0.043	0.042	0.040
0.500	0.046	0.051	0.050	0.049	0.048	0.047	0.045	0.043	0.042	0.040
0.750	0.051	0.051	0.050	0.049	0.049	0.047	0.045	0.044	0.042	0.041
1.000	0.046	0.051	0.050	0.050	0.049	0.047	0.045	0.043	0.043	0.040
1.250	0.051	0.051	0.050	0.049	0.049	0.047	0.045	0.043	0.042	0.040
1.500	0.051	0.051	0.050	0.049	0.048	0.047	0.045	0.043	0.042	0.040
1.750	0.046	0.051	0.050	0.049	0.048	0.047	0.045	0.043	0.042	0.040
2.000	0.051	0.051	0.050	0.049	0.048	0.047	0.045	0.043	0.042	0.040
2.250	0.046	0.051	0.050	0.049	0.048	0.047	0.045	0.043	0.042	0.040
2.500	0.051	0.051	0.050	0.049	0.048	0.047	0.045	0.043	0.042	0.040

Bibliography

Y. Abed, G. Har-Zion, and M. Redlich. Lip posture following debonding of labial appliances based on conventional profile photographs. *The Angle orthodontist*, 79(2): 235–239, 2009.

J. Allanson, P. O'Hara, L. Farkas, and R. Nair. Anthropometric craniofacial pattern profiles in down syndrome. *American journal of medical genetics*, 47(5):748–752, 1993.

J. E. Allanson and R. Hennekam. Rubinstein-taybi syndrome: Objective evaluation of craniofacial structure. *American journal of medical genetics*, 71(4):414–419, 1997.

T. W. Anderson. *An introduction to multivariate statistical analysis*, volume 2. Wiley New York, 1958.

R. Armann and I. Balthoff. Male and female faces are only perceived categorically when linked to familiar identities. and when in doubt, he is a male. *Vision Research*, 63(0):69 – 80, 2012. ISSN 0042-6989. doi: http://dx.doi.org/10.1016/j.visres.2012.05.005. URL http://www.sciencedirect.com/science/article/pii/S0042698912001496.

S. F. Arnold. *The theory of linear models and multivariate analysis*, volume 2. Wiley New York, 1981.

A. G. Belyaev, A. A. Pasko, and T. L. Kunii. Ridges and ravines on implicit surfaces. In *Computer Graphics International, 1998. Proceedings*, pages 530–535. IEEE, 1998.

P. Billingsley. *Probability and measure*. John Wiley & Sons, 2008.

U. Bonde, V. Badrinarayanan, and R. Cipolla. *Multi scale shape index for 3d object recognition*. Springer, 2013.

C. E. Bonferroni. *Teoria statistica delle classi e calcolo delle probabilita*. Libreria internazionale Seeber, 1936.

F. L. Bookstein. Principal warps: Thin-plate splines and the decomposition of deformations. *IEEE Transactions on pattern analysis and machine intelligence*, 11(6):567–585, 1989.

F. L. Bookstein. Shape and the information in medical images: A decade of the morphometric synthesis. In *Mathematical Methods in Biomedical Image Analysis, 1996., Proceedings of the Workshop on*, pages 2–12. IEEE, 1996.

F. L. Bookstein. Landmark methods for forms without landmarks: morphometrics of group differences in outline shape. *Medical image analysis*, 1(3):225–243, 1997.

A. W. Bowman and A. Azzalini. *Applied smoothing techniques for data analysis*. Clarendon Press, 2004.

A. W. Bowman and A. Azzalini. *R package* `sm`*: nonparametric smoothing methods (version 2.2-5.4)*. University of Glasgow, UK and Università di Padova, Italia, 2014. URL URLhttp://www.stats.gla.ac.uk/~adrian/sm,http://azzalini.stat.unipd.it/Book_sm.

A. W. Bowman and M. T. Bock. Exploring variation in three-dimensional shape data. *Journal of Computational and Graphical Statistics*, 15(3), 2006.

A. W. Bowman, S. Katina, J. Smith, and D. Brown. Anatomical curve identification. *Computational Statistics & Data Analysis*, 2014.

Y. Bromberg, O. Katz, and Y. Silberberg. Ghost imaging with a single detector. *Physical Review A*, 79(5):053840, 2009.

C. Brönmark, T. Lakowitz, and J. Hollander. Predator-induced morphological plasticity across local populations of a freshwater snail. *Plos one*, 6(7):e21773, 2011.

A. M. Bronstein, M. M. Bronstein, and R. Kimmel. Three-dimensional face recognition. *International Journal of Computer Vision*, 64(1):5–30, 2005.

V. Bruce, A. M. Burton, E. Hanna, P. Healey, O. Mason, A. Coombes, R. Fright, and A. Linney. Sex discrimination: how do we tell the difference between male and female faces? *Perception*, 1993.

W. Che, X. Zhang, Y.-K. Zhang, J.-C. Paul, and B. Xu. Ridge extraction of a smooth 2-manifold surface based on vector field. *Computer Aided Geometric Design*, 28(4): 215–232, 2011.

P. Claes, M. Walters, M. D. Shriver, D. Puts, G. Gibson, J. Clement, G. Baynam, G. Verbeke, D. Vandermeulen, and P. Suetens. Sexual dimorphism in multiple aspects of 3d facial symmetry and asymmetry defined by spatially dense geometric morphometrics. *Journal of anatomy*, 221(2):97–114, 2012.

D. Colbry, G. Stockman, and A. Jain. Detection of anchor points for 3d face veri. cation. In *Computer Vision and Pattern Recognition-Workshops, 2005. CVPR Workshops. IEEE Computer Society Conference on*, pages 118–118. IEEE, 2005.

T. F. Cox and M. A. Cox. *Multidimensional scaling*. CRC Press, 2000.

S. Cunningham, N. Hunt, and C. Feinmann. Perceptions of outcome following orthognathic surgery. *British Journal of Oral and Maxillofacial Surgery*, 34(3):210 – 213, 1996. ISSN 0266-4356. doi: http://dx.doi.org/10.1016/S0266-4356(96)90271-5. URL http://www.sciencedirect.com/science/article/pii/S0266435696902715.

L. K. de Paula, A. C. O. Ruellas, B. Paniagua, M. Styner, T. Turvey, H. Zhu, J. Wang, and L. H. S. Cevidanes. One-year assessment of surgical outcomes in Class III patients using cone beam computed tomography. *INTERNATIONAL JOURNAL OF ORAL AND MAXILLOFACIAL SURGERY*, 42(6):780–789, JUN 2013. ISSN 0901-5027. doi: {10.1016/j.ijom.2013.01.002}.

E. W. Dijkstra. A note on two problems in connexion with graphs. *Numerische mathematik*, 1(1):269–271, 1959.

S. C. Doney, V. J. Fabry, R. A. Feely, and J. A. Kleypas. Ocean acidification: the other co2 problem. *Marine Science*, 1, 2009.

I. L. Dryden and K. V. Mardia. *Statistical shape analysis*, volume 4. Wiley Chichester, 1998.

D. Eberly. *Ridges in image and data analysis*, volume 7. Springer Science & Business Media, 1996.

L. Eidson, L. H. Cevidanes, L. K. de Paula, H. G. Hershey, G. Welch, and P. E. Rossouw. Three-dimensional evaluation of changes in lip position from before to after orthodontic appliance removal. *American Journal of Orthodontics and Dentofacial Orthopedics*, 142(3):410–418, 2012.

P. H. Eilers and B. D. Marx. Flexible smoothing with b-splines and penalties. *Statistical science*, pages 89–102, 1996.

R. Elston. On fisher's method of combining p-values. *Biometrical journal*, 33(3):339–345, 1991.

L. Evers, D. Molinari, A. Bowman, W. Jones, and M. Spence. Efficient and automatic methods for flexible regression on spatiotemporal data, with applications to groundwater monitoring. *Environmetrics*, 2014.

L. G. Farkas and S. A. Schendel. Anthropometry of the head and face. *American Journal of Orthodontics and Dentofacial Orthopedics*, 107(1):112–112, 1995.

S. Fitzer, L. Vittert, A. Bowman, and M. Cusack. Ocean acidification impacts mussel shell shape and thickness: problematic for protection? *Submitted to Global Change Biology*, 2015.

D. M. Gay. Brown's method and some generalizations, with applications to minimization problems. Technical report, Cornell University, 1975.

P. Gunz, P. Mitteroecker, and F. L. Bookstein. Semilandmarks in three dimensions. In *Modern morphometrics in physical anthropology*, pages 73–98. Springer, 2005.

J. F. Hair, W. C. Black, B. J. Babin, R. E. Anderson, and R. L. Tatham. *Multivariate data analysis*, volume 6. Pearson Prentice Hall Upper Saddle River, NJ, 2006.

P. W. Hallinan, G. G. Gordon, A. L. Yuille, P. Giblin, and D. Mumford. *Two-and three-dimensional patterns of the face*. AK Peters, Ltd., 1999.

P. Hammond, T. J. Hutton, J. E. Allanson, L. E. Campbell, R. Hennekam, S. Holden, M. A. Patton, A. Shaw, I. K. Temple, M. Trotter, et al. 3d analysis of facial morphology. *American journal of medical genetics Part A*, 126(4):339–348, 2004.

F. Han and S.-C. Zhu. Bayesian reconstruction of 3d shapes and scenes from a single image. In *Higher-Level Knowledge in 3D Modeling and Motion Analysis, 2003. HLK 2003. First IEEE International Workshop on*, pages 12–20. IEEE, 2003.

J. Hartmann, P. Meyer-Marcotty, M. Benz, G. Häusler, and A. Stellzig-Eisenhauer. Reliability of a method for computing facial symmetry plane and degree of asymmetry based on 3d-data. *Journal of Orofacial Orthopedics/Fortschritte der Kieferorthopädie*, 68(6):477–490, 2007.

T. Hastie and W. Stuetzle. Principal curves. *Journal of the American Statistical Association*, 84(406):502–516, 1989.

T. J. Hastie and R. J. Tibshirani. *Generalized additive models*, volume 43. CRC Press, 1990.

R. J. Hennessy, A. Kinsella, and J. L. Waddington. 3d laser surface scanning and geometric morphometric analysis of craniofacial shape as an index of cerebro-craniofacial morphogenesis: initial application to sexual dimorphism. *Biological psychiatry*, 51(6): 507–514, 2002.

H. Henseler, B. S. Khambay, A. Bowman, J. Smith, J. Paul Siebert, S. Oehler, X. Ju, A. Ayoub, and A. K. Ray. Investigation into accuracy and reproducibility of a 3d breast imaging system using multiple stereo cameras. *Journal of Plastic, Reconstructive & Aesthetic Surgery*, 64(5):577–582, 2011.

B. K. Horn and M. J. Brooks. *Shape from shading*. MIT press, 1989.

Y. Huang, Y. Wang, and T. Tan. Combining statistics of geometrical and correlative features for 3d face recognition. In *BMVC*, pages 879–888, 2006.

M. O. Irfanoglu, B. Gokberk, and L. Akarun. 3d shape-based face recognition using automatically registered facial surfaces. In *Pattern Recognition, 2004. ICPR 2004. Proceedings of the 17th International Conference on*, volume 4, pages 183–186. IEEE, 2004.

N. A. Kamenos, H. L. Burdett, E. Aloisio, H. S. Findlay, S. Martin, C. Longbone, J. Dunn, S. Widdicombe, and P. Calosi. Coralline algal structure is more sensitive to rate, rather than the magnitude, of ocean acidification. *Global change biology*, 19(12): 3621–3628, 2013.

S. Katina. In discussion with. *NA*, 2015a.

S. e. a. i. L. V. Katina. The definitions of three-dimensional landmarks on the human face: an interdisciplinary view. *Journal of anatomy*, 2015b.

D.-S. Kim, K.-H. Huh, S.-S. Lee, M.-S. Heo, S.-C. Choi, S.-J. Hwang, and W.-J. Yi. The relationship between the changes in three-dimensional facial morphology and mandibular movement after orthognathic surgery. *JOURNAL OF CRANIO-MAXILLOFACIAL SURGERY*, 41(7):686–693, OCT 2013. ISSN 1010-5182. doi: {10.1016/j.jcms.2013.01.011}.

Y.-K. Kim, N.-K. Lee, S.-W. Moon, M.-J. Jang, H.-S. Kim, and P.-Y. Yun. Evaluation of soft tissue changes around the lips after bracket debonding using three-dimensional stereophotogrammetry. *Angle Orthodontist*, 2015.

J. Koenderink and A. Doorn. Surface shape and curvature scales. *IVC*, 10:557–565, 1992.

J. T. Kost and M. P. McDermott. Combining dependent p-values. *Statistics & Probability Letters*, 60(2):183–190, 2002.

R. S. Kramer, A. L. Jones, and R. Ward. A lack of sexual dimorphism in width-to-height ratio in white european faces using 2d photographs, 3d scans, and anthropometry. *PloS one*, 7(8):e42705, 2012.

H. Le. Locating fréchet means with application to shape spaces. *Advances in Applied Probability*, pages 324–338, 2001.

C. E. Lefevre, G. J. Lewis, T. C. Bates, M. Dzhelyova, V. Coetzee, I. J. Deary, and D. I. Perrett. No evidence for sexual dimorphism of facial width-to-height ratio in four large adult samples. *Evolution and Human Behavior*, 33(6):623–627, 2012.

C. Loader. *Local regression and likelihood*, volume 47. springer New York, 1999.

H. S. Loos, D. Wieczorek, R. P. Würtz, C. von der Malsburg, and B. Horsthemke. Computer-based recognition of dysmorphic faces. *European Journal of Human Genetics*, 11(8):555–560, 2003.

M. Maeda, A. Katsumata, Y. Ariji, A. Muramatsu, K. Yoshida, S. Goto, K. Kurita, and E. Ariji. 3d-ct evaluation of facial asymmetry in patients with maxillofacial deformities. *Oral Surgery, Oral Medicine, Oral Pathology, Oral Radiology, and Endodontology*, 102(3):382–390, 2006.

A. P. Mangan and R. T. Whitaker. Partitioning 3d surface meshes using watershed segmentation. *Visualization and Computer Graphics, IEEE Transactions on*, 5(4): 308–321, 1999.

K. McNeil. *Analysis of Three-Dimensional Facial Shape*. PhD thesis, The University of Glasgow, 2012.

M. Meyer, A. Barr, H. Lee, and M. Desbrun. Generalized barycentric coordinates on irregular polygons. *Journal of graphics tools*, 7(1):13–22, 2002.

M. A. Muquit and T. Shibahara. A high-accuracy passive 3d measurement system using phase-based image matching. *IEICE Transactions on fundamentals of electronics, communications and computer sciences*, 89(3):686–697, 2006.

A. Naftel and M. Trenouth. Stereo-assisted landmark detection for the analysis of changes in 3-d facial shape. *Informatics for Health and Social Care*, 29(2):137–155, 2004.

A. Odén and H. Wedel. Arguments for fisher's permutation test. *The Annals of Statistics*, pages 518–520, 1975.

Y. Ohtake, A. Belyaev, and H.-P. Seidel. Ridge-valley lines on meshes via implicit surface fitting. In *ACM Transactions on Graphics (TOG)*, volume 23, pages 609–612. ACM, 2004.

J. O. Ramsay. Functional data analysis. *New York: Springer*, 2006.

D. Rueß, A. Luber, K. Manthey, and R. Reulke. Accuracy evaluation of stereo camera systems with generic camera models. *ISPRS-International Archives of the Photogrammetry, Remote Sensing and Spatial Information Sciences*, 1:375–380, 2012.

C. Samir, J.-P. Vandeborre, and M. Daoudi. Automatic 3d face recognition using topological techniques. In *Multimedia and Expo, 2005. ICME 2005. IEEE International Conference on*, pages 450–453. IEEE, 2005.

C. Samir, A. Srivastava, and M. Daoudi. Three-dimensional face recognition using shapes of facial curves. *Pattern Analysis and Machine Intelligence, IEEE Transactions on*, 28(11):1858–1863, 2006.

C. Samir, A. Srivastava, M. Daoudi, and E. Klassen. An intrinsic framework for analysis of facial surfaces. *International Journal of Computer Vision*, 82(1):80–95, 2009.

A. Srivastava, C. Samir, S. H. Joshi, and M. Daoudi. Elastic shape models for face analysis using curvilinear coordinates. *Journal of Mathematical Imaging and Vision*, 33(2):253–265, 2009.

A. Srivastava, E. Klassen, S. H. Joshi, and I. H. Jermyn. Shape analysis of elastic curves in euclidean spaces. *Pattern Analysis and Machine Intelligence, IEEE Transactions on*, 33(7):1415–1428, 2011.

F. M. Sukno, J. L. Waddington, and P. F. Whelan. 3-d facial landmark localization with asymmetry patterns and shape regression from incomplete local features. 2014.

B. Sun, M. P. Edgar, R. Bowman, L. E. Vittert, S. Welsh, A. Bowman, and M. Padgett. 3d computational imaging with single-pixel detectors. *Science*, 340(6134):844–847, 2013.

H. D. Tagare et al. A theory of photometric stereo for a class of diffuse non-lambertian surfaces. *IEEE Transactions on Pattern Analysis and Machine Intelligence*, 13(2): 133–152, 1991.

X. Tu, M. Subbarao, and Y.-S. Kang. A new approach to 3d shape recovery of local planar surface patches from shift-variant blurred images. In *Pattern Recognition, 2008. ICPR 2008. 19th International Conference on*, pages 1–5. IEEE, 2008.

M. Whitlock. Combining probability from independent tests: the weighted z-method is superior to fisher's approach. *Journal of evolutionary biology*, 18(5):1368–1373, 2005.

C. Wilkinson. *Forensic facial reconstruction*. Cambridge University Press, 2004.

F. W. WORMS, T. M. SPEIDEL, R. R. BEVIS, and D. E. WAITE. Posttreatment stability and esthetics of orthognathic surgery. *The Angle Orthodontist*, 50(4):251–273, 1980.

S. Yoshizawa, A. Belyaev, H. Yokota, and H.-P. Seidel. Fast, robust, and faithful methods for detecting crest lines on meshes. *Computer Aided Geometric Design*, 25(8):545–560, 2008.